Optically manipulated control over micron-scale signalling dynamics for directing cellular differentiation and migration

James Ware, BSc (Hons)

Thesis submitted to the University of Nottingham

for the degree of Doctor of Philosophy

September 2016

Abstract

Cellular microenvironments are an important area of study, and their implications with regard to development, tissue function, and disease, mean that they have particular relevance in tissue engineering. The development of tissue engineered therapeutics is underpinned by the understanding of how the cells exist in their natural environment. A fundamental lack of insight into the signalling mechanisms within microenvironments, due to in part a lack of appropriate technologies, has meant that the therapeutic potential of tissue engineering is limited. To this end, the development of a micropatterning technology that enables control over solute signalling dynamics on the micron scale has been investigated.

A bespoke holographic optical tweezers (HOTs) system was used to precisely position cells and controlled release vehicles into three-dimensional arrangements that resemble basic cellular micro-architectures. Via optical manipulation, release vehicles could be patterned to create solute release patterns to mimic signalling events *in vitro*.

A proof of concept was established to demonstrate fluorophore release from microparticles positioned with high precision, into previously unobtainable micron-scale patterns. Such developments required optimisation of the system and protocols, for use with cell and microparticle manipulation and, creating a tool-set suitable for address unsolved biological questions.

Biological investigations were completed to demonstrate how the HOTs can be used to control zonal cell differentiation and migration. These processes are

paramount to cell microenvironment function, and this study has shown that the HOTs patterning setup is capable of achieving such signalling models *in vitro*. Herein is presented compelling evidence that optically manipulated release sources can achieve new levels of precision over signalling dynamics, over the length scales suitable for even the smallest cell microenvironments.

It is hoped that through the better *in vitro* modelling of such cellular microenvironments and other signalling events, investigators will be able to elucidate new mechanisms through which cells proliferate and function.

Publications and Presentations

Journal Publication

Kirkham, G. R., Britchford, E., Upton, T., **Ware, J.**, Gibson, G. M., Devaud, Y., Ehrbar, M., Padgett, M., Allen, S., Buttery, L., and Shakesheff, K. Precision assembly of complex cellular microenvironments using holographic optical tweezers. Sci. Rep. 5, 8577 (2015).

Conference Publications and Presentations

Ware, J., Kirkham, G., Allen, S., Shakesheff, K. and Buttery, L. Optically controlled patterning of biochemical-laden microparticles for targeted developmental and chemotactic signalling gradients. International Society for Stem Cell Research (ISSCR). San Francisco; June 23-28th 2016

Upton, T., Britchford, E., Kirkham, G., **Ware, J.**, Gibson, G. M., Devaud, Y., Ehrbar, M., Padgett, M., Allen, S., Buttery, L., and Shakesheff, K. Using holographic optical tweezers as a tool to investigate cellular interactions. European Cells and Materials

Britchford E., Kirkham, G., Upton, T., **Ware, J**., Gibson, G. M., Buttery, L., Padgett, M., Allen, S. and Shakesheff, K. 3D Micro-Patterning of Biological Structures using Holographic Optical Tweezers. Tissue Engineering and Regenerative Medicine International Society (TERMIS-AM). Washington; December 13-16th 2014

Acknowledgements

I wish to thank my academic supervisors Prof. Kevin Shakesheff, Dr. Lee Buttery and Dr. Stephanie Allen for their backing and direction over the course of this project.

I am also incredibly grateful for the advice and guidance of the other “tweezer team” members, Dr. Emily Britchford, Thomas Upton and in particular Dr. Glen Kirkham for his continued assistance and input into my academic development and training.

I would like to thank our external collaborators the University of Glasgow for the construction and design of the holographic optical tweezer (HOTs) system and Teresa Marshall, Paul Cooling and Christine Grainger-Baltby for their assistance and technical training.

I would also like to thank all of those involved in the BBSRC Doctoral Training Partnership (DTP), and for giving me this opportunity and enabling me to develop as a confident researcher.

Many thanks also goes to my friends in the Tissue Engineering group, the DTP cohort, and other friendships that have feigned interest in my research, they have been invaluable and will not be forgotten, especially little Matty. I wish also to say thank you to my girlfriend, Sarah, whose unwavering support and affection has made this process all the more easy.

I would like to extend appreciation to my family, especially my younger brother, Duncan, for his valuable input and encouragement throughout my PhD. Lastly,

I would like to dedicate this thesis to my family members that have sadly passed away in recent times, in particular my auntie (Alison Main), for her kindness, devotion and unfaltering interest in my life and studies, she would have been so proud. This thesis is dedicated you, Ali.

Abbreviations

Θ	Degrees
ω	Angular Frequency
γ	Strain
η	Viscosity
G’	Storage Modulus
G’’	Loss Modulus
γlv	Interfacial Tensions Between Liquid-Vapour Phase
Γsv	Interfacial Tensions Between Solid-Vapour Phase
Γsl	Interfacial Tensions Between Solid-Liquid Phase
µg	Micrograms
µL	Microlitres
µm	Micrometres
µM	Micromolar
2D	Two-Dimensional
3D	Three-Dimensional
AM	Acetomethoxy
BSA	Bovine Serum Albumin
DMEM	Dulbecco’s Modified Eagle Medium
DMSO	Dimethyl Sulfoxide
ECM	Extracellular Matrix
EDTA	Ethylenediaminetetraacetic Acid
Em	Emission

Ex	Excitation
ES cell	Embryonic Stem Cell
Eth-D1	Ethidium Homodimer-1
FGF	Fibroblast Growth Factor
FCS	Foetal Calf Serum
G	Centrifugal G Force
HEPA	High Efficiency Particulate Air
HOTs	Holographic Optical Tweezers
HS cell	Haematopoietic Stem Cell
iPS cell	Induced Pluripotent Stem Cells
LIF	Leukaemia Inhibitory Factor
mΩ	Milliohns
mES cell	Mouse/Murine Embryonic Stem Cell
mg	Milligrams
mL	Millilitres
mm	Millimetres
mM	Millimolar
MMP	Matrix metalloproteinase
MSC	Mesenchymal Stem Cell
MTS	3-(4,5-dimethyl-2-yl)-5-(3-carboxymethoxyphenyl)-2-(4- sulfophenyl)-2H-tetrazolium
NA	Numerical Aperture
Nd:YAG	Neodymium-Doped Yttrium Aluminium Garnet
Nm	Nanometre
PBS	Phosphate Buffered Saline

PDMS	Polydimethylsiloxane
PDGF	Platelet-derived Growth Factor
PEGDA	Polyethylene Glycol Diacrylate
PFA	Paraformaldehyde
PLGA	Poly(lactic-co-glycolic acid)
PolyHEMA	Poly(2-hydroxyethyl methacrylate)
RGD	L-Arginyl-Glycyl-L-Aspartic acid
SD	Standard Deviation
SLM	Spatial Light Modulator
SS cell	Somatic Stem Cell
TGF	Transforming Growth Factor
U	Units
ULGT	Ultra Low Gelling Temperature
UV	Ultraviolet
v/v	Volume/Volume
WCA	Water Contact Angle
w/v	Weight/Volume

Table of Contents

List of Figures

List of Tables

1. Introduction

1.1 General introduction

This thesis details the development of a micropatterning tool-set capable of fabricating complex cell models. Furthermore, the thesis explores the many applications of such a technology, demonstrating its benefits to the fields of tissue engineering and stem cell research. This chapter serves to discuss the current literature of relevance to this thesis, explaining how this project fits into the wider research effort.

1.2 Tissue engineering

Tissue engineering and stem cell research comprise the broader field of regenerative medicine [1]. Through the combination of engineering, materials science, and cell biology, tissue engineering was born. With a broad set of aims, including the development of functional biological analogues for replacing damaged tissues, and to restore, maintain or improve tissue function [2,3].

The concept of tissue engineering was first conceived in 1933, when it was shown that murine tumour cells could survive on a biocompatible polymer membrane, be implanted into a chick embryo and proliferate [4]. Almost 50 years later, and the fabrication of artificial skin was demonstrated. Through the seeding of fibroblasts onto collagen scaffolds, a treatment for extensive burn injury was developed [5]. The use of stem cells to regenerate tissues and organs through implantation of cell-laden matrices predominates the current goals of tissue

engineering [6,7].The progress of various tissue engineering technologies is comprehensively reviewed by Kim and Evans (2005) [8].

It has, however, become increasingly evident that the organisation of cells, stem cells in particular, within these tissue-engineered architectures is more complex than previously thought. Thus, further basic research is required to understand how these cells function in their native environment. Without such research, the therapeutic potential of tissue engineering is limited.

1.3 Stem cell research

The current definition of a stem cell is any cell that has the capacity for self-renewal, and the ability to differentiate into several cell types; however, this working definition also recognises the important aspects of clonality and potency specifically associated with such cells [9]. Stem cells have an integral role in development from the very beginning of embryogenesis, and found in the inner cell mass of most eutherian organisms [10] are the embryonic stem (ES) cells [11] (Figure 1.1).

1.3.1 Embryonic stem cells

ES cells are termed ‘pluripotent’, able to differentiate into all of the somatic cells types from the three primary germ layers (endoderm, mesoderm, and ectoderm) [12]. These pluripotent cells are observed after the development of the blastocyst from the ‘totipotent’ morula, able to differentiate into all of the somatic and placental cells, and it is well-reported that ES cells play an integral part in embryogenesis. The blastocyst is made up of three main architectures, the

trophoblast, blastocoel, and ES-cell-composed inner cell mass (Figure 1.1). Human ES cells are commonly used in embryological research as they offer an *in vitro* model of development where direct *in vivo* experiments would not be possible due to ethical considerations [13].

ES cells are isolated from pre-implantation embryos, and then cultured to the blastocyst stage of development [14]. The isolation process often results in the destruction of the embryo, however, recent developments have reduced the incidence of embryo damage [15]. In the natural embryonic development, there are many interactions involved in maintaining pluripotency that are highly complex, to replicate this suppression of differentiation *in vitro*, leukaemia inhibitory factor (LIF) can be used. LIF forms a heterodimer between the LIF receptor and gp130, and, through the Janus kinase/signal transducers and activators of transcription (JAK/STAT) pathway, pluripotency is maintained [16]. Both murine and human ES cells can divide many times in culture so long as they retain their pluripotency [17], pluripotency being identified by the presentation of cell surface markers Oct-3/4, Sox2, and NANOG[18].

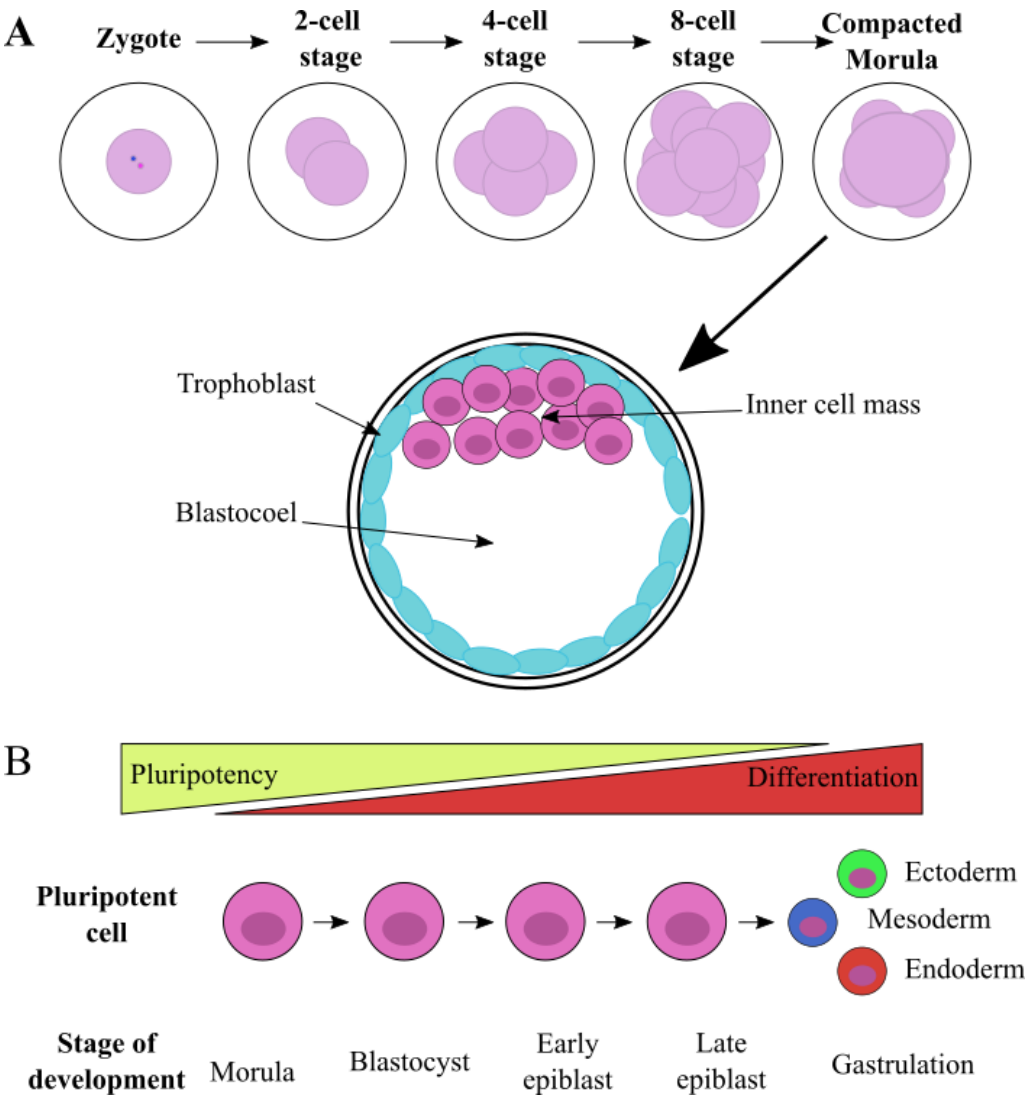

Figure 1.1 Embryonic stem cell and embryonic development

Diagrammatic representation of the formation of the compacted morula from a zygote (A), and the development of pluripotent embryonic stem cells up until Gastrulation. Then as pluripotency decreases and cells begin differentiating through the stages of embryonic development leading to the formation of the three primary germs layers. Images are not to scale.

1.3.2 Somatic stem cells

Somatic stem (SS) cells do not possess pluripotency, but are instead multipotent, meaning that they can differentiate into the cell types of the tissue from which they are isolated. Examples include mesenchymal, haematopoietic, and umbilical cord stem cells. SS cells can be directly derived from an individual, and then expanded for autologous re-implantation [19]. It is this property that makes them an attractive area of research for the development of tissue-engineered therapies. Furthermore, these cells are less ethically controversial than ES cells, as their extraction does not lead to the destruction to the organism from which they are derived.

As SS cells have been used for clinical applications for many years, the best-known example being the use of bone marrow for transplantation. Within the bone marrow lies the haematopoietic stem cells that are capable of differentiating into both the myeloid and lymphoid lineages that make up the blood [20]. Another widely studied SS cell type is the mesenchymal stem cell, shown *in vitro* to differentiate into multiple mesodermal lineages, including myocytes, neurones, chondrocytes, osteoblasts, and adipocytes [21,22]. Mesenchymal stem cells have been investigated for their capacity to regenerate bone and other tissues, but, like other SS cells, their clinical applications are heavily restricted [23].

1.3.3 Induced pluripotent stem cells

Although in nature adult stem cells cannot revert to a pluripotent state, they can be regenerated by nuclear reprogramming. This is the technique that alters gene activity by the introduction of nuclei/genes into a cell's cytoplasmic environment

[24]. Induced pluripotent stem (iPS) cells were first created by the retroviral delivery of five key genes, *Oct-3/4, Klf4, Sox2,* and *c-Myc,* into mouse fibroblasts [25]. This technique was later developed through the selection for Nanog that left 'germ line competent' iPS cells [26,27,28]. Soon after the generation of mouse iPS cells, human iPS cells were formed [29]. Again coming out of Kyoto University, this discovery offered new opportunities for studying various disorders (e.g. blood disorders and neurodegenerative conditions) using these cells derived from donors afflicted with these disorders [30,31].

1.3.4 Stem cell niche

All stem cells are found within a specific 'niche', the microenvironment that provides instructive cues for differentiation and regulation of quiescence. Simple experiments co-culturing ES cells with bone marrow stromal cells have resulted in increased levels of differentiation to haematopoietic stem cells [32], thus demonstrating the importance of the environment around stem cells (Figure 1.2). As well as other cell types having an effect upon the niche, diffusible signals of growth factors and morphogens play an integral role in regulating self-renewal and cell fate commitment in adult stem cells. These signals can be released in a paracrine manner from cells within the niche, by the juxtacrine route of cell-contact-dependent signalling, and by the autocrine signal through which the cell signals to itself. Signals from outside the niche are also of the utmost importance; paracrine signals mediated by cytokines, pH, ATP, metabolites, etc., associated with tissue damage and other stresses, are necessary for triggering specific differentiation when new cells are required. Using the aforementioned signalling

mechanisms, the stem cell niche and its diverse components are able to influence stem cell behaviour.

The extracellular matrix (ECM) is also an important part of most cell niches; it is well-known that integrins, major receptors that permit communication between the ECM and cells, are involved extensively in crosstalk with the growth factors and morphogens mentioned above [33]. The ECM has an integral role in stem cell determination via cell adhesion [34], and so plays an important part in the development and maintenance of the niche. The components of almost all ECMs comprise proteoglycans, non-proteoglycan polysaccharides, fibres, and other glycoproteins. However, the complexity and integration of these components is still far from being understood [35].

Diffusible signals are of great importance for the development of certain niches, and represent, in the model organism *Drosophila melanogaster*, highly active areas of research. The development of the germline stem cell (GSC) niche that forms within a well-defined environment is an excellent model for studying niche development [36]. Early work demonstrated how somatic cells, like the cyst progenitor cells found within the *Drosophila* GSC niche, produce cyst cells that 'nurture' the GSCs within the normally functioning niche [37]. Diffusible TGF-β signalling is also important in the upkeep and development of this niche [38,39], showing just how multifactorial niche development can be. Mammalian organisms rely upon diffusible signalling just as much, in the human intestine, highly specialised villi are required to increase surface area for absorption of digested foods. Their complex structures and cell organisation are formed and maintained by stem cells residing in an intestinal crypt that provides the specialised cell types required during intestinal lining homeostasis. Cellular

organisation and development within a crypt relies heavily upon diffusible signals, with Wnt and Notch signalling providing a proliferative signal [40] and BMP and TGF-β providing the differentiative compartment [41]. Through dynamic signalling events involving these factors, adult stem cells in the bottom of the crypt proliferate as transit amplifying cells which then undergo differentiation into paneth, goblet, and entero-endocrine cells that make up the various types of villi along the intestinal tract [42]. Other important signalling molecules include; Hedgehog, which is capable of transmitting information over several cell diameters and has been extensively studied for its role in the formation of the wing imaginal disc [43]. Wnt/Wg ligands, that act over long range and are known to be regulated in a spatiotemporal manner to elucidate specific developmental patterning events [44]. RTK growth factors, including Epidermal Growth Factor (EGF), Fibroblast Growth Factor (FGF), and Platelet-derived Growth Factor (PDGF) that are required for morphogenesis, growth and patterning [45].

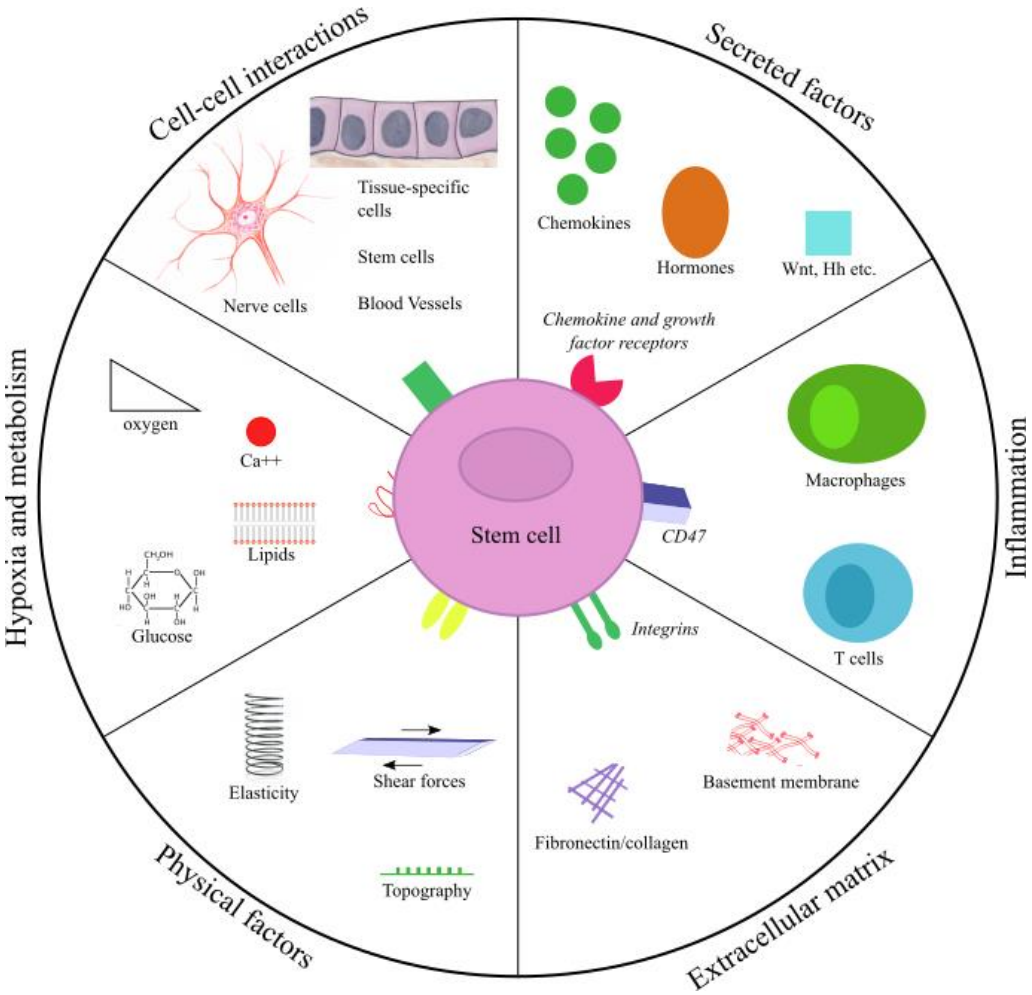

Figure 1.2 Stem cell niche factors

Schematic showing the various factors (Physical, ECM, Inflammatory, Secreted, cell-cell, other factors) and examples of which, that interact in the dynamic stem cell niche. Adapted from Lane *et al.* (2014) [46].

1.4 *In vitro* cell modelling

Mammalian cell culture involves the dispersal of tissues into single cells or aggregates, grown in conditions that resemble the natural conditions of the body. The growth of cells in this way began in glass bottles or plates, hence the term '*in vitro'* was coined from the Latin '*vitrum*', meaning glass. However, even today, cell culture methods are yet to mimic exactly the natural conditions of a living organism, or '*in vivo*', from the Latin '*vivere*', to live. As such, all cell culture systems, basic to advanced, are termed 'model systems' [47]. *In vitro* cell modelling has provided investigators with a means to assess cellular function, development, and disease progression.

Two-dimensional (2D) cell culture, or monolayer culture, has been widely used to investigate many different biological functions. Such culture models are generally easy and convenient to set-up, and yield highly viable cells, however, by definition they lack the three-dimensional (3D) microenvironment of intact tissues. The use of 2D culture has been reported to provide misleading and nonpredictive data for *in vivo* responses [48–50], and as such, 3D micropatterning technologies are highly sought after. Monolayer culture models have been used with great success, furthering understanding of the natural cell environment, however, this introduction mainly focusses on more advanced 3D cell culture models.

1.4.1 Disease modelling

The development of tissue-engineered models of disease shows great promise. Great advances have been made through the development of animal disease

models, including transgenic mice that to some degree recapitulate human conditions. However, it remains difficult to isolate the cellular or molecular aetiology of a disease in animal models. This challenge has led to an effort from tissue engineers to develop better *in vitro* models of disease.

One such example of a successful cell-based disease model is the fabrication of diseased cardiac stem cell assays to overcome substantial differences between human and animal genomes. A successful model for the inherited cardiomyopathy long QT syndrome, characterised by a prolonged QT interval and delayed repolarisation resulting in a lethal polymorphic ventricular tachycardia. Human iPS cells were generated from dermal fibroblasts obtained from a long QT syndrome sufferer. iPS-derived cardiomyocytes were developed that presented with the same prolonged action potential as seen with the disease [51]. This model has since been employed to assess drugs that may be suitable as treatments for the disease.

Whilst these cell models hold great promise, and are advantageous over animal models, they are still subject to limitations. The iPS-cell-derived cardiomyocytes are usually immature and not representative of those from adult cardiac muscle [52], and the cell-based assays do not fully reflect the environmental and epigenetic factors of the disease. A solution to this is the construction of cardiac tissues that mimic the native microenvironment. Tissue engineers have demonstrated the construction of aligned cardiac muscle cells that better replicate the structure and function observed on the tissue level [53,54]. Such an appreciation of the single cell organisation and the environment around it is seen as the clear path to achieving successful *in vitro* disease models. Further analysis and review of the current

technologies involved in the development of better *in vitro* cell models for disease have been completed by Benam *et al*., 2015 [55].

1.4.2 Developmental biology

Embryonic development is known to occur through highly complex and tightly regulated cell-cell and diffusible signalling interactions. One of the most commonly studied *in vitro* cell models for embryonic development is the embryoid body (EB). Named for their likeness to post-implantation embryos, the morphogenic events in EBs have been shown to bare close resemblance to multiple aspects of embryonic development. EBs have been shown to be able to form a primitive endoderm [56,57], exhibit epithelial to mesenchymal transition [58], and form all three primary germ layers [59,60]. Furthermore, the process of mouse embryo cavitation has also been examined using EBs [61].

EBs have been used as a unique tool to investigate developmental biology due to their mimicry of post-implantation embryos as discussed above. Furthermore, the establishment of this model has contributed to a reduction in the number of animal experiments required for pharmacological testing [62]. Whilst much of the development made in the elucidation of embryogenesis was achieved by virtue of EB research, the limitations of EBs must be acknowledged. A phenomenon of EB formation that brings into question the use of EBs as *in vitro* models is the reported stochastic patterning and development that occurs during this process. The signalling environment within an EB is thought to lead to this chaotic development, and, as such, EB-based embryogenesis-like development requires further clarification.

A recent *in vitro* cell model breakthrough was the formation of organoids for a wide range of different tissues. The term organoid encompasses all 3D organotypic culture systems, said systems being derived from ES cells, iPS cells, cell lines and organ explants[63]. Unlike EBs, most organotypic culture relies upon artificial ECM and soluble factor supplementation to facilitate self-organisation into structures that resemble native tissues. Following the development of an intestinal organoid culture system, comprising matrigel supplemented with key endogenous niche signals (Wnt, Noggin and R-Spondin)[64], many other organoids have been successfully developed. The discussion of these innovative *in vitro* model systems is not discussed here, but it is well reviewed by Fatehullah *et al.,* 2016[63].

1.5 Micropatterning

In the biological world, patterns exist in a range of complexity; they form the building blocks of life itself[65]. Pattern formation, the generation of this complex ordering[66], has been scrutinised by many scientists in the fields of molecular biology, tissue engineering, developmental biology, and other disciplines. Theoretical models have been constructed to explain the organising behaviours of biological systems[67], however, there is still much to be learnt about how cells are organised into tissues during development and repair[68]. As was previously discussed, cells are organised within their niche by a variety of different signals, the combinations of these complex interactions can bring about pattern formation within the niche or throughout the tissue. Organised structures of stripes [69], waves [70], and perhaps of most interest, branching patterns can be formed [71]. Branching patterns are essential in many areas of development, uteric

bud branching has been investigated; to engineer a functional kidney this branching pattern must be replicated exactly [72,73].

Recreating pattern formation is a major goal for tissue engineers that are hoping to induce pattern organisation in regeneration. To reach this goal, it is necessary to understand how stem cells in certain patterns and topological configurations can develop into functional tissues. Research into the development of complex stem cell patterns is currently very popular, and there are a number of methods that can be utilised to create such patterns.

There are a variety of different techniques used by researchers to investigate the importance of patterning in development and tissue engineering. These include micropipette aspiration, atomic force microscopy (AFM), lithography, stencils, microfluidics, magnetic tweezers, acoustic tweezers and optical tweezers. For the purpose of this literature review these methods are discussed in varying degrees of depth depending on how relevant they are to this project. More in-depth comparisons of these techniques are available elsewhere [74].

Micropipette aspiration involves using a glass pipette with a variably sized bore and tip, suction can be applied to the pipette to allow the manipulation of single cells by manually moving them from one position to another [75]. This process can be highly time consuming and is technically demanding, however, recent work has incorporated a robotic system that can track and capture single cells [76]. AFM works by running a sharp tip over a surface, any movements made by deflections from the surface are recorded by laser scanning analysis, thus showing the biophysical properties of the surface sample. AFM has many uses, commonly it is used as a microscope, but other tasks, including spectroscopic analysis, surface

modification, force measurements, and manipulation are also possible [77]. Using an AFM probe, simple 2D movements can be achieved by pushing or pulling cells, however, more complex tasks like positioning or patterning require multiple probes. There are a variety of lithographic methods of patterning available at present, the premise for this method is that surfaces can be shaped into complex high-resolution patterns, such that cells then populate these modified areas in accordance with the commanded pattern [78]. This technique would be good for patterning cells upon a variety of different surfaces; however, the patterns could only be manipulated in 2D. Microfluidics is a standalone method for cellular manipulation [79,80], but it can be used alongside lithographic techniques to provide nutrient-containing media for longer-term patterning, and also to introduce a 3D aspect to patterning in ECM biopolymers. The manipulation of cells via microfluidics systems is usually less precise than other patterning techniques, however, it does allow the formation of co-culture spheroids through hydrodynamic cellular patterning, an important technique for the manipulation of interactions between different cell types in 3D [80].

Lithographical techniques have been used to alter the topography of surfaces to evaluate their effect on cells. Using controlled micro- and nano-topographies, it has been shown that cell migration, differentiation and even consistent genetic changes can be brought about by altering the material surface morphology [81]. Using different topologies can be used to micropattern cell patterns by providing specific areas for the cells to adhere to. Using these techniques, many cells can be positioned onto micron-scale surface patterns, however, resolution is generally low and 2-dimensional due to random seeding of the cells onto these attachment areas [82].

Magnetic [83,84], acoustic [85,86], and optical tweezers [87] are all direct patterning techniques involving the positioning of cells into complex patterns or arrays. However, the forces they utilise to achieve this are quite different for each technique, consequently, different limitations and advantages apply to each. Therefore, the nature of the application determines which approach is most appropriate. Magnetic tweezers are an important tool for investigating the tensile strength or forces exerted by cells and molecules [88]. Due to their simple design, magnetic tweezers are popular in the field of biophysics, and can be easily modified to fit the experiment. As the name suggests, they are equipped with magnets, and, guided by the use of microscopy, they can be used to manipulate cells and particles laden with magnetic beads [89]. The major limitation associated with this simple setup is that patterns can only be made in 2D, and is thus incapable of the 3D patterning towards which modern tissue engineering is advancing. There are now magnetic tweezer systems that utilise the power of several electromagnets to crudely control cell/particle position in 3D space [88], however, the simplicity and robustness of the original system is lost with this development. Acoustic tweezers also are limited to 2D, however, if patterns are created within a gel or semi-solid structure, they can be stacked to create 3D configurations. Acoustic tweezers have the ability to create complex arrays of patterns comprised of many cells across a surface [90]. They work by propagating a sound wave along a surface, generating leakage waves which cause pressure fluctuations in the medium [91]. This in turn leads to the propagation of acoustic radiation forces that act upon the suspended cells or particles, moving them to areas of high pressure nodes [92]. Acoustic tweezers are able to move objects seamlessly whilst only introducing a low level of mechanical vibration to the

suspension [93]. The low level of disturbance that acoustic manipulation has been shown to evoke makes this method of patterning highly desirable for tissue engineering purposes. For cellular patterning, a high level of precision is required; acoustic tweezers achieve such a level, however, the optical tweezers are yet more precise. MacDonald et al. (2002) illustrated this precision with the manipulation of high-refractive-index silica particles using the optical tweezers. His team were able to create high-resolution 3D patterns whilst simultaneously rotating the whole silica particle structure; the team proffered the use of optical tweezers to create extended crystalline complex structures [94], previously requiring unimaginable meticulousness. Optical tweezers have also been used to pattern surfaces, an operation required for a variety of different applications, and the nanoscale fabrication of advanced materials requires the precision that optical tweezers offer. One such application is the production of templates for the 3D self-assembly of materials used in advanced optics. Colloidal particles, the building blocks for such material assemblies, can be patterned and affixed to surfaces using optical manipulation. [95] Advanced materials like colloidal crystals can be precisely formed in such a way [96]. Guffey and Scherer (2010) used optical trapping to manipulate and pattern individual gold nanoparticles fastidiously, a great achievement in the field of nanotechnology. The group calculated that the patterning precision they achieved had less than 100nm of standard deviation, optical manipulation alone is capable of such precision [97]. Optical tweezers have proved to be an effective tool for certain applications of micro-manipulation, and show promise as a biological patterning device.

1.6 Concentration gradients

As previously discussed, soluble factor signalling and, in some cases, gradient formation is of known biological importance. In the field of stem cell research, solute signalling can direct processes such as cellular migration [98–101], stem cell differentiation [102,103], and cellular development [104,105]. Soluble factor signalling within the *in vivo* environment is complex, and involves molecular recognition between soluble molecules and ECM components in addition to spatiotemporal interactions. This complexity is limiting to the *in vivo* study of soluble transport, and is therefore one of the many areas that benefits from the use of well-defined *in vitro* modelling platforms. A large proportion of modelling platforms are based around mimicking the native ECM with synthetic hydrogels. Investigators have developed means by which to study soluble transport and the formation of gradients within these hydrogels [106].

Early attempts to understand the influence of soluble signalling on cells used platforms such as the Boyden chamber [107,108], Zigmond chamber [109], and Dunn chamber [110]. These techniques permitted the observation of cellular behaviour in response to a linear concentration gradient, with gradient stability lasting for many hours. Whilst these methods were highly suitable for certain cellular applications, the study of *in-vivo*-like concentration gradients at the single-cell level was not possible. Recent developments towards this goal include the use of the agarose/petri dish and micro-aspirator to recreate chemical environments on much smaller scales [111]. These different technologies have led to a much greater understanding of how cells respond to various signalling pathways,

however, they are yet to recreate the diminutive scale of relevance to many cell types and models [112].

One technology that is more suitable for developing and maintaining stable micron-scale chemical gradients is microfluidics. Microfluidic devices are typically fabricated in polydimethylsiloxane (PDMS) using soft lithography [113] to create a series of channels suitable for the receiving the injection of small volumes through inlets. The injection, typically controlled by syringe pumps, and channel design can be used in such a way as to mix signalling chemicals and buffers to yield controlled linear and non-linear gradients with spatial flexibility across a sample. Using microfluidics, cellular chemotaxis can be studied effectively and efficiently [114]. Whilst the benefits of microfluidics are well-documented, there still exists disadvantages of using the technique with cells. Flow within microfluidic devices generates shear stress that has been reported to adversely affect cell health, and this has limited the use of microfluidics for cell-based experimentation [115]. Recently, developments have been made to reduce the intensity of shear stress within microfluidic devices [116], and these are seen as the way forwards for cell-based uses of this technology.

1.7 Microparticles - Controlled and localised release

Controlled release microparticles are a well-established means by which to deliver encapsulated molecular cargo to cells and tissues [117]. By altering the polymer formulation and encapsulation method employed, control over the microparticle release characteristics can be achieved. Microparticle physicochemical properties related to biocompatibility have been thoroughly investigated [117–120].

Microparticles have been used *in vivo* to deliver systemic drug therapies in the case of certain cancer treatments. In one case, the therapeutic molecule, retinoic acid, was encapsulated into polymer microparticles subsequently administered to mice with head-and-neck tumours. Tumour volume was later measured and compared to that of a control group, showing the local delivery of retinoic acid to have led to a 53% reduction in tumour volume[121].

Various *in situ* tissue engineering applications[122,123] have utilised microparticles to promote cell survival *in vivo* by providing a temporary substrate for cell adhesion and locally delivering morphogens [124–126]. Those involved in these successful studies herald microparticles as a suitable technology for delivering instructive cues and signalling molecules to their immediate vicinity. Perhaps they could be used in a similar manner, to mimic autocrine signalling and influence cellular differentiation.

1.8 Optical manipulation

In the early 1970s, a new field of laser-based optical trapping was born; its pioneer was Arthur Ashkin of the AT&T Bell Laboratories. Ashkin showed that 'optical forces' could displace and levitate dielectric particles at the micron scale [127], and he developed the 'optical levitation trap' [128] to demonstrate this. He went on to develop 3D traps based on counter-propagating laser beams, and then the single-beam gradient optical trap, or 'optical tweezers' as they are now known, capable of trapping particles of 25 nm in diameter [87]. He employed these optical tweezers in a wide range of experiments, including the manipulation of live bacteria and viruses [129,130,131].

In order to describe the forces generated by these optical tweezers, it is first essential to understand how forces of light may be compared. Photons carry both energy and momentum; if these photons are absorbed by an object, the momentum from the photon beam of power *P*, is transferred to a reaction force *F* on the object, given by:

$$F = \frac{nP}{c}$$

,where c is the speed of light and n is the refractive index of the surrounding medium [87].

The reaction force necessary allows the optical tweezers to trap high-refractive-index objects (*n* particle < *n* media) [132], however, this reaction force creates traps for small objects (particles smaller than the applied wavelength of light) in a different manner to that observed with larger objects. When the trapped particle is much smaller than the laser wavelength, the conditions for Raleigh scattering are satisfied and the 'small particles' develop an electric dipole moment in response to the light's electric field. The light's electric field is most intense at the point of focus, and so the small object is drawn into the focal point and trapped by the Lorentz force due to the laser's electric field gradient [133]. The intricacies of trapping such small particles are discussed further by Molloy and Padgett[134], in this literature review the trapping of larger objects is focussed on, those of the micron scale.

If the object to be trapped is larger than the wavelength of the light, then refraction of the light rays is observed, causing a redirection of the momentum transferred to it by the photons. The resulting forces, or recoil, draws the object

towards the higher flux of particles at the point of focus [135]. Two main forces that result from the transfer of energy and momentum from photons to an object are antagonistic to one another, and are termed the 'gradient' and 'scattering' forces. The scattering force occurs due to the absorption of momentum from photons in a beam and the resulting Fresnel reflections [136]; it acts like a fan blowing the particles down the optical axis. In order to create a stable optical trap, the axial gradient force must dominate; this occurs when the beam separates quickly away from the focal point, the use of a microscope objective with a high numerical aperture that focuses the light as much as possible achieves this [137]. These axial forces create the stable trap, and any small displacement of the object results in a 'restoring force' back towards the focal point [87,135]. The stable optical trap created by the aforementioned forces is shown in the diagram below (Figure 1.3).

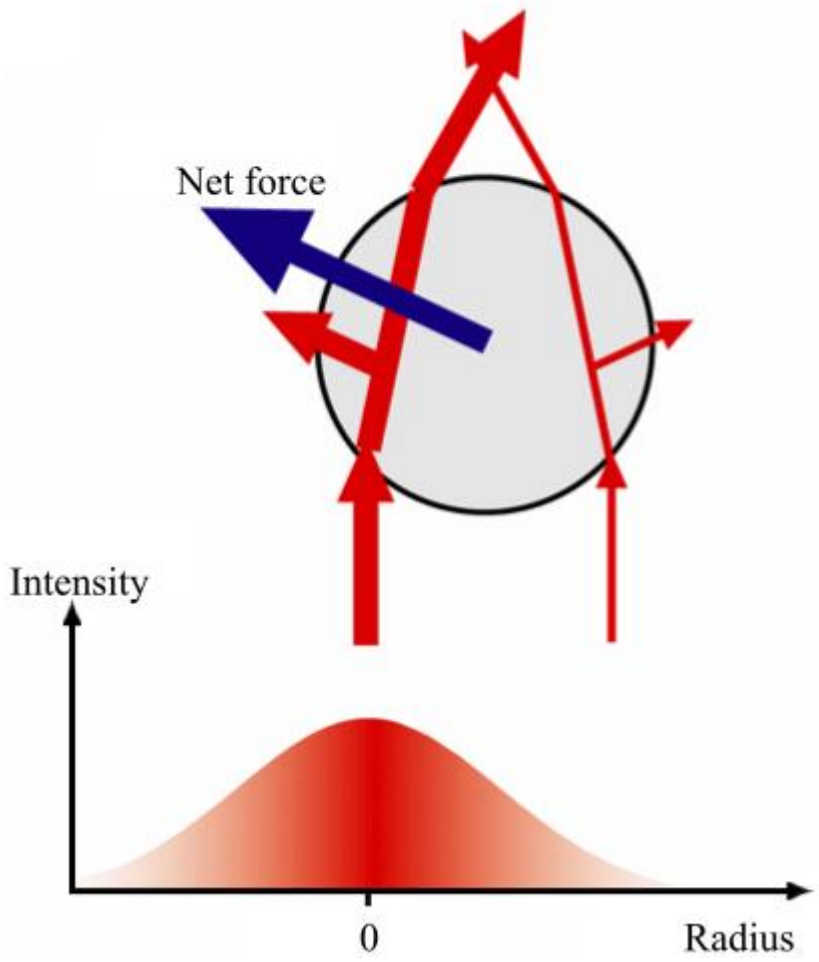

Figure 1.3 Optical trapping

Simple diagrammatic representation of the optical trapping of a dielectric particle, of greater size than the laser wavelength, the gradient forces allow xy-axis movement of the particle and the scattering force acts against gravity to permit z axis movement. Figure adapted from Gouesbet *et al.* (1999) [138].

The scattering force is known to be isotropic, its momentum is the same when measured in different directions, and the net momentum of the scattering force is transferred in the forward direction. This can be pictured on the quantum level, as photons from the laser beam are all travelling in the forward direction, then being scattered isotropically. By applying Newton's second and third laws, the conservation of linear momentum can be deduced, by which the object must receive the photon's original momentum thus applying a forward force upon the object [139].

Optical tweezer development since 1986 [87] has mainly been driven towards tailoring the original design to specific purposes in the fields of physics [140] and biology. However, in the early 1990s, a method for trapping multiple objects by the scanning of one single beam trap along a variable number of positions was developed [141]. This research was of particular importance as it allowed for the manipulation of objects that were previously not trappable. The work of Koen Visscher prompted the development of the truly multi-trap-creating optical tweezers commonly used today. Eric Dufresne and David Grier from the University of Chicago developed this 'hexadeca tweezer' [142]; optical tweezers which creates multiple traps from a single laser beam using diffractive optical elements. Their work demonstrated the first arrays of traps, and the formation of complex 3D patterns made from sub-micron silica spheres.

The aforementioned diffractive optical elements can either be static and etched into glass, or in the reconfigurable form of a spatial light modulator (SLM)[143,132,144], a phase hologram that can be controlled in real-time. Although there are various types of SLM, the most commonly used variety will be focussed on, the phase-only, liquid crystal, reflective SLM. Liquid crystal SLMs

are available as either electrically- [145] (Boulder), or optically- [146] (Hamamatsu) addressed, the character of the liquid crystal governs the properties of the SLM as a whole[147]. The SLM works by applying small well-defined voltages to an array of areas spread across the layer of liquid crystals, to which the liquid crystals respond by realigning themselves. This realignment changes their optical properties, allowing the controller to create selected phase shifts upon the incident beam that in turn control the beam angle and divergence [146]. This feature defines the modern optical tweezers, known as holographic optical tweezers (HOTs), which permit the formation of complex patterns of cells and particles alike via optical manipulation. Such control of multiple elements makes the HOTs a promising tool for the future of niche biomimicry and the replication of developmental models. The configuration of the modern HOTs varies depending on their use, but it is generally based upon the schematic shown in Figure 1.4.

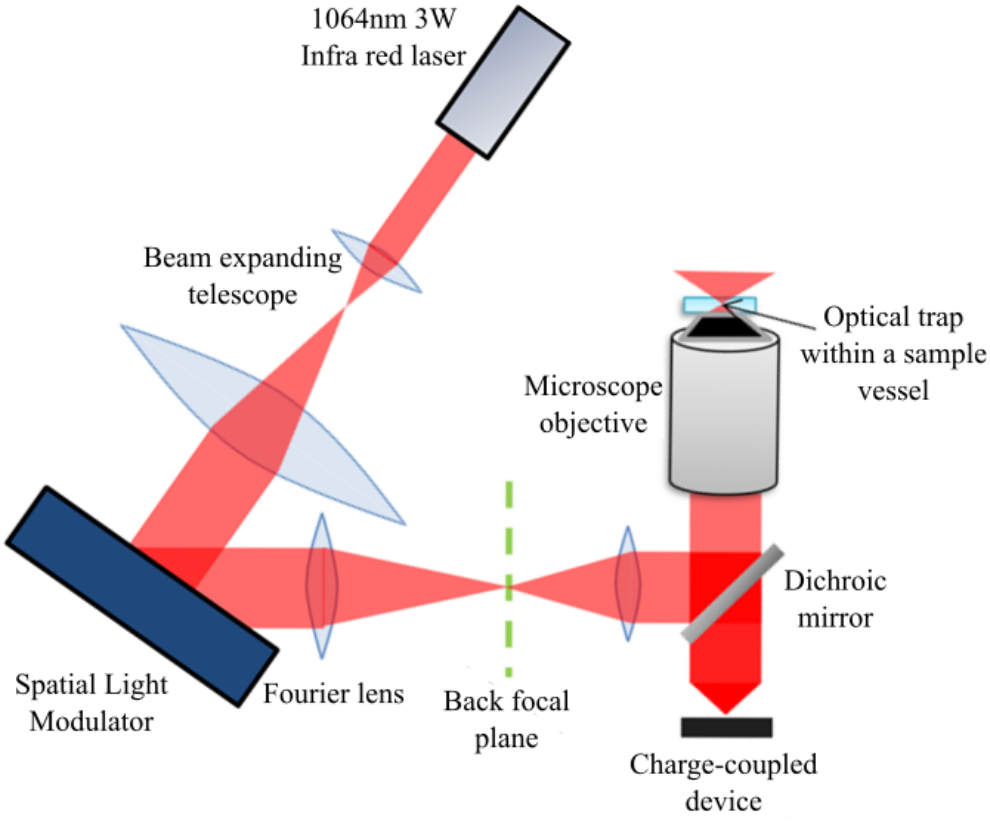

Figure 1.4 HOTs schematic

The schematic above shows a simplified standard HOTs setup. The 1064 nm laser beam is widened through a beam telescope to illuminate the spatial light modulator. The diffracted beam of the first order passes through the Fourier lens. The back focal plane must be perpendicular to the optical axis which passes through the front and rear focal points.

1.9 Optical manipulation of cells

The first optical manipulation of living cells was demonstrated by Ashkin in 1987, here, damage to the samples was clearly apparent [131]. This led to the use of a longer wavelength Nd:YAG laser to avoid such short wavelength induced damage [130,131], and later biological experiments used a similar laser source. There have been a variety of experiments using the 'long wavelength' 1064 nm infrared laser to test the viability of biological material. Early *Escherichia coli* experiments tested the laser's effect with up to 3 W of power from source. It was discovered that the longer wavelength lasers (1064 nm) caused far less thermal damage to biological objects compared to the aforementioned shorter wavelength sources[130]. Further viability studies, with *E. coli* encapsulated within a gelatin structure, showed the effect of optical manipulation upon bacteria using 200 mW for 10 minutes, then 100 mW for a further hour. Their results showed that a small number of the bacteria were damaged (qualitatively shown via propidium iodide staining), however, the majority of the bacteria could be recovered from the structure and cultured[148]. Methods of reducing the exposure of the living cells to the laser have been suggested; one such technique used optically-trapped objects to push cells. The premise was that the object being trapped, rather than the cells, would experience the laser energy, and could be used to manipulate the cells in a gentler manner [149]. This group of researchers reported increased cell survival with the use of this indirect method compared to direct optical manipulation.

From the current literature, it appears that the optical tweezers cause minimal, if any, damage to cells manipulated for short periods (~1 hour) [150]. However, it remains to be seen what other effects might occur. The aforementioned studies of Adam Engler (2006) neatly demonstrated how surface elasticity affects stem cell differentiation. The effect pressure has upon osteogenesis has been well covered [151,152].

1.10 The Project

1.10.1 Aims and objectives

This thesis will present the work completed towards three main aims. The first main aim was to develop the HOTs into a micropatterning setup suitable for creating micron-scale cell and release source patterns, the second was to demonstrate the HOTs-based positioning of localised release sources to mimic diffusible cell niche signalling, and the third was to use the HOTs patterning setup to investigate cellular differentiation and migration models. These three aspects were compiled to create an overarching aim: **Establishment of a micropatterning tool to facilitate the creation of user-defined biology-inspired microenvironments with directed control over the signalling dynamics.**

- **Development of the HOTs micropatterning setup**

The HOTs represent the crux of this thesis, and as such, it was important to show that the HOTs can be used to position small cells and delivery sources in patterns that would be suitable for producing basic cell microenvironments.

Specific objectives included:

  - Simple cell-based pattern formation
  - Optimisation of polymer microparticles for optical manipulation
  - Obtaining quick release microparticles
  - Cell and microparticle co-patterning
  - Stabilisation of HOTs-patterned arrangements

- **Positioning of release sources for localised release**

With the objective of having a micropatterning setup capable of mimicking cell niche solute signalling, it was necessary to show that the HOTs patterning setup was capable of achieving this with the previously developed quick release microparticles.

Specific objectives included:

  - Assessing the mobility of fluorophores across hydrogels
  - Encapsulation of fluorophores
  - Proof of concept localised delivery of fluorophores
  - Demonstrating release and uptake of calcein AM
  - Zonal delivery to cell aggregates

- **Investigating differentiation and cellular migration with the HOTs patterning setup**

The final aim was based on the application of the developed technology from this thesis, whilst also developing the proof of concept of the HOTs patterning setup as a tool for patterning localised delivery sources. The third sub-objective was to investigate cellular differentiation and migration in response to zonally delivered signalling molecules.

Cellular differentiation

Specific objectives included:

- Encapsulation of retinoic acid into microparticles
- Selection of a suitable biological response with which to test the HOTs patterning setup
- Selection of highly-loaded retinoic acid microparticles for HOTs patterning
- Demonstration of HOTs-controlled zonal differentiation of embryonic stem cell aggregates

Cellular migration

Specific objectives included:

- Isolation and culture of chemotactically-active primary osteoblasts
- Optimisation of ‘simple’ delivery sources HOTs patterning
- Use of PDGF-BB-loaded agarose beads for directing osteoblast chemotaxis
- Using advanced analysis techniques to quantify chemical concentrations following localised release

2. Materials and Methods

This chapter provides a detailed description of the materials and fundamental methodologies that were employed in this thesis. Any additional details going beyond the general materials and methods will be discussed in the relevant chapters.

Materials

2.1 Cell Culture

2.1.1 Cell Types

2.1.1.1 Mouse Embryonic Stem Cells

Feeder-free mouse embryonic stem (mES) cells (cell line – CGR8) at passage 8 were predominately used for this project. They are a germ-line competent cell line derived from the inner cell mass of a 3.5 day male pre-implantation mouse embryo. Their initial establishment is described by Nichols *et al.* (1990) [153].

2.1.1.2 Primary mouse calvarial cells

Primary mouse calvarial cells were isolated as part of this project and this is detailed in Section 6.3.1 and Chapter 6.

2.1.2 Cell culture medium

Relevant cell culture medium was prepared in a sterile environment, with all components being passed through a 0.22 µm sterile filter. Medium was then stored at 4^{o}C and kept for up to two weeks.

2.1.2.1 General cell culture medium

mES cell passage and differentiation experiments used general cell culture medium, that comprised of: Dulbecco's Modified Eagle Medium (DMEM) with 10% (v/v) FCS, Penicillin (100 U/mL) / streptomycin (100 µg/mL) (15070-063, Gibco, Invitrogen, UK), 1% L-glutamine (2 mM) and 100 µM 2-Mercaptoethanol (50 mM) (31350-010, Gibco, Invitrogen, UK).

2.1.2.2 mES cell culture medium

General cell culture medium was supplemented with LIF (106 U/mL) (ESGRO® ESG1106, Millipore, UK) (mES medium); 500 U/mL LIF was added to CGR8 mES cells for continuous culture maintaining pluripotency.

2.1.2.3 Retinoic acid differentiation medium

Serum starvation was completed to ‘prime’ mES cells for retinoic acid differentiation, it comprised mES cell-culture medium without the FCS component.

2.1.2.4 mPC cell culture medium

mPC cells were cultured in Minimum Essential Medium Alpha (αMEM, Lonza) with 10% (v/v) FCS, Penicillin (100 U/mL) / streptomycin (100 µg/mL) (15070-063, Gibco, Invitrogen, UK), 1% L-glutamine (2 mM).

2.1.2.5 Cryopreservation medium

Cells were prepared and stored in liquid nitrogen (-196°C to -210°C) in cryopreservation medium containing FCS and 10% (v/v) dimethyl sulfoxide (DMSO) (D5879, Sigma-Aldrich, UK).

2.1.2.6 Aggregation Medium

Aggregation media was used for Avidin Biotin crosslinking, and comprised; DMEM, 1% FCS, 2 mM L-glutamine and 1% Penicillin (100 U/mL) / streptomycin (100 µg/mL).

2.2 Delivery Vehicles

2.2.1 Polymer microparticles

Microparticles were fabricated with the following materials and chemicals: Poly(lactic-co-glycolic acid) (PLGA) 50:50 DLG 4A, molecular weight 56 kDa (Lakeshore Biomaterials, USA) and Triblock copolymer PLGA-PEG-PLGA (Mw 7500) (TBIIF) were used for microparticle formulations used in this project. TBIIF was a kind gift from Omar Qutachi (University of Nottingham, UK) and it was synthesised as previously described[120,154]. Dichloromethane (DCM) (Fisher Scientific, UK) was used for a solvent and polyvinyl alcohol (PVA) (Sigma-Aldrich, UK) was used as an emulsifier.

Polymer microparticles were used to encapsulate the following molecular cargos: Rhodamine-123 (R302, Thermo Fisher Scientific, UK), Calcein Green AM (C1430, Thermo Fisher Scientific, UK), Calcein Blue AM (C1429, Thermo Fisher Scientific, UK) and all-trans Retinoic acid (R2625, Sigma Aldrich, UK).

2.2.2 Agarose Beads

Agarose beads (Agarose Bead Technoloiges, UK) were used for creating simple points of localised solute release sources, by soaking the dried beads in different solutions. Soak solutions used, included: Calcein green AM (C1430, Thermo Fisher Scientific, UK) and Platelet-derived growth factor BB (PDGF-BB) (P3201, Sigma Aldrich).

2.3 Consumables

General lab ware used for this project included: tissue culture flasks (T25, T75, T175 and T450 cm^2) (Nunc, Thermo Fisher Scientific, UK), tissue-culture treated and non-tissue-culture treated plastic well-plates (Falcon, BD Biosciences, UK), filter tips (TipOne StarLab, UK), universal tubes (20 mL), Eppendorf tubes (Sarstedt Ltd. UK), glass bottom dishes (35 mm) (CELLView, Greiner bio-one, UK, plugged serological pipettes, sterile glass aspirators, assay plates (96-well) (Costar, Thermo Fisher Scientific, UK), petri dishes, cryo-vials and filters (0.22 µm) and parafilm (Thermo Fisher Scientific, UK).

2.4 Additional Materials

2.4.1 Chemicals

All chemicals were purchased from Sigma-Aldrich, UK unless otherwise stated. The following chemicals were used throughout this project: formalin solution (HT501128), paraformaldehyde (PFA) (P6148), Triton X-100 (X100), bovine serum albumin (BSA), and polyHEMA (P3932).

2.4.2 Antibodies

For immunocytochemistry analysis of cells, the following antibodies were used:

Table 2.1 List of primary antibodies

Antibody	Host species	Dilution	Manufacturer
Stra8	Rabbit	1:100	Abcam (ab49602)
DAZL	Rabbit	1:100	Abcam (ab34139)
Anti-phospho-Histone H2A.X	Rabbit	1:400	Cell Signalling Technology (#2577_
Brachyury	Goat	1:100	R&D Systems (AF2085)
Nestin	Chicken	1:1000	Abcam (Ab81755)
GATA-4	Rabbit	1:1000	Abcam (Ab63398)
Oct-3/4	Rat	1:100	R&D Systems (MAB1759)

Table 2.2 List of Secondary antibodies

Antibody	Host species	Dilution	Manufacturer
Anti-Goat IgG Polyclonal, Alexa-Fluor 546 (Ex/Em:556/573 nm)	Donkey	1:200	Invitrogen (A11056)
Anti-Rabbit IgG Polyclonal, Alexa-Fluor 488 (Ex/Em:495/519 nm)	Goat	1:200	Invitrogen (A11008)
Anti-Rabbit IgG Polyclonal, Alexa-Fluor 546 (Ex/Em:556/573 nm)	Goat	1:200	Abcam (ab175471)
Anti-Chicken IgG Polyclonal, Alexa-Fluor 546 (Ex/Em:556/573 nm)	Goat	1:200	Invitrogen (A11040)
Anti-Rat IgG Polyclonal, Alexa-Fluor 546 (Ex/Em: 556/573	Goat	1:200	Invitrogen (A11081)

Methods

2.5 Cell Culture

All cell culture was performed in a class II microbiological safety cabinet (Envair, UK) with high efficiency particulate air (HEPA) filters, and cell cultures were kept in 37^{o}C humidified 5% CO_2 containing incubators (Sanyo Electric, USA).

2.5.1 Embryonic stem cells

Embryonic stem cells were used for the bulk of this project, for the optimisation and proof of concept biological investigation. The mES cell line, CGR8, was used for this project and they were grown directly onto pre-treated gelatin coated T25 flasks. These 'feeder-free' cells were maintained in 5 mL of mES cell culture medium, with medium changes daily until 80-90% confluency was reached. For passage, the cells were detached with trypsin/EDTA solution at room temperature for 5 minutes. The trypsin/EDTA was then neutralised with General cell culture medium and centrifuged to form a cell pellet. The supernatant was aspirated and the pellet of cells resuspended in a volume of mES cell culture medium, determined by the appropriate cell seeding required. Fresh gelatin coated T25 flasks were then prepared, with excess gelatin solution being aspirated and the required cell density was seeded. Cells were passaged every 1-2 days and splitting ratios of 1:2 or 1:4 were used depending on how quickly confluency needed to be reached.

2.5.2 Hanging Drop

To create uniformly sized cell aggregates, mES cells were suspended in cell culture medium following detachment from the cell culture surface by trypsin/EDTA treatment. Cells were grown in mES medium with or without FCS dependent upon the application. So called, serum starved cells, were cultured for 24 hours in serum-free mES medium. Cell suspensions were diluted to 2 x 10^4 cells/mL in aggregation medium (Section 2.1.2.6) and then, using a multi-flow pipette (8 tips), 25 µL volumes were deposited onto the underside of a 60 mm petri dish lid to form 8 rows. The resulting 64 isolated cell suspension droplets were then inverted as the petri dish lid is placed on the petri dish containing PBS. This allows the droplets to hang from the lid, and the roughly 500 cell suspension to collect at the bottom of the droplet. Hanging droplets were cultured for 24 hours and then the resulting cell aggregates were collected from the individual droplets.

2.5.3 Surface modification of embryonic stem cells

mES cells were engineered to increase aggregation by creating reactive residues on the mES cell surface. Naturally occurring sialic acid residues were biochemically altered through a periodate oxidation step to exhibit reactive aldehyde groups [155]. Using biotin hydrazide, these groups are biotinylated facilitating the subsequent cross-linking with free or coated avidin protein.

2.5.4 Cryopreservation and reanimation

Confluent cells were cryopreserved for storage by detaching the cells using trypsin/EDTA solution, neutralising in cell culture medium (cell type appropriate) and centrifugation. The cell supernatant was then aspirated and the cells of the pellet resuspended in cryopreservation medium at a density of 1 x 10^6 cells/mL. 1mL cell suspension aliquots were then added to cryovials and added to a CoolCell cell freezing container. The cell freezing container, once full, was cooled to -80^{o}C for 48 hours before containing cryovials could be transferred to liquid nitrogen storage tanks.

Reanimation of cells stored in liquid nitrogen was accomplished by removing the required cell containing cryovials from the liquid nitrogen storage tank and then rapid thawing in a water bath at 37^{o}C. Thawed cell suspensions were then transferred to 9 mL of cell culture medium (cell type appropriate) and centrifuged to pellet the cells. The DMSO containing supernatant was removed and replaced with fresh cell culture medium and seeded into the appropriate flasks.

2.5.5 Isolation and culture of mouse primary calvarial cells

Murine primary calvarial (mPC) cells have been well described in terms of their response to bone remodelling recruitment and osteogenic differentiation signalling [156,157]. mPC cells were isolated from 1-to-3-day old CD-1 mice pups using a collagenase digestion technique. Neonatal mice calvariae were extracted and washed in PBS containing 100 U/mL penicillin, 25 µg/mL amphotericin B and 100 µg/mL streptomycin. A laminar flow hood (Envair, UK) and sterilised

dissection equipment were used to prevent any contamination of the isolated cells.

The calvariae from each litter of pups were collected in antibiotic and antifungal containing PBS, and placed in a class II microbiological safety cabinet. The calvariae were then cut into many pieces using sterilised scissors to increase the total surface area for digestion. Digestion was completed with a solution of 1.4 mg/mL collagenase IA and 0.5 mg/mL trypsin II S for 12 minutes on a roller (Stuart Roller Mixer SRT6) at 37^{o}C. Cells released from the first round of digestion were discarded via aspiration. Fresh digestion solution was added and incubated for a further 12 minutes. This second round of digestion was also discarded via aspiration. The digestion process was repeated once again and the cell population was collected with an equal volume of FCS and placed on ice. Two further populations were collected in this manner and were pooled together.

The pooled suspension was then filtered through a 70 µm cell strainer and centrifuged (MSE Mistral 1000, Scientific Laboratory Supplies Ltd, UK) for 5 minutes at 300 g. The resulting cell pellet was resuspended in mPC medium containing Minimum Essential Medium Alpha (αMEM) (Lonza, UK) with 10% FCS, 100 U/mL penicillin, 100 µg/mL streptomycin and 2 mM L-glutamine. Cells were then seeded in T75 cm^2 flasks (15 pups / T75 cm^2 flask), and incubated at 37^{o}C for 24 hours. At 24 hours, non-adherent haematopoietic cells were removed by washing twice with PBS before the medium change. For cryopreservation cells were grown to 80% confluence before standard cryopreservation (detailed in Section 2.5.4) at a density of 1x10^6 cells/mL.

2.5.6 Mouse primary calvarial cell culture

Cells were reanimated from cryopreservation and maintained in cell culture flasks of varying size containing primary calvarial cell medium. Cells were passaged in the same manner previously described (Section 2.5.6), and used up to passage 3.

2.5.7 Cell viability analysis

To assess cell viability, the LIVE/DEAD® cell assay (Sigma, UK) was used The kit contains two probes; calcein AM and ethidium homodimer-1 (EthD-1) that recognise intracellular esterase activity and plasma membrane integrity, respectively. “Viable”, metabolically active cells are distinguished by the enzymatic conversion of the non-fluorescent calcein AM to florescent calcein via intracellular esterase activity. Calcein is a polyanionic dye available in a number of different fluorescing colours with different excitation and emission (exc/em) wavelengths; green (495/515), blue (322/445) and (577/590). Non-viable cells are distinguished using EthD-1. EthD-1 enters cells with damaged membranes, fluorescing red; excitation/emission wavelength of 495 to 635 nm, upon binding to nucleic acids. Cell cultures were incubated in pre-warmed LIVE/DEAD® solution containing 2 μM calcein AM and 4 μM EthD-1 in medium (appropriate for cell type) for approximately 20 minutes at 37°C with 5% CO2 and 95% humidity. Cells were then washed with PBS before fluorescent image analysis. LIVE/DEAD® solution was prepared fresh each use.

2.5.8 Cell proliferation

To assess cellular proliferation, the CellTiter 96 AQ one solution cell proliferation assay was used. Changes in cell number could be assessed by colourimetric detection of soluble coloured formazan. Formazan, with an absorbance peak at 490 nm, is formed as a result of bio-reduced tetrazolium compound [3-(4,5-dimethyl-2-yl)-5-(3-carboxymethoxyphenyl)-2-(4-sulfophenyl)-2H-tetrazolium, inner salt] (MTS) with an electron coupling reagent phenazine ethosulfate (PES). Actively metabolising cells are able to achieve this bio-reduction through dehydrogenase enzymes producing NADPH or NADP. The formation of MTS product is directly proportional to the number of metabolically active cells. For experimental use, 100 µL MTS reagent was added to cell cultures containing 1000 µL cell culture medium and incubated for 1 hour at 37^{o}C. Following incubation, 100 µL of MTS/cell culture medium solution was transferred to 96-well plates, typically multiple repeat wells were used for each sample (n=6). Absorbance was then measured at 490nm using a Tecan i-control Infinite 200 plate reader (Tecan). To assess proliferation over time, time-points were taken and the mean absorbance for each sample was calculated, blank control readings were subtracted from experimental readings.

2.5.9 Senescence β-Galactosidase Staining Kit (Cell Signalling Technology)

This kit is designed to detect β-Galactosidase activity, a known characteristic of senescent cells that is not found in pre-senescent, quiescent or immortal cells [158]. Growth media was removed from the cells to be tested and then washed with PBS. The washed cells were then fixed in 1x fixative solution (#11674) for 15 minutes at room temperature, and then washed with PBS twice. β-Galactosidase

staining solution that contains the reactive substrate X-Gal was added to the fixed cells and incubated at 37°C in a dry incubator without CO_2 that might affect the pH levels. With the staining solution still on the plate, the cells were assessed under a microscope to identify a development of blue colour, the positive staining for β-Galactosidase.

2.5.10 Sample fixation

Cell fixation was essential for immunocytochemistry and other histology based analyses, to ensure that the cell morphology and internal cellular architecture are preserved. Formalin (10% v/v in dH20) was used for fixing monolayers for alizarin red staining, discussed in Chapter 6, but for the most part, paraformaldehyde (PFA) (3.7% w/v in PBS) was used. Use of both fixatives required medium removal from the cellular sample and three PBS washes. Formalin was then added to cell samples for at least 30 minutes to ensure complete fixation. Samples were then washed and then stored in PBS at 4°C. PFA, which is polymerised formaldehyde is a larger molecule than formalin, creating a strong and highly linked network. This allows for better permeability and it is why PFA is more suitable for immunocytochemistry, allowing better ingress of antibodies into cell aggregates and tissues. PFA was added to samples for 20 minutes so as to prevent over fixation of the sample. Again, PFA was removed and then the sample was washed in PBS before sample storage.

2.6 Hydrogels and preparation

Bovine (G1393, Sigma-Aldrich, UK) and porcine (G9136, Sigma-Aldrich, UK) gelatin were purchased as a lyophilised powder and then dissolved in dH_2O at

80°C. The resulting pre-gel solutions were then incubated at 37°C until needed for cell encapsulation. For gelation, the pre-gel solutions were cooled to 4°C for at least 30 minutes to achieve complete gelation.

Collagen type I, (high concentration) from rat tail (Corning, UK) was prepared on ice by diluting the stock concentration of 9 mg/mL with a solution of sterile 10X PBS, sterile dH_2O, and 1N NaOH to create the desired final working concentration. Collagen concentrations of 3 mg/mL were typically used, unless otherwise stated. The collagen solution was then incubated at 37°C to gel for 30 minutes.

BD Matrigel (Matrix Growth Factor Reduced) (BD Biosciences, Oxford, UK) was melted at 4°C on ice, and then diluted as required. The matrigel solution was then incubated at 37°C to gel for 15 minutes.

Type IX Ultra Low Gelling Temperature (ULGT) agarose (Sigma-Aldrich, UK) was prepared in PBS at the required percentage by weight, and autoclaved at 126°C for 20 minutes using a Prestige Medical Classic portable autoclave. The resulting solutions were stored at 37°C, and cooled to ~23°C for 5 minutes to allow for gelation before use.

Gelatin methacrylate (GelMA) that was synthesised in-house by Pritesh Mistry and Elisabetta Prina (University of Nottingham, UK) as described previously [159,160]. Briefly, type A porcine skin gelatin was mixed at 10% (w/v) into PBS at 60°C and stirred until fully dissolved. Methacrylic anhydride (Final concentration 8% v/v) was added until the target volume was reached at a rate of 0.5 mL/min to the gelatin solution under stirred conditions at 50 °C and allowed to react for 1 hour. The fraction of lysine groups reacted was modified

by varying the amount of MA present in the initial reaction mixture. Following a 5X dilution with additional warm (40 °C) PBS to stop the reaction, the mixture was dialysed against distilled water using 12–14 kDa cutoff dialysis tubing for 1 week at 40 °C to remove salts and methacrylic acid. The solution was lyophilised for 1 week to generate a white porous foam and stored at −80 °C until further use.

2.7 Immunocytochemistry

To assess cell surface proteins and other antigens present within cells, immunocytochemistry approaches were employed so that subtle changes in cellular differentiation and development could be visualised by fluorescence microscopy.

2.7.1 Sample preparation

Fixed cell samples were permeabilised in 0.1% (w/v) Triton X-100 (diluted in PBS) for 40 minutes at room temperature for cell monolayers, and 90 minutes for cell aggregates. Following permeabilisation, samples were covered in blocking solution for 30 minutes at room temperature. The blocking solution comprised of 1% BSA (w/v) (in PBS) and 3% (v/v) serum from the animal in which the secondary antibody was raised. Thusly, the blocking step prevents non-specific binding of the secondary antibody.

2.7.2 Antibodies

The list of primary antibodies used in this project is detailed in Table 2.1. Antibodies were reconstituted in 1% BSA (w/v) (in PBS) as indicated in the

supplier's guidelines. Following the removal of the blocking solution, the sample was washed in 1% BSA (w/v) (in PBS) with 3 5-minute washes and then samples were incubated with sufficient primary antibody solution to cover the entire sample, and left overnight at 4^{o}C.

Secondary antibodies used have been listed in Table 2.2 , all secondary antibodies used were conjugated to Alexa-Fluor molecules and diluted in 1% BSA (w/v) (in PBS) at concentrations indicated by the suppliers. Following 3 5 minute washes in 1% BSA (w/v) (in PBS) to ensure complete removal of the unbound and excess primary antibody, the samples were incubated with the required secondary antibody at room temperature for 2 hours in the dark. Samples were then washed in 1% BSA (w/v) (in PBS), again 3 5 minute washes.

2.7.3 Hoechst co-staining

In some cases, counter staining of the samples was employed, for this, 5µg/mL Hoechst solution was added to the sample and incubated for 15 minutes at room temperature. Samples were either imaged immediately, or Prolong Gold Antifade mountant (Thermo Fisher Scientific, UK) was applied for sample storage. Samples were imaged within 48 hours if ProLong was used.

2.8 Optical manipulation

2.8.1 Technical setup and optical trapping procedure

The HOTs used for this research is based on a Nd:YAG, solid state, infrared (1064 nm), 3 W maximum output, continuous wave, class 4 3.2 mm beam diameter laser adapted for biological applications (Laser Quantum). Optical

manipulation with multiple optical traps is achieved by expanding the laser beam so that it overfills the aperture of the spatial light modulator (SLM) chip (512x512 pixel – Ferroelectric liquid crystal (FLC) array) (Laser 2000). This is then coupled into the optical tweezer system by imaging the SLM on to the back aperture of a high numerical aperture oil immersion microscope objective lens (40x 1.3 NA Zeiss, Plan-NeoFluar). The resulting traps can then be focussed anywhere within the field of view, controlled by the computer controlled holograms generated by the SLM giving full axial and lateral control over the trapping beam[161].The control of phase shift permits 3D control outside of the focal plane.

Samples are then mounted onto a motorised stage (ASI, MS-2000) allowing for accurate control over a large area, including well-plates and large patterning gaskets. Illumination of the sample is provided by a LED and condenser, which can be imaged using a complementary metal–oxide–semiconductor (CMOS) camera connected to a computer. All laser light is reflected back into the objective by a polarising beam-splitter while transmitting the bright field illumination onto the sample, creating a visible image of the sample field of view (164x123µm).

The hardware is simply controlled by the 'red tweezers'[162,163] control program (OpenGL engine and LABVIEW interface) (National Instruments) designed by M.Padgett's group (University of Glasgow, UK). Figure 2.1 (below) shows a screenshot of this interface.

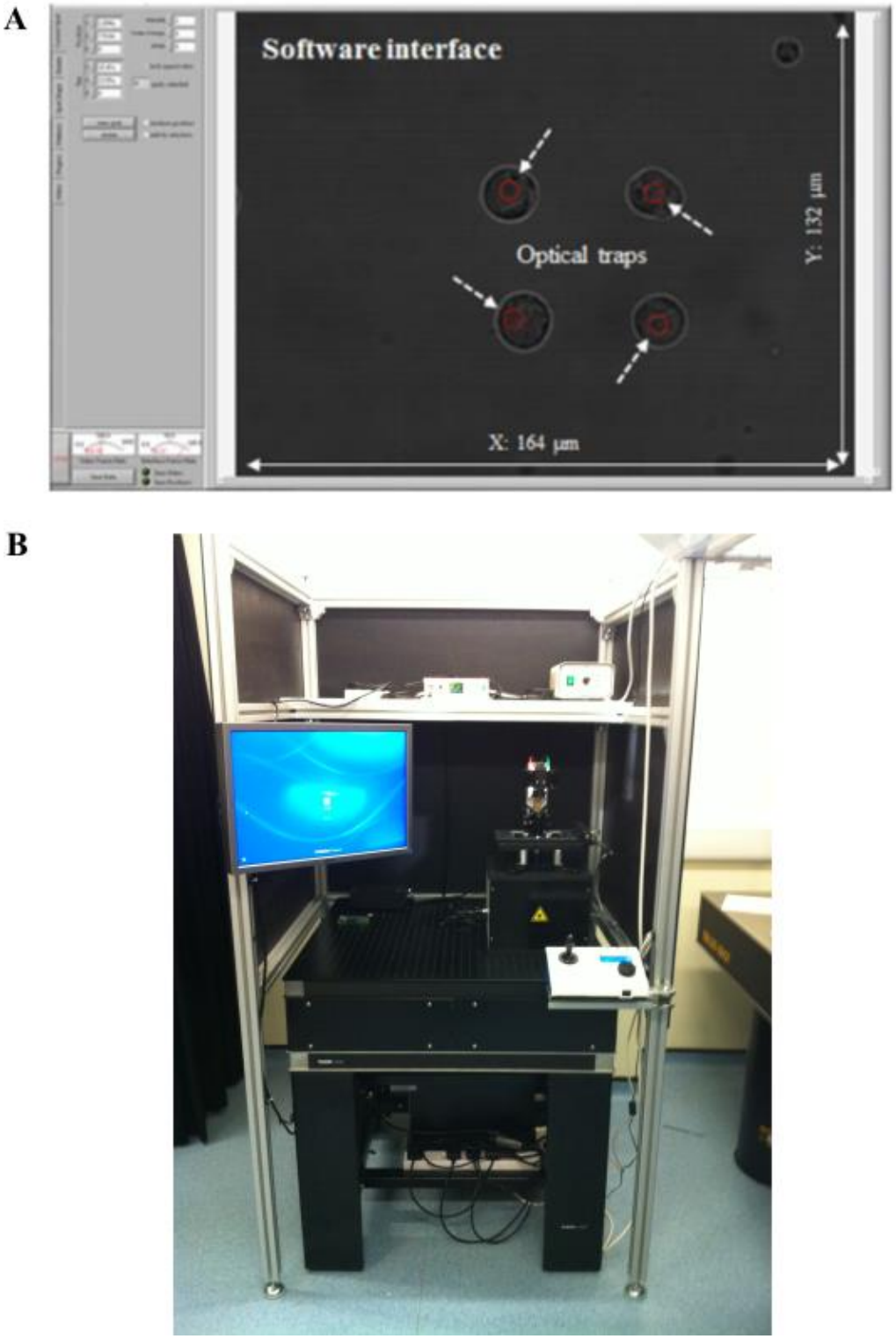

Figure 2.1 Screenshot of the Red Tweezers Labview interface and HOTs platform

LabView software interface (A) for operating the HOTs pictured (B), optical traps, shown by red circles allow the simultaneous manipulation of multiple objects (mES cells pictured). The field of view is 164 x 123 µm. Figure created with help from Dr. Emily Britchford (University of Nottingham).

2.8.2 Environmental Chamber

To facilitate live cell manipulation experiments on the HOTs, an insulated environmental chamber was built around the microscope stage of the HOTs. The chamber was supplied with a gas mixture of 5% CO_2, 10% O_2 and 85% balanced N_2 (BOC industrial gases, UK) to generate 'incubator-like' conditions. Ambient air temperature was maintained at 37^{o}C using a thermostatic heater. A cooling loop containing mineral oil was passed around the microscope stage to enable sample temperature reduction for temperature-based cross-linking of hydrogels.

2.8.3 Basic patterning gasket

The basic patterning gasket comprised a coverslip glass bottomed 35mm culture dish, a polyHEMA coating, and medical grade silicone micro-wells (CultureWell chambers). The micro-wells were stuck to the polyHEMA coated glass with silicone adhesive to yield low volume single chambers for HOTs patterning.

2.8.4 Multi-lobed patterning gasket

Developments to the basic patterning gasket are discussed later in Chapter 4, but briefly, the use of a makerbot (replicator 2) 3D printer to form exclusion molds are described. Thermoplastic poly(lactic acid) (PLA) was extruded to fabricate the 3D mold for the multi-lobed gasket, the design was developed using TinkerCAD.

The gasket was fabricated using a Sylgard 184 elastomer kit, briefly the two components were mixed in a 10:1 ratio and left to degas for an hour. The PLA

mold was then attached to the base of a petri dish with silicone adhesive and the degassed sylgard elastomer was poured around it. The petri dish was left on a flat surface at room temperature for at least 72 hours before the cross-linked elastomer could be removed. The resulting elastomer gasket was then attached to coverslips via electrostatic interaction to form the multi-lobed gasket. PolyHEMA could then be added to the gasket to create an anti-biofouling surface.

2.8.5 Surface coatings

PolyHEMA is biomaterial that has a number of attractive properties for use as a surface coating, it is optically transparent and acts as an anti-biofouling agent such that it prevents electrostatic interactions and cellular adhesion[164,165]. It is for these reasons that PolyHEMA was used to coat the coverslip glass slides used for patterning, the surface coating was initially applied by dip coating the glass coverslips into PolyHEMA solution (See Material Preparation) and then air dried for two hours prior to use. To prevent delamination of the PolyHEMA coated glass, coatings were not kept for longer than 24 hours prior to use.

2.9 Microparticles

2.9.1 Fabrication

Microparticles were fabricated using both a single (Oil in Water) and double emulsion system (Water in Oil Water), whereby polymer and loaded molecule were dissolved in dichloromethane (DCM) [166]. The polymer was a blend of triblock TBIIF with PLGA at a range of different ratios.

The fabrication of double emulsion PLGA microparticles was accomplished by using the water in oil in water emulsion method (W/O/W), previously described by Bible[167]. A PVA solution was prepared by adding 3g of PVA to 1 litre of distilled water and was then left overnight stirring gently. Before use, the PVA solution was filtered using a 0.2 µm Nalgene filter unit attached to a vacuum pump. 200 mL of the filtered PVA was then added to a 250 mL beaker. Microparticles were made with and without TBIIF copolymer, so the polymer composition varied depending on the microparticles required, this was weighed out to give a total of 1g into a screw top PTFE vial and the necessary volume of DCM was added using a glass pipette. The PTFE vial was then sealed, and placed on an orbital shaker for 30 minutes until the polymer was fully dissolved. If loading was required, this was prepared in a 100µL aliquot with HSA (100 mg/mL); generally it was possible to load up to 5% protein/molecular cargo. The 100µL aliquot was then added to the polymer/DCM mix and homogenised for 2 minutes at a specific speed to yield certain microparticle sizes creating the primary emulsion. The primary emulsion was then added to the filtered PVA in the 250mL beaker and further homogenised for 2 minutes to form the secondary emulsion. The beaker was then carefully positioned on a magnetic stirrer plate, and a glass magnetic stirrer bar was added, the beaker was stirred at 300RPM for 4 hours in the fume hood to allow for the DCM to evaporate. The microparticles were then collected by centrifugation achieved by splitting the beaker contents evenly between four 50mL centrifuge tubes, spun at 3000 RPM for 3 minutes. The supernatant is removed and the particles were washed with 50mL distilled water three times, the contents of the four tubes were then transferred to one tube and given a final spin. The supernatant was carefully

removed; the tube was covered in blue roll, snap frozen in liquid nitrogen and freeze dried (Edwards Modulyo D, IMA Edwards, UK) for 2 days. For long term storage, the particles were vacuum packed and kept frozen (-20^{o}C).

The Water in Oil (W/O) single emulsion method can be used if the active agent to be encapsulated in soluble in the oil phase. Unlike the W/O/W method, the polymer and agent to be encapsulated are dissolved in the required amount of DCM and added to 200 mL of 0.3% (w/v) PVA and homogenised at the required speed (4000 rpm unless otherwise stated) for 2 minutes. The resulting single emulsion is then treated in the same manner as previously described for W/O/W microparticles to form W/O microparticles.

2.9.2 Sizing by Laser Diffraction

To assess the size of the microparticle batches, a Coulter LS230 machine was used; this entailed suspending a small mass (~25 mg) of the particles in ultra-pure water in the coulter cell. The particles were then stirred gently and an obscuration value was calculated, this is the percentage of light that is attenuated by the scattering and absorption of the suspended particles. An obscuration value between 8-12% was required for appropriate laser diffraction. When this was achieved, an expanded laser beam (750 nm) is passed through the microparticles scattering the light, the light was then focussed by a Fourier lens onto a detector array. An inversion algorithm using a Garnett optical model (Micromeritics ASAP 2000) was then employed to calculate the particle size distribution in the sample.

2.9.3 Scanning Electron Microscopy (SEM)

In order to assess the morphology of the microparticles, SEM imaging was required. A dusting of microparticles was attached to an adhesive conductive carbon disk. The disks were then gold sputter coated for 5 minutes at 30 mA using a Balzers SCD 030 sputter coater. Electron microscopy was completed using a JSM 6060LV SEM with an accelerating voltage ranging from 10-15 kV, micrographs were taken at various magnifications depending upon the size of the particles being imaged.

2.9.4 Encapsulation Efficiency of Microparticles

Microparticles were made containing protein/molecules for delivery and to fully characterise them, a measure of the encapsulation efficiency was required. Using an adapted version of the method published by Sah (1997)[168], the loading could be determined. 15 mg of loaded PLGA microparticles were dissolved in 750 µL of DMSO and 2150 µL of 0.02 % $_{(w/v)}$ SDS in 0.2 M NaOH for 1 hour at room temperature.

2.9.5 BCA assay

150µL aliquots of each solution were added to a well plate and a bicinchoninic acid assay was performed using a micro BCA protein assay kit. The results of this kit are observed as a colourimetric change when Cu^{2+} is reduced to Cu^{1+} which is chelated by BCA, the level of reduction corresponds to the concentration of protein in the sample. Appropriate standards of HSA were created, and after 2 hours of incubation at 37^{o}C, the plate was scanned at 562 nm

on a plate reader. The total protein content was then calculated via a polynomial equation of the standard curve, and the encapsulation efficiency was calculated from the theoretical expected loading of the microparticles.

2.9.6 *In Vitro* Release Study

To ascertain the release kinetics of the microparticles created, release studies were set up (25 mg in 1.5 mL PBS) in triplicate. The tubes were then placed on a gyrotwister and gently rocked at 5 RPM at 37^{o}C. At defined time intervals, usually daily, the tubes were centrifuged at 3000 RPM for 3 minutes. The supernatant was then carefully removed and stored at -20^{o}C. The microparticles were then resuspended in 1.5 mL PBS and returned to the incubator; this process was repeated over 12 days to ensure complete release from the microparticles.

2.10 Microscopy

Generally, Hoffman contrast microscopy with a Nikon Eclipse TS100 inverted microscope (Nikon Instruments, UK) was used to view cells through culture and for any non-fluorescent imaging of cells. For lower magnification imaging, the analysis of alizarin red staining (Section 6.2.2), a Nikon SMZ1500 stereomicroscope (Nikon Instruments, UK) was used, and images were captured using an imaging screen and Nikon Digital Sight DS-Fi2 imaging system. Fluorimetric analysis and phase contrast time-lapse imaging was completed with a Leica DMRBE inverted microscope (Leica, UK). Image processing and time-lapse acquisition was accomplished using Velocity imaging software (Improvision, UK). Confocal imaging was used for fluorescence imaging of

immuno-stained cellular aggregates using a Zeiss LSM880 confocal laser scanning microscope and accompanying Zen imaging software (Zeiss, UK).

2.10.1 Confocal image acquisition and post-image processing

Cell aggregates were imaged using confocal microscopy, detailed in Section 2.10, using the following acquisition settings. A step size of 0.8 µm was used to image a 50 µm section of the cell aggregate, yielding 63 frames. To correct for signal variation through the aggregate, due to poor light penetration, final comparable images were processed from the slices averaged. The microparticles and FITC signal were averaged through a smaller number of sections to preserve the signal and permit better visualisation whilst maintaining their xy position relative to the aggregate. However, their z position was most likely different to the focal point viewed for the cell aggregate, and so the merged images (Figure 5.13) purely representative as it falsely shows the microparticles on the same plane as the aggregate.

3. Results – Optimisation of HOTs for Micropatterning Cells and Microparticles

3.1 Introduction

Cell and tissue development is dependent upon the physicochemical microenvironment. In the case of stem cells, cell fate can be determined by the cells' positioning within the microenvironment and, amongst other things, its exposure to certain chemical stimuli. The ability to replicate such positioning of cells and delivery of chemical signals has a plethora of different applications in the fields of biophysics, developmental biology and tissue engineering. However, most current micropatterning technologies are unable to provide the required precision and accuracy to fabricate such microenvironment signalling and cellular patterning.

As discussed in Chapter 1, HOTs can be used to position dielectric objects with micrometre precision. As such, HOTs are a tool that could be developed into precision micropatterning technology for fabricating complex cellular microenvironments. Current methods of micropatterning biological materials include: bioprinting, micro-contact printing and microinjection. However, as previously mentioned, these technologies are generally unable to achieve a single-cell patterning resolution of <100 μm [74]. Current micropatterning

technologies are effective for a number of applications, and great progress has been made in the fabrication of macroscale architectures. However, they fail to accurately recreate the complex micron-scale arrangement required to appropriately recreate the functionally-critical tissue/niche minutiae.

One instance of this functionally-critical micrometre-scale patterning is in early embryogenesis. Precise architectural cellular arrangements and spatially defined morphogen signalling are vital to ensuring appropriate development. In the developing embryos, cell fates and body plan are defined. The development of axis and polarity by geometric positioning are thought to be essential to this process [169]. Acquiring cellular polarity requires chemical, and spatial cues from the small number of cells that make up the early embryo. The initial blastomere formation comprises only 2 cells dividing twice to form the 4-cell and 8-cell stages, these structures both have an approximate diameter of 80 μm [170]. Further to this, there are many examples of adult microenvironments where micron-scale cellular organisation is imperative for appropriate development and function of the tissue. The hematopoietic stem cell niche exemplifies this phenomenon, as haematopoietic stem cells (HSCs) differentiate and develop according primarily to their surrounding microenvironment. Micron-scale biological and chemical organisation within the HSC niche allows for proper differentiation into both the lymphoid and myeloid components of blood [171].

To attempt to recreate these structures with any of the aforementioned current micropatterning techniques would not be possible. This underscores the need for better micron-scale patterning platforms that can accurately replicate natural tissue. To address this need, the present thesis demonstrates the patterning of cells and release sources of biochemical factors using HOTs, and reports HOTs

development into a viable micropatterning tool. The aim of this research is to provide a means to create and study complex biomimetic cellular architectures and the important chemical signals that they require. This approach utilises the HOTs ability to directly position microscopic cells and release sources with great spatial resolution and accuracy in 3D [172–175].

This chapter describes the application of HOTs to manipulate cells and release sources into basic patterns. These basic patterns serve as a proof of concept for the development of small cell microenvironments, showing how both biological and chemical cues can be tailored. Blank PLGA microparticles were used to demonstrate the principles of setting-up local release sources for the controlled delivery of diffusible molecules. In this chapter the means by which release sources were developed and optimised for optical manipulation, and basic cells and microparticle patterning are described. The chapter culminates with a discussion of the approaches employed to the stabilisation of such patterns, with a mind to extended cell culture and temporally-controllable diffusible molecular delivery.

3.2 Chapter experimental overview

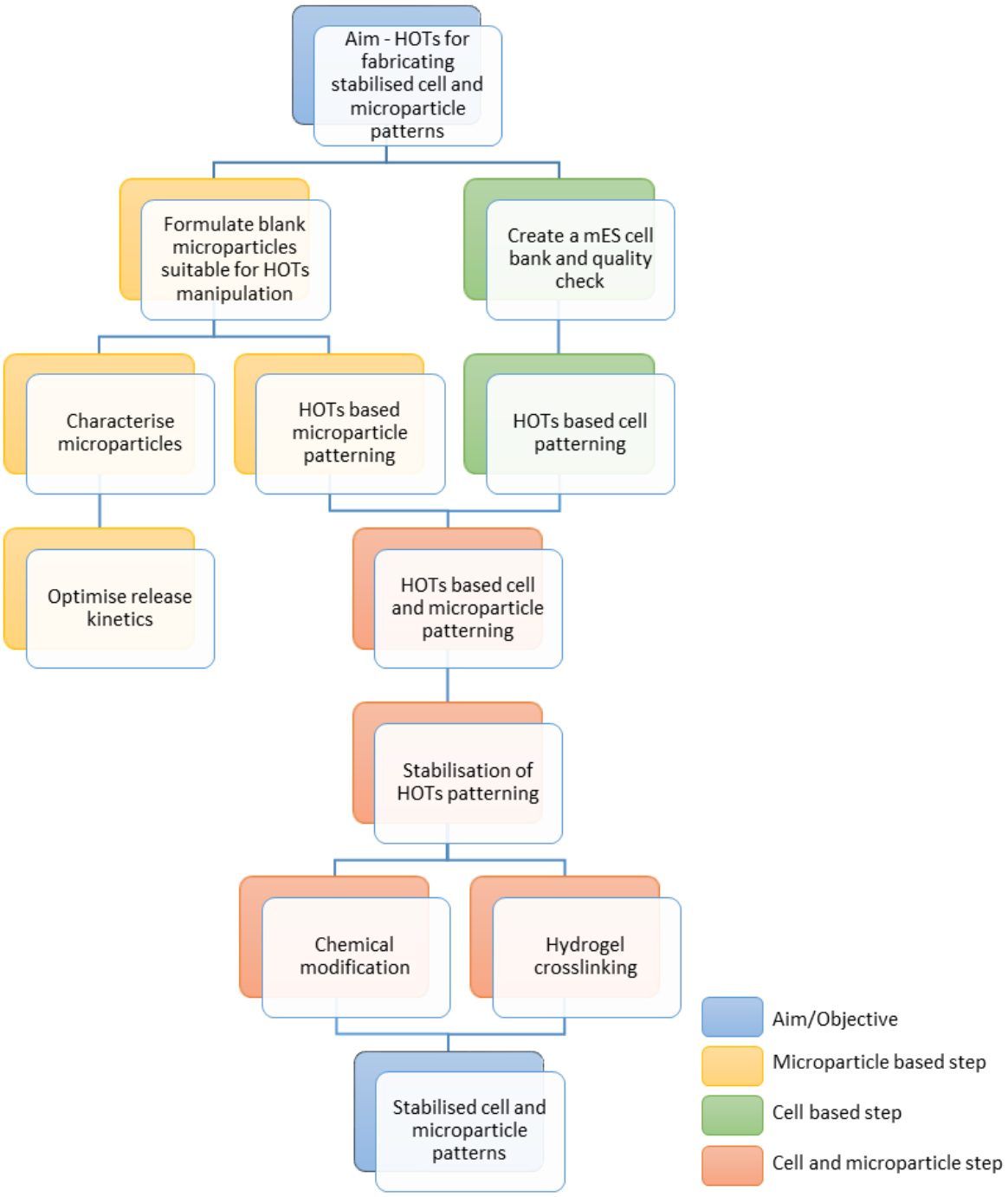

3.3 Materials and Methods

3.3.1 Patterning with the holographic optical tweezers

See Section 2.8.1 for the technical setup and trapping procedure.

3.3.2 Optical trapping study

During the optimisation of the microparticle formulation process, it was necessary to assess whether a given batch of microparticles was suitable for optical manipulation. To be suitable for optical manipulation, the object's refractive index must be sufficiently different to that of the surrounding medium. Typically, 1 mg of each microparticle batch was suspended in 10mL of cell culture medium to create a dilute suspension to be added to a patterning gasket. This gasket containing the dilute suspension of microparticles was then observed using the HOTs. A single trap was then made, under standard operating conditions (Section 2.8.1), and manipulation of a single microparticle in turn attempted in the x, y and z planes. If the optical trap created was amenable to the easy manipulation of the microparticle, then the optical properties of that batch of microparticles were deemed suitable for basic optical manipulation. Further to this, the stability of the trap was assessed by its ability to move microparticles across the surface of the glass coverslip. The optical trap was moved at a set speed of 32 μm/s (The minimum velocity that permits efficient patterning), and if the microparticle stayed within the trap it was deemed that the microparticle formulation was appropriate for optical manipulation and patterning. This simple test allowed the distinguishing of both strong and weak optical traps, a

distinction that is important for deciding with which microparticle formulation to proceed.

3.3.3 Encapsulation of rhodamine 123 into PLGA microparticles

As previously described, the rhodamine 123-laden microparticles were fabricated according to the w/o/w emulsion technique described in Section 2.9.1. A loading of 1.6% (w/w) was achieved by using 16 mg of calcein green AM in 1 g of polymer.

3.3.4 Rhodamine 123 release study

The *in vitro* release study for rhodamine -123-laden microparticles was completed as described in Section 2.9.6. Rhodamine 123 was quantified using a KC4 plate reader (Labtech International, UK), and fluorescence was read at 530nm following excitation at 480nm.

3.3.5 Biotinylation of ES cell surfaces

mES cells (CGR8) were surface-modified to create reactive residues to facilitate biotin binding. This process makes use of the naturally occurring sialic residues exhibited on the surface of mES cells [176]. Sodium periodate was used to biochemically alter sialic acid through oxidation to form reactive aldehyde groups [155]. These reactive groups were then able to link to biotin hydrazide, yielding a cell surface that is biotinylated and can be cross-linked with free avidin protein [177,178], or avidin localised on other objects (see Section 3.3.6).

3.3.6 Avidin-coating of microparticles

Polymer microparticles were suspended in an avidin solution of 80 µg/mL at a density of $4x10^5$ microparticles/mL. The resulting suspension was left for 6 hours on a Stuart Roller Mixer SRT6D (Scientific Laboratories Supplies, UK) at 15 rpm. Microparticles were then collected by centrifugation for 5 minutes (200 g, Sigma 1-16K). Collected microparticles were then suspended in aggregation media prior to patterning. For long-term storage, the microparticles were freeze-dried and then stored at -80^{o}C.

3.3.7 Patterning with avidin-coated microparticles

The standard patterning procedure detailed in Section 2.8.1 was adapted to facilitate the stabilisation of cell and microparticle patterns with the avidin-biotin interaction. mES cells (CGR8) were chemically modified with sodium periodate and then incubated with biotin, modifying the cell surface and allowing for cross-linking via the avidin bridge as described in Section 3.2.4. These cells were suspended in avidin-containing aggregation medium and added to polyHEMA-coated glass-bottom culture dishes. Avidin-coated microparticles were prepared as described in Section 3.3.6 and were added to the patterning gasket. Cells and microparticles were trapped and positioned in predefined arrangements, utilising the avidin-biotin interaction to stabilise the created patterns as they are formed.

3.3.8 Preparation of hydrogels

As described in Section 2.6.

3.3.9 Patterning with agarose ULGT

The standard patterning procedure detailed in Section 2.8.1 was adapted to facilitate the stabilisation of cell and microparticle patterns within an agarose hydrogel. mES cells (CGR8) were suspended in a 1.0% (w/v) solution of type IV ULGT agarose at 37ºC, and the suspension was added to polyHEMA-coated glass-bottom culture dishes. Cells and microparticles were trapped and positioned in previously defined arrangements. Once the desired patterns had been formed, the HOTs cooling setup was used to lower the temperature on the microscope stage to ~23ºC. After the temperature had been lowered, the hydrogel formed a gel, and the created pattern was locked into place without the need for optical trapping. Cell culture medium was then added to the culture dish if required for culture.

3.3.10 Spin coating polyHEMA onto glass coverslips

The polyHEMA surface coating was applied to a No. 1 round glass coverslip (22mm diameter) using a Laurell WS 650 Spin Coater. The glass coverslip to be coated was added to the centre of the microscope slide adapter within the protector of the spin coater. A vacuum was applied to the system that holds the coverslip in place on the microscope slide adapter, and the protector was closed. 500µL of polyHEMA solution (5, 6, or 10% [w/v]) was then pipetted onto the coverslip through the access point in the protector. A coating programme consisting of a 500rpm start phase (15s), spreading phase of either 30 or 400 g (30s), and finally a slowdown phase of 8 g (15s) was initiated. Once the programme was complete, the vacuum was turned off and the coated coverslip removed. Coated coverslips were kept in a slide box at room temperature for no

longer than 1 week, in most cases the coverslips were studied without intervening storage.

3.3.11 Water contact angle assessment

Surface wettability, or the hydrophilicity of a surface, can be studied by static water contact angle measurements. Using the sessile drop technique, a liquid sample is vertically deposited as a droplet onto a surface; the contact angle is then defined as the angle between the tangents at the solid-liquid and liquid-vapour interfaces. Hydrophilic surfaces with high wettability have a low water contact angle, whilst hydrophobic surfaces with low wettability have a high water contact angle. To assess the wettability of the PolyHEMA-coated glass surfaces, droplets of ultra-pure water (18.2 mΩ cm^{-1} at room temperature) were deposited onto each air-dried coverslip. Static contact angles were then recorded using an optical contact angle meter (CAM 200) (KSV Instruments, Finland). Droplet profiles were calculated in triplicate and defined using the well-known Young equation (Equation 3.1) that describes the balance at the 3-phase contact of solid, liquid, and vapour [179].

Equation 3.1 The Young equation

A static contact angle is obtained when the surface tension forces; γsv (solid-vapour), γsl (solid-liquid), and γlv (liquid-vapour) are in equilibrium.

$$\gamma sv - \gamma sl = \gamma lv \cos$$

3.4 Results and Discussion

3.4.1 Simple cell patterning

HOTs can generate multiple individually controllable optical traps, and precision pattern cells and other objects with the bespoke click-and-drag 'Red Tweezers' software (University of Glasgow). To demonstrate this, mES cells were patterned into pre-specified cluster sizes, ranging from 2 to 9 cells, and then more complex arrangements (Figure 3.1). The mES cells typically measure 10-15 μm in diameter, and could be manipulated easily in micrometre increments and positioned into arbitrary 2D structures.

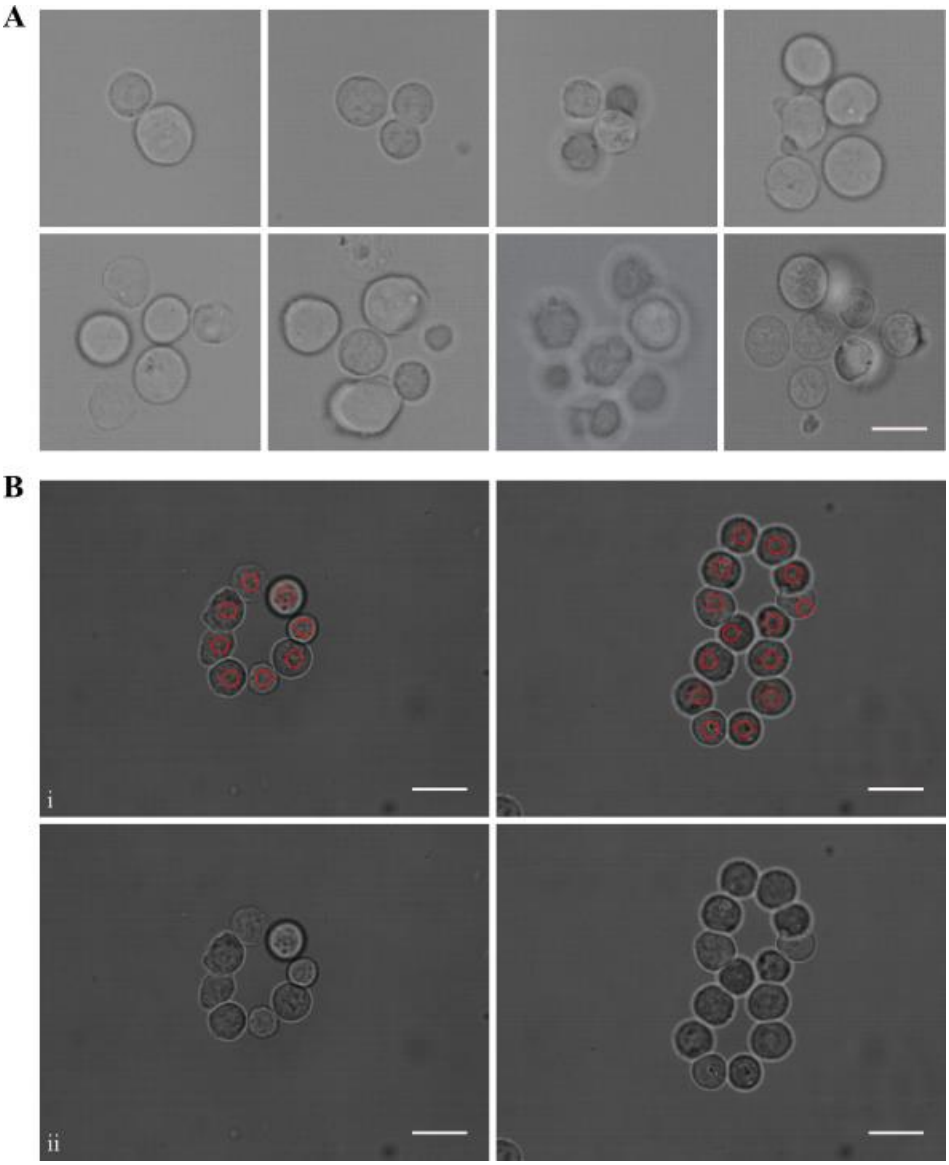

Figure 3.1 Simple cell patterning with HOTs.

A. Micrographs showing the formation of differently sized CGR8 mES cell clusters, from 2-9 cell in size, created using the HOT platform B. i. Micrographs showing the '8-cell ring' and the 'figure of 8' cell patterns, held in place by 8 and 14 optical traps respectively. ii. Cell patterns retaining their geometric position and pattern once the optical traps are removed, but only for a short while, ~5minutes. Cell patterning was limited to a maximum of 30 minutes. The scale bars represent 20µm.

Figure 3.1 also demonstrates the HOTs level of precision and control. Such direct cellular patterning can be used to investigate cellular interactions to determine how they affect cellular behaviours such as differentiation. In addition to monoculture patterning, multiple cell type patterning has been demonstrated [150], offering the potential for further investigations.

3.4.2 Optimisation of polymer microparticles for optical trapping

Polymer microparticles have been used with optical tweezers previously [180], however, it was understood that different fabrications would not be suitable for forming a stable optical trap and allowing optical manipulation. Initial optical trapping studies were completed on various microparticle formulations that could be used for future experiments. The microparticle batches used in this trapping study were characterised to determine why certain microparticles are better for optical manipulation than others.

3.4.3 Microparticle fabrication

Previous work by Dr Helen Cox (Thesis, 2013, University of Nottingham, UK) (Table 3.1) informed the choice of homogenisation speed and polymer percentages used for the W/O/W double emulsion preparation of blank microparticles. Using a range of polymer percentages we were able to fabricate 3 microparticles sizes that could be used for subsequent experiments.

Diameter size description (µm)	DCM volume (PLGA % [w/v])	Primary rpm	Secondary rpm	Diameter size achieved (µm)
1-3	50.00mL (2%)	9000	9000	1.8 ± 0.6
1-5	20.00mL (5%)	4000	9000	2.5 ± 0.8
5-10	10.00mL (10%)	4000	9000	6.8 ± 5.6
10-20	6.67mL (15%)	4000	9000	13.8 ± 7.5
20-30	5.00mL (20%)	4000	9000	26.2 ± 13.5
50-100	5.00mL (20%)	4000	2000	86.6 ± 24.6

Table 3.1 Fabrication of differently-sized PLGA microparticles.

The complete range of microparticle sizes that can be fabricated using the W/O/W double emulsion method of manufacture and Silverson homogeniser, up to 100µm in size. A mean particle diameter was recorded from 3 microparticle batches for each formulation, with standard error of the mean also calculated.

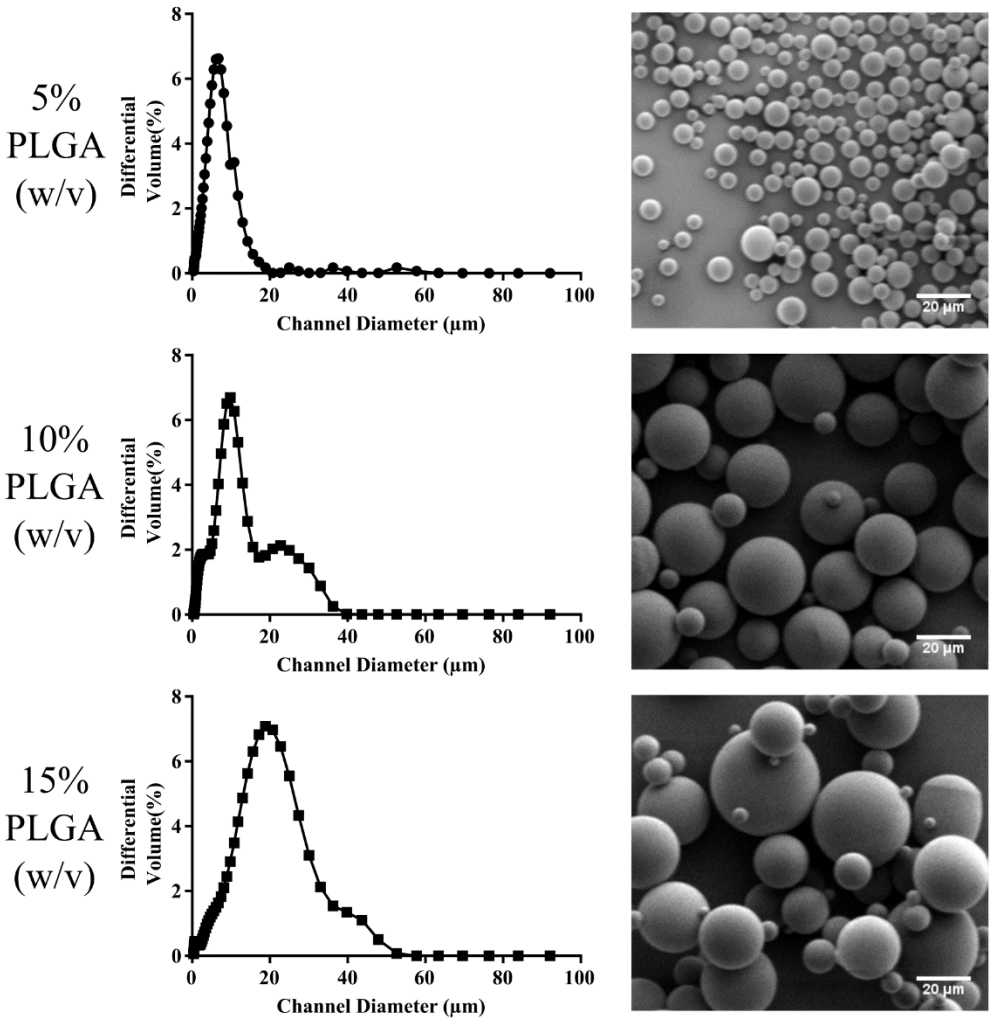

Figure 3.2 Characterisation of blank PLGA microparticles.

Assessment of the microparticle diameter size distribution across the batch and SEM micrographs to show morphology of 3 different PLGA microparticle batches, 5, 10, and 15% PLGA polymer % (w/v).

The 3 batches fabricated (Figure 3.2) had the expected median diameters, and displayed a spherical non-porous morphology. The sizes obtained were considered to be suitable for demonstrating different microparticle release sources for the optimisation and proof of concept for HOTs as a micropatterning platform. The 3 size ranges of microparticle batches fabricated were intended to show that release sources could be used that were smaller than the cells that were to be used with the development of the HOTs. The mES cells (CGR8) were generally 10-15 μm in diameter, so the average 5% PLGA microparticles were smaller, the 10% PLGA microparticles were of a similar size and the 15% PLGA microparticles were larger.

3.4.4 Optical trapping study

To form a stable optical trap capable of manipulating the controlled release of microparticles, the object being manipulated must have a suitably different refractive index to that of the surrounding medium. The forces required to hold the object in place are attained through the adequate refraction of the focussed laser through the object creating the optical trap. If the degree of refraction and summation of the refractive forces are not sufficient to overcome the forces within the liquid medium and gravity, a stable trap will not form. The simplest way to test whether the formulations were yielding trappable microparticles was to suspend the formulation in an appropriate cell culture medium and attempt the trapping of single particles. Figure 3.3 shows the results from the trapping study for the formulations tested.

Formulation	Polymer % (w/v)	Aqueous phase	Size range (µm)	Manipulation possible?	Minimum velocity achieved (32µm/s)?
PLGA	5	water	1-5	NO	NO
PLGA	10	water	5-10	YES	NO
PLGA	15	water	10-20	YES	NO
PLGA	5	HSA	1-5	YES	NO
PLGA	10	HSA	5-10	YES	YES
PLGA	15	HSA	10-20	YES	YES
PLGA:TBIIF	5	HSA	1-5	YES	YES
PLGA:TBIIF	10	HSA	5-10	YES	YES
PLGA:TBIIF	15	HSA	10-20	YES	YES

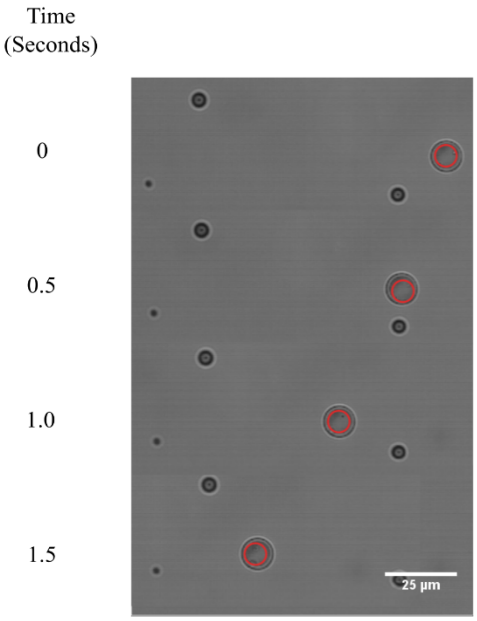

Figure 3.3 Microparticle trapping study.

A. A table showing the microparticle batches tested for their ability to be optically manipulated. Also listed is whether the microparticle batch could be manipulated at a velocity of 32 µm/s without falling out of the trap. The minimum velocity of 32 µm/s was chosen due its efficient patterning speed and ease of selection through the use of the HOTs controlling joystick. B. Showing how the 'minimum velocity achieved' test was completed, by assessing the distance a microparticle could be manipulated in 1.5 seconds the average velocity could be calculated.

Figure 3.3 shows that various formulations of PLGA microparticle do not trap well and that some do not trap at all. Those that do not trap are thought to have an insufficiently dissimilar refractive index to that of the surrounding medium. This prevents an optical trap forming, and the microparticle is rapidly expelled from the trapping area. This issue was alleviated by the addition of human serum albumin (HSA) to the aqueous phase; the hypothesis behind this is that the albumin protein will have an elevated refractive index and will permit the formation of an optical trap. All of the HSA-containing microparticles were able to be manipulated, but the 5% polymer batch was not suitably stable when moved at 32 μm/s (chosen as the minimum velocity for efficient patterning). However, the larger microparticles formulated in the same way were able to be manipulated easily. The integration of TBIIF copolymer at a ratio of 90:10 (PLGA:TBIIF) yielded a full size range of microparticles that were all suitable for optical manipulation.

3.4.5 Optimising release kinetics

One of the major advantages that polymer microparticles have to offer is their amenability to the modification of release kinetics by changing the fabrication process. To achieve the desired release kinetics for the preliminary concept studies, very quick release over 7 days with a low burst release, the PLGA:TBIIF copolymer ratio was modified. Using HSA and rhodamine 123 as the encapsulated cargo, we tested a range of polymer:copolymer ratios to identify a suitable formulation. Rhodamine 123 is a small fluorophore that would serve well as a reference small molecule with a molecular weight of 320 g/mol, while

HSA is a reference large protein with a molecular weight of 66.5 kDa and an isoelectric point of pI 4.7.

A range of microparticle batches were fabricated and characterised prior to the completion of *in vitro* release studies. Due to the suitable trapping and size of the PLGA:TBIIF 5 µm microparticles, all release optimisation was completed using this method of fabrication.

Figure 3.4 shows the characterisation of different PLGA:TBIIF blends loaded with rhodamine 123, as the ratio of TBIIF to PLGA is increased, polydispersity within the microparticle batch sizing increases slightly. Observed in the coulter sizing and SEM micrographs, microparticle polydispersity is a common problem associated with the emulsion fabrication technique. However, for this application it was not an issue, as particular microparticle sizes can be selected with HOTs through image-based sizing. Handling the higher 80:20 and 70:30 ratio microparticles was slightly more difficult due to the elevated TBIIF, yielding 'sticky' microparticles, as seen in the SEM micrographs. The incorporation of TBIIF slightly improved the encapsulation efficiency of active rhodamine 123 (Figure 3.5) indicating that it either preferentially incorporates with the TBIIF, or that the activity of the fluorophore is better-maintained with TBIIF. This observation, whilst not important at this stage of development, would be useful for later encapsulation of bioactive molecules and proteins that can be damaged in the encapsulation process [181].

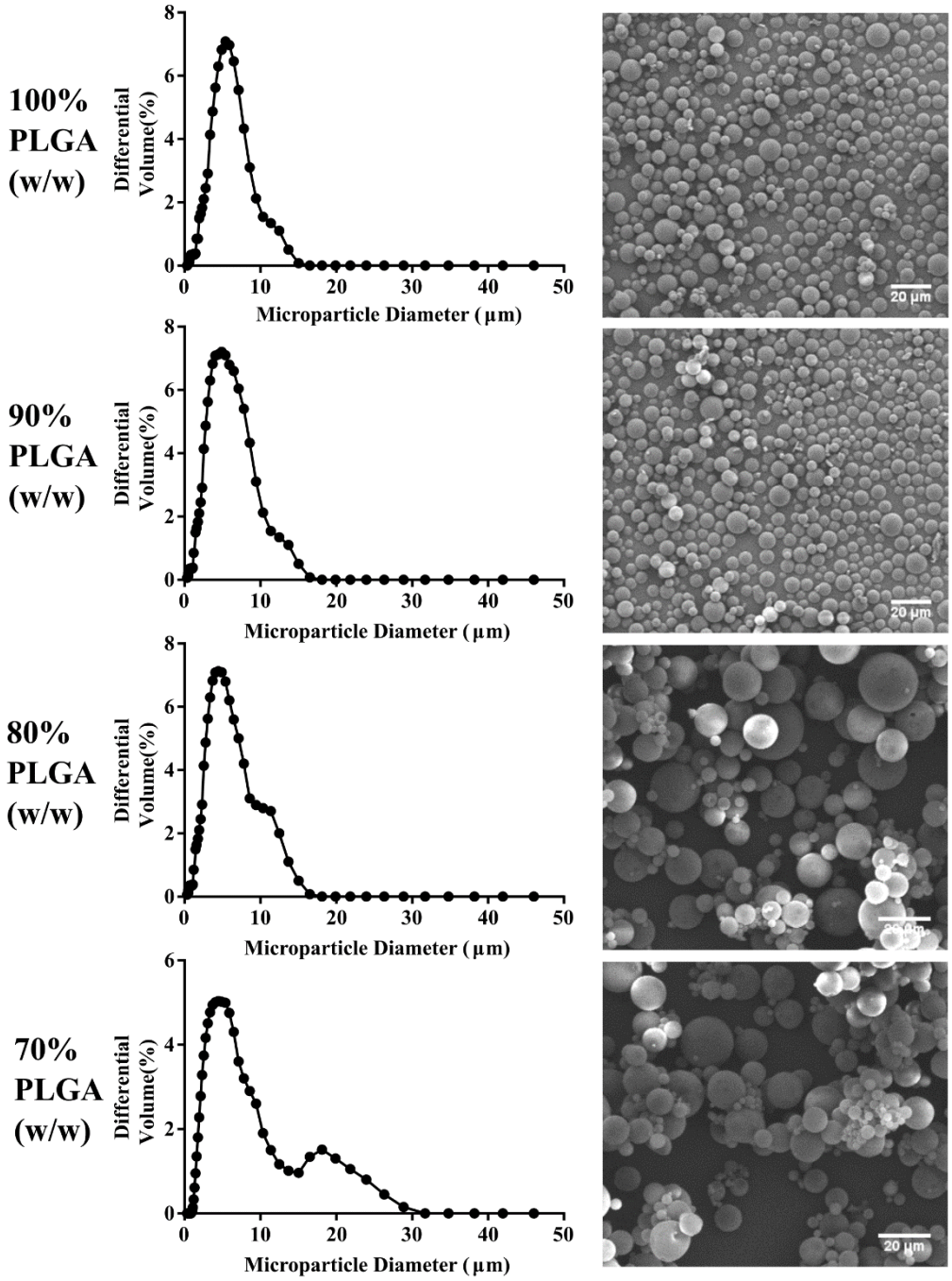

Figure 3.4 Characterisation of PLGA:TBIIF rhodamine 123 microparticles.

Assessment of the microparticle diameter size distribution of different rhodamine 123 microparticles with different ratios of PLGA:TBIIF, ranging from 100-70% PLGA with the rest being made up of TBIIF copolymer. Coulter analysis showed the size distribution of the microparticle batches and SEM was used to image the dry microparticles to assess their morphology and confirm sizing analysis.

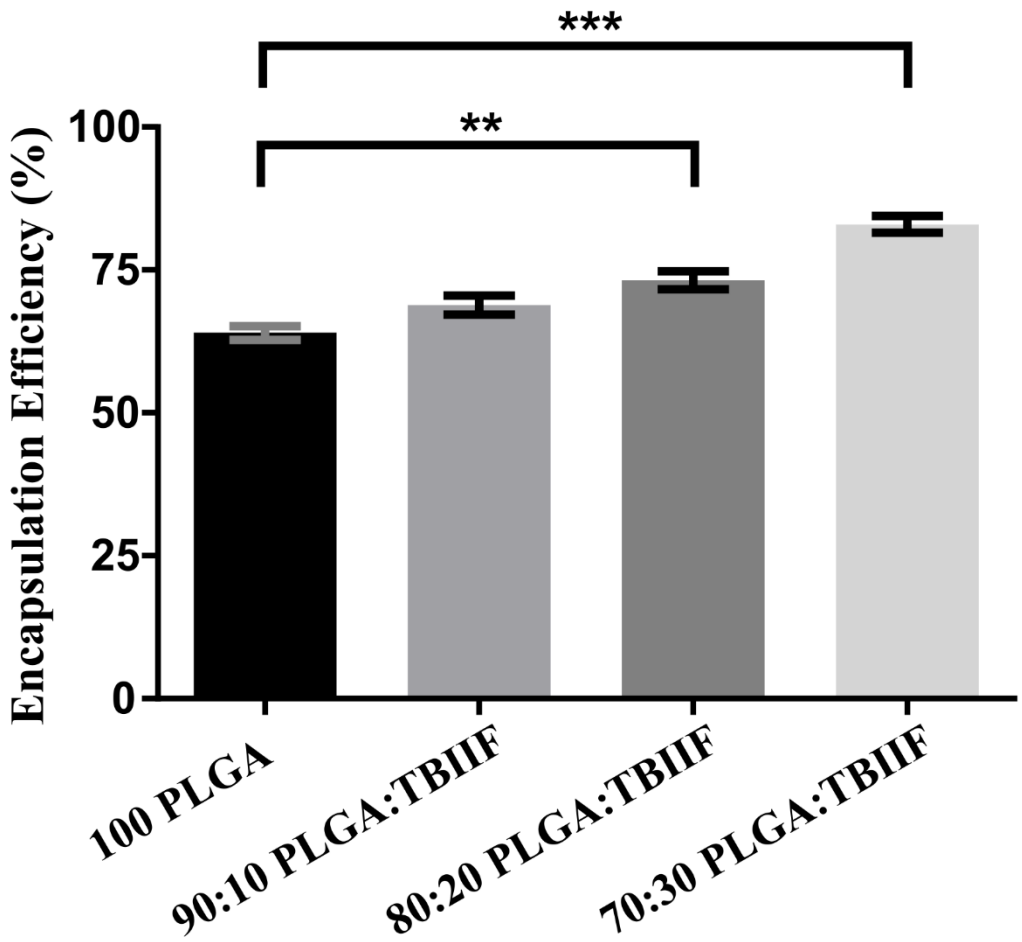

Figure 3.5 Encapsulation efficiency of rhodamine 123.

Graph comparing the percentage efficiency of rhodamine-123-loading into 4 different microparticle batches with varying ratios of PLGA to TBIIF copolymer. Dry microparticles were dissolved so that their contents could be analysed for estimated loading of rhodamine-123 Error bars show standard error of the mean from 3 separate batches for each formulation. Statistical analysis was completed to show significant difference of estimated loadings between 100 PLGA and batches containing TBIIF. T-test analyses were performed and the significant difference was indicated accordingly, *** = 0.01 and ** = 0.0045.

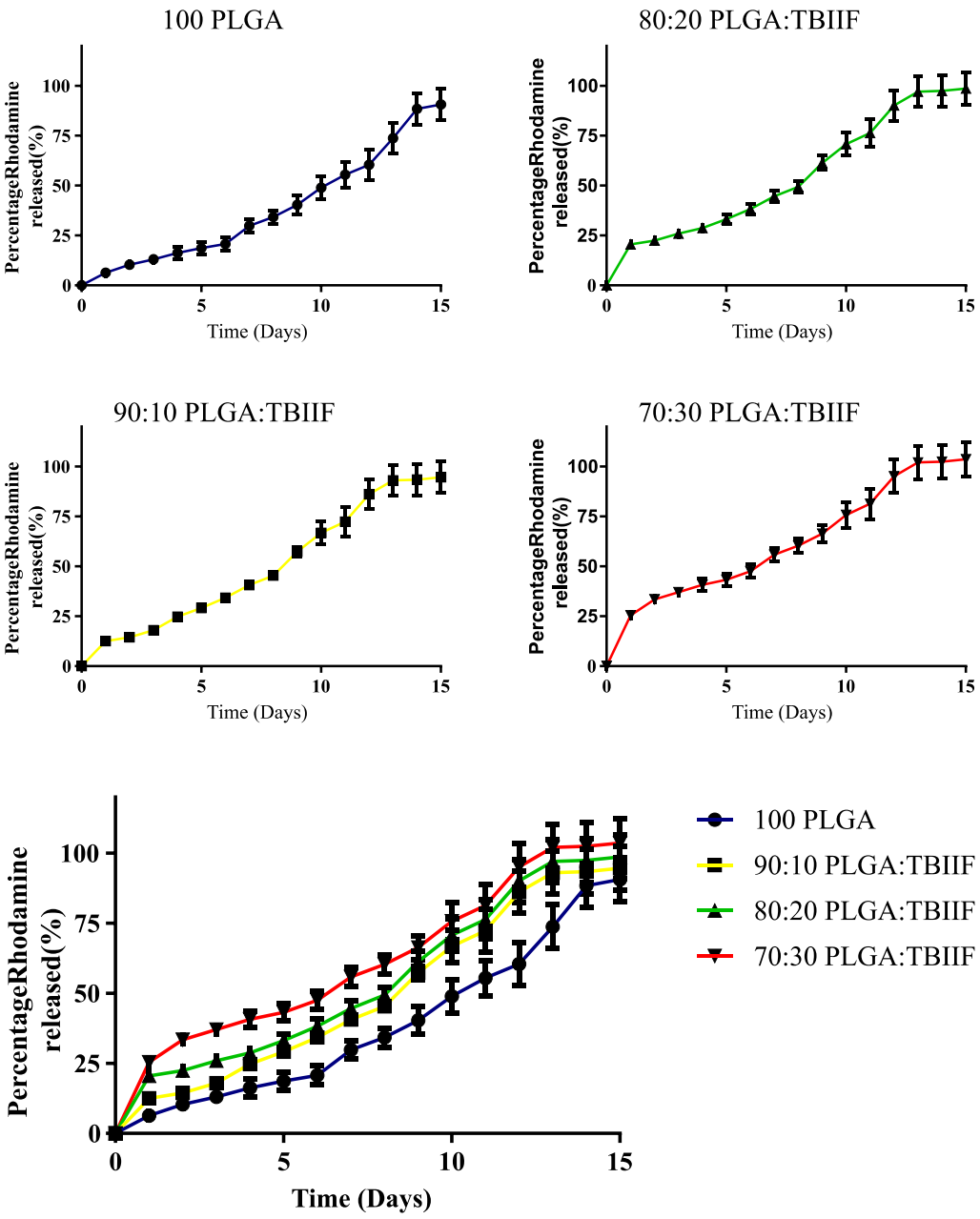

Figure 3.6 Release study for rhodamine 123 microparticles.

Individual plots and a combined plot showing the percentage of encapsulated rhodamine 123 released from each microparticle batch over 15 days of an *in vitro* release study. Error bars show the cumulative standard error of the mean calculated for triplicate samples from each microparticle batch.

The greatest change expected by altering the ratio of PLGA:TBIIF was to the release kinetics, TBIIF as a hydrophilic molecule has previously been shown to increase release through the enhancement of water ingress into the microparticle [120]. *In vitro* release studies were completed over a 15-day period (Figure 3.6), and showed the expected increase in rhodamine 123 release with the increase in TBIIF. The incorporation of TBIIF decouples the release rate from the polymer degradation time, the effect of TBIIF would be more profound if the PLGA used (50:50) had a slower degradation rate as standard.

At this stage in the HOTs development, these fast-releasing microparticles were suitable for all pilot experiments, however, through the use of different PLGA polymers, slow-release microparticles for much longer experiments could be developed. By altering the lactic to glycolic acid ratio in PLGA, one can achieve a wide range of degradation times, and hence release rates, for encapsulated molecules [182].

3.4.6 Patterning cells and microparticles using HOTs

In order to demonstrate the HOTs ability to precisely position cells into predefined 2D arrangement, simple patterns were formed in a cell culture medium suspension. Cells were diluted to low seeding densities to allow adequate surface space to create distinct cell patterns. In these initial studies, single patterning gaskets (fabrication described in Section 2.8.3) were used, meaning that the patterns created were surrounded by other un-patterned cells and release sources. To ensure that the patterned structure of cells, or the arrangement of microparticles, is the only stimulus, the patterned structure must be isolated; a solution to this problem was developed later (Section 4.4.10).

Initial experiments were designed to test the potential applications of certain cell and microparticle patterns, and as a proof of concept for future experiments involving the controlled release of stimuli.

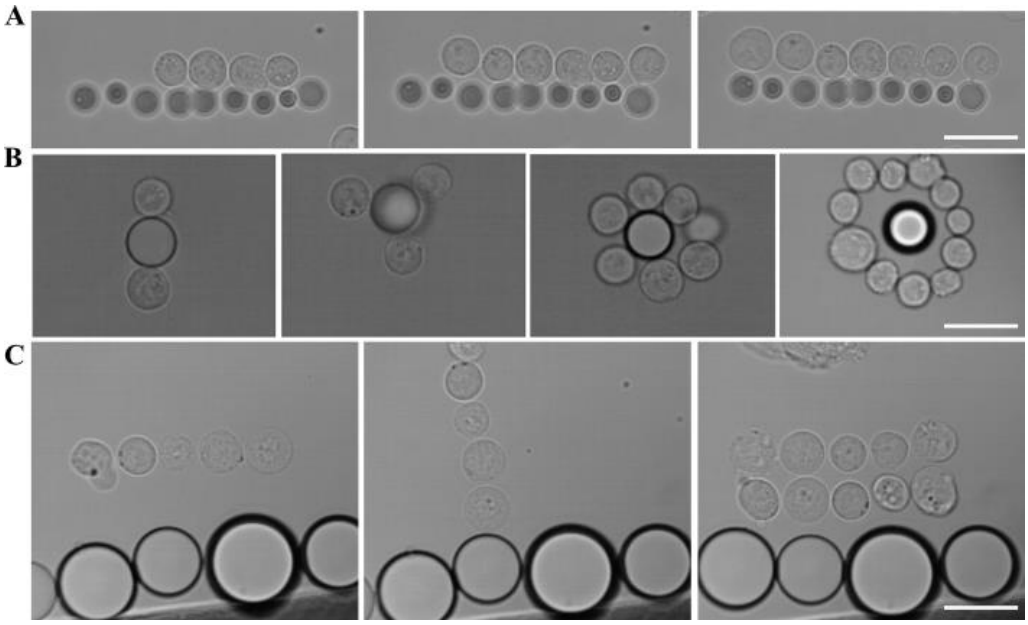

Figure 3.7 Cell and microparticle patterning.

A. Micrographs showing the creation of cell and microparticle lines using the HOTs platform to position 5% PLGA (w/v) microparticles. B. Simple cell and microparticle patterns created with 10% PLGA (w/v) microparticles. C. Different cell patterns formed on an arrangement of large 15% PLGA (w/v) microparticles. The scale bars represent 20 μm in length.

Figure 3.7 demonstrates the use of small, medium and large microparticles as potential release sources for a HOTs-formed microenvironment. It was important to show that the release source could be built within a structure as well as at a particular point outside of the pattern to prove the versatility of the optically-manipulated release sources.

3.4.7 Stabilising cell and microparticle structures

In this chapter the optimisation of some the first steps in developing the HOTs as a micropatterning tool have been demonstrated and discussed, including manipulating cells into small patterns, fabricating a selection of microparticles suitable for optical manipulation and the encapsulation of a variety of different molecules, and then the optimisation of the microparticle release kinetics. Another aspect to be addressed is the HOTs capacity to maintain a micropatterned cell and microparticle pattern for extended periods of time. All patterning heretofore discussed was locked into position by the presence of optical traps on the HOTs setup. To permit the culture of such cell patterns or to observe molecular release from microsources over days, the created patterns must be moved to a cell culture incubator. Any movement of the patterning gasket would disturb the created structure, and patterns would be lost.

3.4.8 Optical manipulation of avidinated microparticles

The first approach to stabilising the fabricated microparticles and cells structures was to use a well-described avidin-biotin interaction. Avidin protein is derived from avians and amphibians, and has a high affinity for the co-factor biotin. These binding proteins have been utilised for many purification and detection

applications, and recently has been used to form large multicellular aggregates by selectively adding biotin to the cell surface [155]. When biotinylated cells are suspended in avidin-containing medium, they have the ability to bind to one another, as demonstrated in Figure 3.8. In order to stabilise the cell and microparticle structures created with the HOTs, with help from Dr. Omar Qutachi (University of Nottingham, UK) the microparticles were coated in avidin solution and biotinylated the cells as described in Section 3.3.6. By doing this, it was hypothesised that cell and microparticle aggregates could be formed with the HOTs and then bound together via the biotin-avidin interaction.

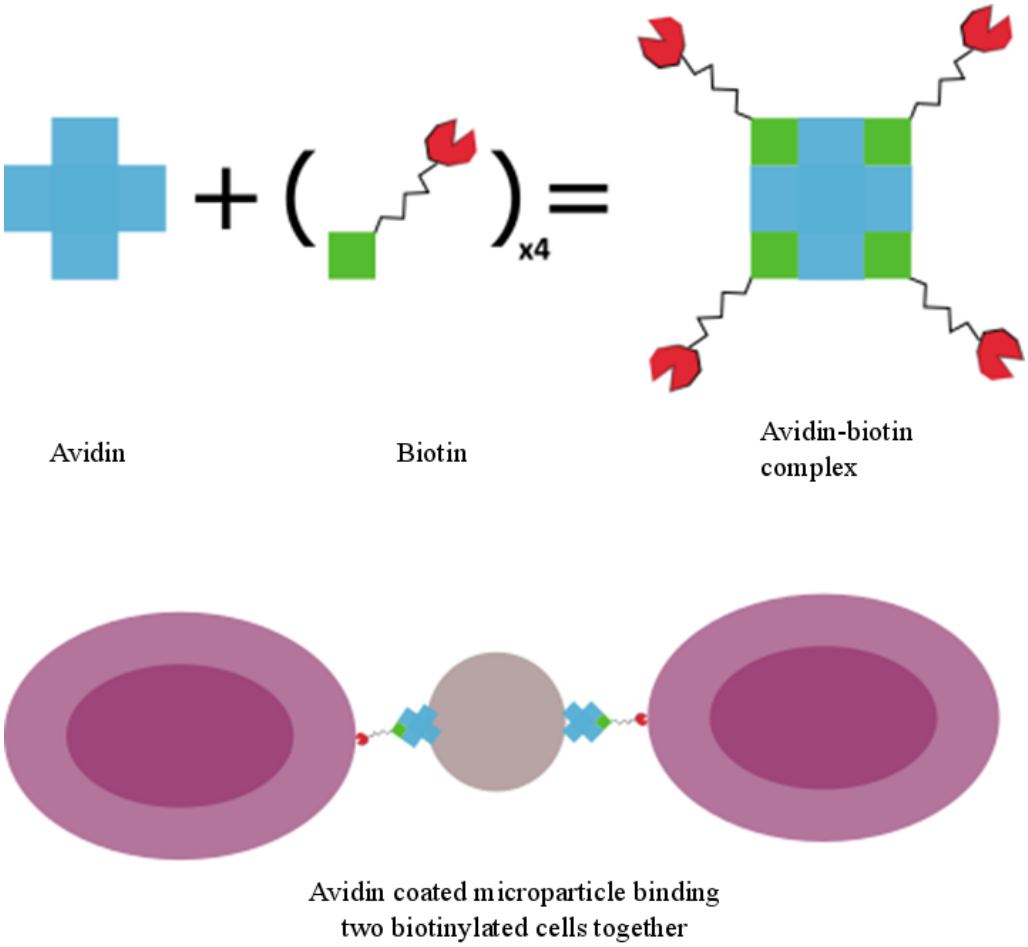

Figure 3.8 Avidin-biotin interaction.

A diagrammatic representation of the avidin-biotin interaction and the interaction between avidin-coated microparticles and biotinylated cells.

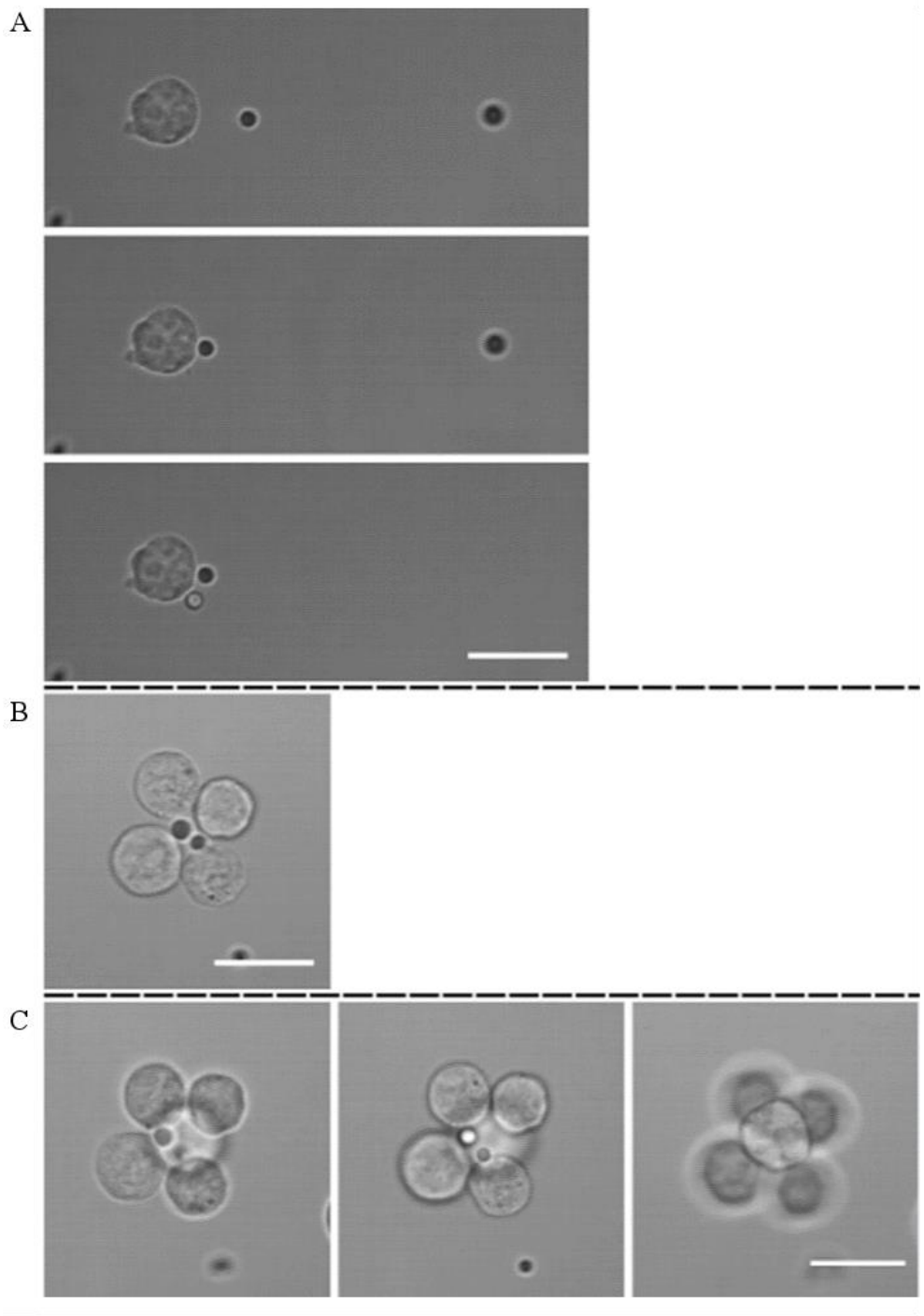

Figure 3.9 Avidinated microparticle patterning.

A. Micrographs showing the attachment of avidin-coated microparticles to a single CGR8 mES cell using the HOTs patterning platform. B. A micrograph showing the formation of a 2D pattern of 4 CGR8 mES cells around two avidin-coated microparticles. C. A set of 3 micrographs showing the bottom, middle and top planes (left to right) of a 3D avidin-biotin stabilised cell and microparticle structure. The scale bars represents 20 µm.

Figure 3.9 A shows 2 avidin-coated microparticles being positioned on the surface of a single mES cell; the microparticle seems to fix to the cell within seconds as it cannot be separated by trapping. The interaction is so strong that the HOTs force is insufficient to separate the cell from the microparticles. Figure 3.9 B shows how the avidinated microparticles can be incorporated into a 2D cell pattern: the cells are locked with one another utilising free avidin in the medium, and the microparticles are directly bound to the biotinylated cells. The use of avidinated microparticles even permits the creation of simple 3D cell structures, Figure 3.9 C demonstrates this with the fabrication of a 6-cell 'sphere' containing 2 avidinated microparticles. The whole structure was stable, and optical trapping was not necessary after the avidin-biotin interactions had formed.

Whilst the avidin-biotin interaction was strong and was able to preserve structural integrity of a pattern, it was still free to move around in the liquid medium. This was both an advantage and disadvantage, to wit, it was advantageous that the technique offered the creation of stable non-adherent structures, giving more flexibility to the choice of cells used for micropatterning e.g. marrow mesenchymal stem cells [183]. However, for the establishment of different release profiles, patterned cells might need to be positioned at specific distances from the release source, and hence they would not be in direct contact - such patterning would not be stabilised by the avidin-biotin interaction.

3.4.9 Optical manipulation within a hydrogel

The next approach to maintain patterned structures was to use a hydrogel system to lock the micropattern in place once it has been fabricated, allowing

transportation of the patterning gasket for extended culture and more complex imaging not possible on the HOTs setup.

The setup requirements of this hydrogel were quite restrictive when it came to choosing one that would be suitable for the micropatterning tool. There are a wide variety of different cell-culture-suitable hydrogels available for sustaining cell growth and development, however, for use with the HOTs, many were unsuitable. The hydrogel would need to be cross-linked in such a way that it would not damage the cells, the pre-gel solution that the cells would be patterned in must not be too viscous to prevent optical manipulation, the hydrogel must be optically suitable (suitable refractive index for optical trapping and transparency for imaging), and the gel must be as bio-inert as possible.

The need for a bio-inert pattern-locking mechanism was based on the fact that the HOTs were being developed to create cellular microenvironments from the 'bottom up'. The aim of the HOTs patterning platform was to allow the creation of such microenvironments with complete control over the cues within them. If the hydrogel contained a potent cue or stimulus, it would be impossible to discern what was affecting cellular development.

There are a number of cell-culture-suitable hydrogels which undergo cross-linking following a change in temperature. So long as that temperature change was suitable for the cells within the gel, such a temperature-sensitive hydrogel seemed like the least invasive method of cross-linking. A selection of thermosetting hydrogels commonly used in cell culture applications was assessed and the results are shown in Table 3.2.

Table 3.2 Hydrogel selection for use with the HOTs.

The selection criteria for stabilisation hydrogel are outlined below and the table shows how Agarose ULGT was initially chosen as a front runner hydrogel.

Hydrogel	Optically Suitable	Pre-gel a suitable temperature range	Short gelation time	Bio-inert?
Gelatin (Bovine)	NO			
Gelatin (Porcine)	YES	YES	NO	
Matrigel	YES	YES	YES	NO
Collagen Type I	YES	YES	YES	NO
Agarose ULGT	YES	YES	YES	YES

The type IX, ULGT agarose was chosen as the most suitable hydrogel tested, although Matrigel and collagen had suitable properties, the well-reported bioactivity of these extracellular matrix (ECM) hydrogels [184] precluded them from use at this stage. After choosing to proceed with agarose for the hydrogel patterning experiments, a range of concentrations were tested to assess their capacity to permit cell proliferation (Figure 3.10). The different hydrogels were seeded with mESCs, and then proliferation was assessed via the MTS assay as described previously (Section 2.5.8). For this assay, readings were taken at 24-, 48-, and 72-hour time points.

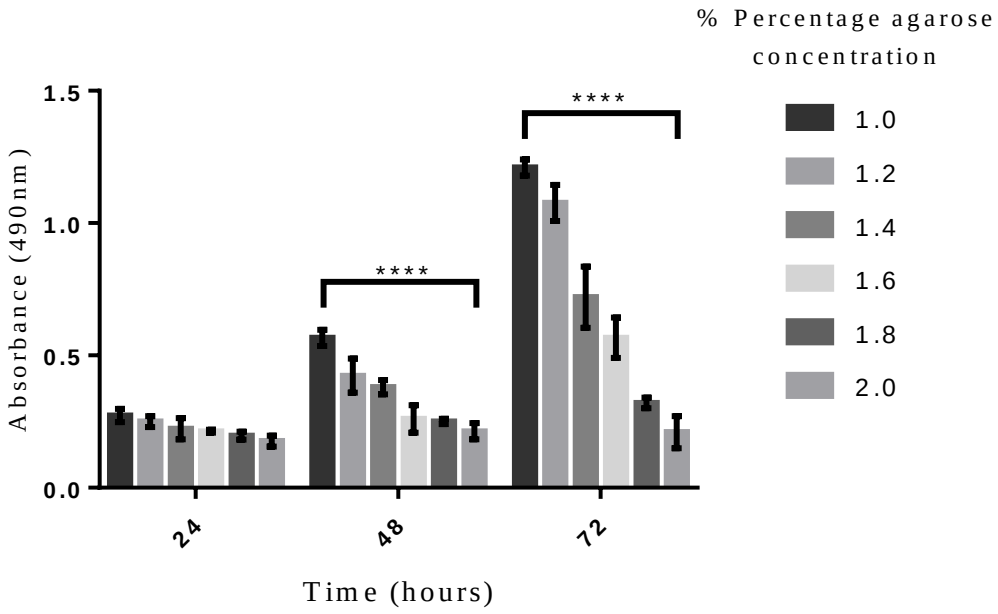

Figure 3.10 Proliferation of mES cells encapsulated within agarose (ULGT)

Proliferation of CGR8 mES cells cultured in a range of agarose ULGT agarose hydrogel concentrations (1.0 – 2.0% (w/v)). Metabolic activity of the cells at 24, 48, and 72 hours was measured by MTS assay (absorbance 490 nm). Data are expressed as the mean ± SD of triplicate samples and significant differences were assessed by ordinary one-way ANOVA. Statistical significance was expressed as **** ($P<0.0001$).

The proliferation assay showed the expected reduction in proliferation rate of the mES cells when seeded into agarose as compared to those cultured on gelatin-coated tissue culture plastic [48]. When comparing the different concentrations of agarose, the data showed that the higher percentage hydrogels had a restrictive effect upon the proliferation of CGR8 mES cells. Following this study, lower percentage agarose hydrogels (<1.0% w/v) were tested; however these did not form a stable gel when cooled using the HOTs cooling setup (data not shown).

Previous work completed by Dr. Emily Britchford (University of Nottingham, UK) characterised agarose gelation kinetics by rheological investigations. Viscosity curves and optimised oscillatory amplitude and frequency sweeps were completed to measure sample viscosity and study the solution-gel, gel-solution transition, respectively. It was determined that the agarose remained a liquid at 37^{o}C and then gelled rapidly at temperatures below 25^{o}C, and once the hydrogel structure was formed, melting would not occur below 55^{o}C (Appendix, Figure 8.1). These gelation characteristics were deemed highly compatible for gel-based optical manipulation and subsequent culture at 37^{o}C.

3.4.10 Cell patterning in agarose ULGT

The standard polyHEMA-coated coverslips were prepared with patterning gaskets mounted onto them, and the HOTs patterning was completed in the 1.0% agarose ULGT solution. Cells were patterned into an 8-cell ring structure and, using the water-based cooling system, the patterning gasket and hydrogel medium were cooled to ~23^{o}C. By removing the optical traps individually, it was determined whether the hydrogel had gelled sufficiently and locked the cell pattern in place.

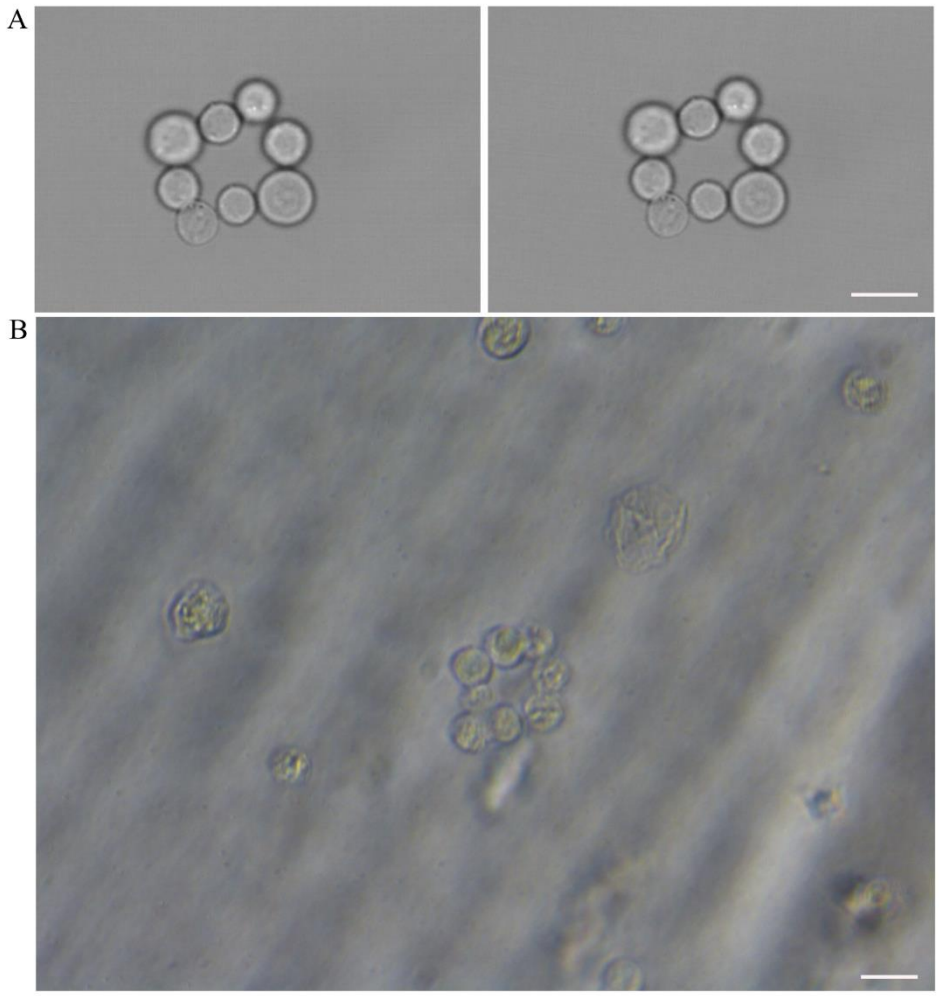

Figure 3.11 Hydrogel stabilised cell pattern.

A. Shows 2 micrographs, one is the 8-cell ring held into position with 8 optical traps in a solution of agarose ULGT at 37ºC (left) using the HOTs patterning platform, and the other is after cooling the environmental chamber to ~23ºC and the stabilised cell pattern held in position by the agarose hydrogel (right). B. A micrograph showing the same pattern created in A after transportation to a cell culture suite and imaged at a lower magnification. The scale bars represent 20 µm in length.

The thermo-responsive agarose hydrogel cross-links quickly (Appendix, Figure 8.1), and the intricate cell pattern is locked in place after only short-term exposure to the optical trap (all trapping completed under 15 minutes). Figure 3.11 B shows the mES cell pattern after transportation to the cell culture lab; there appears to have been some movement of the cells, but the general pattern has been retained.

3.4.11 Improving the anti-biofouling surface for patterning in hydrogels

The HOTs ability to manipulate objects relies upon the generation of a force sufficient to overcome the forces holding said object in place. Such competing forces include shear and tensile stress, corresponding to the viscosity of the medium and the interactions between the object and the surface they settle on. As previously described, the glass coverslips used for patterning were coated in a layer of polyHEMA to reduce the possible electrostatic interactions between the cells and the hydrophilic glass surface. Various other surface coatings were previously tested (Table 3.3) by Dr Glen Kirkham and Dr Emily Britchford (University of Nottingham, UK), however, polyHEMA was deemed to be the best choice, with the greatly reduced ‘sticky cell’ issues.

Table 3.3 Optimisation of surface coatings

A table showing the surface coatings tested previously, and whether certain surfaces led to cell sticking during HOTs based patterning. Cell sticking was assessed by eye and through not being able to optically manipulate cells that had settled on the surface of the patterning gasket.

Surface coating	Coating Method	Cell sticking (Yes/No)
Pluronics-F68	Passive adsorption	Yes
Pluronics-F127	Passive adsorption	Yes
PDMS	Passive adsorption	Yes
Sialinated glass	Purchased	Yes
Alginic acid	Passive adsorption	Yes
Hyaluoronic acid	Passive adsorption	Yes
Pectic acid	Passive adsorption	Yes
PolyHEMA	Passive adsorption	No

In the early stages of this project, patterning was only completed in low-viscosity cell culture medium, in which cells and microparticles could be manipulated easily. However, when using agarose hydrogel, the increased viscosity posed a problem to optical manipulation and patterning, cells were sticking down and could not be manipulated. PolyHEMA is able to prevent cell adhesion by two main mechanisms, firstly, a structure formed of many long chains that sterically prevents contact between molecules and the surface it is coated on, and secondly, due to its being highly hydroxylated, it is very hydrophilic [164,165]. The polyHEMA surface becomes highly hydrated, increasing the energetic requirements of removing water for cells to attach. To address the issue of cells sticking in agarose, the hydrophilicity of polyHEMA-coated surfaces fabricated using different methods was assessed.

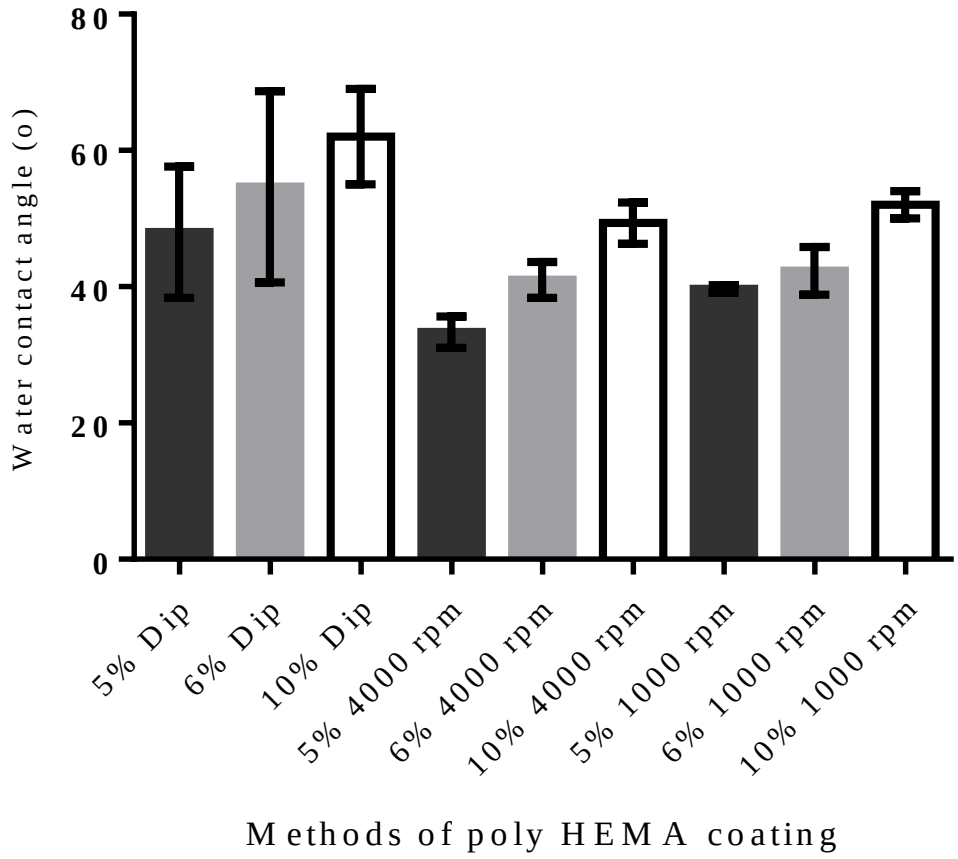

Figure 3.12 Hydrophilicity of different polyHEMA coatings

The graph shows the water contact angle formed with the sessile drop technique. Error bars represent the standard error of the mean from triplicate readings. A 1-way ANOVA statistical test was performed to assess variance between the mean WCA for each water-surface interface. The means were significantly different across the dataset to a P value of 0.0013 (**).

Figure 3.12 shows that regardless of the method chosen to coat the polyHEMA to coverslip glass, the use of 5% polyHEMA achieves the most hydrophilic coating. High-speed spin coating, however, does improve the hydrophilicity of the surface; the 5% polyHEMA solution, when applied via spin coater at 4000rpm, created the most hydrophilic surface coating with a water contact angle of 33 ± 1.3^{o}. Using this fabrication method, the cell patterning in agarose was improved; far fewer cells became stuck to the surface. This result was surprising, as previous work with polyHEMA had shown that thicker coatings were just as effective as thin coatings [185]. That the high-speed spin coating did increase hydrophilicity and reduce cell-sticking issues may have been due to the topography of the surface coating, as smooth surfaces have been shown to reduce cell adhesion and interface interactions [186].

3.5 Conclusions

The aim of this chapter was to report the optimisation of the various aspects of the HOTs patterning platform, and to demonstrate how they will be used to create micropatterns representative of a dynamic cell microenvironment. Cells can be manipulated with high precision into complex micrometre-scale arrangements with release sources. Polymer-based microparticles have been optimised for optical manipulation and adapted to provide a wide range of desirable sizes and release kinetics. The developments in this chapter are used in subsequent chapters to permit more complex proof of concept work that shows how release sources can be used with the HOTs platform to create biomimetic representations of the solute signalling to cells in development. This chapter describes possible methods for stabilising such cell and microparticle structures

and has yielded options to suit different needs and applications. The pattern stabilisation offered by hydrogels was exploited often in the experiments which informed the next chapter.

Throughout the early stages of this project, as detailed in this chapter, new challenges have been observed that must be overcome before HOTs can perform effectively as a micropatterning tool. It has been described just how the optimisation of the polyHEMA surface coating was important in improving patterning outcomes with the agarose hydrogel. However, certain issues remain, for instance, the patterning of a small subset of cells and microparticles within a suspension of cells and microparticles is problematic. Surrounding 'unpatterned' cells and microparticles in effect contaminate the intricately patterned cell and microparticle arrangement. To address this, the patterned cells and microparticles must be isolated so as to be sure that there are no external factors affecting the patterned cellular behaviour and arranged release points. The importance of this issue, and the proposed solution, are discussed in the next chapter.

4. Results - Proof-of-concept delivery of molecular signals to micropatterned cells

4.1 Introduction

In this chapter the two aspects of delivery relating to this thesis are discussed; firstly, the delivery of solute signals as a proof of concept for morphogen signalling, and secondly, the delivery of isolated release sources to the patterning area in a controlled manner.

The former of these two aspects is essential to the core concept of the HOTs patterning system being developed. There is a great need for innovative technologies that can recreate molecular gradients that occur in nature. Morphogen signalling is important for many biological processes, including the polarization of tissues and cells during embryogenesis, and the coordination of adult cells via chemotactic cues. For any investigations into the subtleties of these phenomena to occur, there must be a tool-set capable of controlling the chemical environment, and of tailoring molecular gradients at the micrometre scale. In this chapter the development of HOTs to create such molecular signals with spatial and temporal flexibility is discussed.

With regard to spatial flexibility, it is important to isolate the patterned release sources from the unpatterned, so that there is no unwanted or background signalling occurring in the patterning area. This chapter details how a simple development of the HOTs patterning gasket can achieve this isolated patterning, and how it permits the formation of spatial signalling control.

The development of the HOTs patterning setup to achieve spatio-temporally-controlled signalling is imperative to a number of different developmental models. One such model that exemplifies the importance of diffusible signalling for both cell development and guidance is the nervous system. Axons are guided on very specific routes, and their neuronal fate is differentially determined based principally on morphogen signalling. As previously discussed, a morphogen is classically defined as a signalling molecule that elicits a differential cell response depending on its concentration. Morphogens are typically secreted or released molecules that drive the organisation of cells into patterns [187], and in the case of axon guidance these morphogens determine both the neuronal fate and path of the developing neurons [188–190]. A gradient of Sonic Hedgehog (Shh) and bone morphogenetic proteins (BMP) act in the early neural tube to specify ventral and dorsal neurons respectively. The complex interplay of these gradients and others is essential in the development of the nervous system, and it is this complexity that is required for recreating the aforementioned developmental models.

The HOTs patterning setup was developed with these complex mechanisms in mind, and this chapter details the early proof of principle experiments that show how the release of molecules can be visualised, accomplished with multiple signals and spatio-temporal control. Demonstration of these proof of principle experiments was only possible after overcoming several key difficulties

associated with the system. The ability to visualise or quantify solute gradients is an area of study in itself, and has proven difficult to accomplish even without the added complications of HOTs-based patterning. In some cases, investigators have had to rely on computational modelling [191], particularly where solute concentrations are too low to visualise. The difficulties encountered and approaches to solving them are described in this chapter, detailing how proof-of-principle solute delivery experiments were conducted.

4.2 Chapter experimental overview

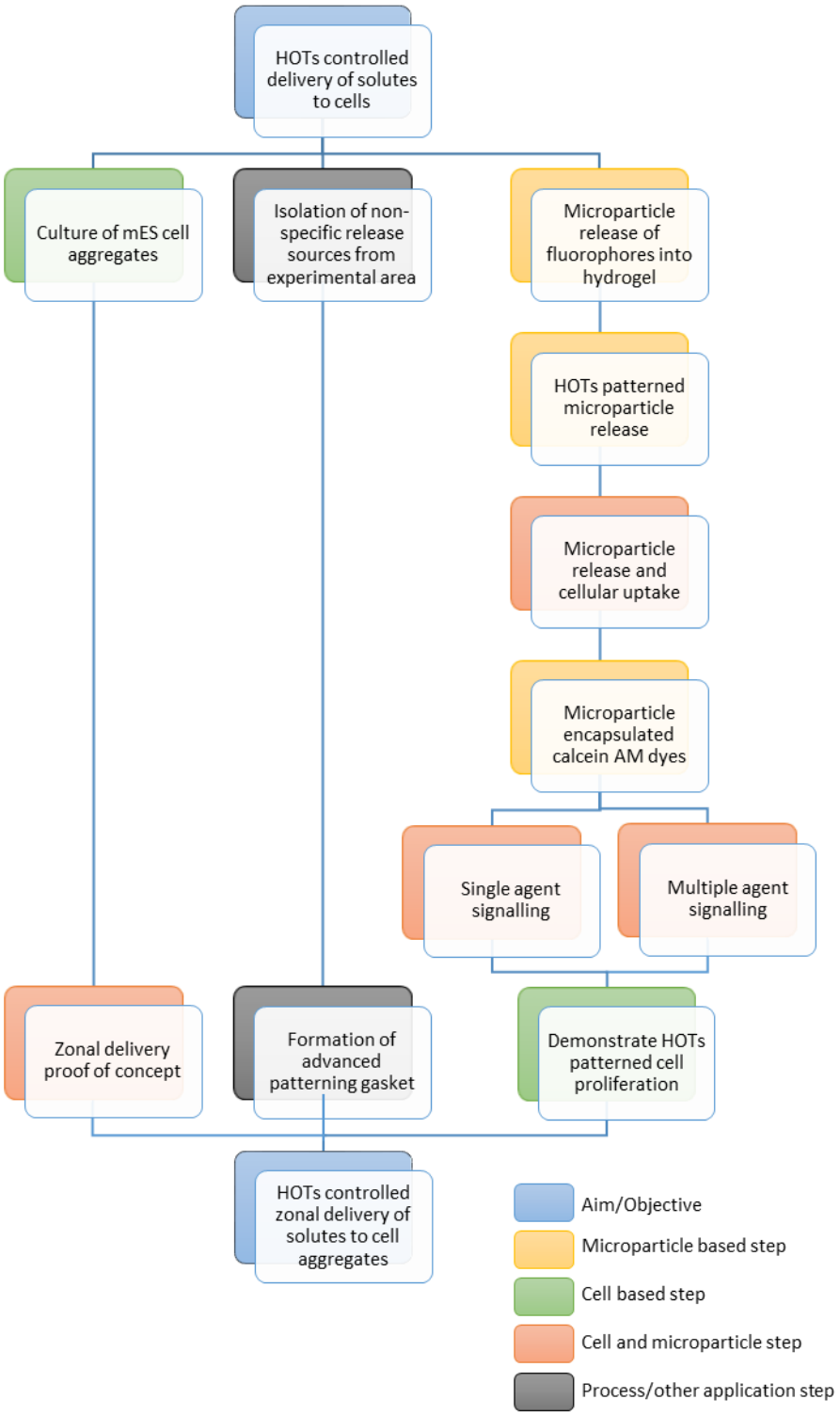

4.3 Materials and Methods

4.3.1 Rhodamine 123 release from microparticles into a hydrogel

A 1.4% ULGT agarose solution was prepared, as previously described (Section 2.6), and was poured into 60mm dishes. The hydrogel was then left to cool at room temperature for 10 minutes, or until gelled. With the use of a 4 mm bore biopsy punch, a hole was removed from the centre of the agarose gel. Rhodamine-123-laden microparticles were then suspended at a concentration of 1 mg/mL and were added to the 4mm void within the agarose. Bright-field and fluorescence microscopy were used to image the dishes daily, a Nikon dissection microscope was used (Section 2.10).

4.3.2 Encapsulation of calcein AM into PLGA microparticles

As previously described, the calcein-AM-laden microparticles were fabricated according to the w/o/w emulsion technique described in Section 2.9.1. A loading of 0.1% w/w was achieved by using 1 mg of calcein green AM in 1 g of polymer.

4.3.3 Calcein AM release study

The *in vitro* release study for calcein-AM-laden microparticles was completed as described in Section 2.9.6. Calcein AM was quantified using a NanoDrop spectrophotometer (ND-1000, Labtech) at 384 nm to measure calcein green AM and 322 nm for calcein blue AM related absorbance.

4.3.4 Post-encapsulation bioactivity of calcein AM

To assess the effect encapsulation has upon calcein AM bioactivity, 25 mg of 0.1%-loaded calcein-AM-laden microparticles were suspended in 1mL of 0.1% DMSO and incubated at room temperature for 10 days on a GyroTwister 3D Shaker (Labnet International Inc., Dorset, UK). The solution was then centrifuged for 5 minutes at 3000 rpm (MSE, Mistral 1000) and the supernatant was carefully removed. 100 µL of the supernatant was then added to 1mL of cell culture medium to yield an estimated concentration of 2 µM calcein green AM (0.01% DMSO) based on complete release of calcein green AM from microparticles and 100% loading efficiency. The resulting post-encapsulation calcein green AM solution was then added to a confluent monolayer of mES cells (CGR8) grown under standard culture conditions. The cells were incubated in this solution for 45 minutes at 37^{o}C and then imaged by fluorescence microscopy.

4.3.5 Cell viability assessment

After the analysis of calcein green AM and calcein blue AM dual release experiments, cell viability was assessed to ensure that the cell structures were not dead and leading to false positive green fluorescence signals. A negative control pattern of cells and microparticles was fabricated and then irradiated with ultraviolet (UV) light for 30 minutes to ensure cell death. The pattern was then assessed for cell viability using the LIVE/DEAD® cell assay as described in Section 4.3.5. For the experimental patterns, just ethidium homodimer 1 (EthD-1) was added. Viability was determined as previously described (Section 2.5.7).

4.3.6 Patterning with gelatin methacrylate

The GelMA was prepared as described in Section 2.6 and then dissolved in 80^{o}C photoinitiator (Irgacure 2959 0.5% (w/v)) to yield a 10% (w/v) GelMA solution, and stored in the dark at 4^{o}C until use. This solution was warmed to 37^{o}C and then added to the patterning gasket to a maximum volume of 100µL. Cells and microparticles to be patterned were added directly to the patterning gasket as required under sterile conditions. Once patterning was completed, the GelMA solution was cross-linked with a 5 second burst of UV light from a distance of 5cm resulting in an output of 30 W/cm^2 using a UV lamp (Omnicure S2000, JentonUV, UK) The GelMA was left for 5 minutes to ensure complete cross-linking. If prolonged cell culture was required, cell culture medium was added on top of the cross-linked GelMA before incubation at 37^{o}C with 5% CO_2.

4.3.7 Formation of the PDMS lobed patterning gasket

To create the lobed patterning gasket, an internal mould was made for the gasket to be cast around it. The internal mould was designed using a simple open source Computer Aided Design (CAD) approach (Tinkercad). The design was then 3D printed with polylactic acid (PLA) filament using a MakerBot Replicator 2. The printed internal mould was then glued to a 60 mm petri dish (using a non-toxic silicone rubber compound). Sylgard 184 silicone elastomer was prepared as described previously and was left to degas for 4 hours at room temperature. The degassed solution was then carefully added to the internal-mould-containing petri dish up to a depth of 5mm so as not to cover the mould and to create a suitable volume patterning gasket. The petri dish was covered with its corresponding lid and left for 5 days at room temperature to fully cure. Once

cured, the PDMS was removed from the petri dish and cut to size to leave the internal-mould-shaped area surrounded my PDMS. The PDMS lobed patterning gasket is then glued to polyHEMA-coated coverslip glass and stored at room temperature until required. Before use in cell patterning, the PDMS lobed patterning gasket was UV sterilised for 1 hour.

4.4 Results and Discussion

4.4.1 Visualising release in agarose

In Chapter 3 the fabrication of rhodamine-123-encapsulated PLGA:TBIIF microparticles was described, *in vitro* release studies were completed to show that through the addition of TBIIF, release can be accelerated. For the purpose of these studies, a plate reader was used (as detailed in Section 2.9.6) to record the levels of rhodamine 123 fluorescence signal in supernatants so that the concentration could be quantified from a standard curve. For creating a proof of concept for the delivery of loaded molecules from microparticles to patterned cells, this method would not be appropriate. In order to track the delivery of a fluorophore from release point (microparticle) to target (patterned cells) fluorescence microscopy was deemed the best option. Pilot experiments were designed to show the principle of release of rhodamine 123 from a microparticle release point to a surrounding agarose gel.

Further to the visualisation of a rhodamine 123 fluorescence signal over time, two microparticle batches were tested alongside one another. PLGA microparticles without the addition of TBIIF were compared to the PLGA:TBIIF (70:30) batch, each with the same rhodamine 123 loading (Section 3.3.3). The comparison was important as it would test the ability to qualitatively assess subtle differences in fluorescence signal.

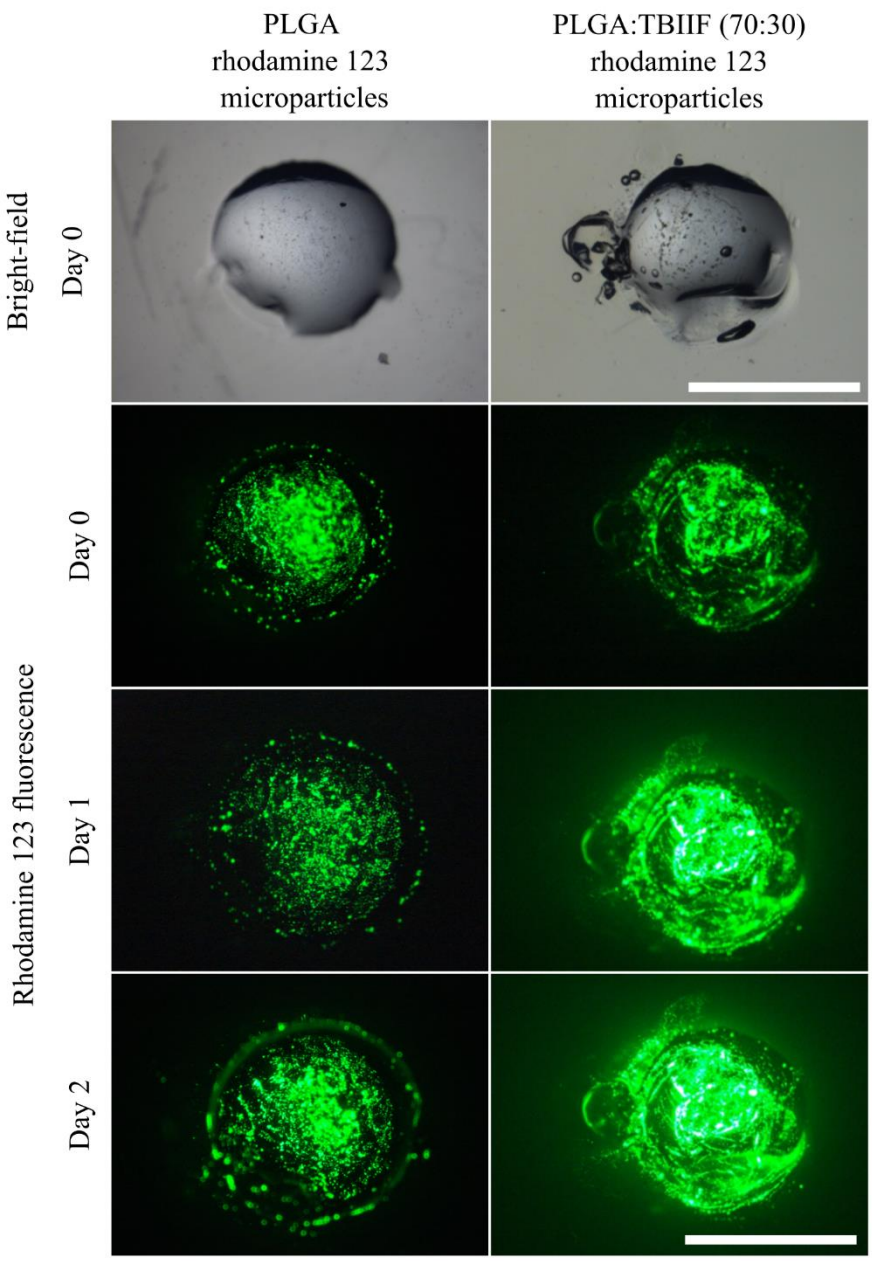

Figure 4.1 Mass release of rhodamine 123 from PLGA microparticle suspension into agarose hydrogel

The release of rhodamine 123 from PLGA and PLGA:TBIIF (70:30) fabricated microparticles in a suspension localised in bored-out holes in agarose hydrogel (1.4% w/v). A disc of agarose hydrogel was formed and 2mm holes were created as a source chamber for containing the suspension of microparticle. Daily fluorescence micrographs were taken using the Nikon dissection microscope to visualise release of rhodamine 123 into the surrounding hydrogel. The scale bars represent 2 mm.

Figure 4.1 shows the bright-field micrographs of the two bored-out holes from the agarose disks with barely visible microparticle suspensions filling the voids. The fluorescence images show the rhodamine 123 signal over the following 2 days. Even with fluorescent imaging, the diffuse rhodamine 123 signal can be seen around the original bore site by day 1 when compared with day 0 of the TBIIF-containing microparticles. All imaging was completed with the same acquisition settings for each sample at the same focal plane, however, the day 1 and 2 signals for the TBIIF microparticles seems over-exposed. This was most likely due to the expectedly elevated mobilisation of free rhodamine123 in this sample, allowing a greater fluorescence signal to be observed at that focal plane. Regardless of this, two clear observations can be made: a greater amount of rhodamine 123 has been released from the microparticles containing TBIIF, and that the mobile rhodamine 123 is able to diffuse into the surrounding hydrogel.

This pilot experiment supports the idea that the planned delivery of fluorescent molecules can be visualised using conventional fluorescence microscopy. However, for the proof of principle HOTs experiments a much lower signal was expected to be present due to the small number of microparticles being used. For this reason, more advanced microscopy may be required for the adequate visualisation of a delivered signal. Confocal microscopy lends itself to such analysis because of its ability to remove out-of-focus signal and image discreet optical sections in thick samples such as the hydrogels being used [192]. The thick hydrogel samples represent an especial issue for the conventional wide-field optical microscopy used in Figure 4.1, because as the sample increases in thickness, fine detail is more difficult to resolve due to the abundance of out-of-focus light in the planes above and below the focal plane.

4.4.2 Patterning rhodamine 123 microparticles in agarose

Following on from the visualisation of bulk rhodamine 123 fluorescence signals shown in Figure 4.1, microparticle pattern was fabricated using the HOTs and stabilised it using ULGT agarose as described in Section 3.3.9. For this test, no cells were incorporated into the pattern to reduce any possible auto-fluorescence in the samples. Figure 4.2 shows the formation of a PLGA:TBIIF (70:30) rhodamine-123-loaded microparticle pattern and the subsequent agarose-stabilised pattern. This figure further demonstrates one's ability to distinguish between the differently sized microparticles within each batch, and in this case a complex pattern has been formed with four 10 µm and eight 5 µm microparticles.

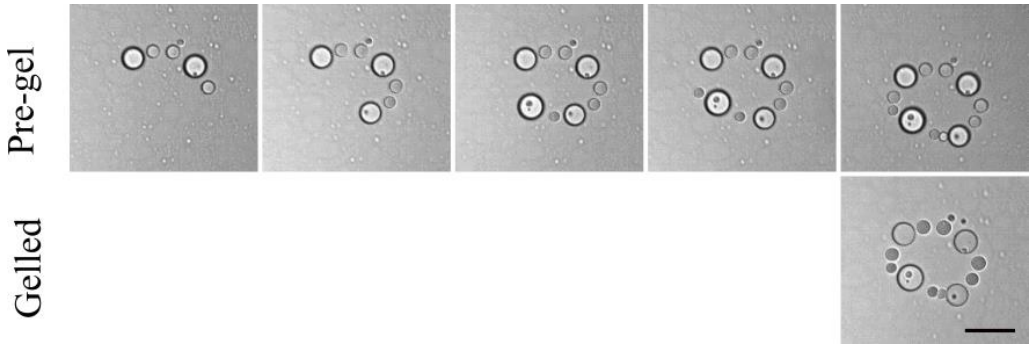

Figure 4.2 Patterning PLGA microparticles in agarose hydrogel

The figure shows the development of a microparticle pattern in the pre-gel 1.4% ULGT agarose at 37ºC with the HOTs patterning platform, and the subsequent thermally sensitive gelation and stabilisation of the pattern. Gelation was accomplished in 5 minutes with a temperature of 23ºC and the optical traps could be removed from the microparticles. The scale bar represents 20 µm.

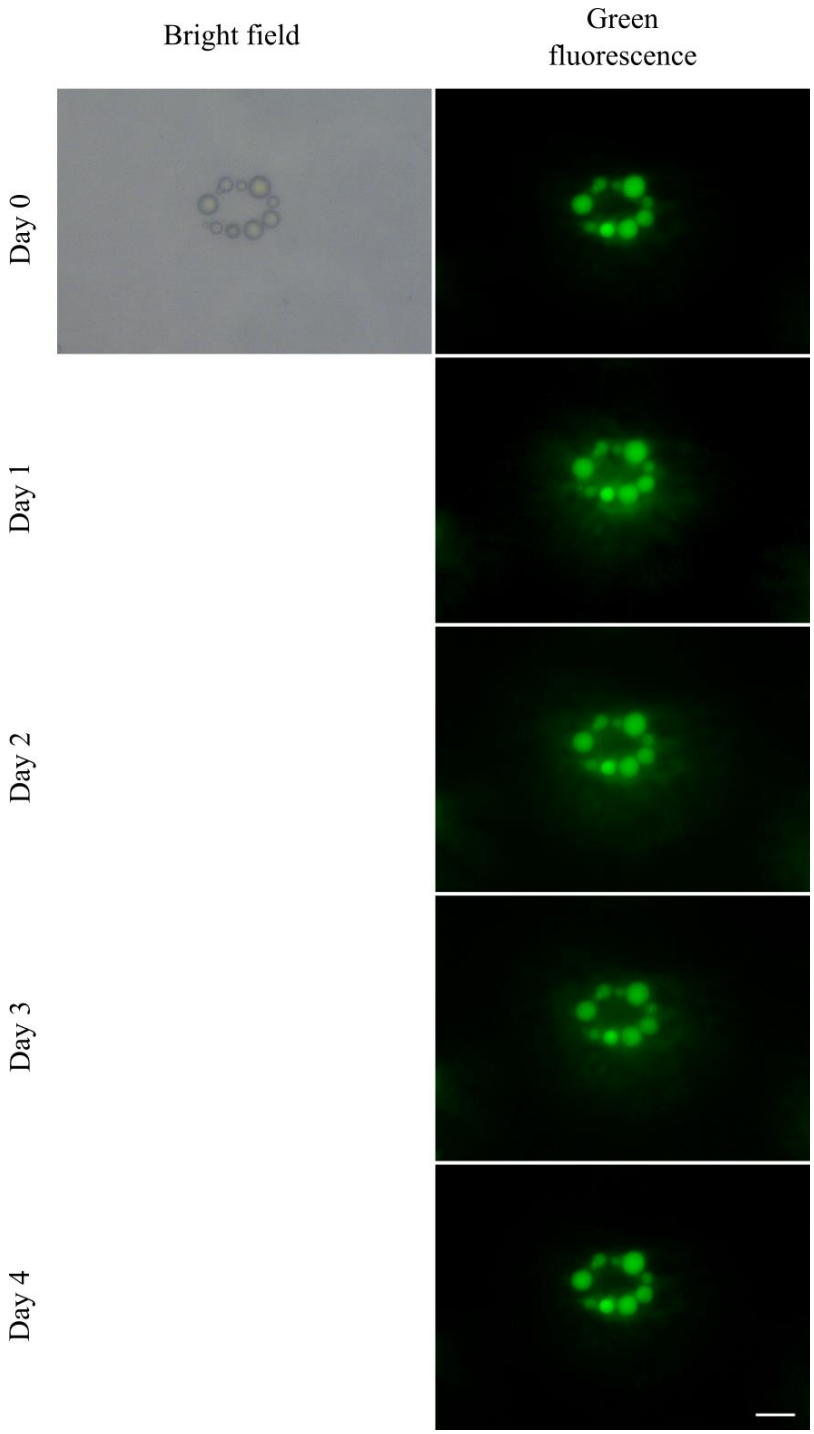

Figure 4.3 Observing rhodamine 123 release from a microparticle pattern

Figure 4.3 shows a ring of nine PLGA:TBIIF (70:30) rhodamine-containing microparticles fabricated using the HOTs and stabilised in 1.0% ULGT agarose hydrogel. Fluorescence micrographs are shown for the following four days of assessment to visualise the rhodamine 123 within the microparticles and surrounding the pattern during release. The Scale bar represents 20µm.

By day 1, a weak but clearly discernible fluorescence signal is observable outside of the ring and filling the inside. This surrounding halo of fluorescence signal is retained until day 4 where it is reduced significantly. This observation coincides with the initial burst phase release of the microparticles, as shown in Figure 3.6. The lag phase of release observed with these microparticles (Figure 3.6) starts at around day 3 where release rate is greatly reduced after the initial burst release. This reduction of release rate could explain why the fluorescence becomes less visible at day 4. Mobile rhodamine 123 that has been released will be drawn into the surrounding agarose until an eventual equalisation of the concentration throughout the entire hydrogel. Therefore, the elevated and visible signal observed on days 1-3 could be reliant on a high release rate that is constantly replacing the mobile fraction of previously released rhodamine 123.

This observation is reinforced by the literature data for rhodamine 123 mobility [193,194], where the diffusion coefficient is $2.8 \times 10^{-10} m^2 s^{-1}$ in water [195]. The loss of a rhodamine signal after 3 days does not necessarily mean that there is not enough being released, it could be that it is just suboptimal for visualisation. The high mobility of this small molecule is not representative of larger growth factor proteins, but it does show that there is a rapid delivery of encapsulated molecules to the surrounding area of the release point. However, it is not sufficient as an adequate proof of principle for delivery of molecules to cells, as the molecule is not retained by cells like growth factors and signalling molecules that will bind to recognition sites on the cell-surface to elicit signal transduction.

4.4.3 Delivery of molecules to cells

One of the issues with the observation of rhodamine 123 release is the fact that it is intrinsically fluorescent and so there is a strong signal present in the microparticles that makes weaker surrounding signals harder to visualise. A better method of showing delivery from microparticles to cells would be the use of a fluorescent cellular reporter that is activated in the presence of a delivered signal. This is, however, rather complex and is potentially fraught with obstacles to be surmounted, delaying the development of the HOTs and not necessarily required for future biological investigations. A simpler option that achieves a similar outcome is the use of acetoxymethyl viability dyes such as calcein AM. The acetoxymethyl derivative of fluorescent calcein can be transported through the cellular membrane into live cells. The acetoxymethyl group occludes the chelating site on calcein so that it cannot bind Ca^{2+}, Mg^{2+}, or other ions which induce its fluorescence emission. Calceins chelating ability and resulting fluorescence explain its historical use as a fluorescent Ca^{2+}-indicator [196]. Calcein AM's main application is now for labelling live cells [197], it is able to enter the cell due to the acetoxymethyl ester conferring a neutral charge on the molecule. Once inside a living cell and in the presence of esterase activity, the acetoxymethyl group is cleaved to reveal the chelator region, thus permitting fluorescence emission after excitation at 495 nm.

4.4.4 Fabrication of calcein green AM microparticles

Calcein green AM was seen as an ideal candidate for encapsulation and use as a proof of concept for delivery from release sources and uptake by cells. As with the rhodamine 123 dyes, calcein green AM was loaded with HSA at a loading of 0.1% (w/w) into PLGA:TBIIF (70:30) polymer solution. The desirable release kinetics demonstrated in Figure 3.6 should be also seen with calcein green AM due to the similar molecular weight and molecular properties, however, subtle chemical differences could lead to vastly different kinetics so it would have to fully characterised.

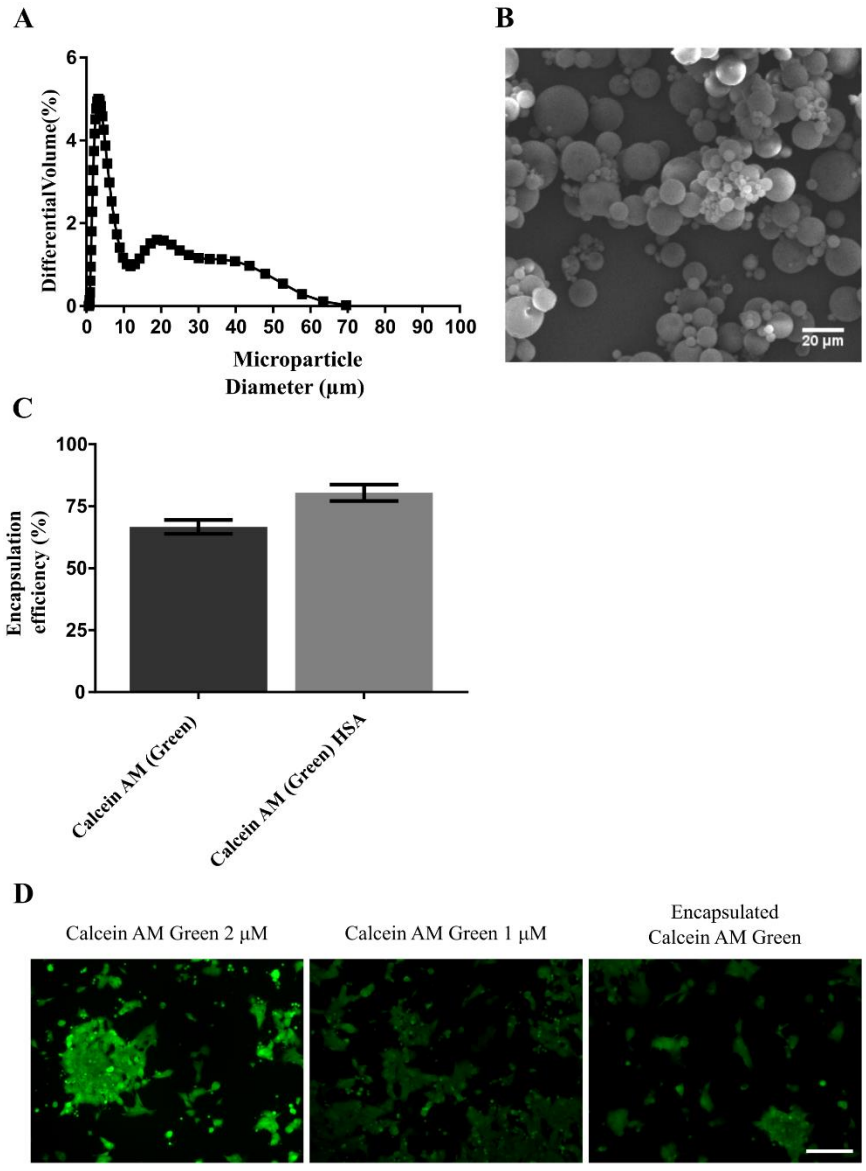

Figure 4.4 Characterisation of calcein green AM laden microparticles

A. Microparticle size distribution by differential volume. B. SEM micrograph of the microparticles allowing for analysis of their morphology. C. Average estimated encapsulation efficiency of calcein green AM and HSA into this batch of microparticles. D. Representative fluorescence micrograph of each condition for the post-encapsulation bioactivity assessment, whereby, mES cells were incubated with different calcein AM solutions. From left to right, fresh "Calcein AM Green 2 µM", fresh "Calcein AM Green 1 µM" and the calcein AM solution extracted from a suspension of calcein AM containing microparticles, estimated by microparticle mass and estimated encapsulation efficiency, to yield 2 µM Calcein "Encapsulated Calcein AM Green". The scale bar represents 50 µm.

The calcein-AM-encapsulated microparticles were prepared as described in Section 4.3.2, and were fully characterised in Figure 4.4. Their expected 5 µm diameter was measured, as previously described, using dynamic light scattering. SEM imaging was once again employed to assess microparticle morphology; the microparticles were non-porous and were prone to aggregating with one another as observed previously with PLGA:TBIIF (70:30) blends.

To assess the encapsulation efficiency of calcein AM, the microparticles were digested as described in Section 2.9.4 and the supernatants were analysed using a NanoDrop spectrophotometer (Section 4.3.3). The NanoDrop was required due to the absorbance peak for calcein green AM was in the UV spectrum (384nm); the plates used in the Tecan plate reader would create false positive absorbance as the polystyrene well-plates also absorbed short wavelength light. Using the NanoDrop, standard curves were prepared and the concentration of calcein green AM could be accurately measured alongside the HSA concentration (Section 2.9.5). Figure 4.4 C shows the encapsulation efficiency of calcein green AM is fairly high at 66.1 ± 1.3%, whereas the HSA encapsulation is 80.1 ± 1.4%. The discrepancy in encapsulation efficiency between the two molecules could have been due to the preferential adsorption of negatively charged HSA on the surface of the microparticle as well as being encapsulated.

An important consideration when encapsulating a bioactive molecule like calcein green AM is that its functionality cannot be assessed by simply recording its presence by absorbance. Damaged and non-functional molecules could still yield absorbance but not be able to function as intended. During the encapsulation there are various conditions that can be particularly damaging to molecules, and particularly proteins, including the shear forces of

homogenisation and the exposure to solvents [198]. Therefore, the functionality of the encapsulated molecule or protein should be tested prior to use. To assess the activity of calcein AM, working concentration (2 µM) and half working concentration of calcein green AM was added to mES (CGR8) cells as described in Section 4.3.4. Fluorescence micrographs of the cells showed a strong fluorescence signal for the 2 µM concentration and a weaker response with the 1 µM concentration (Figure 4.4 D). An appropriate mass of calcein-AM-encapsulated microparticles (based on loading) were digested to yield a 2 µM solution of post-encapsulated calcein green AM as described in Section 4.3.4. This solution was also added to a monolayer of mES cells and imaged in the same way as with the known concentrations of calcein AM. The post-encapsulated calcein green AM stained cells and yielded a fluorescence signal that was less than the 2 µM-treated cells but slightly more intense than the 1 µM-treated cells. We did not expect a full response as seen in the 2 µM sample, as the encapsulation efficiency was 66.1 ± 1.3% (Figure 4.4 C). The fact that the signal was greater than the 1 µM sample led us to believe that minimal damage was occurring to the calcein green AM due to the encapsulation process. This assay was only a qualitative assessment, but it supported the case that there was a suitable proportion of active calcein green AM being encapsulated within the microparticles.

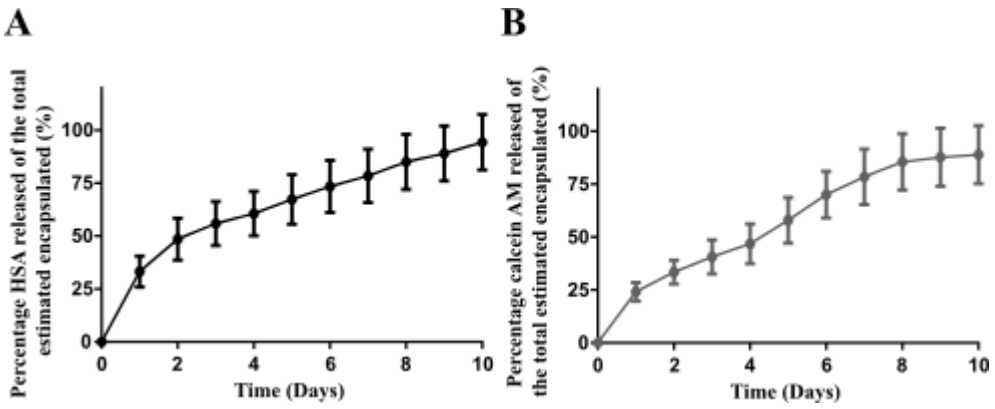

Figure 4.5 Calcein-AM-loaded microparticle *in vitro* release study

A. Release kinetics of HSA from calcein-AM-loaded microparticles assessed by BCA assay. B. Calcein green AM release from the same batch of microparticles. Calcein green AM concentration was analysed by NanoDrop spectrophotometry from the daily supernatants. The release studies for both HSA were analysed simultaneously from the same release study completed over 10 days. The error bars represent the cumulative standard error of the mean for triplicate.

Release studies were completed for the calcein-AM-encapsulated microparticles, and as before both HSA and calcein green AM concentration was assessed from the daily supernatants of the *in vitro* release study. Figure 4.5 shows a plot for both HSA (Figure 4.5 A) and calcein green AM (Figure 4.5 B) describing the released percentage mass of the total HSA estimated to be encapsulated. As expected, the release curve for calcein green AM is very similar to the release of rhodamine 123 (Figure 3.6) for the PLGA:TBIIF (70:30) microparticle batch. Interestingly, there is a significant burst release recorded for HSA which backs up the theory that the protein was preferentially adsorbing to the surface of the polymer microparticles as discussed earlier. The surface-located-HSA would be released rapidly over the first 24 hours contributing to the observed ~35% burst release (Figure 4.5 A).

4.4.5 Patterning calcein green AM microparticles in agarose

The microparticles were fabricated with the same formulation as those which tested suitable for optical trapping (Figure 3.3), and therefore it was assumed that this batch would trap just as well. Manipulation was possible and a mES cell ring structure was formed (Figure 4.6), once the cell ring had been formed, calcein-AM-loaded microparticles were added to its centre. The cell and microparticle structure was then positionally stabilised with ULGT agarose as previously described. The micropattern-containing hydrogel could then be incubated and cultured to assess for fluorescent calcein signal indicating a successful release of calcein green AM from the microparticles and uptake by the surrounding cells.

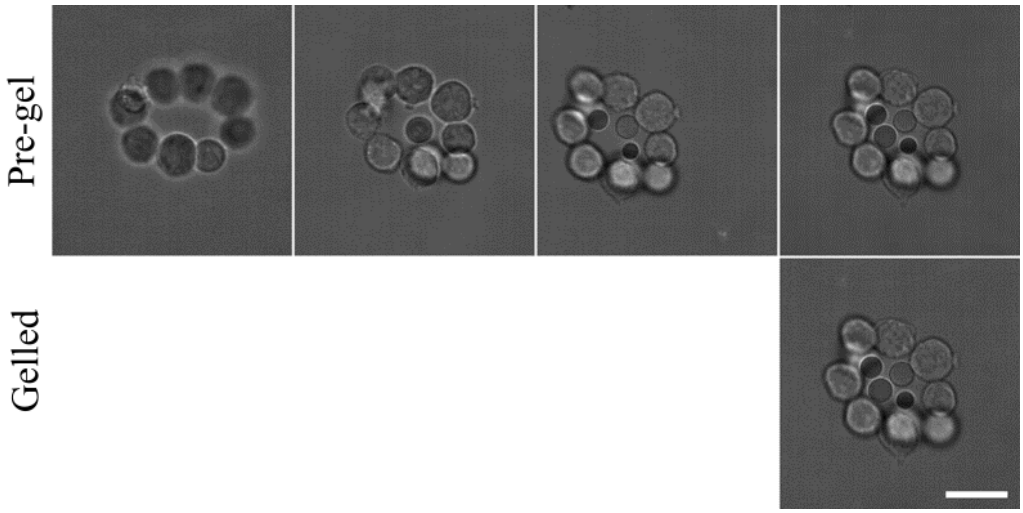

Figure 4.6 Patterning calcein-AM-laden microparticles with mES cells stabilised in agarose

The fabrication of a mES cell ring containing four calcein-AM-laden microparticles in liquid pre-gelled ULGT agarose (1.0%). Microparticles were sequentially positioned from the surrounding pre-gel solution into the centre of the mES cell ring. The patterns were then stabilised by gelling the agarose hydrogel through a temperature reduction to 23ºC, yielding a stabilised HOTs-fabricated pattern. The scale bar represents 20 µm.

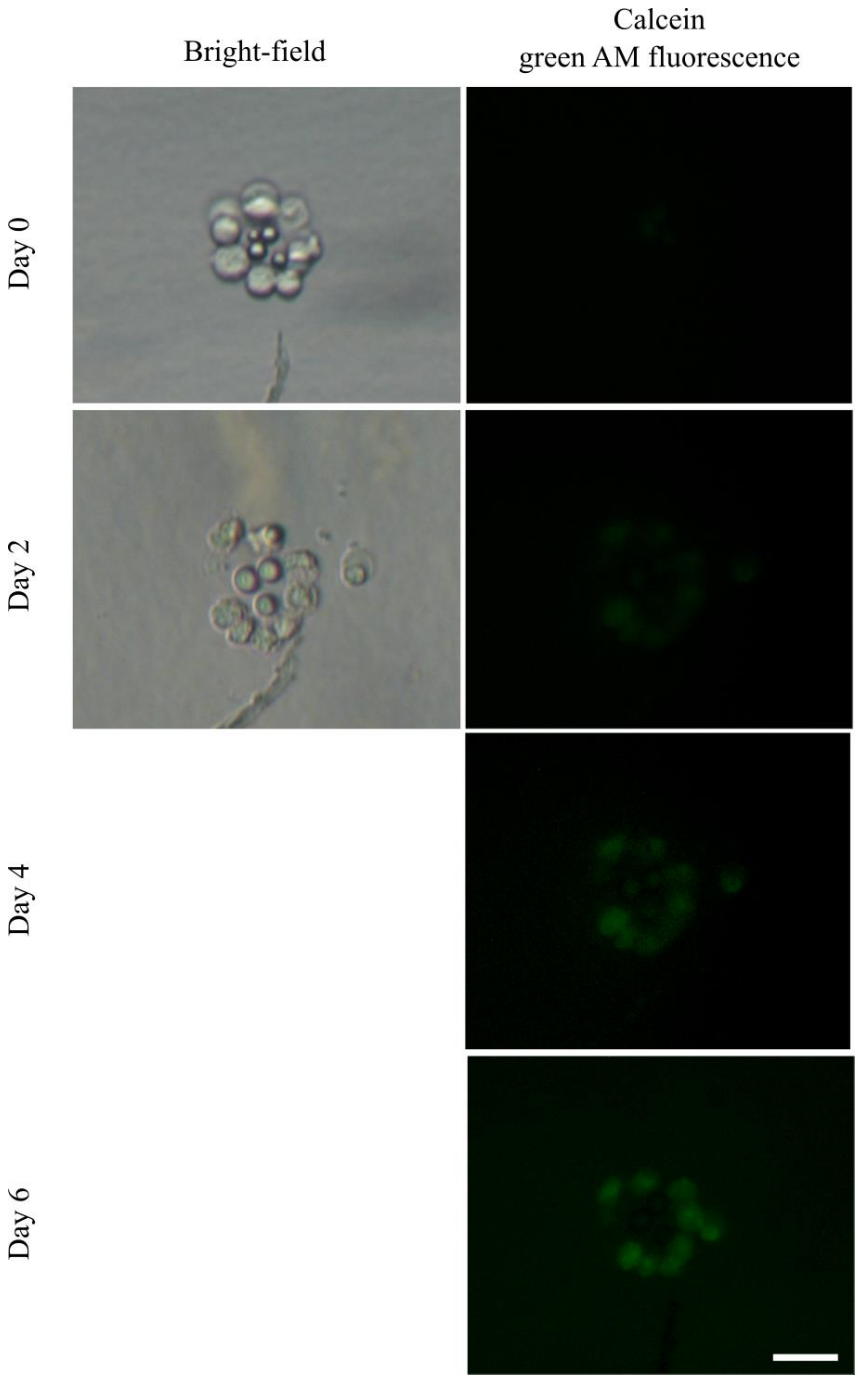

Figure 4.7 Calcein green AM delivery to a HOTs-patterned cell ring

The figure shows an agarose-hydrogel-stabilised microparticle pattern made up of four calcein-AM-laden microparticles positioned within an 8-cell mES ring and stabilised in agarose. The pattern formation of a similar cell-microparticle structure is shown in Figure 4.6. Fluorescence microscopy was used to visualise calcein fluorescence signal in the surrounding cells. The scale bar represents 20 µm.

Cell rings containing calcein green AM microparticles were fabricated as shown in Figure 4.6 and then cultured for 6 days. The patterns were imaged daily to observe the successful uptake of calcein green AM by the surrounding cells (Figure 4.7). By day 2 a very weak calcein signal can be seen in the surrounding cells when fluorescently excited at 495 nm. This signal increased slightly and reaches a maximal signal at day 6. This gradually increasing signal was not seen with the rhodamine 123 release (Figure 4.3) as there was nothing retaining the fluorophore, and so it dissipated into the surrounding hydrogel sink. With Calcein AM, cells are able to retain the esterase-modified calcein within their cell membrane, and hence the signal increases. The signal was expected to be observed by day 1 according to the rapid burst release kinetics of this batch of microparticles (Figure 4.5), however there was no signal over the background (data not shown). This is most likely explained by the insufficient delivery of calcein green AM over the first 24 hours, as although the release rate is at its greatest, only a small mass of calcein green AM is present and for an adequate signal to propagate, at least 48 hours of release was required. 48 hours of release equates to 34% release of calcein green AM from the microparticle batch, and by day 6, 70% will have been released, thus explaining the increase in fluorescence signal.

The cell pattern in Figure 4.7 does not seem to be proliferating, something that would be expected over the 6-day culture period. The use of calcein green AM as a reporter for delivery from the microparticles also assesses the cells' metabolic state. The fact that a fluorescence signal is formed indicates that the cells are alive (with esterase activity) [199], however they are not dividing. Something in the HOTs patterning process was detrimental to cell proliferation,

and more investigation was required to explain it. Regardless of the detriment to cellular proliferation, the use of calcein AM was a suitable proof of principle for showing that precisely patterned microparticles could be used to deliver molecular cargo to cells in a temporally-controlled manner.

In order to develop this proof of concept for the HOTs system being able to control the diffusible signalling of a cell microenvironment it was required that multiple signals be delivered. Commonly in cell and tissue development, multiple signals are required to ensure both specific and appropriate cell differentiation. In the case of the developing spinal cord, the specific order of the dorso-ventral axis is determined by the antagonistic activities of diffusible Shh and Wnt proteins [44]. In order to develop the HOTs into a valuable micropatterning tool, such dual soluble signalling models must be achievable.

4.4.6 Fabricating calcein blue AM microparticles

To demonstrate the ability of the HOTs to deliver multiple signals to a patterned cell organisation, the calcein green AM method was used once again. Calcein blue AM is a similar probe to that of the previously used green-emitting calcein AM, but its emission spectrum is in the blue wavelength region (450 nm) and it is excited at 360 nm. The delivery of two differently coloured probes was deemed suitable as a proof of concept for multiple signal delivery, and so calcein blue AM microparticles were fabricated. Due to the mechanism of calcein AM, blue or green, the microparticles containing each probe will be indistinguishable with the acetoxymethyl group intact. Therefore, to be able to distinguish between the two batches of microparticle when patterning on the HOTs, the calcein-blue-AM-laden microparticles were formulated in such a way that they would be

larger than the calcein-green-AM-laden microparticles. By altering the polymer:DCM ratio as previously described (Table 3.1), differently sized microparticles can be fabricated. The optical trapping study discussed in Chapter 3 (Figure 3.3) offered a suitably sized microparticle formulation that could be easily manipulated. PLGA:TBIIF (70:30) was dissolved in DCM to yield a 15% polymer solution known to produce 10-20 µm sized microparticles when used with the aforementioned emulsion-based preparation of microparticles (Section 2.9.1). Calcein blue AM microparticles were fabricated at a loading of 0.1% (w/w) according to this method and were fully characterised (Figure 4.8).

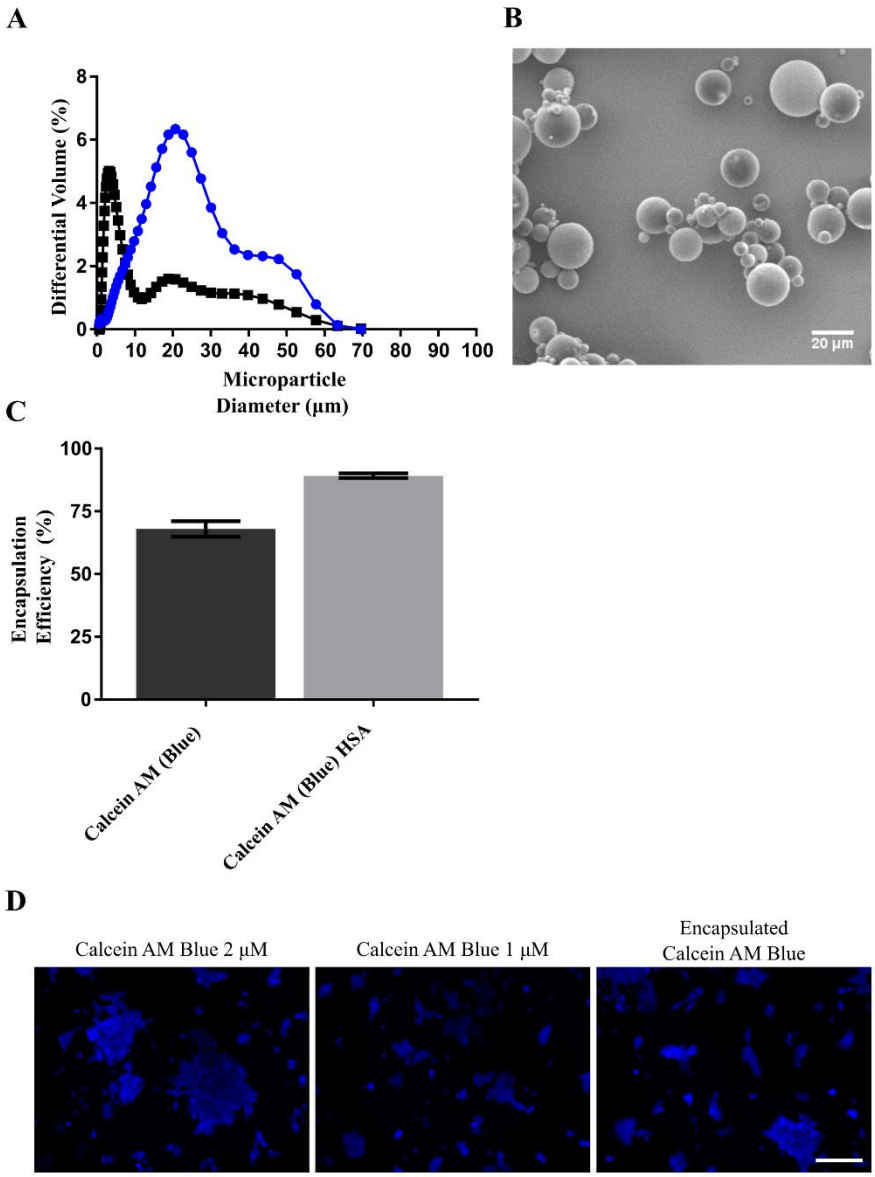

Figure 4.8 Characterisation of calcein blue AM microparticles

A. Microparticle size distribution by differential volume, comparing the sizing for calcein AM Green microparticles (Black) to Calcein AM Blue microparticles (Blue). B. SEM micrograph of the microparticles allowing for analysis of their morphology. C. Average estimated encapsulation efficiency of calcein blue AM and HSA into this batch of microparticles. D. Representative image of each condition for the post-encapsulation bioactivity assessment. From left to right, fresh "Calcein AM Green 2 µM", fresh "Calcein AM Green 1 µM" and the calcein AM solution extracted from a suspension of calcein AM containing microparticles, estimated by microparticle mass and estimated encapsulation efficiency, to yield 2 µM Calcein "Encapsulated Calcein AM Green". The scale bar represents 50 µm.

Figure 4.8 A shows the sizing of the microparticle batches obtained for the calcein-blue-AM-laden microparticles as compared to the standard calcein-green-AM microparticles. This new batch was shown to be larger than the calcein green AM batch and would be easily distinguishable on the HOTs system during patterning. SEM imaging (Figure 4.8 B) shows the microparticle morphology to be non-porous and with high polydispersity in terms of sizing. The encapsulation efficiency of calcein blue AM was high at 71.5 ± 0.74%, and similarly to the calcein green AM microparticle analysis (Figure 4.4 C), there was an elevated encapsulation of HSA over calcein blue AM. The important assessment of the functionality of bioactive molecules after encapsulation, as previously discussed, was repeated with the calcein-blue-AM-laden microparticles. The post-encapsulation bioactivity of calcein blue AM is shown in Figure 4.8 C; the 2 µM calcein blue AM gives a strong fluorescence signal in mES cells. A similarly strong response is also observed in the post-encapsulation and 1 µm sample wells. It may be the case that the calcein blue AM requires less calcein to yield a suitable fluorescence signal, and with this in mind we can deduce that the encapsulation process is not particularly affecting calcein blue AM function.

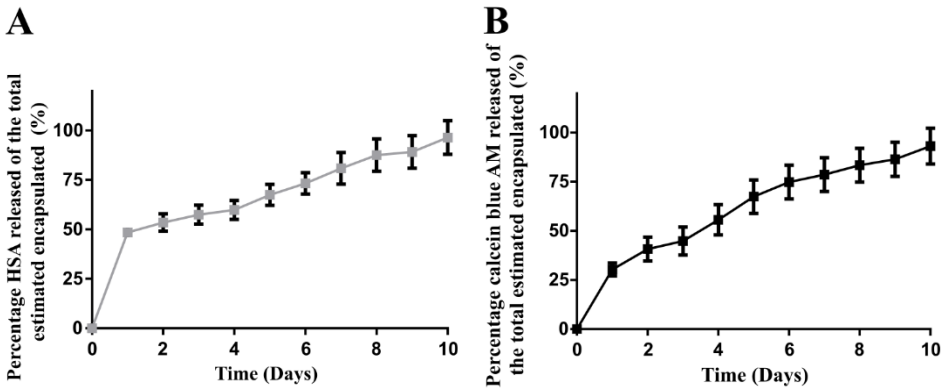

Figure 4.9 Calcein-blue-AM-loaded microparticles *in vitro* release study

A. Release kinetics of HSA from calcein-blue-AM-loaded microparticles assessed by BCA assay. B. Calcein blue AM release from the same batch of microparticles. Calcein blue AM concentration was analysed by NanoDrop spectrophotometry from the daily supernatants. The release studies for HSA were simultaneously assessed from the same release study completed over 10 days. The error bars represent the cumulative standard error of the mean for triplicate batches of each microparticle formulation.

Release studies were completed for the calcein blue AM microparticle batch as described previously (Section 2.9.6). As before, the calcein green AM molecule was loaded with HSA as a carrier protein, and the release of HSA was also assessed. Figure 4.9 shows the plots for HSA (Figure 4.9 A) and calcein blue AM (Figure 4.9 B) release over 10 days. The HSA shows a similar release curve to that of calcein green AM release, however there is an elevated burst release over the first 24 hours up to almost 50%. This could be explained by the increased internal porosity of larger polymer microparticles during drug release [200,201], leading to elevated hydration of the microparticle, and hence the higher burst release. However, it was initially thought that the smaller microparticles (calcein-green-AM-laden) would have a faster release rate due to their increased surface area to mass ratio. From these two conflicting theories it was hypothesised that the size difference was less of a factor with respect to the, expected to be greater, internal porosity of the larger microparticles. Future development of the microparticles would be required for tailoring their release kinetics to fit desirable delivery profiles, however these would need to be specific to the molecular cargo being delivered.

The calcein blue AM release follows a similar trend to that of the calcein green AM, with a burst release of 30.2 ± 3.4% followed by a sustained release over the following 9 days. The sustained release was shown to be important in the formation of a visible fluorescence signal in Figure 4.7, and it was necessary that this batch also presented with such release kinetics.

4.4.7 Multiple signal patterning

As previously discussed, two differently labelled (green and blue emission spectra) calcein green AM dyes were loaded into separate microparticle formulations. Calcein-green-AM-laden microparticles that were ~5 μm in diameter (Figure 4.4) and a larger sized batch laden with calcein blue AM (Figure 4.8) sized ~20 μm in diameter. These particles were patterned around the standard eight mES cell ring with four of each microparticle batch. The differently loaded microparticles were differentiated from one another by size.

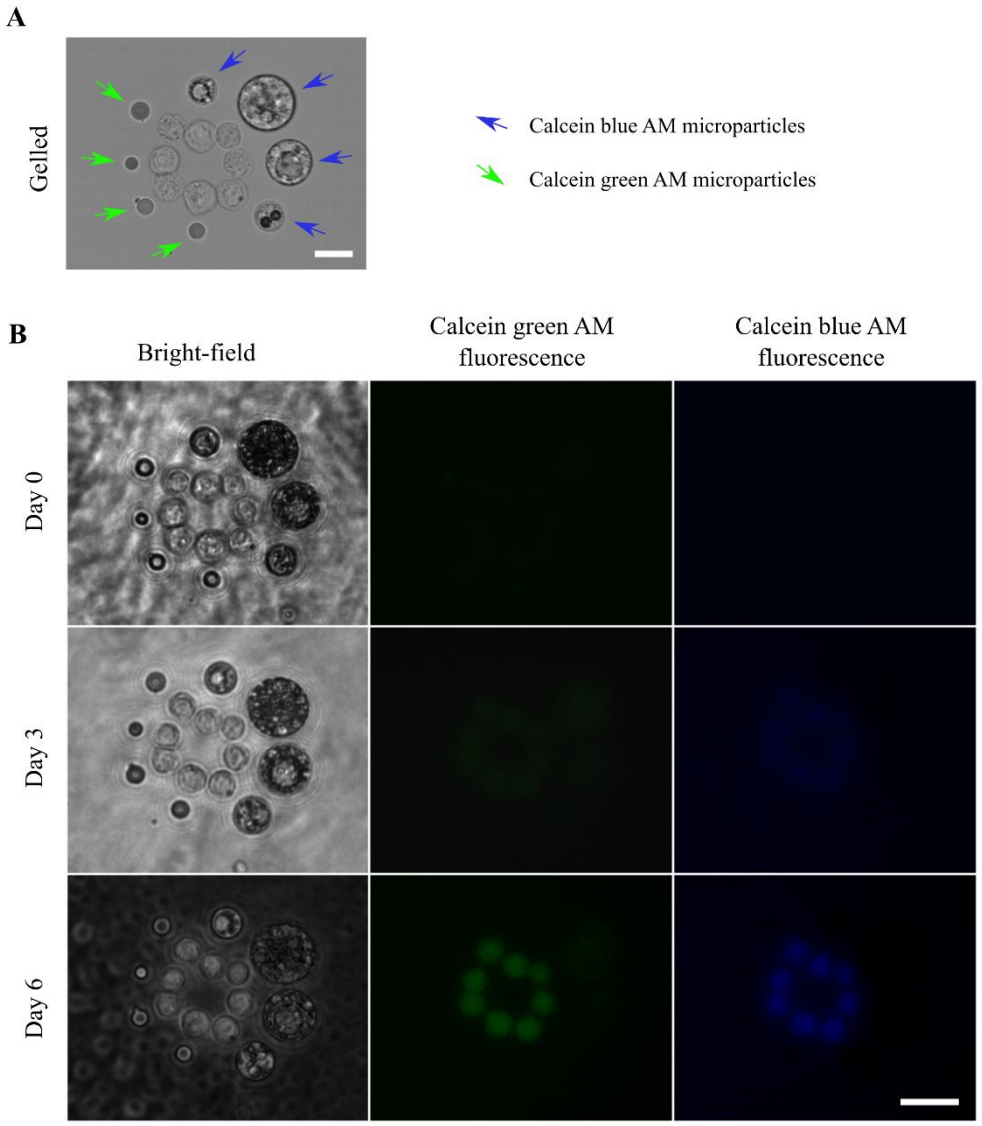

Figure 4.10 Dual signal HOTs patterning

A. ULGT agarose hydrogel gelled pattern of eight mES cells surrounded by four calcein-green-AM- and four calcein-blue-AM-laden microparticles positioned using the HOTs patterning platform. B. Fluorescence micrographs showing calcein fluorescent signals from the mES cell ring, thus indicating successful delivery of the dual calcein AM signals from the microparticles to the cells where the acetomethoxy group of calcein AM is cleaved, yielding fluorescent calcein. The scale bar represents 20 µm.

Figure 4.10 A shows the cell and microparticle structure as stabilised in ULGT agarose with the differently loaded microparticles labelled by coloured arrows. The gelled structure was moved to an incubator and cultured for 6 days, and during this culture period the pattern was imaged every 48 hours. Figure 4.10 B shows the development of both green and blue fluorescence signal after 3 days and the stronger signals on day 6. As previously observed, the development of a visible signal takes longer than the *in vitro* release study would indicate; a fluorescence signal is first seen at 48 hours after a significant burst release in the first 24 hours, and then the signal intensifies gradually as the microparticles break down further.

Cell proliferation is once again not occurring, but by virtue of calcein AM conversion it was possible to conclude that the cells were alive (possessed of esterase activity and retaining cell membrane integrity). If the cells were dead at day 0, there would be no fluorescent calcein signal due to a lack of esterase activity needed to facilitate hydrolysis of the acetoxymethyl group. If the cells were initially alive and able to convert the calcein AM to fluorescent calcein, and then died, the calcein would have been free to leak out of the cell as the cell membrane broke down. Neither of these possibilities seemed likely, given the strong fluorescence signal, but it was prudent to check the cell viability with another method to reduce the likelihood of false positives. Figure 4.11 shows two cell patterns formed in the same way, the experimental pattern is the same as in Figure 4.10 at day 6. The negative control pattern was irradiated after gelation, as described in Section 4.3.5, and then Live/Dead Cell Viability Assay probes were added.

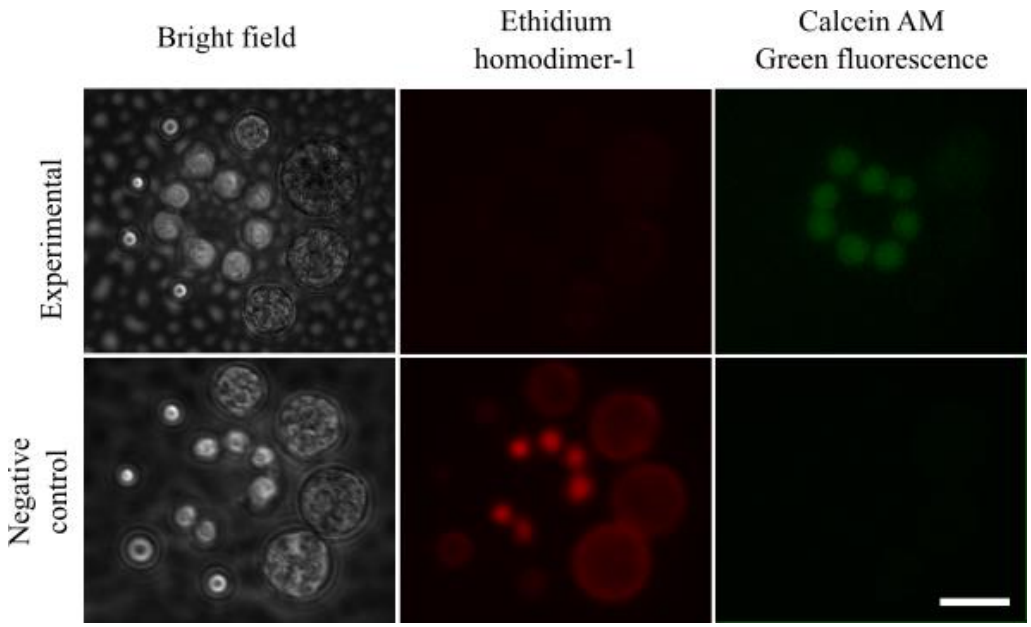

Figure 4.11 Post-culture HOTs-patterned cell viability assessment

Fluorescence micrographs of two HOTs-fabricated cell and microparticle patterns. The experimental pattern is from the previous figure (Figure 4.10), and the negative control was an irradiated (UV 30 minutes) cell pattern to confirm that the Live/Dead Cell Viability Assay was functional. The red cells are EthD-1-positive (dead), while the green cells are calcein-positive (alive). Scale bar represents 50 µm.

The experimental pattern only had the EthD-1 added, as the calcein AM had already been added (Figure 4.10) and no red fluorescence was observed, indicating membrane integrity. However, the negative control cells showed a strong EthD-1 fluorescence signal, indicating that the cell membranes had been disrupted. Damage to the cell membrane, one of the key indicators of cell death, permits the ingress of EthD-1 into the cell where it then binds to DNA, increasing in fluorescence intensity [202]. Further evidence to suggest that calcein staining is specific to living cells is shown by the lack of any fluorescence signal with the negative control cell pattern.

These data inspire confidence in the calcein AM delivery experiments, and suggest that the cells are not dying in the current HOTs procedure. However, they do not explain the lack of cellular proliferation previously shown in these agarose hydrogels (Figure 3.10).

4.4.8 Explaining the lack of cellular proliferation

Previous literature suggests that the capacity for cell proliferation can be reduced by cell stress; one of the mechanisms to combat various stressors is the adoption of a permanent cell-cycle arrest that is termed senescence [203]. The hallmarks of senescence include: permanent growth arrest [204], increase in cell size [205], expression of senescence-associated β-galactosidase [206], and the release of cytokines and growth factors [207]. In order to assess cellular senescence, the expression of β-galactosidase can be stained for [208]. Initially, the ULGT agarose's effect on cellular senescence was tested. Given the previous work showing that proliferation of mES cells in 1% ULGT agarose did occur, cellular senescence was not expected. Further to this, another hydrogel, GelMA was

tested following its reported successful use with cell culture systems [159]. Figure 4.12 shows three mES cell monolayers grown and then stabilised in either 10% GelMA or 1% ULGT agarose, and a negative control without hydrogel stabilisation.

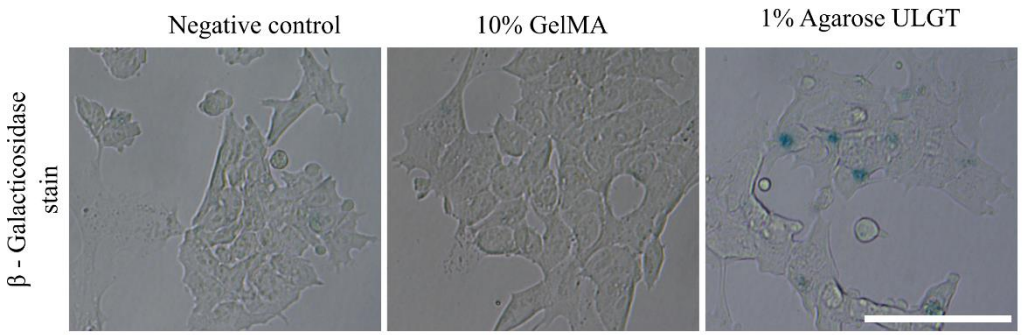

Figure 4.12 β-galactosidase assay for hydrogel-associated senescence

Representative bright-field micrographs of mES cell monolayers grown without hydrogel stabilisation (Negative control) with 10% GelMA and 1% ULGT agarose. The two hydrogels were gelled according to the methods previously outlined. The blue regions show the β-galactosidase, indicating cellular senescence, in the samples stabilised by agarose. The scale bar represents 20 μm.

The negative control (-ve) and GelMA-stabilised cell monolayers show no positive β-galactosidase staining, whereas those stabilised with ULGT agarose show significant blue staining. The ULGT-agarose-stabilised monolayer showed areas of β-galactosidase positive blue staining, whilst other more densely populated areas were unstained (data not shown). This result was seen in all the replicate wells (n=3) and led to the following hypothesis. Whilst the mES cells were able to proliferate when seeded at a suitably high cell density, as shown in Figure 3.10, when isolated, like when subjected to HOTs patterning or under the conditions of the ULGT-agarose-stabilised cells of Figure 4.12, cells do not proliferate and enter senescence.

Work completed by Dr Emily Britchford (Thesis (2015), University of Nottingham, UK) showed that HOTs-patterned mES cells could proliferate without ULGT agarose stabilisation. From these data and the agarose-linked induction of β-galactosidase (Figure 4.12), it was deduced that agarose was the cause of cellular proliferation's arrest among HOTs-patterned cells.

4.4.9 Cell patterning in GelMA

GelMA's reported use for 3D cell culture [160,209–211] and demonstrated ability to support even sparsely seeded cell growth (Figure 4.14) made it a strong and candidate for stabilising HOTs-patterned structures. The pre-gel solution of GelMA was tested for its suitability for the patterning and stabilisation of cell structures (Figure 4.14). GelMA is cross-linked by UV light, as described in Section 4.3.6, and as such cell viability assessment was required to show that this exposure to potentially damaging short wavelength light was not detrimental to cellular viability.

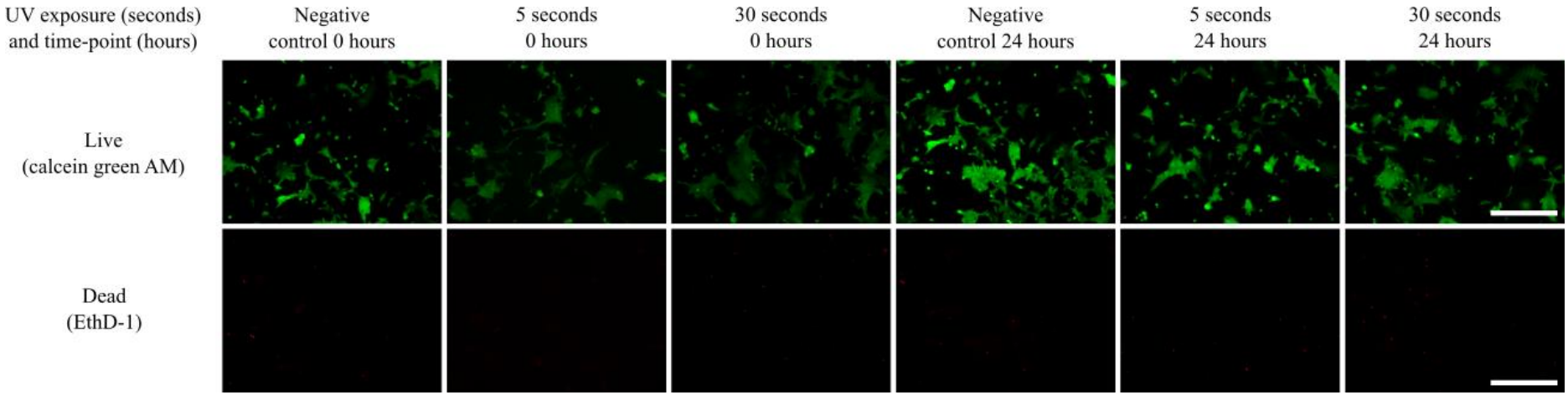

Figure 4.13 Live/dead assessment of mES cells grown with cross-linked GelMA (10%)

Live/dead assessment and fluorescence micrographs of the live (calcein-AM-positive) and dead (EthD-1-positive) mES cells after exposure to different doses of UV crosslinking (0, 5 and 30 seconds). Imaging was completed directly after exposure (0 hours) and after 24 hours. The scale bars represent 50 µm.

Figure 4.13 shows the results of a LIVE/DEAD© viability assessment that qualitatively shows the effect of UV exposure on mES cells in GelMA. Cells exposed for 5 seconds received the dose required for the complete cross-linking of a volume suitable for HOTs patterning. Cells exposed for 30 seconds received six-times the HOTs patterning dose, a dose far higher than they would receive for any future experimentation. Cells were analysed directly after exposure and after 24 hours to assess direct cell death and any delayed effects. Such delayed cell damage could be through the action of UV-induced mutagenesis leading to lethal mutations that might not be observed directly after UV exposure. For these proof of concept experiments, such potential mutations are not relevant, but they may detrimentally affect biological development, a consideration that is addressed at a later point in this thesis. In all of the samples, including the negative control, few dead cells were evident, as is typically the case. With the exposure to UV there was no significantly elevated rate of cell death observed, and it can be concluded that the minimal exposure to UV and cross-linking within GelMA was not causing the death of the mES cells.

As with the agarose hydrogel, it was important to show that cells can be manipulated within the GelMA pre-gel solution and that the resulting patterns can be stabilised for culture. Further to this, analysis of the patterned cells' proliferation was undertaken to show that GelMA could support HOTs-patterned cell growth.

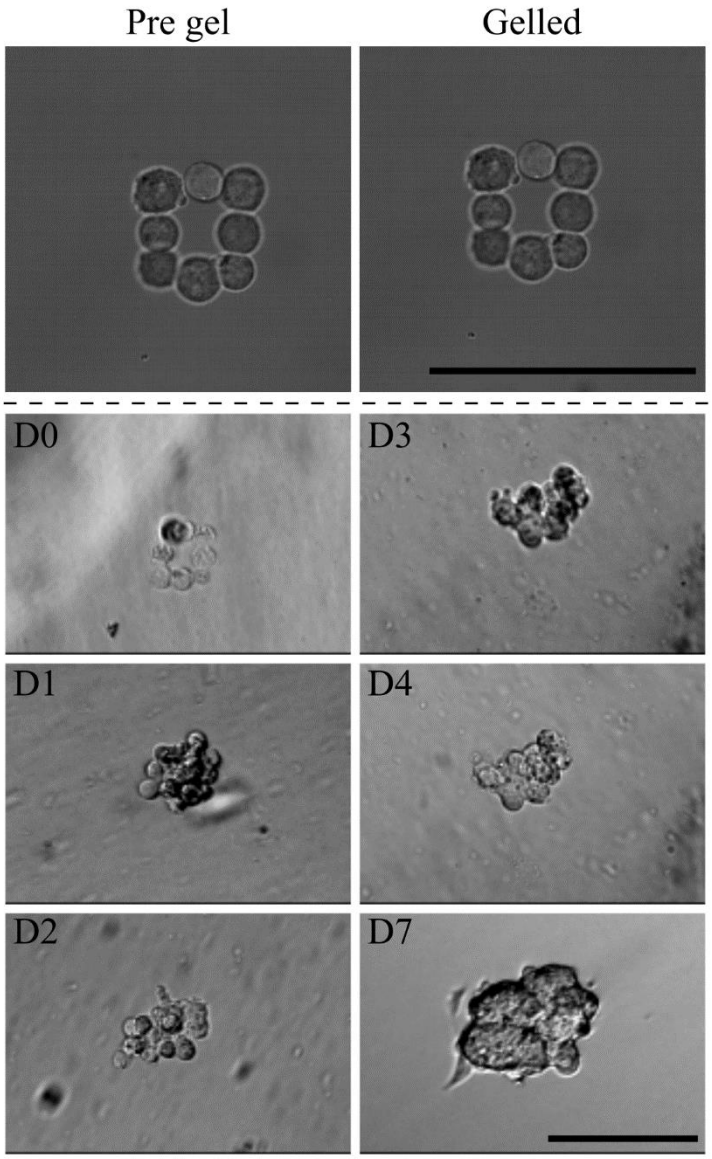

Figure 4.14 Proliferation of a mES cell ring stabilised by GelMA

Formation of a mES cell ring in pre-gel GelMA with the HOTs patterning platform, and subsequently gelled and stabilised via UV crosslinking. The stabilised cell structure was then cultured as usual and imaged to assess proliferation over a 7 day period of normal cell culture. The scale bars represent 50 µm.

Figure 4.14 shows that the pre-gel solution was suitable for the HOTs optical manipulation of cells into the ring pattern. This pattern could then be rapidly cross-linked, yielding a GelMA-stabilised cell ring. The cell ring was cultured for 7 days and its proliferation was imaged. The ring pattern was lost after 24 hours as the cells divided and reorganised themselves to form a small cell aggregate. This aggregate can be seen to grow for 7 days after pattern formation into a large rounded cell aggregate typical of 3D-cultured mES cells.

The GelMA offers binding motifs for the mES cells to recognise and supports their growth, whereas the bio-inert agarose does not. Whilst the agarose provides a blank canvas to create cell microenvironments, the GelMA permits cell growth. Through the demonstration of GelMA- and ULGT-agarose-patterning two systems for HOTs patterning have been detailed, each with different advantages and disadvantages. The bioactive nature of GelMA, arising from its derivation from collagen, means that RGD (L-arginine, glycine, and L-aspartic acid) bind sites [212] and MMP (matrix metalloproteinase)-sensitive degradation sites are retained [213]. These recognition sites support cell proliferation, as shown in Figure 4.14, but they could also influence cellular development detracting from the HOTs based signalling. The initial idea of the HOTs patterning platform was to develop a means to control every aspect of the patterned microenvironment. The use of GelMA prevents this and demonstrates the importance of being able to use bio-inert agarose as an alternative.

4.4.10 Development of the patterning gasket

Heretofore, HOTs patterning was done according to the methodology outlined in Section 2.8.1. This approach was suitable for achieving early proof of

principle experiments and founding the basis for delivering small molecules to HOTs-fabricated cell patterns. However, due to the mobility of these delivered molecules, even the low numbers of unpatterned release sources surrounding a cell pattern of interest become an issue. To accurately control the spatial characteristics of a diffusible molecular signal, we need to ensure that the patterned signal origin is the only source of release. To achieve this, the patterning gaskets were adapted from a simple cell culture dish, as detailed in Section 2.8.3, to a more complex multi-lobed gasket. Figure 4.15 explains the development and use of the multi-lobed gasket. It describes how experimental through-put can be increased whilst simultaneously providing a means to isolate cell patterns from unpatterned release sources.

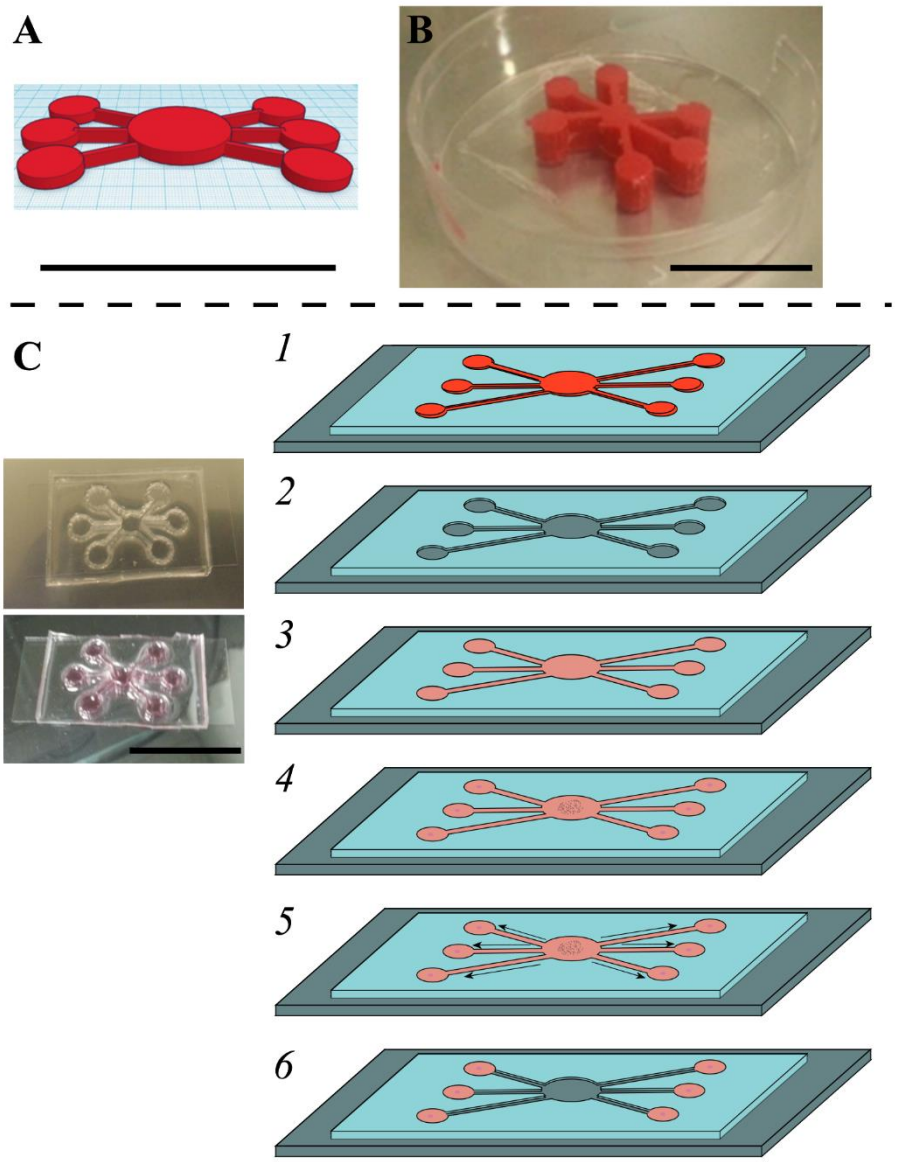

Figure 4.15 The design and approach for patterning with the lobed patterning gasket

How the lobed patterning gasket was designed (A), fabricated (B) and used (C). A. Internal mould design created with Tinkercad. B. 3D-printed PLA mould. C. Steps taken to use the lobed patterning gasket: 1) in a petri dish (see B), the PDMS gasket was formed around the internal mould; 2) the PDMS gasket was removed from the petri dish and glued to a glass coverslip; 3) the lobed patterning gasket was filled with pre-gelled hydrogel; 4) release sources were added to the central reservoir and cells to the outer lobes; 5) individual release sources were then translocated as required via optical manipulation to each cell-containing lobe and patterned; 6) the hydrogel was crosslinked and the central reservoir and channels excised. The scale bars represent 20 mm.

Figure 4.15 A shows the CAD-designed (Tinkercad) 3D model for the six-lobed patterning gasket mould. This design was printed as described in Section 4.3.7, using Makerbot's Replicator 2 3D printer. Figure 4.15 B shows the PLA mould mounted onto a petri dish and ready for the addition of silicone elastomer and formation of the six-lobed patterning gasket. Figure 4.15 C explains the steps taken when using the patterning gasket for HOTs patterning, and how release source patterning can be achieved so that experiments are isolated from the surrounding unpatterned release sources.

The development of this patterning gasket enabled the HOTs to manipulate objects, including microparticles, from a reservoir to an experimental area much like a microfluidics system. Once the required number of microparticles have been positioned in one of the six surrounding lobes, and the hydrogel medium is cross-linked, the reservoir containing unpatterned microparticles can be excised. This removal of unintended signalling means that spatio-temporal control over the signals being developed from patterned microparticle release sources can be achieved.

To demonstrate this spatio-temporal control, PLGA:TBIIF (70:30) rhodamine-123-loaded microparticles, characterised in Figure 3.4, were added to the reservoir, and individual microparticles were translocated to each of the four lobes of the four-lobed patterning gasket. The agarose hydrogel was cross-linked and the reservoir region excised, yielding an individually patterned release source in each of the surrounding lobes (Figure 4.16).

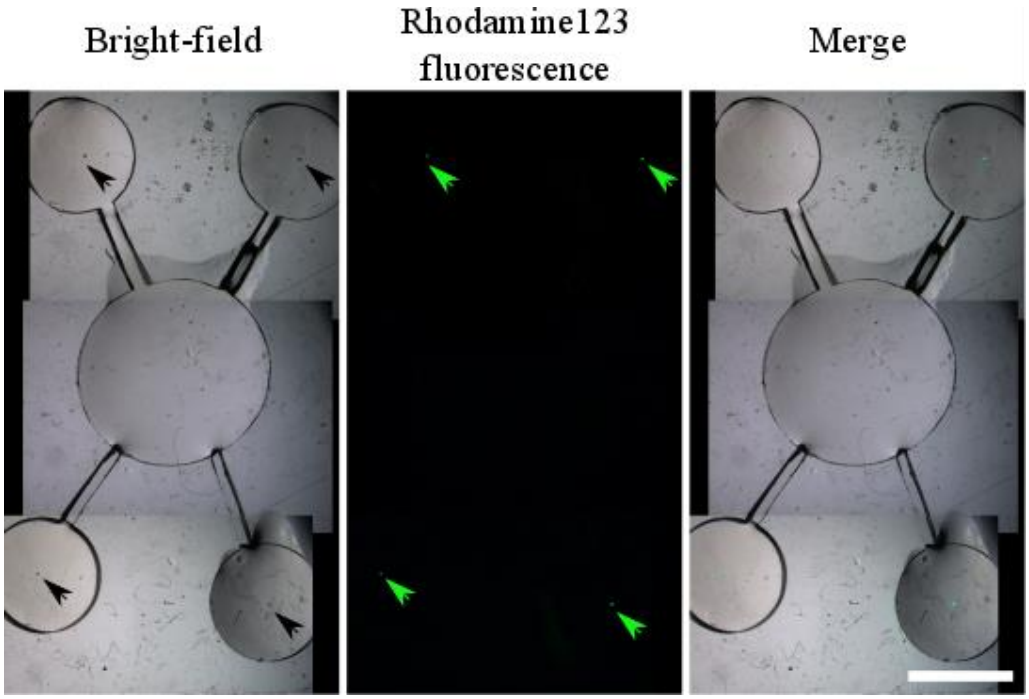

Figure 4.16 Demonstration of the four-lobed patterning gasket

A bright-field and fluorescence micrograph of the four-lobed gasket after individual rhodamine-123-laden microparticles (Indicated by arrows) were translocated from the central reservoir and isolated in the outer lobes of crosslinked GelMA using the HOTs patterning platform. The central reservoir was excised to separate it from the external lobes before any rhodamine-123 diffused out. The scale bar represents 5mm.

4.4.11 Spatio-temporal control of solute delivery

It was important to confirm the lobed patterning gasket's functionality with actual cell experiments, to demonstrate usability and to identify a spatially controlled response to a delivered molecule. It has previously described how signals delivered from controlled-release microparticles can be tailored to create different signalling characteristics. This aspect of the HOTs micropatterning platform is highly important to its unique selling point, precisely recreating the signalling conditions of cell niches. However, temporal control represents just one facet of the HOTs unique selling point. The ability to position release sources in specific configurations, offering spatial control over the signal, is also a defining feature of the HOTs platform. It was hoped that with the patterning gasket and the removal of any contaminating unpatterned release sources, spatio-temporally-controlled signalling could be attained.

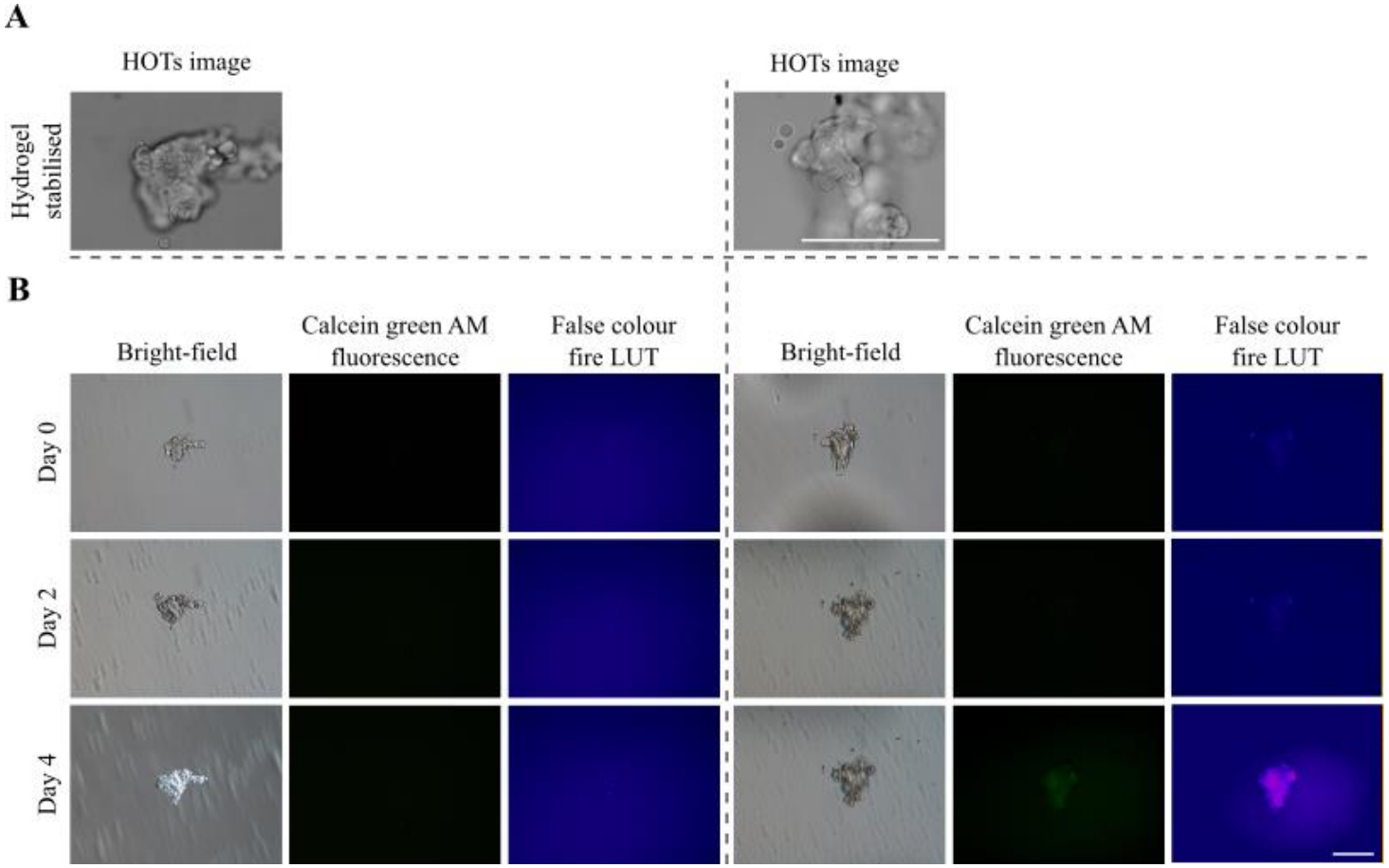

Figure 4.17 Calcein green AM delivery to mES cell aggregates using the lobed patterning gasket

A. GelMA-stabilised mES cell aggregates with one (Left) and two (Right) calcein-green-AM-laden microparticles optically positioned in close proximity to them using the HOTs patterning platform and the multi-lobed patterning gasket. B. Subsequent imaging of the cell aggregates, including fluorescence microscopy to analyse calcein fluorescence signals over 4 days. A false colour Lookup Table (LUT) has been applied to a 32-bit version of the fluorescence micrographs to emphasise the subtle calcein signal produced in the two microparticle sample. The scale bars represent 50 µm.

To best show the formation of a spatially controlled delivery, a larger cell structure was used. Due to the basic nature of these proof-of-principle experiments, it was deemed unnecessary to pattern this cell structure, and so small mES cell aggregates were formed as described in Section 2.5.2. These small cell aggregates could be injected into the surrounding lobes of a patterning gasket individually, and then the required microparticles could be brought to them as described in Figure 4.15.

Figure 4.17 A shows two small cell aggregates with one and two calcein-green-AM-containing microparticles positioned around them. Figure 4.17 B shows the subsequent imaging of these two aggregates, the cell aggregate (Left) with one microparticle shows no green fluorescence signal after 4 days. However, the two-microparticle cell structure yields a low but discernible calcein signal at day 4 across the whole structure. False colour Fire LUTs were used to help identify the signal over the background.

The halo of low level fluorescence surrounding the day 4, two-microparticle structure was most likely an artefact from the fluorescing cell structure. This was observed previously when using longer exposure times, and was thought to be due to reflected light from the calcein-containing cell structure.

This work showed that the patterning gasket could be used to fabricate isolated release experiments, however it did not show that control over spatial characteristics of the delivery was possible. The signal at day 4 must have been developing over the first few days before reaching an adequate level for observation at the set acquisition settings. From this work, it was deduced that a greater signal would be required in order to observe a spatial response across a

cell aggregate. With the small mass of calcein green AM delivered in Figure 4.17, the released solutes would diffuse all around the aggregate well before the signal was visible and, as such, no zonal response could be visualised. In an attempt to identify such a zone of delivery, slightly larger cell aggregates were grown and a greater number of release sources were used.

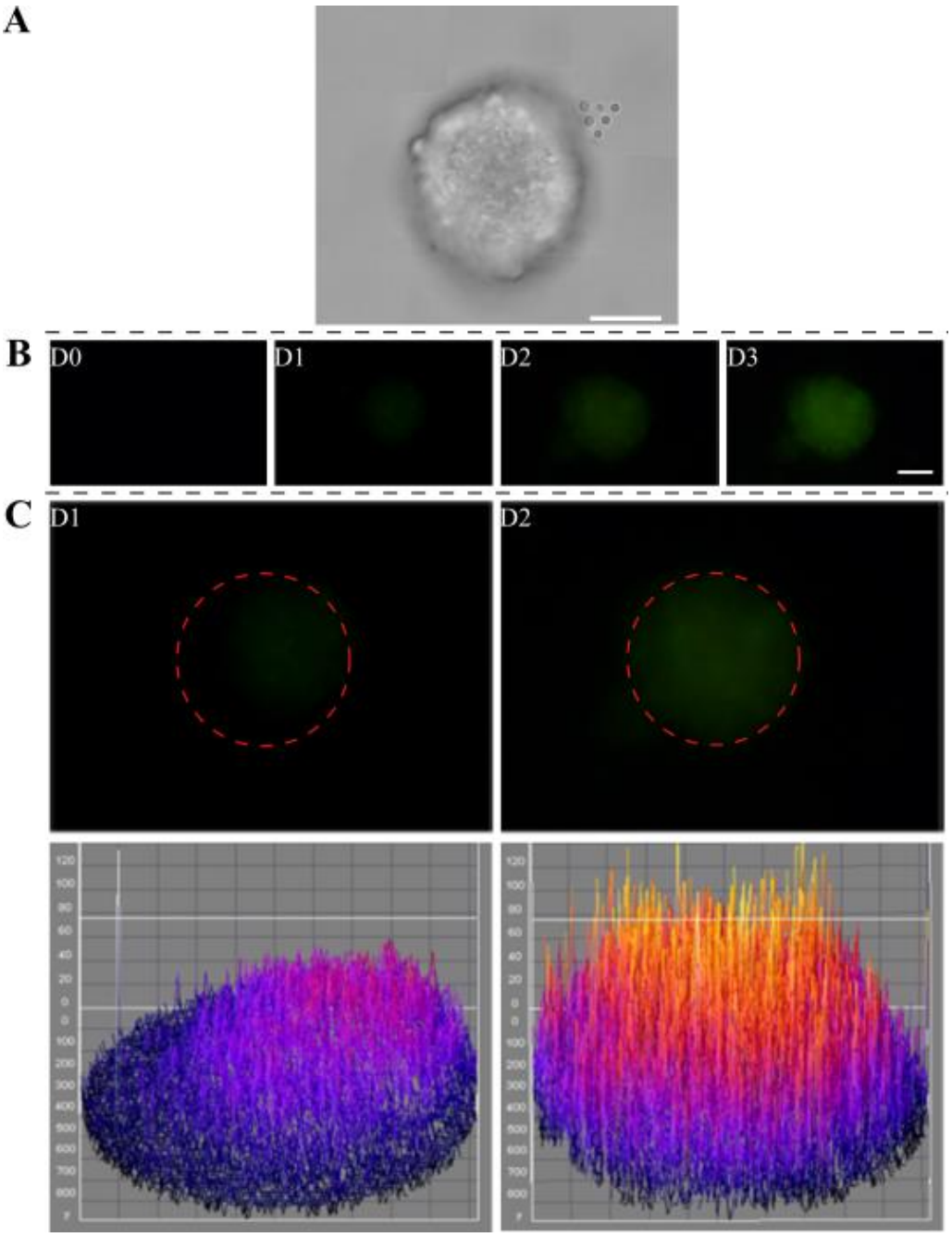

Figure 4.18 Spatio-temporal control of calcein AM signalling

Proof of concept for evoking a zonal cellular response to calcein AM using the HOTs patterning setup. A. A mES cell aggregate with calcein-AM-laden microparticles positioned in close proximity to one side of the cell aggregate. B. Subsequent fluorescence micrographs of the cell aggregate, analysing calcein fluorescence signal over 3 days. C. The same cell aggregate with a red circle showing the position of the mES aggregate relative to the fluorescence signal on day 1 and 2, and then the post-image analysis plot of the grey values (false colour LUT) in the red circle. The scale bars represent 50 µm.

Six calcein-AM-containing microparticles were patterned in close proximity (5 µm) to a 50 µm diameter mES cell aggregate using the lobed patterning gasket (Figure 4.18 A). The patterned microparticles were completely isolated from unpatterned release sources and other cell aggregates and stabilised in GelMA (10%). Figure 4.18 B shows a strong calcein signal forming over 3 days of cell culture, and with the whole aggregate fluorescing by day 2. A very weak signal can be seen at day 1, and this is better represented in Figure 4.18 C showing the day 1 and 2 fluorescence images with a red ring indicating the aggregates position relative to the signal. As before, a Fire LUT was used to better identify the calcein signal over the background, and this signal was graphically represented to display the grey value of each pixel within the red circle. The day 1 plot shows that an elevated signal was measured on the side of the release source, resulting in a gradient of fluorescence intensity across the aggregate. By day 2, this gradient was no longer visible and the entire aggregate was fluorescing.

One potential explanation for this may lie in the fact that during the microparticle burst release, there is sufficient concentration of calcein green AM only within the direct zone about the release source (microparticles). Such temporally linked peaks in concentration yield responses only in close proximity, however over time and normalisation of the concentration through the gel, the rest of the aggregate responds.

The identification of this zonal response to a delivered molecule gives strong evidence that the HOTs platform can achieve spatially tailored molecular signalling. To further demonstrate the power of this novel micropatterning platform, biologically relevant experiments must be developed. Delivery of

larger molecules and proteins would potentially introduce further difficulties, and these need to be addressed before the technology can be claimed a fully functioning micropatterning tool-set.

4.5 Conclusions

In this chapter it is discussed how we overcame initial difficulties met when attempting to create a proof of concept for the delivery of molecules using HOTs-patterned microparticles. By adapting the method from involving an intrinsically fluorescent released molecule, rhodamine 123, to a delivery-dependant fluorophore, calcein AM, it was possible to create models of molecular delivery to a patterned cell architecture. As previously discussed, the capability to control multiple signals would be necessary to replicate even the most basic developmental models, and so we showed how this could be achieved with calcein blue AM and differently sized release sources.

Whilst developing these demonstrations of the HOTs patterning potential, a drawback with the agarose stabilisation method was observed. Although it was highly effective at stabilising patterns, and almost completely biologically inert, it was not permissive of cellular proliferation. One alternative approach discussed was the functionalisation of the agarose hydrogel, but a simpler option availed itself. The use of GelMA provided a cell supportive pattern-stabilising matrix that was shown to be highly suitable for HOTs patterning. As described previously, gelatin is derived from collagen, a commonly used biomaterial in tissue engineering. Whilst it is far less bioactive than growth-factor-containing Matrigel, it is not as bioinert as agarose. The choice to proceed with GelMA was based on the fact that it offered a compromise as a hydrogel that can promote cellular interaction whilst being less bioactive than other extracellular-matrix-derived hydrogels.

This chapter also detailed how the patterned microparticle release sources can be isolated from those that are unpatterned. As discussed, the isolation of patterned release sources permits the control of the signalling in the patterning area, without any background signalling from unpatterned release sources. Through the development of the lobed patterning gasket it became possible to fabricate multiple isolated experiments in the same gasket. Using the lobed gasket we were able to show the expected zonal response of calcein fluorescence on the proximal side of the mES cell aggregate to the release source.

4.5.1 Hypothesis of proximity release zone mechanism

The presence of this zone of calcein fluorescence at a specific time-point could explain how the microparticle release system is achieving zonal delivery. Whilst it is unlikely that the mobility of the calcein AM molecule is the causal factor in the proximity zone of fluorescence because of its estimated high diffusivity through the hydrogel. The proximity zone most likely had a suitably high concentration of calcein AM at certain time-points (24 hours (Figure 4.18)) permitting the visualisation of cell-containing esterase-cleaved calcein AM in this zone but not others. The timing of this proximity release zone coincides with the burst release phase for the microparticles, further supporting this theory.

For further development of the HOTs platform, biologically significant models were recreated, and a zonally differential response to released factors was demonstrated. These advancements are discussed in the following chapters, where the HOTs patterning setup was used to investigate biological questions.

5. Results – HOTs based directed differentiation of embryonic stem cells

5.1 Introduction

This chapter will describe the approaches taken to demonstrate the HOTs patterning setup's capability to deliver bioactive molecules to a cell-based structure to yield a specific biological response. The developments described explain how the technology can be applied to cell models of differentiation and how the protocol has been improved over earlier approaches. Chapter 4 demonstrated the delivery of fluorophores to cells to provide a working principle. Calcein AM was successfully delivered and converted to fluorescent calcein by intrinsic esterase activity within the cell. To develop this concept and the HOTs pattering setup, a more complex model for delivery and response was devised. A distinction was clearly recognised in Chapter 4 that such work with fluorophores is not a suitable representative of the biological investigations that the HOTs patterning setup is being developed for. In order to bring about a specific biological response via solute signalling, an effector molecule must be presented to responsive cells at an adequate concentration (dependent upon the binding affinity). Generally speaking, the molecule will bind to a surface molecule for further downstream signalling or entry into the cell. Cells provided

with the appropriate signal bring about transcriptional change and then subsequent protein expression occurs as a response.

The ability to show such transcriptional modulation through patterned, spatio-temporal solute signalling is of great interest to many researchers wanting to understand cellular developmental processes. As previously discussed, other technologies are available for delivery of molecular gradients [214–218], however, none can achieve such control of diffusible signalling at the length scales described in this thesis.

This chapter describes the development of a suitable model for directed differentiation of cells exposed to a single molecular signal. Embryonic stem cells are highly prone to undergoing differentiation when grown in culture. As previously discussed, their undifferentiated state is maintained by the presence of LIF in cell culture medium [219,220]. However, upon removal of LIF from the medium, spontaneous and random differentiation occurs [221]. Typically, differentiation is towards germ layer commitment but the overall gene expression pattern can change dramatically within days of LIF removal. Furthermore, development of cellular aggregates or embryoid bodies has been shown to lead to cell populations that are comprised of the three germ layers (ectoderm, mesoderm, and endoderm) [222]. The heterogeneous mixture of cells within embryoid bodies makes the characterisation of defined differentiation events difficult. Whilst monolayer culture is sometimes seen as being more amenable to directed differentiation [223], small and early stage cellular aggregates are a basic but effective representation of a developing embryo.

Use of small cell aggregates, despite their heterogeneous nature, to demonstrate diffusible signalling control with the HOTs platform was seen as appropriate for creating the advanced proof of concept. To achieve any form of directed differentiation or biological response from a mES cell aggregate a highly potent stimulus will be required that yields a significant cellular response. To observe the spatial control of the signalling, the response must also be rapid and only present after exposure to the molecular signal.

Whilst one aspect of this chapter deals with the optimisation of a biological model to suit the HOTs platform. The other tranche focusses on the fabrication of microparticles that were suitable for delivering a bioactive molecule in such a way to illicit the appropriate response. A hypothesis had been developed following the work with calcein AM delivery that zonal delivery around the microparticle release source occurs due to the burst release kinetics associated with these microparticles. The high mobility of the small molecule calcein AM means that it will be diffusing great distances away from the release source quickly. However, during the rapid release stage a sufficiently high concentration of released molecule will be present around the microparticles yielding a zone of calcein response on one side of the mES cell aggregate (Figure 4.18) (Section 4.5.1). If the hypothesis is correct, a similar zonal response could be observed with a bioactive signalling molecule released during the burst phase.

5.2 Chapter Experimental Overview

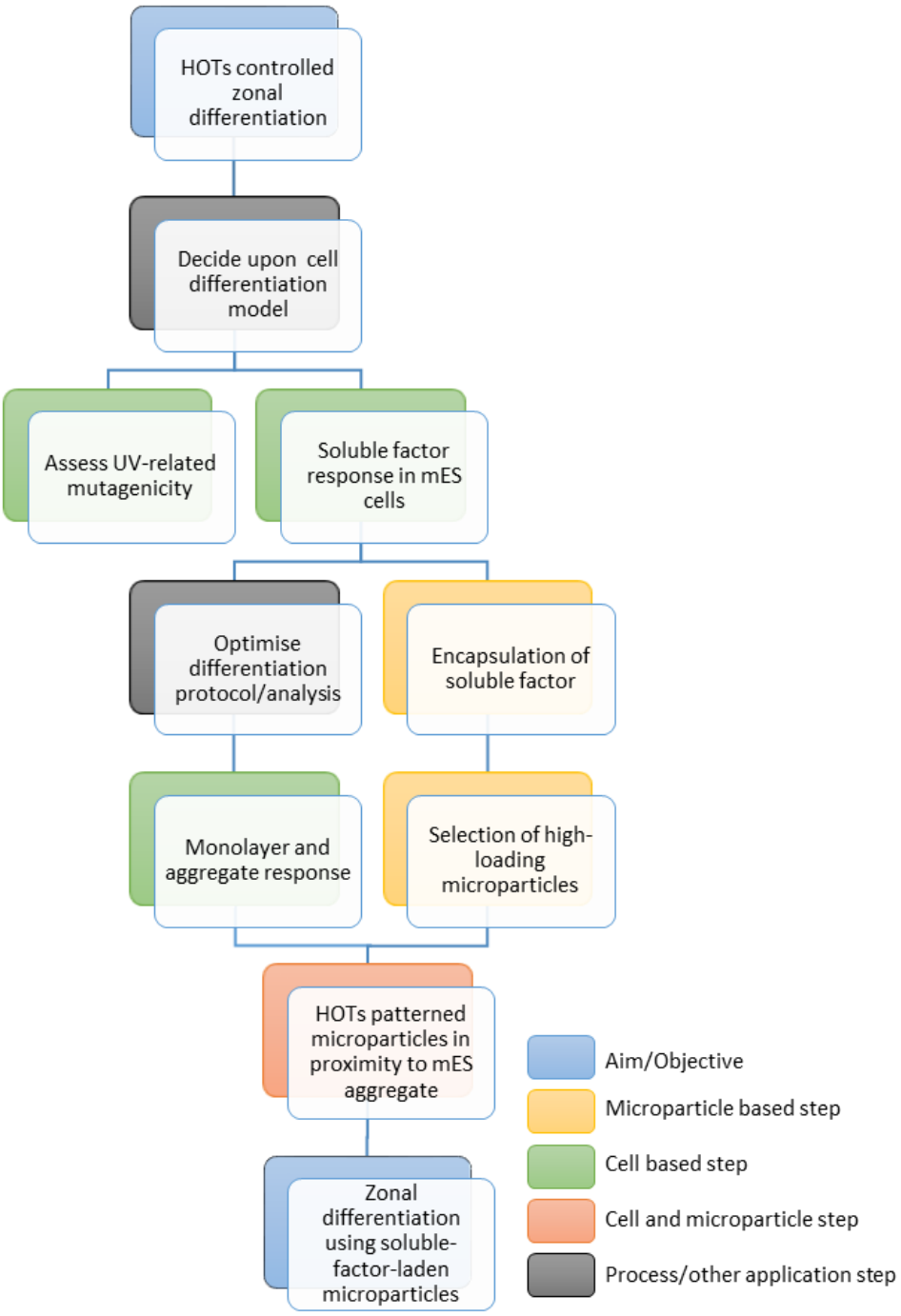

5.3 Materials and Methods

5.3.1 Double Strand Break assay

mES cells at passage 10 were cultured on gelatin coated 6-well plates until 80% confluent. Cell containing wells were then exposed to a UV source as described in Section 4.3.6 for a range of exposure times (0-300 s) (n=3 wells/exposure time), following exposure the cell culture medium was removed and replaced with fresh medium. Cell samples were incubated at standard culture conditions for 24 hours. Samples were then fixed with PFA (3.4%) for 20 minutes and immunocytochemistry was completed for using anti γH2AX antibody (Table 2.1) and the method previously detailed (Section 2.7).

5.3.2 Differentiation media

Retinoic acid differentiation medium without LIF, as previously described in Section 2.1.2.3, was used for initial differentiation protocols. Serum starvation was applied in certain differentiation experiments detailed in this chapter.

5.3.3 Retinoic acid based differentiation of mES cells

CGR8 mES cells were reanimated from cryostorage at passage 8 and were cultured until passage 10. mES cells were then plated onto tissue culture coated plastic well-plates at a seeding density of $5x10^3$ cells/cm^2 and grown until 80% confluent (~48 hours) in the required cell culture medium (Section 2.1.2). Retinoic acid (RA) (R2625, Sigma-Aldrich, UK) is dissolved in DMSO to create a stock solution of 1mM concentration. For RA differentiation of mES cells, working concentrations of 10-1000 nM are achieved by diluting the stock

concentration in fresh ‘RA differentiation medium’. Cells were typically exposed to RA for 24 hours unless otherwise stated.

5.3.4 Cell differentiation analysis

Cells were differentiated by exposure to soluble RA and were assessed by immunocytochemistry described previously (Section 2.7). At the end of the differentiation period, samples were fixed, immunocytochemically stained, and analysed by fluorescence based optical or confocal microscopy as described in Section 2.10.

5.3.5 Retinoic acid encapsulation

RA was encapsulated into PLGA microparticles using both single and double emulsions as described in Section 2.9.1. Single emulsion (W/O) microparticles were formulated accordingly, 700 mg PLGA and 300 mg TBIIF were dissolved in DCM containing 2 mg RA and 10 mg HSA. Double emulsion (W/OW) microparticles were formulated accordingly; a concentrated solution of RA and serum albumin (HSA or BSA) was made up (2 mg RA + 100 µL of HSA (100 mg/mL)) and added to the polymer solution (700 mg PLGA and 300 mg TBIIF dissolved in DCM). Fabrication of double emulsion microparticles was completed as described in Section 2.9.1.

5.3.6 Fluorescent retinoic acid-laden microparticles

FITC-BSA RA microparticles were formulated as described in Section 5.3.6 with the exception that FITC-BSA was used instead of HSA at the same concentration.

5.3.7 HOT patterning

Patterning was completed according to Section 2.8.1 using multi-lobed patterning gaskets as previously described in Section 2.8.4. Stabilisation of the HOTs fabricated microparticle structures was achieved using the GelMA (10%) system as previously described in Section 4.3.6.

5.3.8 Fluorescence-associated cell sorting (FACs)

FITC-BSA RA, non-fluorescent RA microparticles and 5 µm reference beads were suspended in PBS (25 mg/mL) and sonicated for 30 seconds to break up aggregates before being added to separate 5mL FACS tubes under sterile conditions. Sorting and analysis were performed using a MoFlo Astrios Cell Sorter (Beckmann Coulter, UK) equipped with a 488 nm laser at 100 mW of power. Forward scatter (FSC1) and side scatter (SSC) were collected through a filter and the FITC signal was collected in the FL1 channel through a 513/26 bandpass filter. A light scatter gate was drawn in the SSC vs FSC1 plot to include microparticles of a similar size to 5 µm reference beads. Cells within the gate were displayed within a SSC vs 488 513/26 intensity plot allowing a visualisation of the fluorescence intensity distribution within the microparticle batches. Final selection gating was applied to sort based on fluorescence intensity.

Microparticles were sorted over several sessions in separate batches to reduce the time spent suspended in PBS and were freeze dried for long term storage.

5.4 Results and Discussion

This chapter details the use of HOTs for directing differentiation-based development of cells through a local delivery of chemical factors. Cellular differentiation can be analysed through the changes in protein expression by using immunocytochemistry to assess certain resultant surface protein markers. This method of assessment relies upon the direct relationship between effector signal and response where there is a limited potential for non-specific induction.

5.4.1 Assessment of GelMA associated mutagenicity

One such possible variable being introduced is through the cellular exposure to UV light, when cross-linking GelMA. To ascertain whether any DNA damage is occurring, that could be leading to mutations, a double strand break (DSB) assay was completed. To assess the effect that the UV exposure was having on the mES cells, cells were exposed to the UV source exact manner that they would, for cross-linking. Using an antibody for phosphorylated histone H2AX, the earliest indicator for DNA DSB [224], DNA damaged cells can be labelled and then visualised by immunocytochemistry.

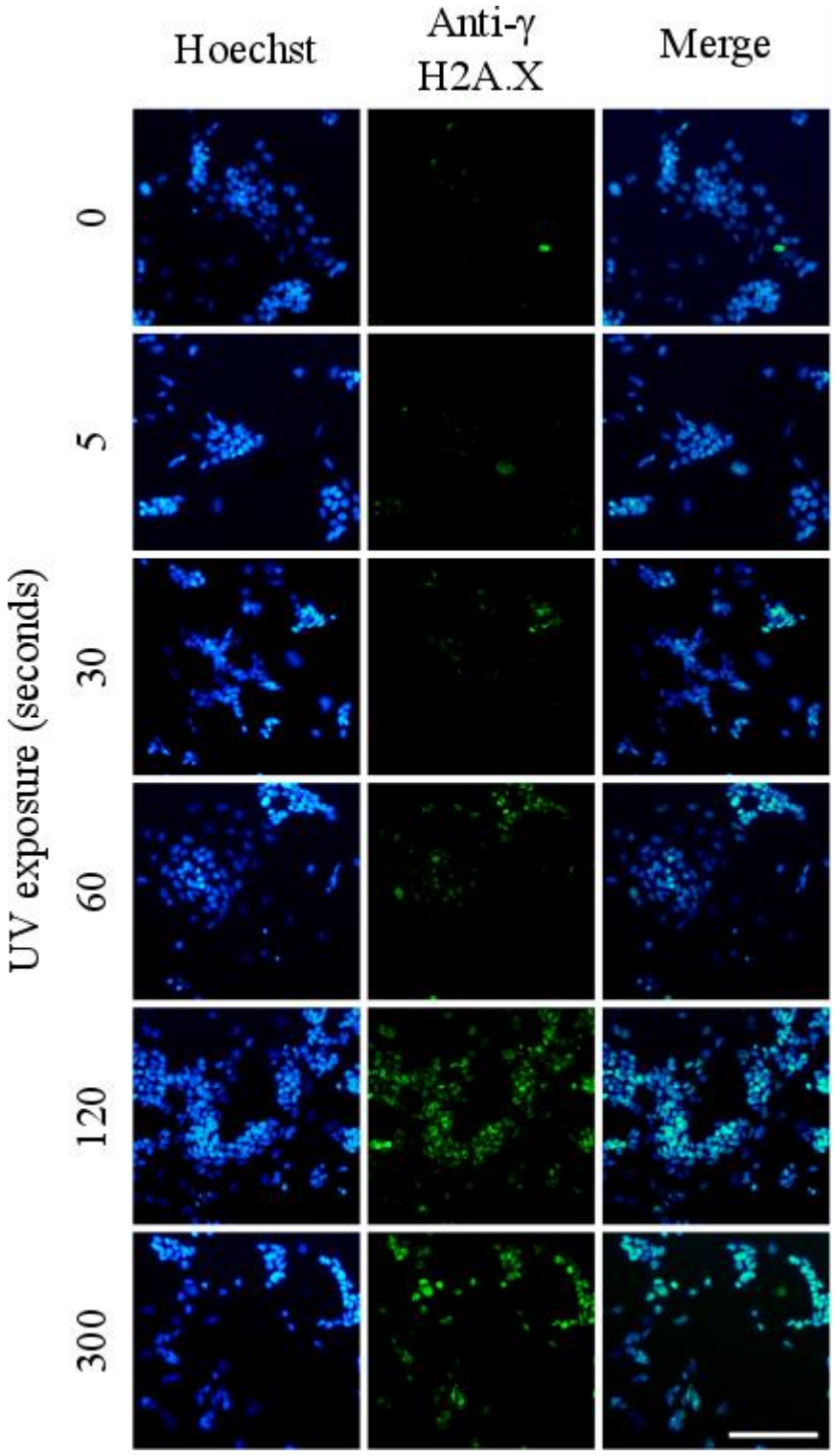

Figure 5.1 Assessment of DNA damage following UV exposure

mES cell monolayers were exposed to a range of different UV exposure times and then cultured for 24 hours, and then the cells were fixed and stained, Hoechst staining permits nuclear visualisation with γH2AX staining overlaid to show potential DNA damage that has occurred.

Figure 5.1 shows that the mES cells are susceptible to DNA damage, with greatly increased γH2AX staining following >60 seconds UV exposure and at 120s almost all of the cells in the field of view are γH2AX positive. However, at UV levels of 5 seconds, the exposure required for complete cross-linking of GelMA (20 μL), there is no clear increase in γH2AX staining over the control (0 seconds). Whilst this result seems to suggest that at the levels of UV exposure relevant to GelMA cross-linking are not detrimental, the presence of γH2AX even at 0 seconds is interesting. This basal level could be explained by the karyotype instability exhibited by mES cells following long-term culture [225], however, reports have suggested that γH2AX may also be present at low levels involved in stem cell proliferation [226]. Regardless, the assay is still able to suggest that the UV exposure used for GelMA cross-linking is not leading to excessive DNA damage, and combined with its favourable cell proliferation and suitability for patterning, it is the lead choice of hydrogel for this project.

5.4.2 Directed mES differentiation using HOTs

Before any HOTs based biological investigations could be conducted, a robust developmental model had to be chosen to further the technology's proof of principle. A comprehensive literary search yielded lots of potential signalling models to replicate with the HOTs patterning approach. However, the model needed to meet certain criteria, including: high sensitivity to the released molecule, sufficiently strong biological response, and a developmental response that could be assessed by immunocytochemistry. The HOTs patterning procedure had been optimised to work well with cells of embryonic origin, and

so for these initial biological investigations, the proven mES cell line (CGR8) was used.

5.4.3 Retinoic acid dependent expression

One such developmental mechanism found to meet the requirements discussed above was the response of mES cells to retinoids. Recent work had shown a robust response of mES cells to low concentrations of RA, displaying considerable elevations of two Retinoic Acid Responsive Elements (RAREs), Stimulated by retinoic acid gene 8 (Stra8) and Deleted in azoospermia-like (Dazl). Recent work has shown that the protein expression of these two RAREs are tightly linked to RA concentration and <800 fold increases have been reported after just 24 hours of exposure [227,228]. These two reporter proteins were also shown to be very lowly expressed without RA supplements. This was an important requirement for these initial experiments as it would allow for even subtle changes in protein expression to be visualised through immunocytochemistry.

To assess the response of mES cells to RA at different concentrations, and optimise the staining procedure, mES cells were exposed to different concentrations of RA for 24 hours and were then fixed and stained for both DAZL and Stra8 protein.

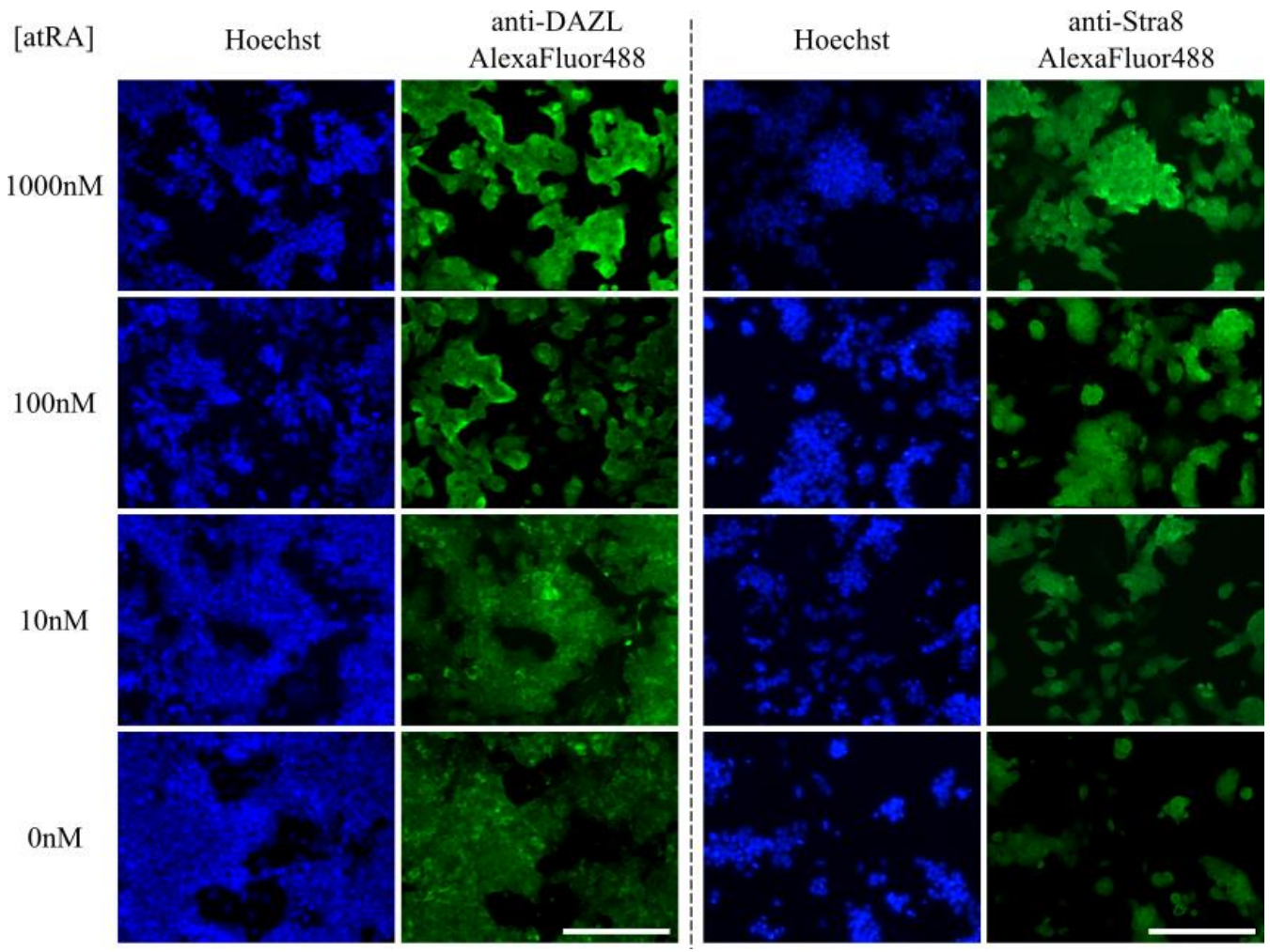

Figure 5.2 Dose response of mES cells to RA

DAZL and Stra8 immunocytochemistry staining showing the response of mES cell monolayers to a range (0-1000 nM) of RA with Hoechst counter-staining. Scale bar represents 100 µm.

The mES cells were shown to respond to RA, with more fluorescence staining seen in the 100 and 1000 nM samples for both Stra8 and DAZL. However, the negative control wells with 0 nM RA supplement also showed with fluorescence staining signal, indicative of high basal Stra8 and Dazl protein expression. This result was not representative of the previous literature and would prove detrimental to HOTs patterning expression due to the similarity in staining intensity. It would make the analysis of low level RA supplemented cells difficult to distinguish between unstimulated cells.

5.4.4 Serum associated expression of RAREs

Previous work with RA stimulated embryonic cells had utilised low serum media to reduce the level of non-specific retinoids in the basal medium. Because the response was so sensitive, even the low levels of retinoids in FCS could be stimulating mES in negative controls. This hypothesis was tested by growing mES monolayers in 0% FCS supplemented medium for 24 hours prior to differentiation. Cells were then given medium supplemented with different concentrations of FCS (Section 5.3.2) and were cultured as normal.

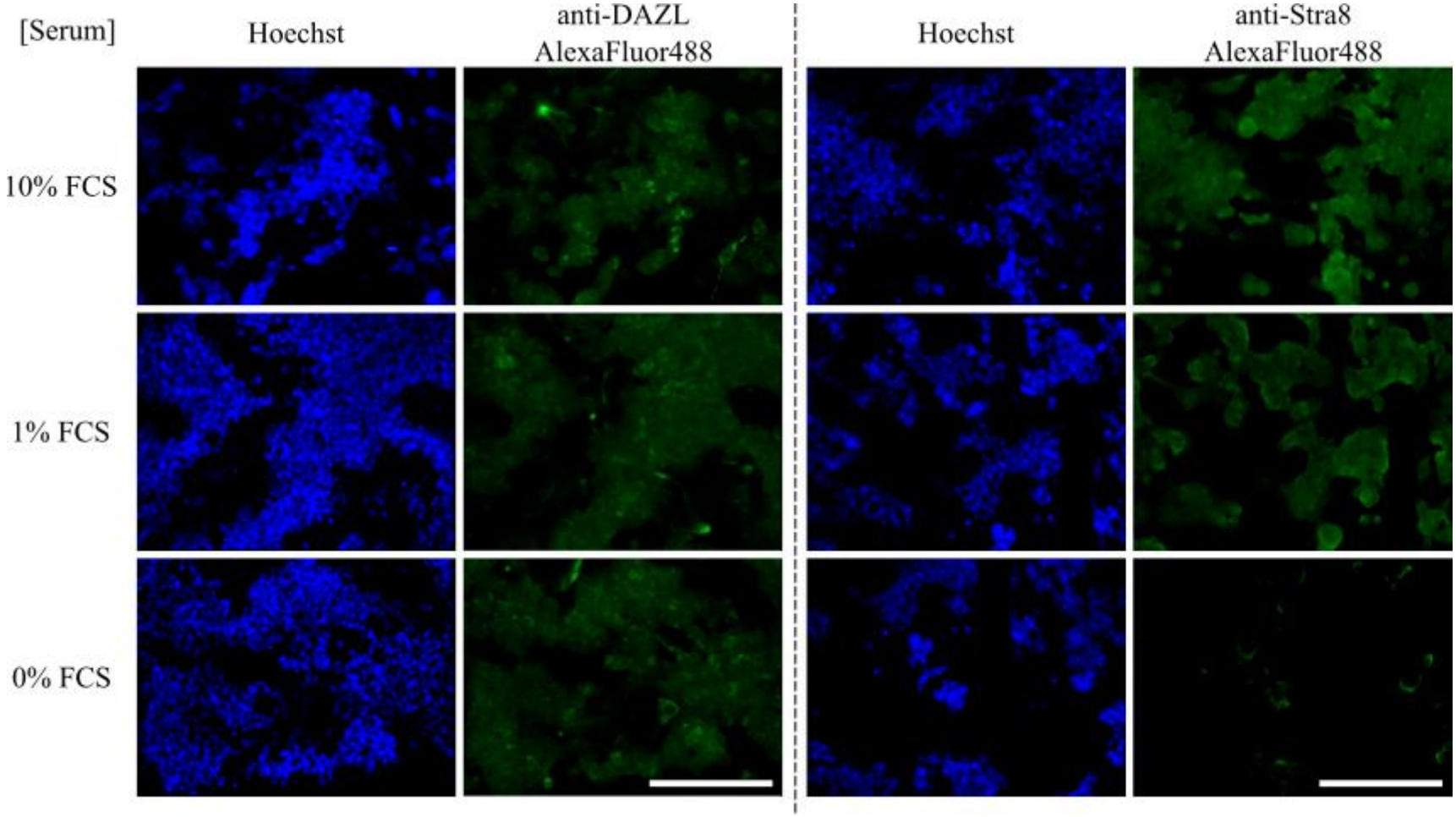

Figure 5.3 Serum starvation of mES cells

Immunocytochemistry showing the staining of DAZL and Stra8 protein, present when mES cells cultured in media containing 10, 1 or 0% FCS and cultured for 24 hours. Scale bar represents 100 µm.

Figure 5.3 shows the different Stra8 and DAZL staining in low passage mES monolayers cultured in 0, 1, and 10% FCS. In the DAZL stained wells, staining is clearly seen at each serum concentration. This indicates that the DAZL protein is not reducing sufficiently after removal of serum and that it would not be a suitable reporter for HOTs based RA delivery. However, the Stra8 response can be reduced dramatically following culture in 0% serum. The stark difference in fluorescence staining between 0 and 1% serum demonstrates just how tightly Stra8 protein is linked to RA concentration. The 0% well shows that Stra8 protein can be reduced sufficiently to yield very low numbers of positive cells in the sample when compared to cells cultured in 1% serum. This result reflected the reported observations with these cells, and would prove suitable for HOTs delivered RA concept experiments. The starvation of serum is common place in differentiation protocols [31,229], however it was necessary to show that these conditioned mES cells were still responsive to RA after serum starvation as they would be used for future HOTs experiments.

The serum starvation was only effective at reducing Stra8 protein levels, DAZL was still present in high levels post serum starvation. This may have been due to the slow turnover of DAZL protein, resulting in high DAZL protein even after gene expression has stopped. For this reason, DAZL was dropped as a readout for the RA response. The presence of Stra8 would be a sufficient marker for RA delivery and mES cell development brought about by HOTs signal patterning.

5.4.5 Dose dependant response to retinoic acid

RA has signalling functions throughout the whole body and at various stages in development, and in 2006 the Page lab showed that external RA signalling led to the expression of the Stra8 gene [230]. The interesting aspect about RA signalling is that a seemingly nonspecific chemical signal is capable of bringing about vastly different effects. The Page group later demonstrated the role that DAZL protein plays in preparing the cell to respond to the RA when required [231]. Further specificity can be encoded by a signals spatio-temporal characteristics and it is well reported that RA signalling is no exception [232,233]. If the Stra8 response to RA occurs is a dose dependent manner, a zonal response could be seen by an area of higher Stra8 protein.

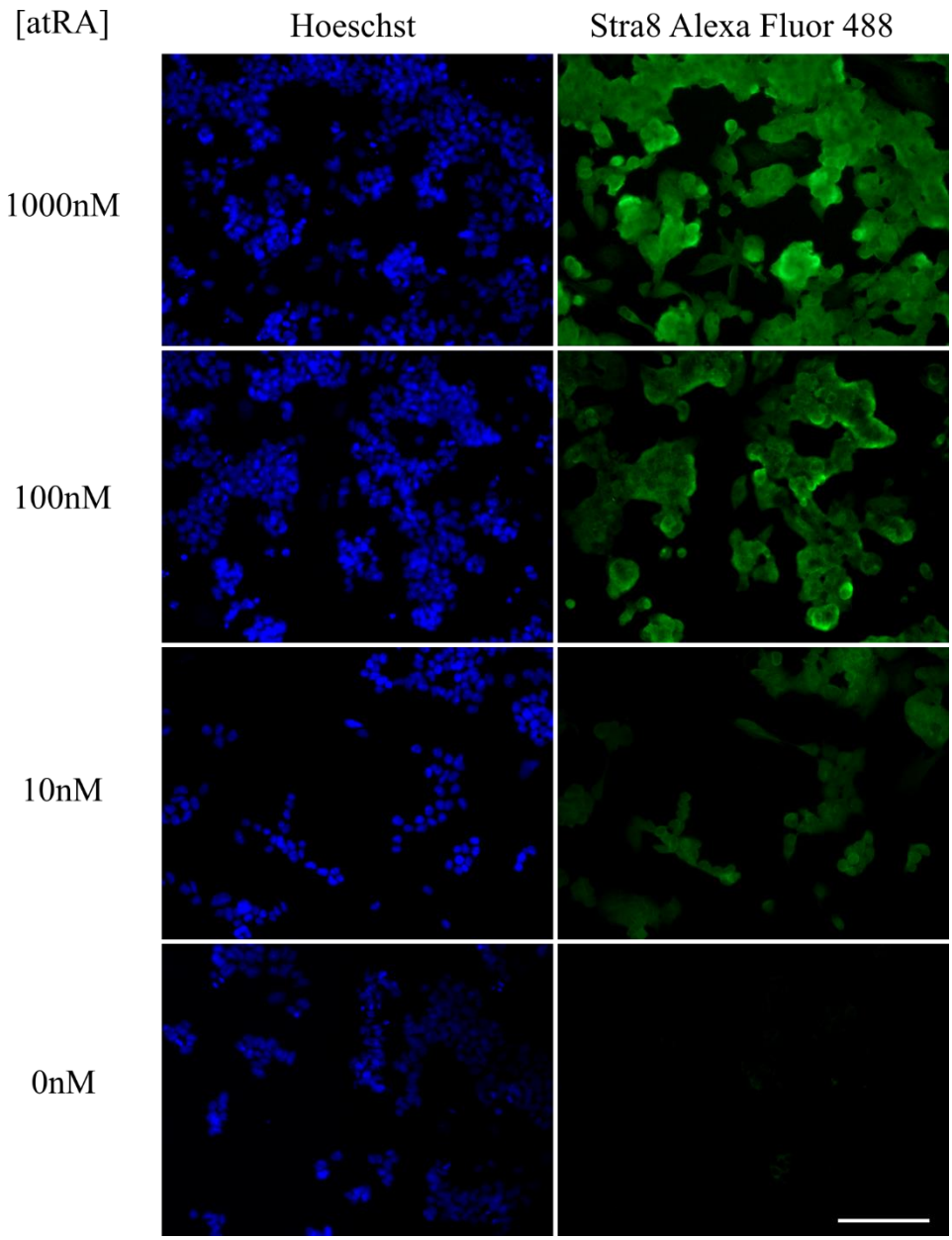

Figure 5.4 Dose reponse of condfitioned mES cells to RA

Stra8 immunocytochemistry staining showing the response of conditioned (serum starved) mES cells to a range (0-1000 nM) of RA with Hoechst counter-staining following serum starvation. Scale bar represents 100 µm.

The dose response experiment in Figure 5.5 shows the response of conditioned mES cells to a range of RA concentrations. As previously described, cells were fixed after 24 hours of RA exposure and stained for Stra8 protein. The fluorescence intensity gives a relating to the amount of Stra8 protein that has been expressed is clearly seen to increase with the increase in RA concentration. Once again, the negative control shows very little fluorescent signal indicating that there are only small numbers of cells expressing Stra8 at a low level. The fluorescence staining intensity observed using 10 nM is visibly greater that the negative control and it gives confidence that the model will be suitable for future delivery experiments.

5.4.6 Retinoic acid dependant response in mES aggregates

Following on from the promising results seen with zonal delivery of calcein AM to mES aggregates, the Stra8-RA response was assessed with serum starved mES cell aggregates. During the aggregation process there are numerous different signalling stimuli occurring that could be altering the response so it was necessary to repeat the dose response experiments again. A dose response assay was completed for the mES aggregates as described in Section 5.3.3.

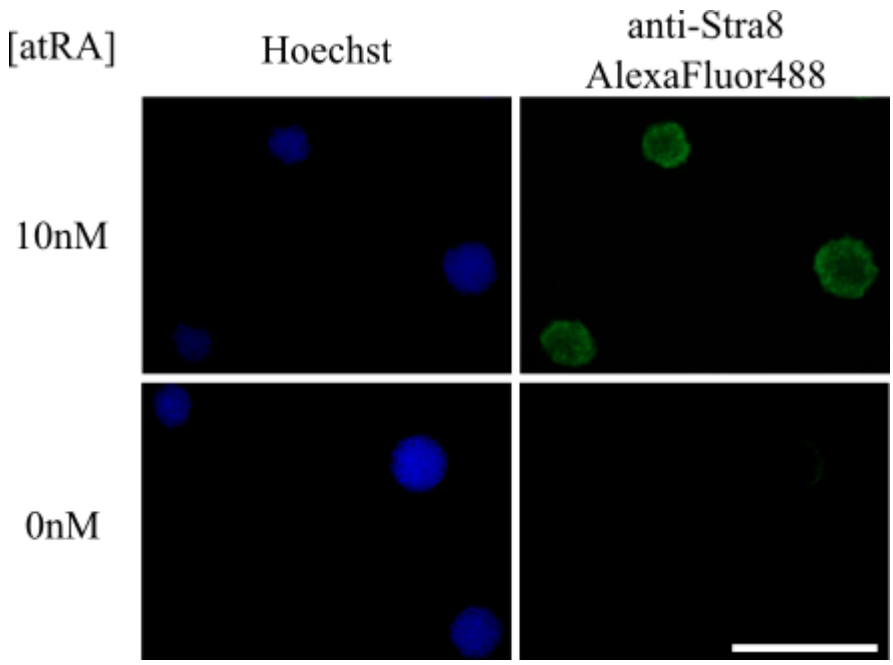

Figure 5.5 Dose response of conditioned mES cell aggregates to RA

Stra8 immunocytochemistry staining showing the response of three conditioned mES cell aggregates with and without RA (10 nM), with Hoechst counter-staining. Scale bar represents 100 µm.

Figure 5.5 shows Stra8 staining in permeabilised mES cell aggregates exposed to either 0 or 10 nM RA for 24 hours. A strong fluorescent signal can be seen in the aggregates posed to 10 nM whereas a negligible signal is present is the negative controls (0 nM), this result supports the case for mES aggregates being used for RA release experiments. The aggregated mES cells are still specifically responsive to added RA. The permeabilisation, detailed in Section 2.7.1, was key for observation of the cells deeper into the cell aggregate. Fluorescent signal can be assessed almost all the way through the aggregates, permitting the observation of any zonal responses throughout the aggregate.

5.4.7 Retinoic acid encapsulation

RA has a molecular weight of 300 g/mol and is hydrophobic but soluble in DCM and other organic solvents. The chemical characteristics of RA make it suitable for single emulsion encapsulation (W/O), as previously described [234,235]. Accordingly, RA was encapsulated using the method detailed in Section 5.4.7, and the microparticles were assessed for 'trappability' as described in Section 3.3.2. The RA-laden W/O microparticles were not suitable for optical manipulation at the sizes required (~5, ~10, or ~15 μm) (Supplementary data). Further methods for encapsulating RA into PLGA microparticles were researched, including the precipitation method [198,236]. However, considering the previous optimisation of W/O/W PLGA microparticles for optical trapping, RA was encapsulated accordingly. A batch of RA-laden microparticles was formulated as described in Section 5.4.7 by the methods detailed in Section 2.9.1 and were fully characterised (Figure 5.6).

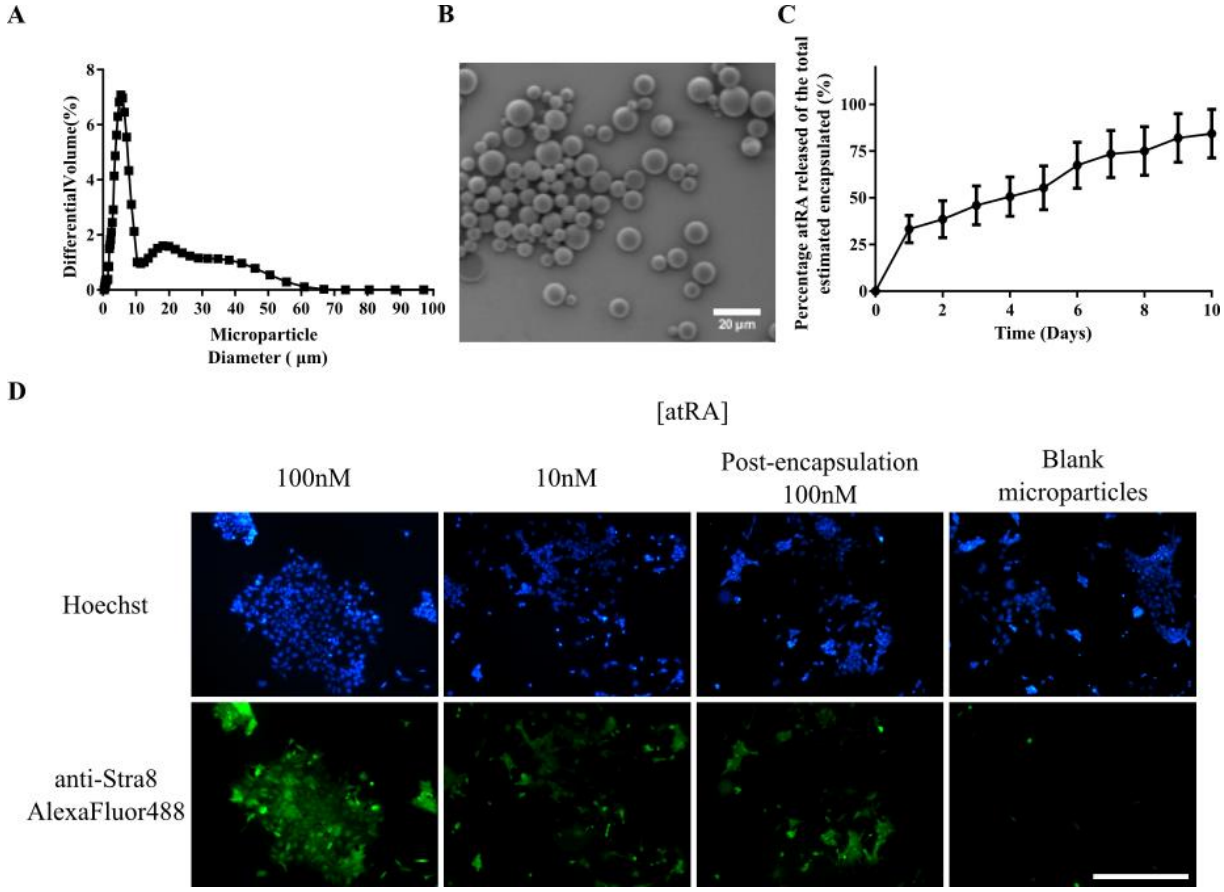

Figure 5.6 Characterisation of RA laden microparticles 1.0

A. Microparticle size distribution by differential volume across the batch as assessed by coulter analysis B. SEM micrograph of the microparticles allowing for analysis of their morphology and validating the coulter analysis data. C. *In vitro* release study of RA over 10 days completed in triplicate (Error bars mark cumulative standard error of the mean) D. Representative fluorescence micrograph of each condition for the post-encapsulation bioactivity assessment comprising fresh solutions of 100 and 10 nM RA and solution extracted from a suspension of RA-containing microparticles, estimated by microparticle mass and estimated encapsulation efficiency, to yield 100 nM RA "Post-encapsulation 100 nM". The scale bar represents 100 µm.

The RA laden microparticle 1.0 batch fabricated (Figure 5.6) showed similar characteristics as previously seen with the calcein AM laden microparticles fabricated in the same way. The microparticles were around 5 µm in size calculated by coulter particle sizing, and SEM showed that the expected spherical and non-porous morphology was formed. An *in vitro* release study was completed for the batch over 10 days, the release kinetics were, as expected, similar to those seen with calcein AM laden microparticles formulated in the same manner. The high burst release that was shown to be favourable for yielding zonal release was observed with the RA laden microparticles. As previously discussed, it was important to complete a post encapsulation bioactivity assay to show that the encapsulation process had not disrupted the activity of RA. The bioactivity assay (Figure 5.6 D) showed that 100 nM of encapsulated RA yielded a greater response to 10 nM of fresh RA but a lower response to that of 100 nM fresh RA. This response was lower than expected and could have been indicative of damage to the RA during microparticle fabrication. The encapsulation efficiency was calculated to be 60.6 ± 4.3%, slightly lower than the calcein AM encapsulation efficiencies (Calcein green AM 66.1 ± 1.3%), and it was assumed that this reduced encapsulation efficiency was the cause of the weaker response observed in the post encapsulation bioactivity assay (Figure 5.6 D).

5.4.8 Improving retinoic acid encapsulation efficiency

To address this reduced encapsulation efficiency, differently formulated RA laden microparticles were fabricated (Batch 2.0) with the aim of creating microparticles with a loading efficiency of >80%. This was important for two

reasons. For these experiments the higher the RA loading the greater the likelihood of a positive response, and for future experiments using expensive growth factors, it was important to obtain higher encapsulation efficiencies to reduce costs of the method.

It has been shown previously that an increase in polymer solution viscosity e.g. by increasing polymer concentration, molecular weight, and lactide content may be advantageous to encapsulation efficiency [237]. However, by modifying the polymer molecular weight or lactide content in a manner to suit encapsulation efficiency, release kinetics would be altered dramatically. Increasing polymer concentration however, would lead to an increase of particle size as shown by Helen Cox (Thesis, 2013, University of Nottingham, UK) previously and potentially and increase in encapsulation efficiency. Changes in release kinetics could still occur and this would have to be assessed.

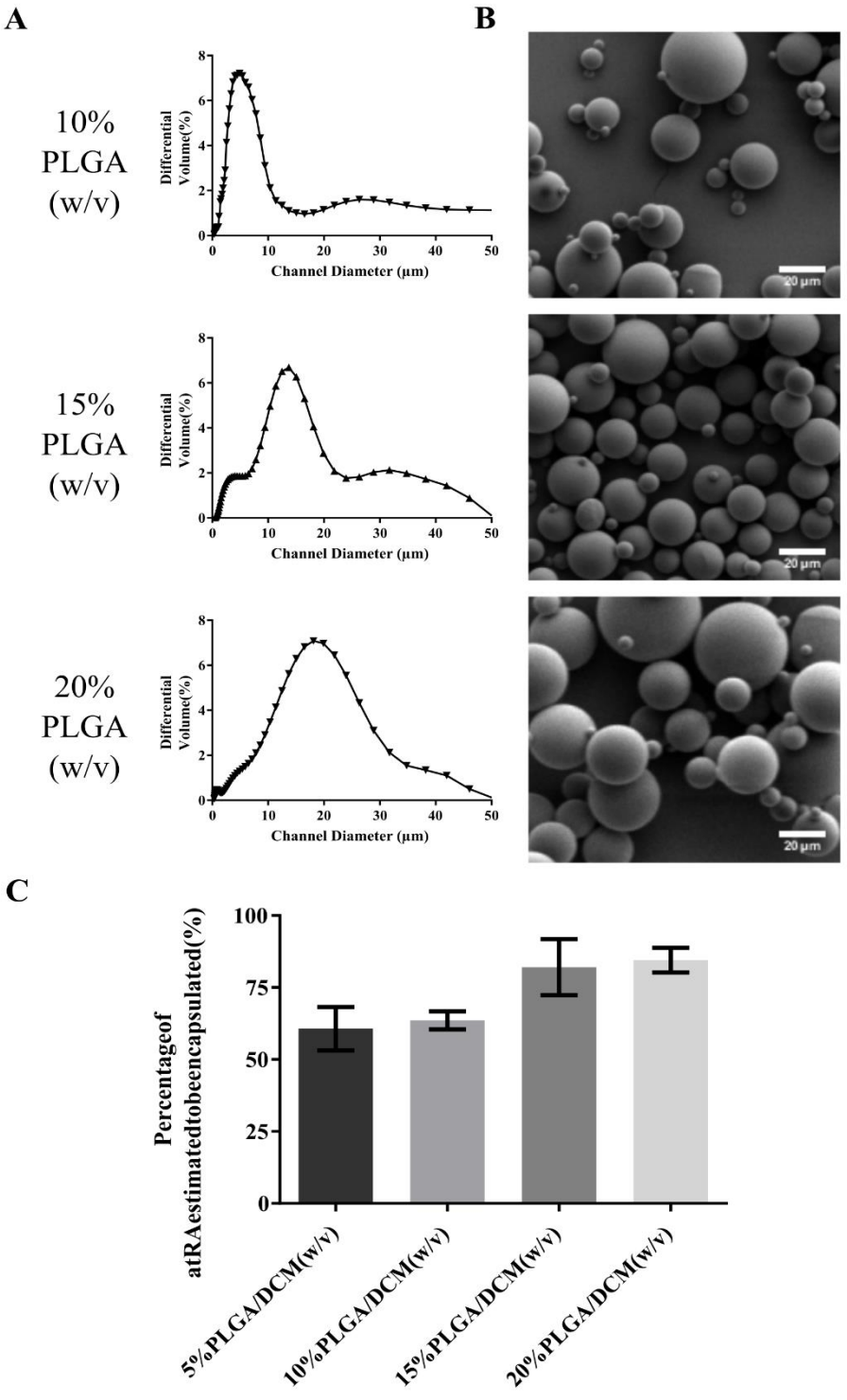

Figure 5.7 Characterisation of optimised formulation RA microparticles 2.0

A. Microparticle size distribution by differential volume for each of the formulations fabricated by way of coulter analysis. B. SEM micrograph of each formulation to assess morphology and validate the particle sizing data. C. Average estimated encapsulation efficiency of RA into each formulation of microparticles.

RA laden microparticles (Batch 2.0) were formulated with different polymer percentages (10, 15, and 20%).

Figure 5.7 shows the characterisation of these batches,

Figure 5.7 A shows the different sizes yielded with these new formulations and their SEM imaging (

Figure 5.7 B). As previously shown, with an increase in polymer %, microparticle diameter also increases. Further to this, it has been reported that by increasing the polymer %, the encapsulation efficiency also increases [117,201],

Figure 5.7 C displays this relationship. The increase in encapsulation efficiency reaches 82.1 ± 5.6% with 15% polymer, an increase of <20% over the initially fabricated 5% polymer batch (Figure 5.6). The 20% polymer batch resulted in the greatest estimated encapsulation of 84.5 ± 2.5%. These highly loaded microparticles were chosen over the 20% polymer batch because the sizing was deemed more appropriate for creating a smaller and better defined release point.

As previously mentioned, the increased polymer concentration may lead to different release kinetics that could prevent a high concentration RA zone from forming. For this reason a 24-hour *in vitro* release study was completed for each of the hour polymer concentration batches fabricated.

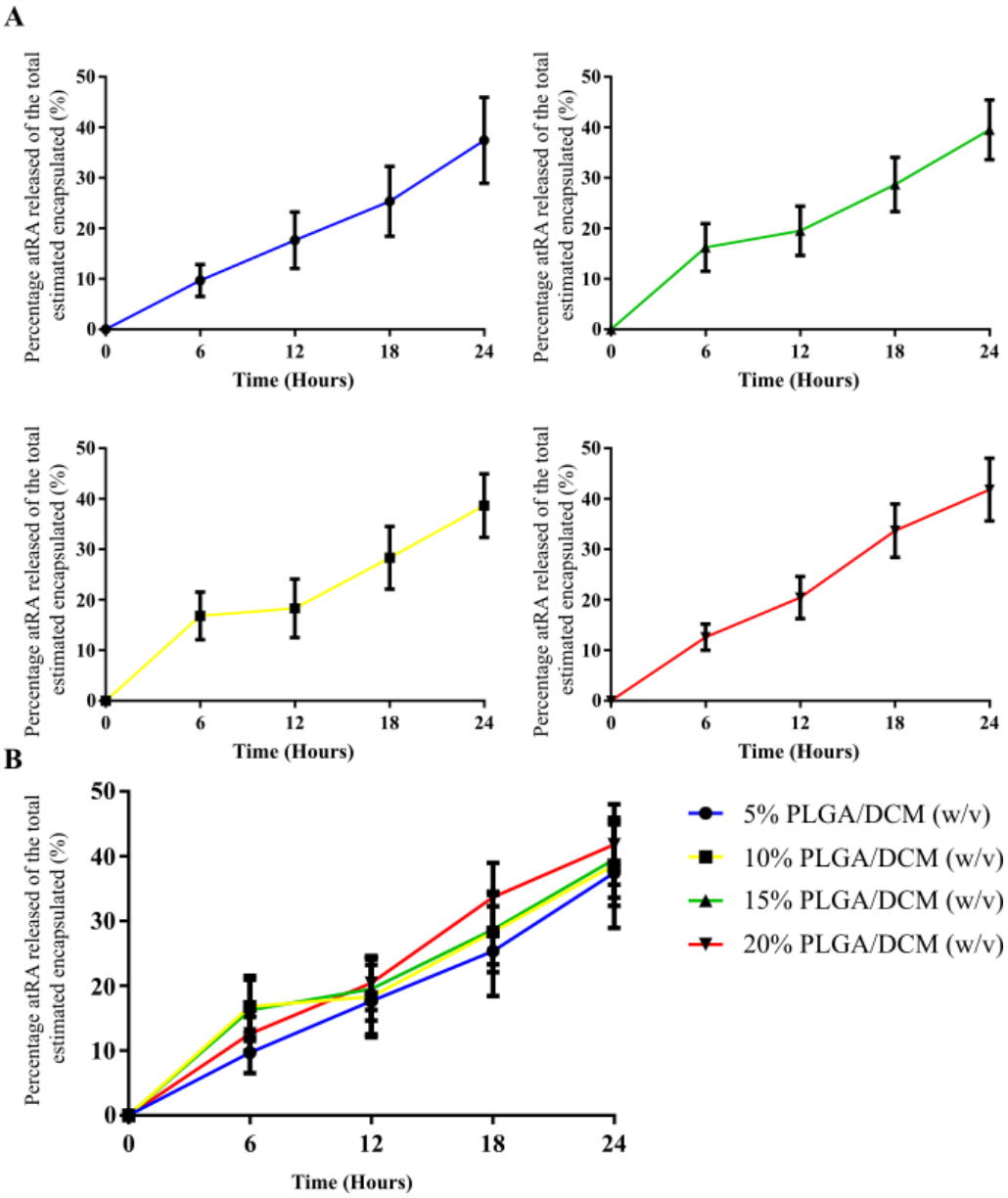

Figure 5.8 24-hour RA release study to assess effect of polymer concentration on release kinetics

A. *In vitro* retinoic acid release plots for each of the formulations characterised in Figure 5.6 (5, 10, 15, and 20% Polymer concentration).over 24 hours with time-points every 6 hours. B. The four formulations release plots compiled on one plot to allow for comparison. All plots are calculated as a mean from triplicate batches with error bars representing cumulative standard error of the mean.

The release studies completed in Figure 5.8 show that the increase in polymer solution viscosity has a minimal effect on the burst release kinetics of RA from these batches. The plots assess the release as a percentage of the estimated encapsulated RA so normalising the release rate between batches. The release studies were only completed for 24 hours as the HOTs RA experiment was only that long, however the release kinetics between the different batches may vary when comparing complete release plots.

5.4.9 HOTs patterning retinoic acid-laden microparticles

Following on from the observation of the highly dose dependent nature of the Stra8 RA response, HOTs patterning experiments were assessed using this responsive marker.

.

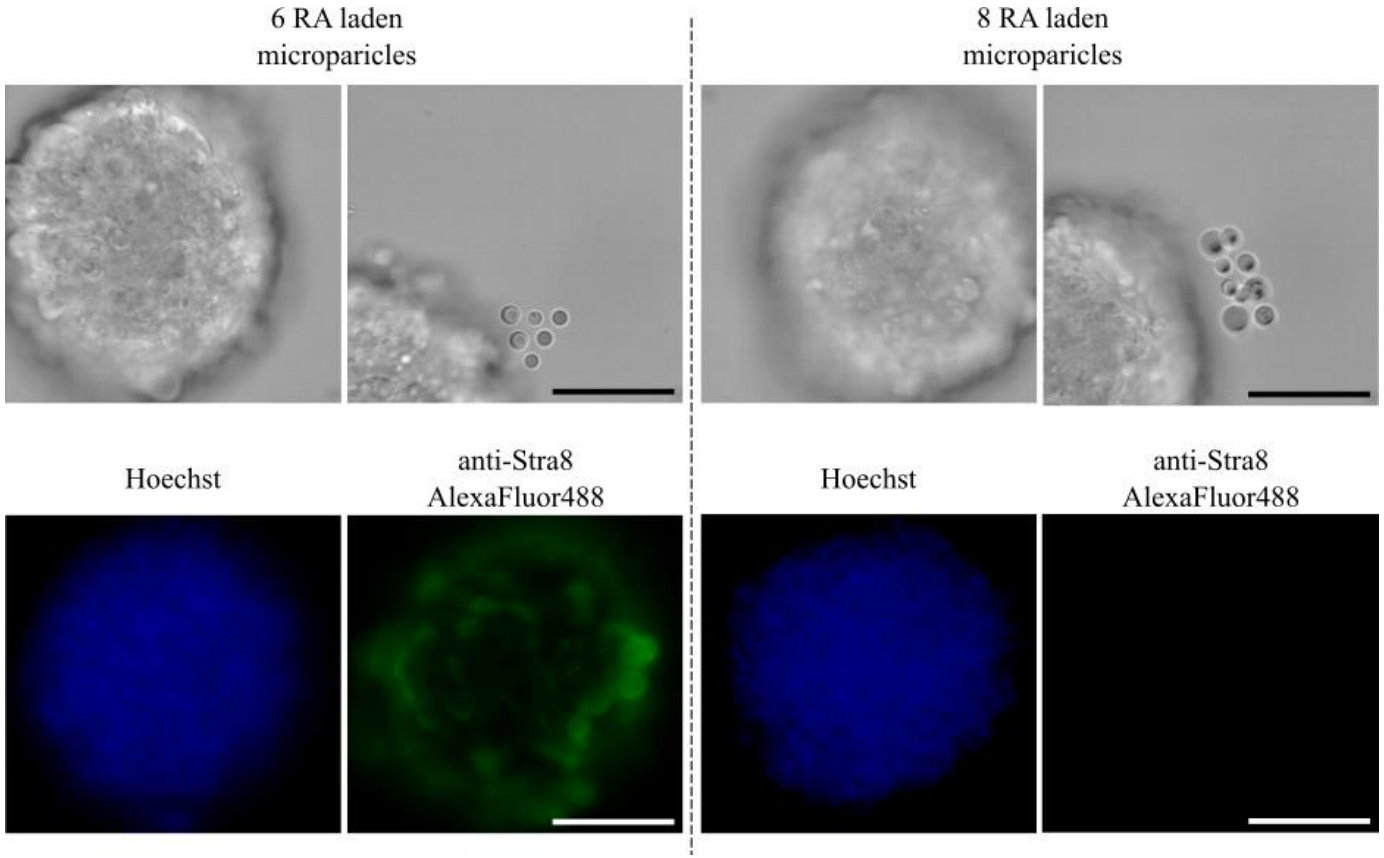

Figure 5.9 HOTs patterned RA microparticles for zonal stimulation of Stra8 in mES aggregates

A. Bright-field micrographs showing the GelMA stabilised 6- and 8-microparticle patterns around mES cell aggregates with a HOTs patterning platform. B. Fluorescence micrographs of the Stra8 immunocytochemistry stained mES cell aggregates seen in A with Hoechst counter-staining. Scale bars represent 50 µm

Figure 5.9 shows two HOTs patterned RA microparticle experiments; using a six and an eight microparticle release source pattern respectively. The mES aggregates were fixed and stained according to the method detailed in Section 2.7. The figure shows the Stra8 staining identifying the cells that have responded to the released RA. The figure shows that variable success was observed with the experiment, the success of the experiment was not dependent on the number of microparticles used but in experiments that gave positive results, the Stra8 linked fluorescent signal was elevated in close proximity to the microparticle release source. This positive result gave us confidence that the general principle of the experiment was working, but that another element of the mechanism was causing problems and variable results. The initial plan was to vary the microparticle number to achieve different responses, however, results were observed irrespective of microparticle number (Figure 5.9), and this approach was changed.

Figure 5.8 details two representative experiments using HOTs to position RA-laden microparticles in close proximity to the mES cell aggregate. The 6-microparticle pattern was repeated (n=4) and a Stra8 response was only visualised 2 in the 4 experiments. Due to the basic fluorescence based optical microscopy used to analyse the immunocytochemistry staining, it was difficult to assess cell aggregates effectively due to the thickness of the sample. Furthermore, comparison between the aggregates was difficult because Stra8 varied depending on the focal plane being viewed. These issues were addressed and were discussed later in this chapter and detailed in Section 2.10.1.

5.4.10 RA microparticle optimisation

The conventional regimen of polymer microparticles for drug delivery is typically accomplished with large numbers of microparticles giving a bulk release. Estimation of encapsulation efficiency, one common tool for analysing microparticle batch characteristics, is only appropriate for providing details on the quantity of loaded cargo within a given mass. However, for the uses detailed in this project, microparticles have been used in much smaller numbers. The use of conventional estimation of encapsulation efficiency tests may not be suitable for such individual microparticle use (

Figure 5.7) as it relies upon all the microparticles being used having the average molecular cargo loading as the entire batch. The current assessments for protein content by BCA assay (as described in Section 2.9.5) and RA by absorbance worked well for calculating supernatant concentrations, however these techniques would not be sensitive enough to analyse such low concentrations as released from the singular microparticles used for HOTs patterning.

A solution was devised that would allow calculation of loaded molecule, in this case RA, by fluorescence intensity of a co-loaded fluorophore. As previously described, the RA microparticles were formulated with HSA to increase refractive index and act as a carrier for active cargo. Instead of adding a further component to the formulation, a fluorescent albumin was used, FITC-BSA. The hypothesis was, that the level of fluorescence would be proportional to the level of co-loaded active cargo (RA). Even very low concentrations of FITC-BSA can be detected by flow cytometry and advanced microscopy techniques so even an individual microparticle should yield a measurable fluorescence.

5.4.11 Fluorescence-based analysis of individual microparticle encapsulation

PLGA:TBIIF (70:30) microparticles loaded with FITC-BSA and RA were fabricated as previously described (Section 2.9.1) and were fully characterised (Figure 5.10).

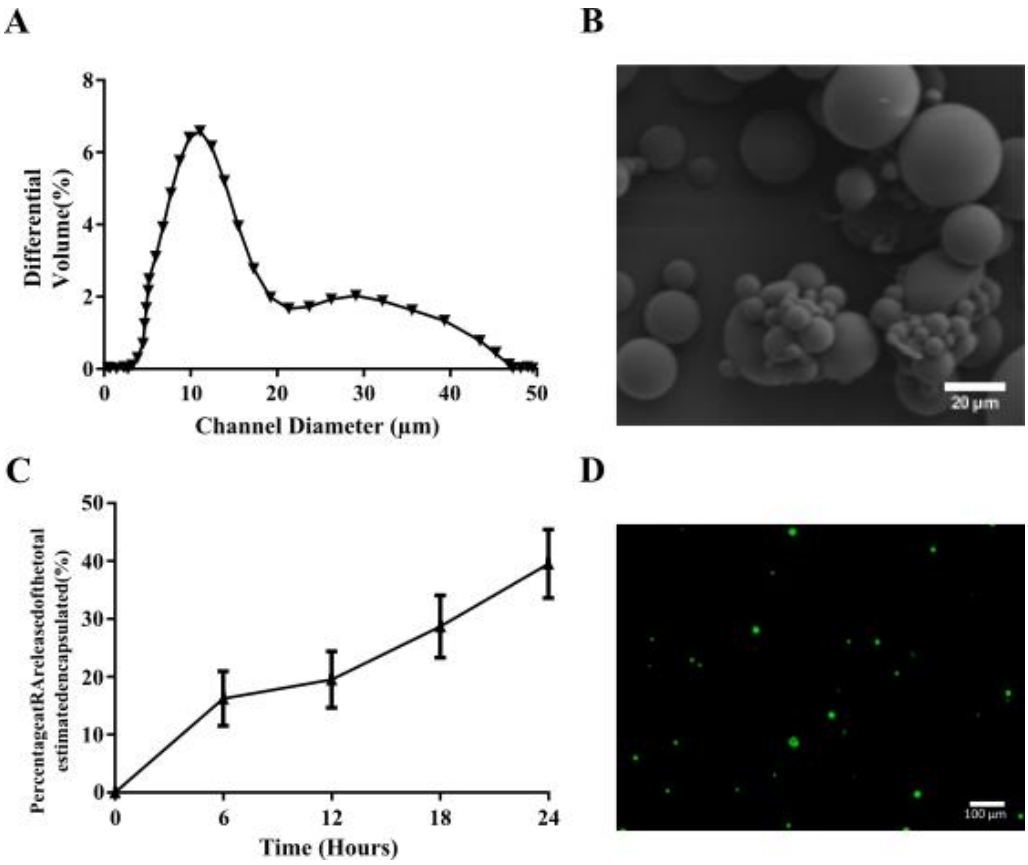

Figure 5.10 Characterisation of FITC co-loaded RA microparticles

A. Microparticle size distribution by differential volume assessed by coulter analysis of the RA microparticle batch B. SEM micrograph of the FITC co-loaded RA microparticles to show morphology and to validate the coulter analysis data C. 24 hour *in vitro* release study with time-points every 6 hours, points are the mean from triplicate samples of the microparticle batch with error bars relating to cumulative standard error of the mean. D. Confocal micrograph of the FITC co-loaded RA microparticles in an attempt to quantify the FITC loading within each microparticle in the field of view.

Figure 5.10 A shows that the batch had an average diameter of 13.5 µm, and as before (

Figure 5.7 C), the 15% polymer formulation batch yielded a similar estimated encapsulation efficiency, in this case 79.2 ± 1.3%. As expected, SEM (Figure 5.10 B) and *in vitro* release studies yielded similar results to the characterisation

of the RA batch 1.0 (Figure 5.6) showing that the incorporation of FITC-BSA made no profound effects of the microparticle morphology and release kinetics. Figure 5.10 D shows a confocal fluorescence based micrograph of the FITC-BSA co-loaded RA microparticles, and the encapsulated FITC-BSA is clearly visible as shown by the green fluorescence. The level of fluorescence was very low for all of the microparticles and long 2 second exposures were required for visualisation. The long exposure requirements meant that calculation of fluorescence intensity by microscopy would not be suitable.

5.4.12 FACS selection of highly loaded microparticles

However, the levels of fluorescence within the microparticles would be easily assessed by flow cytometry and the method would significantly raise through put of the analysis. From the microscopy of the FITC-BSA laden microparticles, it was observed that there were great differences in fluorescence intensity within different microparticles of the same diameter. This observation supported the idea that microparticle loading was variable and that some microparticles contained less than the required amount of FITC-BSA for microscopy-based visualisation.

Flow cytometry is commonly used in cell biology to assess the fluorescent labelling of cells, cells can be characterised into different sub groups or populations by antigen based fluorescent labelling. Different cell populations can then be sorted from a heterogeneous mix based on the levels of fluorescence intensity relating to expressed protein markers. Such cell sorting is completed by FACS and the principles of it could be used to separate the fluorescent FITC-BSA laden RA microparticles based on their individual fluorescent intensity. As

described in Section 5.3.8, flow cytometry analysis and subsequent sorting of the microparticles was completed.

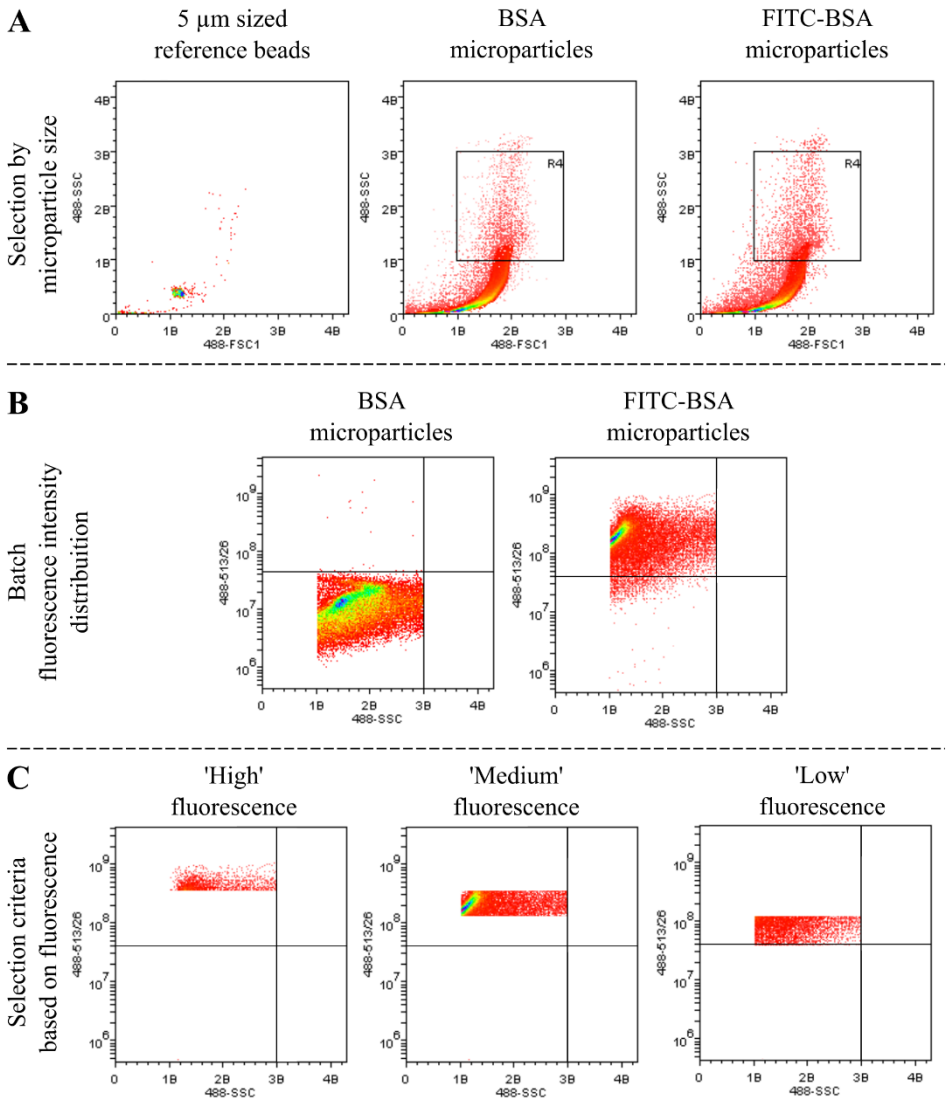

Figure 5.11 Analysis and sorting of the FITC co-loaded RA microparticles

FITC co-loaded RA microparticles were analysed using FACS, A. FACS analysis by means of SSC vs FSC1 to gate for appropriately sized microparticles based on the 5 µm reference beads. B. The R4 gating plotted as SSC vs fluorescent intensity (488-513/26nm) C. Representative images of the sorting gating were used to yield high, medium and low fluorescent intensity microparticle groups.

Figure 5.11 outlines the analysis and selecting the FITC co-loaded RA microparticles to yield 3 different groups of microparticle fluorescence intensity ('High', 'Medium' and 'Low'). The microparticles were initially gated based on their size vs 5 µm reference beads, assessed by forward and side scatter (Figure 5.11 A). As a means of comparison, the non-fluorescent RA laden microparticles were also analysed to provide base line fluorescence intensity. The use of these microparticles as a control ensured that any RA or polymer autofluorescence would be normalised from the FITC labelled batch. When comparing these two batches in the 'Batch fluorescent intensity distribution' (Figure 5.11 B) it can be seen that the FITC co-loaded batch yield a much greater fluorescence intensity. Interestingly, there is still an overlap with a small proportion of the FITC co-loaded batch yielding very low and no fluorescence. This result supports the theory that the loading of these microparticles is non-uniform and could have been the cause for earlier reduced success rate in HOT patterned RA laden microparticle experiments (Figure 5.9). The range of fluorescence intensity recorded from the FACS analysis of the FITC co-loaded RA microparticles was significant. In order to test whether the fluorescence readout was reporting appropriately on RA loading, further gating was applied. Three separate groups were created to select for 'High', 'Medium' and 'Low' fluorescence microparticles, as shown in the representative plots (Figure 5.11 C). Then by running a high density suspension of the FITC co-loaded batch through the FACS process, the 3 separate suspensions ('High', 'Medium' and 'Low') and any sub-'Low' microparticles were separated.

5.4.13 Analysis of the FACS selected ‘high’ loading microparticles

The separate suspensions sorted by FACS were digested as described in Section 2.9.4, and were assessed for both RA and BSA loading as previously described. If the hypothesis that RA loading would occur in a proportional manner to that of FITC-BSA, the sorted groups would yield corresponding levels of RA and FITC-BSA.

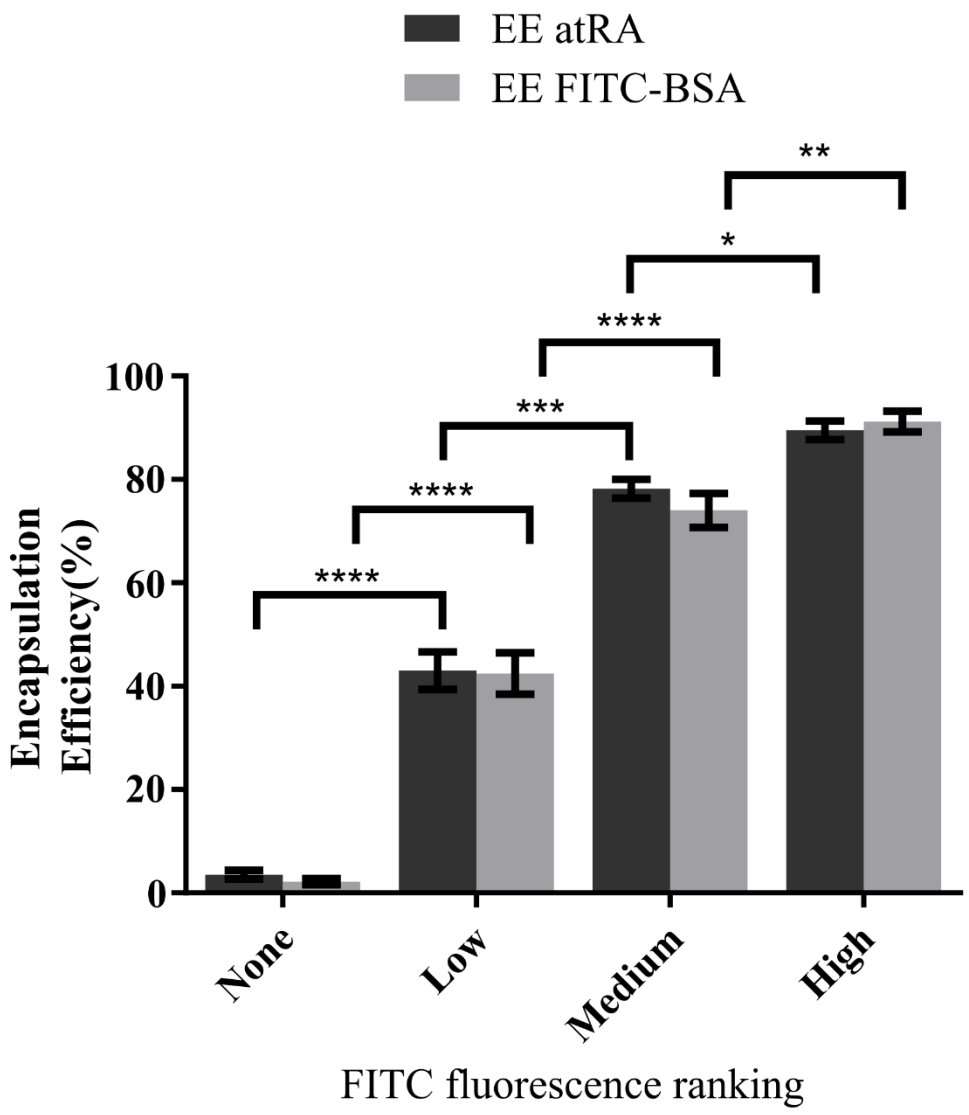

Figure 5.12 Post-sorting encapsulation analysis of the FITC co-loaded RA microparticles

A plot showing the estimated encapsulation efficiency by means of protein (FITC-BSA) and RA loading of the four sorted microparticle groups. Bars relate to the mean encapsulation efficiency from triplicate with error bars showing standard error of the mean. T-test analyses were performed and the significant difference was indicated accordingly, **** = <0.001, *** = 0.0045, *** = 0 01 and * = 0.0253.

Following FACS based sorting of the FITC co-loaded RA microparticle batch (Figure 5.11), the plot above (Figure 5.12) shows that FITC fluorescence is paired with encapsulation efficiency of both BSA and most importantly RA. Where sub-'Low' fluorescence was observed, only very low encapsulation was recorded. With increased FITC fluorescence, greater RA is estimated to be encapsulated within the batch. The triplicate results obtained gave to low standard error about the mean, especially for the 'Medium' and 'High' groups, indicating that variation within these groups is low. Furthermore, the 'High' group is estimated to have an encapsulation efficiency of 89.5 ± 1.8%, almost 10% higher that the unsorted batch encapsulation efficiency.

With both the increased encapsulation efficiency and the selection of 'High' loading microparticles, a more robust and refined release was expected that would benefit future HOT patterning experiments.

5.4.14 HOTs patterning 'high' loading retinoic acid microparticles

Following on from the first attempt to observe a biological zonal response to a HOT patterned microparticle based delivery of RA to a mES cell aggregate, a repeat experiment was designed. Using the 'High' loading FITC-BSA RA microparticles developed previously, HOTs patterning shown in Figure 5.9 was repeated as described in Section 2.8.1. In this round of HOTs patterning, only 6-microparticle triangular patterns were formed using either FITC BSA RA microparticles or 'Blank' BSA microparticles as a negative control. Further to optimisation of the release source, the method of analysis was adapted. Figure 5.9 demonstrated, amongst other things, the need for more advanced microscopy to properly analyse the mES aggregates. As described in Section 2.10, confocal

microscopy was used to obtain multi-stacked images of the mES aggregates labelled with nuclear staining (Hoechst) and AlexaFluor conjugated secondary antibodies. Initially, AlexaFluor488 was used for binding anti-Stra8 antibodies as shown previously, however the penetration of short wavelength light (405nm) to excite the fluorophore would not penetrate well through the dense mES aggregate leading to falsely weaker signals on the underside of the aggregate. To improve this, a longer wavelength AlexaFluor546 was used for aggregate staining that improved the issue. Image acquisition was completed as described in Section 2.10.1.

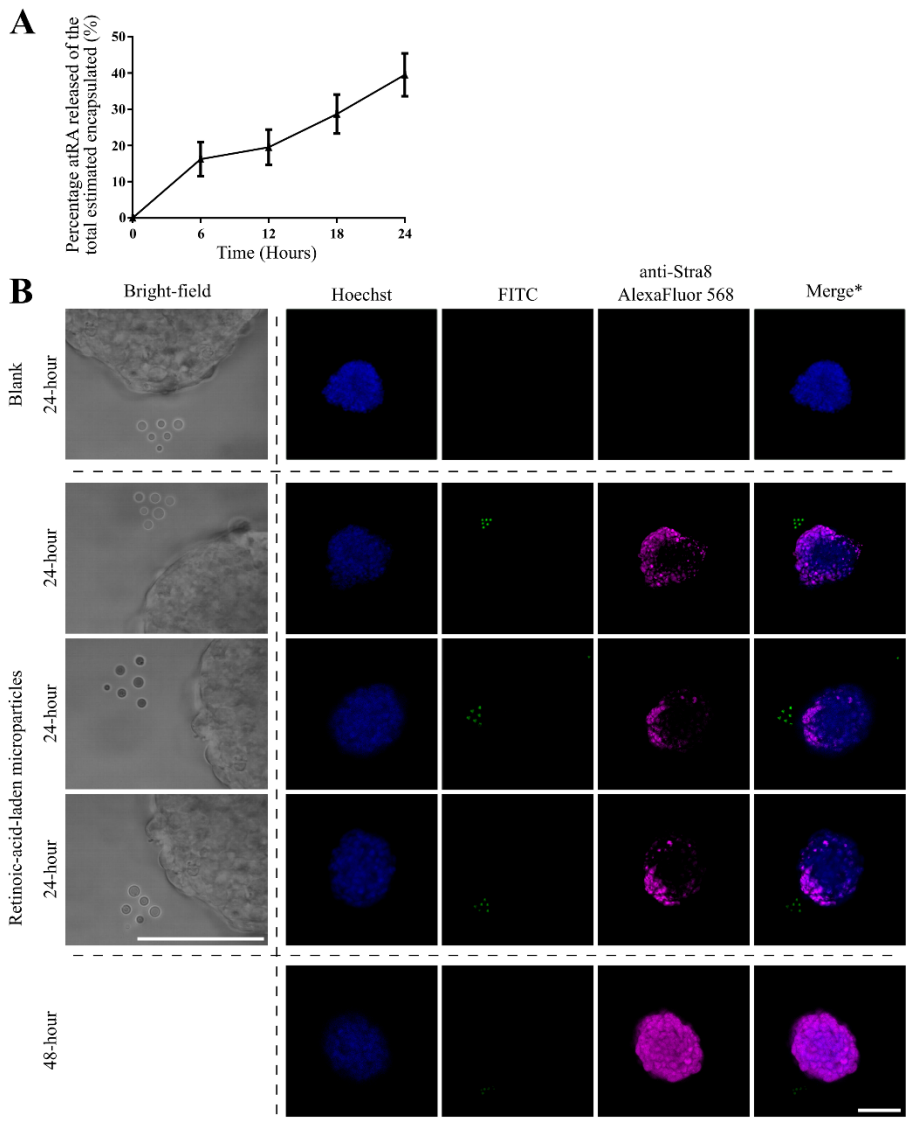

Figure 5.13 Zonal delivery of retinoic acid to an mES cell aggregate

A. Plot of the *in vitro* release study completed over 24 hours for the release of retinoic acid from retinoic acid encapsulated microparticles. Error bars represent the cumulative standard error of the mean. B. Micrographs showing the positioning of 6 retinoic-acid-laden microparticles arranged into a triangular structure in close proximity of the mES cell aggregate with the HOTs patterning platform, and the subsequent immunocytochemistry analysis of the Stra8 protein expression at 24 hours and then a 48-hour time-point. For clarity, the fluorescence images have been adjusted, including brightness, contrast and colour balance processing applied to the whole image. * 'Merge' images are purely representative, the FITC channel was acquired from a slightly different z position. Scale bars represent 50 µm.

The RA zonal patterning experiment (Figure 5.13) was designed to show that a source of RA can be encapsulated in controlled released microparticles, and then positioned in such a way to create a zone of RA. Figure 5.13 A is a plot showing the release of RA from the FITC-BSA co-loaded RA microparticles (Pre-sorted) over 24 hours. By the 24-hour point 39.5 ± 5.9% of the loaded RA will have been released, and it was estimated that in the small volume surrounding the release source, concentrations would be sufficient to illicit a Stra8 response. Whilst the FITC selection of these microparticles has improved the uniformity of the microparticle loading, further variation could still be uncontrolled. The microparticles were initially suspended in PBS for FACS for up to an hour, this hydration of the microparticles would have initiated breakdown and release of RA. During optimisation of the sorting protocol, the 'suspension time' was reduced to 30 mins; however it would still be negatively affecting the release kinetics. Due to the high cost associated with FACS and the relatively slow throughput (~30,000 microparticles/second), it was not deemed appropriate to complete *in vitro* release studies post sorting. Figure 5.13 A displays the pre-sorted release study, and shows that the 'suspension time' of 30 minutes would account for an estimated loss of ~3% of the encapsulated RA.

Using Stra8 as a marker for successful RA response, it is shown that mES Stra8 protein is being highly expressed on the proximal sides of the aggregate to that of the RA release source. In the representative bright field based micrographs (Figure 5.13 B), 4 differently positioned 6-microparticle triangular RA release patterns are formed in close proximity (>20 μm) to the mES cell aggregate. The pattern is stabilised by means of GelMA cross-linking as described in Section 4.3.6. Fluorescence microscopy (Figure 5.13 B) shows the Hoechst stained mES

cell aggregate with either the absence of FITC fluorescence in the case of the negative control (Blank) or fluorescent FITC labelled RA laden microparticles in the experimental samples. Anti-Stra8 AlexaFluor546 antibody fluorescence (Magenta false colour LUT) represents the location of Stra8 protein. The presence of magenta fluorescence corresponds with the position of the RA release point indicating that the RA has been delivered in a zonal manner. The ability to control the regional expression of Stra8 protein by means of HOTs based patterning of a RA signal is proof of concept for the technology. Figure 5.13 B shows that delivery of small bioactive molecules in a highly spatially controlled manner can be achieved. The implications of this are profound, complex spatial and temporal characteristics of developmental signalling can be controlled using this technology. Through the use of sorted 'High' loading RA microparticles, experimental success was raised greatly from the 50% (n=4) to 80% (n=5) Stra8 responding aggregates with the use of FITC sorted RA microparticles. Longer wavelength fluorophores (AlexaFluor546) and a refined confocal imaging protocol yielded zonal responses in 80% of experimental replicates.

Whilst the experiment (Figure 5.13) demonstrates the potential of the technology for use as a tool for patterning molecular gradients, there are still areas that need to be developed. The figure details the outcome of zonal delivery at the 24-hour time-point and it as expected this zonal delivery was not be maintained for longer culture periods. In the 48-hour time-point there is complete staining across the whole aggregate, showing that the static system of release will be suitable for certain applications but not others where a stable and long-term gradient is required. Whilst this is not a drawback of the experiment, it means that use of

the technology for different applications could require new delivery vehicles to be optimised to suit the specific signalling dynamics.

The visualisation of RA-induced Stra8 protein on the proximal side to the release source is a good validation of the zonal release of RA. Further work to quantify the solute gradients formed would provide a greater level of control over the formation of spatio-temporal signalling. However, the quantification of such gradients has been a great challenge. Certain mathematical modelling work has shown great promise in understanding how solute gradients are formed within a hydrated environment [238]. Use of such modelling approaches would be appropriate for understanding the HOTs delivery of solutes from microsources, but such development was not within the scope of this thesis.

5.5 Conclusions

This chapter details the development of the HOTs platform as a means to micropattern signalling dynamics in small cell architectures. Previous proofs of concept have shown that the local delivery of fluorescent molecules that simply rely upon the viability of the cells is possible. Now the ability to precisely deliver molecules that bring about the induction of protein expression in response to a bioactive molecular gradient has been demonstrated. This developmental progression is significant as it shows that the platform can be adapted to suit the highly specific signalling dynamics of different cell models.

The development of a FACS based screening method for assessing individual microparticle loading has been essential for the development of the HOTs patterning setup. Use of this selection method ensures that appropriate amounts

of release source are used, and the reduced variability in microparticle loading ensures that replicated experiments are comparable.

Whilst the RA induced mES Stra8 model demonstrated in Figure 5.13 is not of direct biological significance in itself, the ability to successfully deliver a diffusible signal to a precise area of a cellular aggregate is highly relevant. As previously discussed, appropriate regulation of the developing embryo requires exquisite control over the signalling dynamics and gradient. The HOTs patterning setup development discussed in this chapter details how such zonal signalling can be achieved to fabricate *in vitro* developmental models. This technological advancement is directly appropriate for investigating such developmental microenvironments.

The successful and robust zonal response supports the hypothesis discussed in Section 4.5.1 relating to burst kinetics forming a zone of concentrated signalling molecule around the patterned molecule. Whilst this is a highly suitable characteristic for certain applications, it may not be suitable for models requiring constitutive signalling. To enable longer term signalling (>48 hours) different blends of PLGA, including PLGA 85:15 [119] could be used for sustained release profiles. Alternative encapsulation methods could also be used to deliver tailored signalling dynamics so long as they are suitable for optical manipulation. An alternative encapsulation method is described later in this thesis (Chapter 6).

6. Results – HOTs based chemotactic coordination of primary osteoblasts

6.1 Introduction

The flexibility of polymer microparticles for tailoring release kinetics to suit the specific needs of an experiment make their use with the HOTs very interesting. However, as previously discussed, there is a great amount of optimisation required to fabricate them appropriately. The demand for better methods to develop localised signalling for developmental biology and tissue engineered cell models is great. Principally, this is due to the known importance of locally secreted molecules in early development and during cell migration [187,214,239] . The state-of-the-art in this field is defined by the use of simple hydrogel-based release simple hydrogel-based release sources such as agarose, alginate, and gelatin beads. These hydrogel beads can be soaked in the molecule of interest, and then used as a point of release for an investigation as the encapsulated molecule leaches out by diffusion. Whilst there are many drawbacks to this method of delivery, its simplicity has meant that it is often used by investigators wanting to demonstrate a basic localised release model [240,241]. Agarose beads have been used with great effectiveness in *in vitro* studies of cell signalling, their use was essential in elucidating of the role FGF9 plays in testis development

[242,243]. In this chapter, it is described describe how such simple localised delivery systems can be used with the HOTs platform to achieve greater control over signalling precision.

6.1.1 Bone remodelling and localised release

Every bone in the body is metabolically active, and undergoes continuous remodelling throughout life. Remodelling of the bone involves the osteoclast-mediated removal of mineralised matrix, followed by the formation of new mineralised bone, facilitated by osteoblasts [244]. Bone remodelling is required to repair the skeleton and adjust the skeletal architecture to meet new mechanical needs. Osteoblasts and osteoclasts regulate the homeostatic process of bone remodelling through the formation of a basic multicellular unit with one another [245,246]. The recruitment of these cells to areas requiring remodelling occurs predominantly by localised signalling within the trabecular bone. The interplay between osteoblasts and osteoclasts is an interesting area of study, particularly from a localised-release point of view. Recent research has shown that osteoclasts control the recruitment of osteoblasts via chemotaxis and the release of various signalling molecules, including PDGF-BB [247].

The study of chemotaxis-driven cellular migration is often accomplished using a Boyden chamber [107]. This method assesses the proportion of cells that migrate through a matrix to an area of chemoattractant. Use of the Boyden chamber gives a high-throughput analysis of cellular migration, and it is suitable for many investigations. However, it is not capable of performing in-depth analysis of single cell migration and chemotaxis. Furthermore, there is currently no technology available that would be suitable for enabling the control of soluble

molecule delivery on the micron scale. The HOTs platform would be a highly suitable technology to facilitate the investigation of single cell chemotaxis to precisely positioned release sources.

6.1.2 HOTs platform for directing osteoblast chemotaxis

As well as showing that HOTs-based positioning is capable of working with simplistic localised delivery sources, the HOTs platform has not yet been demonstrated to direct cellular migration. The technology is highly suited to replicating the precise signalling dynamics required to direct cellular chemotaxis. The osteoblast recruitment model is one biological event that could be recapitulated with the HOTs patterning setup, demonstrating its breadth of applicability to *in vitro* cell-based model creation. A patterning tool that can create biomimetic microenvironments closely approximating natural conditions is a greatly sought-after technology. Whilst the HOTs can improve the current options for micropatterning resolution and the propagation of dynamic signalling, this thesis has not discussed the use of more representative cell types of the *in vivo* environment. It has been shown that even the most representative MC3T3 cell line [248] of pre-osteoblastic cells do not accurately represent the behaviour of primary osteoblast cells [249]. Therefore, for the work in this chapter, primary cells were used to demonstrate the applicability of the HOTs with more sensitive cell types that are more representative of the *in vivo* environment.

6.1.3 Concentration gradient analysis

An ongoing limitation for the development of the HOTs patterning platform for creating localised delivery models is the inability to quantitatively measure the

concentration of released solutes. The difficulty is predominantly due to the very low solute concentrations being present in a highly dynamic environment. This makes it difficult to assess at the resolution required. Recent work has shown that solute gradients can be assessed on the mesoscopic scale by taking frozen sections from the area around the release source to assess exact concentration at different distances and time-points [215]. However, this method would not be suitable for the resolution required here. There have been attempts to model the solute gradients formed from individual polymer microparticle release, and these methods have shown great promise over the micron-scale assessment [238]. However, such modelling needs to be developed further to factor in the mobility of solutes over longer time periods. In this chapter the approach to assess protein gradients in hydrated hydrogels using Time-of-Flight Secondary Ion Mass Spectrometry (ToF-SIMS) is discussed. ToF-SIMS measurements give molecular information from the surface of solid materials with an ultimate spatial resolution of less than 0.1 μm. ToF-SIMS is accomplished by exciting a sample with a finely focused ion beam which yields secondary ions and clusters to be emitted from the sample. A time-of-flight analyser then measures the exact mass and intensity of the emitted secondary ions and clusters. From these measurements, the identity of the molecular fragments can be determined, and then their concentration can be calculated. Classically, only thin hydrogels and polymers are analysed via ToF-SIMS, however, new innovative methods have been devised that allow the analysis of thick hydrated samples [250]. In this chapter, the application of this new method for the purpose of analysing the solute content in hydrogels following agarose bead localised release.

Chapter Experimental Overview

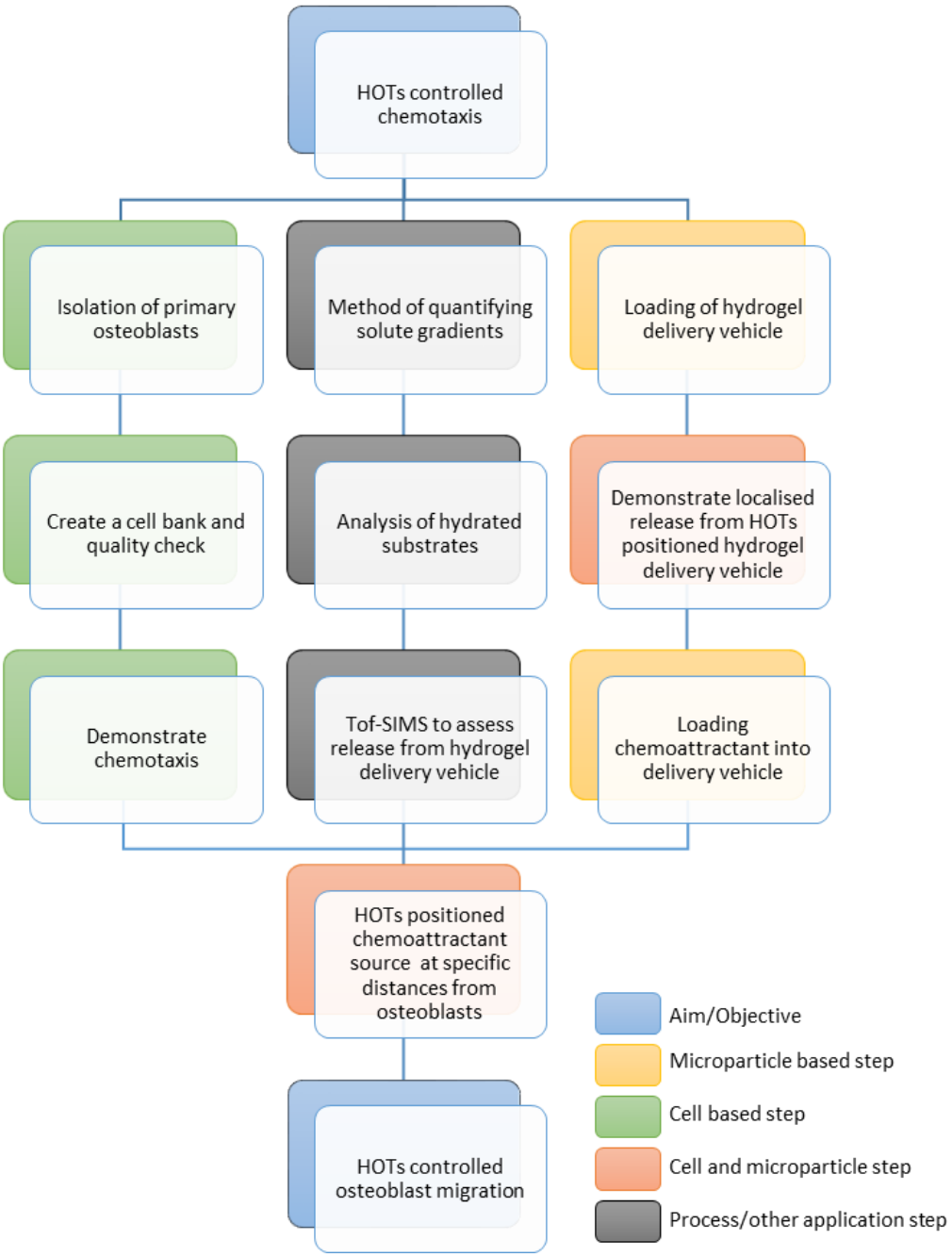

6.2 Materials and Methods

6.2.1 Osteogenesis differentiation

mPC cells were reanimated from cryopreservation and cultured to passage one or two, as required in standard tissue culture flasks. Trypsin/EDTA was used to detach the cells, and they were counted using a Neubauer haemocytometer, as described previously [251]. mPC cells were then seeded into tissue-culture-treated well-plates at a density of 1.1 $x10^4$ cells / cm^2 and incubated overnight at 37°C to ensure adherence. The culture medium was then changed to osteogenic medium by supplementation of mPC medium with 50 µg/mL ascorbate-2-phosphate, 50 mM β-glycerophosphate disodium salt hydrate and 1 µM dexamethasone. Cells were incubated for the desired time-period (typically 7, 14, or 21 days) with medium changes every 2-3 days.

6.2.2 Mineralisation assay

The mineralisation of cell-secreted matrix was assessed by alizarin-red staining of calcium deposits. Formalin (10% w/v) was used to fix cell monolayers for storage prior to the mineralisation assay. Fixed monolayers were washed twice in dH_2O before being treated with alizarin-red staining solution (TMS-008-C, Merck Millipore, UK) for 5 minutes before the alizarin-red solution was removed and cultures were washed repeatedly in dH_2O until no colour was leached out. Staining was then imaged according to Section 2.10.

6.2.3 IBIDI chemotaxis

The µ-Slide Chemotaxis ^{2D} (Thistle Scientific, UK) was used for assessing chemotaxis of mPC cells to PDGF-BB gradients. Cells were trypsinised and counted as usual, before dilution to $3x10^6$ cells/mL. Of the resultant suspension, 6 µL was added to one of the filling ports while the reservoir ports were plugged. The cell suspension was flushed across the entire observation channel by aspirating 6 µL from the other filling port. All filling ports were then covered with cultivation caps and incubated at 37ºC for 4 hours, allowing cells to attach to the tissue-culture-treated surface of the slide. The reservoirs were then filled with 80 µL of mPC culture medium before 18 µL of PDGF-BB was added to one chamber. To achieve a concentration of 10 nM PDGF-BB in one of the chambers, 18 µL of 25 nM PDGF-BB was added to yield a 10 nM solution in stable gradient equilibrium.

6.2.4 Tracking and analysis software

The loaded µ-Slide Chemotaxis ^{2D} was then imaged using phase contrast time-lapse microscopy in an environmental chamber, as detailed in Section 2.10, with acquisition settings of a micrograph every 15 minutes over and 8-hour time-period. Time-lapse experimental data were assessed in ImageJ (NIH) and the MTrackJ plugin was used to manually track the cells within the field of view. Track data was then input into the Chemotaxis and Migration Tool (IBIDI GmbH, Germany) to analyse the net migration and Forward Migration Index (FMI) (Figure 6.1) [252].

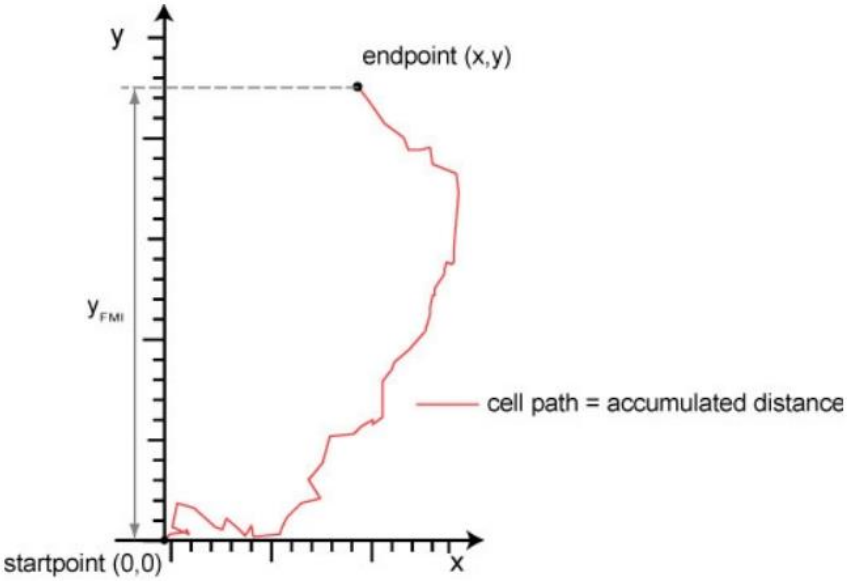

FMI (Forward Migration Index):

$$x\,FMI = \frac{x_{FMI}}{accumulated\,distance} \qquad y\,FMI = \frac{y_{FMI}}{accumulated\,distance}$$

Figure 6.1 Calculation of the Forward Migration Index

Diagram showing how a typical cell migration track can be analysed to rank the migration towards a point. The equations show how the x- and y- Forward Migration Indexes can be calculated.

6.2.5 Optimisation of agarose beads for optical manipulation

Agarose beads (Agarose Bead Technologies, UK) were lyophilised using a freeze dryer (Edwards Modulyo D, IMA Edwards, UK) and were then washed in dH_2O to remove any hydrochloric acid preservative. The washed beads were then lyophilised once more and re-suspended in different soak solutions. Initially, dH_2O-soaked beads were tested, but for optimisation purposes beads were also soaked in either BSA, calcein green AM or α-chymotrypsin depending on their use.

A range of BSA concentrations were used to optimise optical trapping of agarose beads, ranging from 0-10 % (w/v) BSA. For the release study, α-chymotrypsin was used as a soak at a concentration of 5 or 10% (w/v); α-chymotrypsin was used as a reference protein for the expensive PDGF-BB. 5% (w/v) BSA and 25 µM calcein green AM solution was used as a soak for visualising the release of HOTs-patterned agarose beads.

6.2.6 Agarose bead *in vitro* release study

The agarose bead *in vitro* release study was completed in the same manner as previously described for polymer microparticle release studies (Section 2.9.6). 25 mg of lyophilised agarose beads were soaked and then washed as previously described (Section 6.2.6). The washed beads were pelleted once more and re-suspended in 1.5 mL of dH_2O before incubation at 37°C. Hourly, supernatant was removed and frozen, and fresh dH_2O was added in its place. Supernatants were analysed for protein content by BCA assay as previously described (Section 2.9.5).

6.2.7 Agarose bead preparation for TOF-SIMS analysis

Agarose beads were lyophilised using a freeze dryer (Edwards Modulyo D, IMA Edwards, UK) and were then separated into 5 mg aliquots. These aliquots were suspended in a solution of 5 mg/mL α-chymotrypsin in dH_2O for soaking. Beads were left for 24 hours, soaking at room temperature to ensure complete diffusion into the beads. Prior to the use of the α-chymotrypsin-soaked agarose beads, they were pelleted by microcentrifugation (Sigma 2-16K, Scientific Laboratory Supplies Ltd.) at 3000 g for 1 minute. Supernatant was removed and the bead pellet was washed in dH_2O, a process then repeated twice further.

6.2.8 Hydrogel preparation for TOF-SIMS analysis

An aliquot of BSA-soaked agarose beads was washed as detailed in Section 6.2.5, and pelleted again at 3000 g for 1 minute. The beads were then re-suspended in 100 µL of polyethylene glycol dimethacrylate (PEGDA) solution. For the TOF-SIMS analysis of hydrogel proteins gradients, PEGDA (10%w/v) and Irgacure D2959 photoinitiator were kindly gifted by Mr Michael Taylor (University of Nottingham, UK). The suspension was vortexed (Stuart Scientific SA8, Scientific Laboratory Supplies Ltd.) to ensure an equal distribution of beads through the PEGDA solution. 10 µL of the suspension was then pipetted onto the hydrogel curing apparatus (described in Section 6.2.9), and a 12 mm diameter circular coverslip was added on top of the PEGDA suspension droplet. The coverslip was then held in place by a single piece of masking tape, and the hydrogel curing apparatus was inverted and placed on a UV lamp (Figure 6.2) for 2 minutes to allow agarose beads to settle onto the coverslip. The UV lamp was turned on for 5 minutes to ensure complete cross-linking of the PEGDA,

then the hydrogel sample was delicately removed from the hydrophobic Teflon surface to yield a pre-determined-depth (200 µm unless otherwise stated) flat hydrogel disc containing agarose beads distributed across the coverslip surface.

6.2.9 Hydrogel curing apparatus

The hydrogel curing apparatus was designed to create hydrogel disc samples that were suitable for TOF-SIMS analysis of BSA diffusion via a top-down approach. Agarose beads were distributed across the bottom of a hydrogel disc with gel above the agarose bead level to be analysed.

The base of the apparatus was a piece of Teflon that would yield a flat surface for the hydrogel disc, whilst permitting its removal once the PEGDA had been cross-linked. On top of the piece of Teflon, two sets of two 100-µm-thick glass slides were attached with masking tape to form a 200-µm-deep channel on top of the Teflon base. The channel was sufficiently wide to support the 12 mm circular coverslip. The 10 µL of PEGDA solution was then pipetted onto the Teflon base to form a droplet, and then the 12 mm circular coverslip was added on top, held 200 µm above the Teflon base, creating a column of PEGDA solution between the base and the coverslip, ready to be cross-linked to form a hydrogel disc of 200 µm in depth.

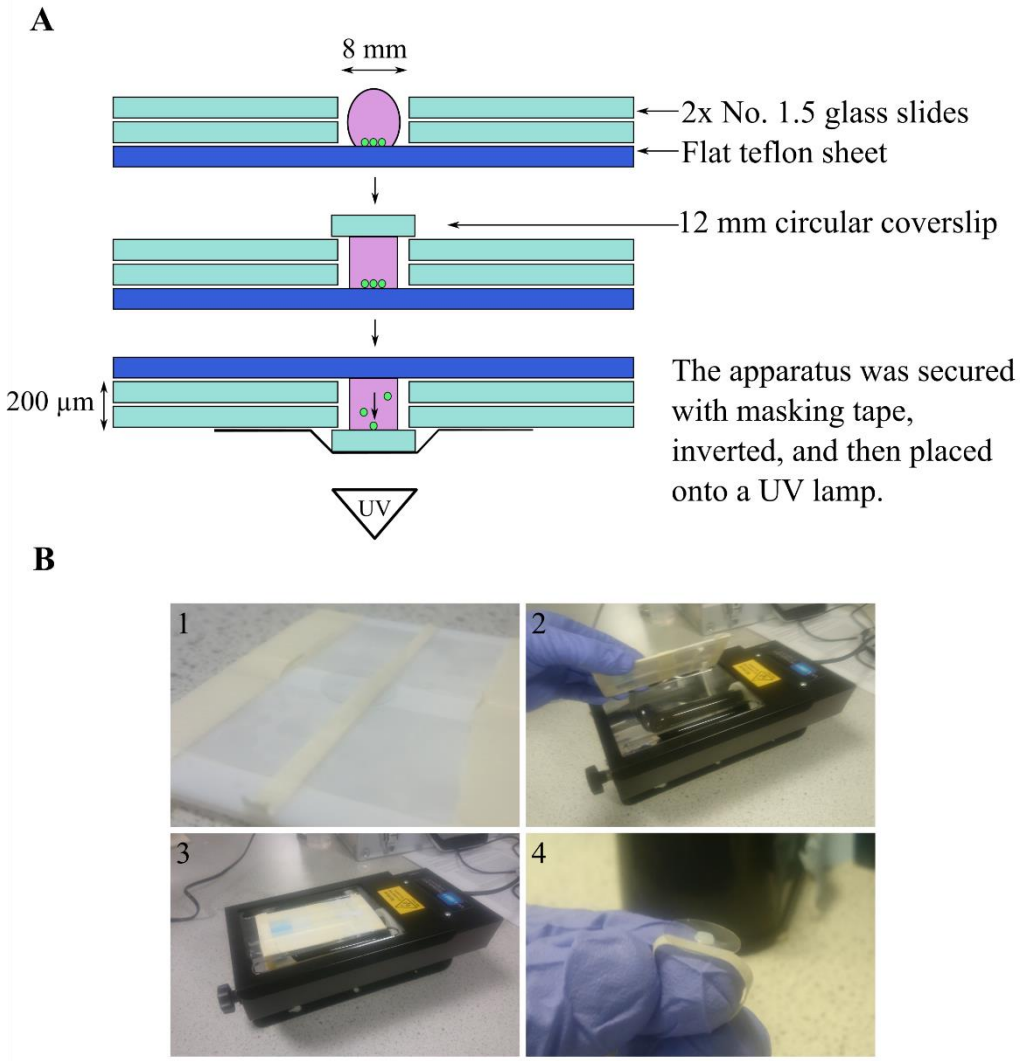

Figure 6.2 The hydrogel curing apparatus

A. Diagrammatic representation of the hydrogel curing apparatus and how hydrogel disks are UV-cured. The gel drop is placed on the Teflon sheet with the agarose beads, the coverslip is then placed on the drop and the apparatus is turned over so that the beads settle on the coverslip. B. Photos of the hydrogel curing apparatus; B1. The un-crosslinked hydrogel held in place on the hydrogel curing apparatus B2. Inverting the gel and placement onto the UV-source B3. Waiting for beads to settle on the surface of the coverslip B4. The hydrogel disk post-UV-crosslinking.

6.2.10 Agarose bead release study within hydrogel discs

Hydrogel discs were prepared with α-chymotrypsin-soaked agarose beads as described in Sections 6.2.9 and 6.2.10. The cross-linked hydrogel discs were then hydrated with dH_2O and left for the required time for that sample. Samples were collected hourly over a 6-hour release study to assess the diffusion of protein within the disc. Samples were snap-frozen and then analysed with ToF-SIMS to assess the protein content of the gel emanating from the release point (agarose bead layer). A standard curve was obtained by analysing PEGDA gels saturated with a known range of α-chymotrypsin concentrations (0.05, 0.5, 5, 50, and 500 µg/mL) and analysed in the same manner as previously described.

6.2.11 ToF-SIMS analysis

ToF-SIMS data were collected using a ToF-SIMS IV instrument (Münster, Germany) equipped with a bismuth liquid metal ion gun (LMIG) and argon cluster sputter gun. The analysis beam for this study was generated by a 25 keV bismuth source liquid metal ion gun utilising a Bi_3^{++} rastered over an area of 100×100 µm with 128×128 pixels. The target current was measured as 0.3 pA, with a total primary ion dose of $9.2x10^{10}$ ions/cm^2. A 10 keV Ar_{1455} cluster ion source was employed to etch through the sample over a 400×400 µm area. Rastering was performed in a non-interlaced mode with one frame of analysis and 3 seconds for sputtering per cycle. The corresponding beam dose was determined to be $6.84×10^{12}$ ions/cm^2. An argon beam target current of 9 nA was employed for all samples. A low energy electron flood gun was employed for charge neutralisation. Data processing was done with SurfaceLab6 (ION-TOF GmbH, Germany). Secondary ion assignments were selected by referring to a

reference database of secondary ions related to the components of the material analysed [253].

6.3 Results and Discussion

6.3.1 Primary osteoblast culture

Recent work has shown that primary osteoblasts are highly receptive to various chemoattractants involved in the bone remodelling process [247,254,255]. The first part of this chapter details the development of batch-tested mPC cells for HOTs patterning experiments. The mPC cells were extracted from the calvarial bone of 2-day-old mouse pup litters, and the osteoblast population of cells was separated as described in Section 2.5.5. To ensure that the cells obtained had osteoblastic properties and were suitable for culture and experimentation, quality checking was completed in the form of a mineralisation assay. The cells were differentiated as described in Section 6.2.1, and were assessed at the endpoint (21 days) for colony formation and mineralisation by alizarin-red staining (Section 6.2.2). Alizarin-red staining is a biochemical assay that indicates the presence of calcific deposition by cells. Alizarin forms precipitates with free calcium, allowing the identification of matrix mineralisation, a crucial step towards the formation of the calcified extracellular matrix associated with bone development. The presence of positive alizarin staining specific to areas of colony formation indicates that the mPC cells have osteogenic potential.

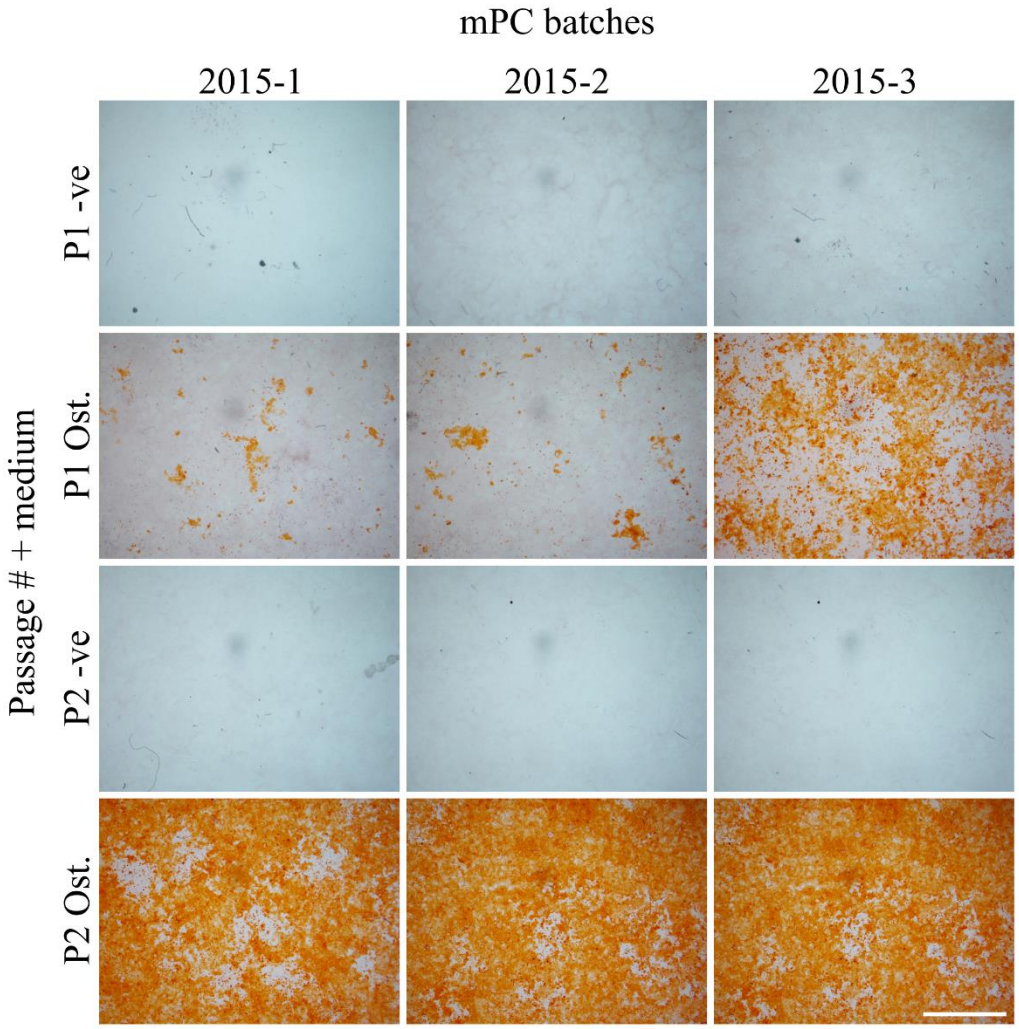

Figure 6.3 mPC quality check by mineralisation assay

Micrographs showing alizarin-red staining in three mPC batches (2015-1, 2015-2 and 2015-3) cultured under osteogenic conditions for 21 days. Cells from each batch were used at either passage 1 or 2 with or without osteogenic medium. Orange precipitate indicates the presence of osteogenesis-associated calcium deposits in areas of colony formation. The scale bar represents 0/5 mm.

Figure 6.3 shows the mineralisation assay that was used for quality control of the extracted mPC cell batches. Two passages were tested for each batch, a passage 1 and 2 sample was tested to show whether expansion through sub-culture would be suitable. The presence of weak orange staining for batches 2015-1 and 2015-2 passage 1 shows that these cells were not very responsive to osteogenic differentiation. However, batch 2015-3 yielded moderate staining well above the negative control, even at passage 1. All three batches gave strong mineralisation responses when differentiated from passage 2, as shown by the strong orange staining across the field of view.

The differential response observed between passage 1 and 2 mPC cells was most likely due to a culture-based priming of the pre-osteoblast population towards an osteoblast cell fate. Cell culture can have profound effects on the population as it is a form of selection for cells that survive those particular culture conditions. There may have been a greater percentage of these cell-culture-suitable cells in passage 2 compared to passage 1.

The responsiveness of these batches to osteogenic differentiation indicates that they are likely of pre-osteoblast or osteoblast origin. Although, their tendency to differentiate is not absolute proof of their chemotactic propensity, it is merely a positive sign. If the cells are of pre-osteoblast or osteoblastic lineage, as evidenced (Figure 6.3), it is likely that they will respond to bone remodelling recruitment signalling.

6.3.2 Cell viability of mPC cells during UV exposure

As previously described, the GelMA hydrogel system utilises potentially harmful UV light to cross-link the gelatin fibres into a hydrogel matrix, stabilising the HOTs-fabricated pattern. To ensure that the UV exposure is not detrimental to cell viability, a Live/Dead Cell Viability Assay assay was performed using a range of exposure times and assessment time-points.

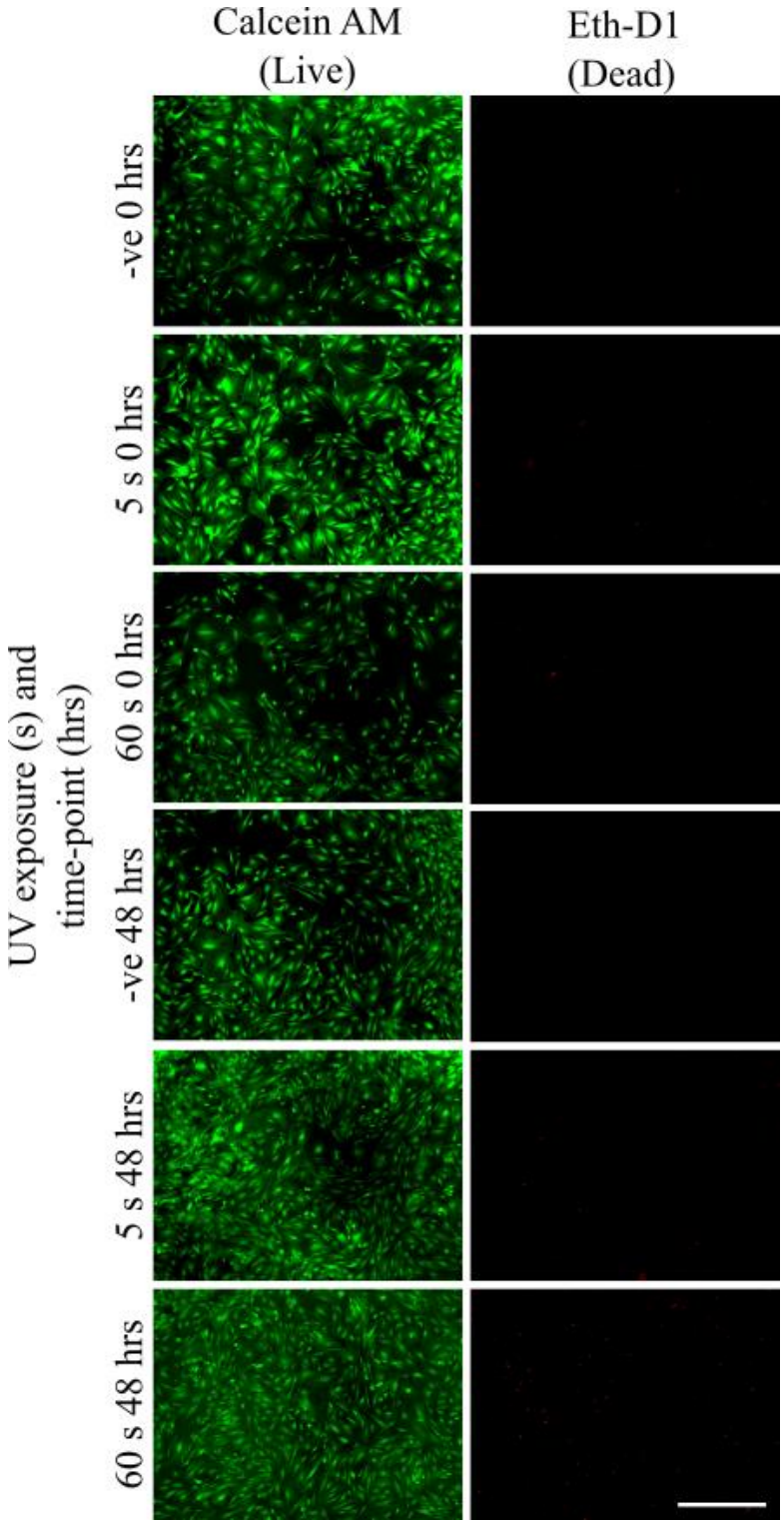

Figure 6.4 Cell viability of mPCs after UV exposure

Fluorescence micrographs of green live (calcein AM) and red dead (Eth-D1) mPC cells in a monolayer after exposure to UV light either 60s, 5s or 0s (-ve). Live/Dead viability assessment was completed at both the 0- and 48-hour time-point. The scale bar represents 50 µm.

The cell viability assay (

Figure 6.4) shows that cells remain viable at both the 0- and 48-hour time-points, even with the maximal UV exposure of 60 seconds. There are a large number of viable cells in all samples, however the number of dead cells does increase after UV exposure at each time-point with respect to the negative control. For all HOTs-based GelMA (10%) stabilisation, a 5-second exposure was sufficient to cross-link the small volumes in the patterning gaskets. If the GelMA volume was greater for the mPC cell patterning, a longer UV exposure time (~60 seconds) would have been required.

Figure 6.4 shows that this would lead to increased cell-death, as per the '60s 48 hrs' sample.

At 0 and 24 hours, samples were assessed to identify any latent cell-death caused by UV exposure. UV induces double strand breaks that can lead to lethal mutations. Such mutations can be repaired to prevent cell death, but they may still introduce mutations that could alter the cell genotype. Such genetic damage cannot be assessed by the LIVE/DEAD© cell viability assay, and so further assessment was required.

6.3.3 Mutagenicity assay after UV exposure

As previously described (Section 5.3.1), the mutagenicity assay by means of immunocytochemistry for γ H2A.X (phosphor S139) protein presence was completed for mPC cells exposed to a range of UV doses.

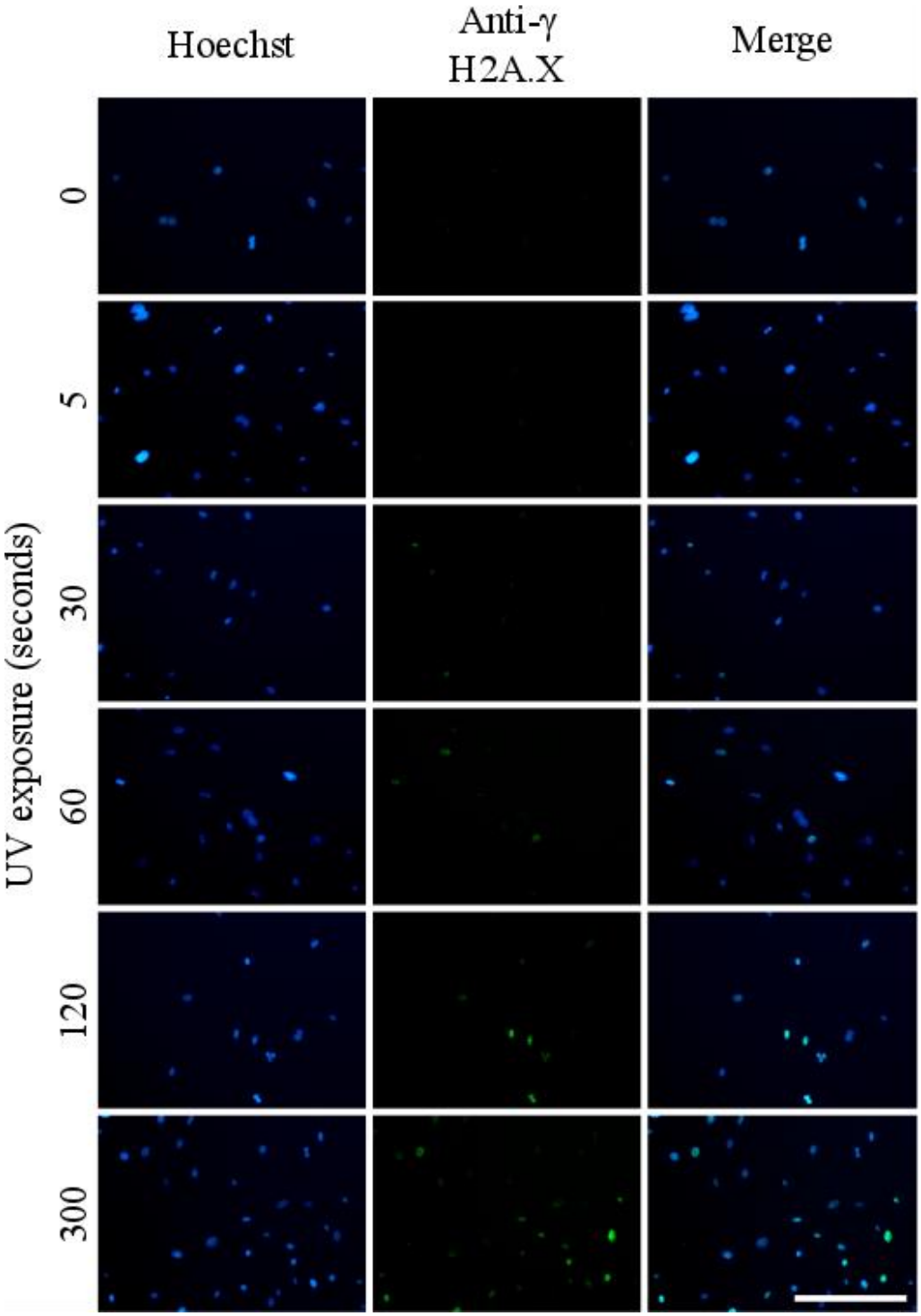

Figure 6.5 Mutagenicity assay for mPC cells

Fluorescence micrographs of anti-γ H2A.X (AlexaFluor488) staining in UV-dosed mPC cell monolayers at a range of different exposure times (0, 5, 30, 60, 120, and 300s). Hoechst was used as a co-stain to show localisation of the γ H2A.X to the nuclear region of UV-damaged cells. Merge column shows micrographs overlayed. The scale bar represents 50 µm.

The mutagenicity assay was completed at the 24-hour point, and a range of UV exposures were assessed. Figure 6.5 shows that DNA damage repair was occurring at a UV exposure of 30 seconds, with increasing presence of γ-H2A.X as the UV dose increased. Importantly, at 5 seconds there was no significant presence of DNA damage repair. The mPC cells were shown to be undamaged at the UV doses used for GelMA (10%) cross-linking, and so further use of the hydrogel stabilisation method could be employed. However, the results for

Figure 6.4 and Figure 6.5 show that such UV exposure can be highly detrimental to the mPC cells with respect to both cell viability and mutagenicity. Care must be taken when conducting further experiments with the cross-linking method, as UV-induced damage could greatly affect results.

6.3.4 Primary osteoblast chemotaxis

Following the successful assessment of the quality and viability of the mPC batches, it was important to show that they were responsive to chemoattractant signals. The HOTs investigation planned was to show that the HOTs can be used to position release sources containing osteoblast recruitment signals to control osteoblast chemotaxis. Therefore, it was necessary to show that the cells being used were capable of responding to such a signal.

As previously discussed, there are other methods available to test chemotaxis on a large scale, one such method that was deemed appropriate for this optimisation was the μ-Slide Chemotaxis ^{2D}. This method was chosen because the optimisation experiment could be completed in a similar manner to the planned

HOTs patterning investigation. Chemotaxis is measured across a collagen-coated surface from a sink to an area of chemoattractant that yields a gradient.

The mPC cell batches that yielded strong mineralisation after osteogenic induction (Figure 6.2) were used for subsequent chemotaxis experiments. The primary cells used in this investigation were likely to have comprised a heterogeneous mix of pre-osteoblast and osteoblast cells. For the chemotaxis optimisation, nascent non-induced cells were used at passage 2 and tested for their chemotactic response. Further to this, mPC cells were induced with 7 days of osteoinduction, as described in Section 6.2.1, to yield a more 'osteoblastic' population of cells. These '7-day differentiated' cells were also assessed for their chemotactic response, to compare it to the nascent mPC cellular response. This test was conducted to ascertain some basic information on the developmental state of the mPC cells, enabling a more informed investigation with the HOTs-patterned delivery of osteoblast recruitment signalling.

As previously discussed, the importance of PDGF-BB as a signalling molecule for the recruitment of osteoblasts to sites of bone remodelling is an interesting area of study. The ability to study how such recruitment signals are able to recruit the required cell types on a single-cell level would be beneficial to the research effort. This chapter details the demonstration of the HOTs patterning setup as a tool for creating controlled molecular signals that can direct osteoblast chemotaxis. For the initial chemotaxis optimisation, a concentration of PDGF-BB known to be potent (10 nM) [254,256] was used to recruit the mPC cells across the chemotaxis chamber.

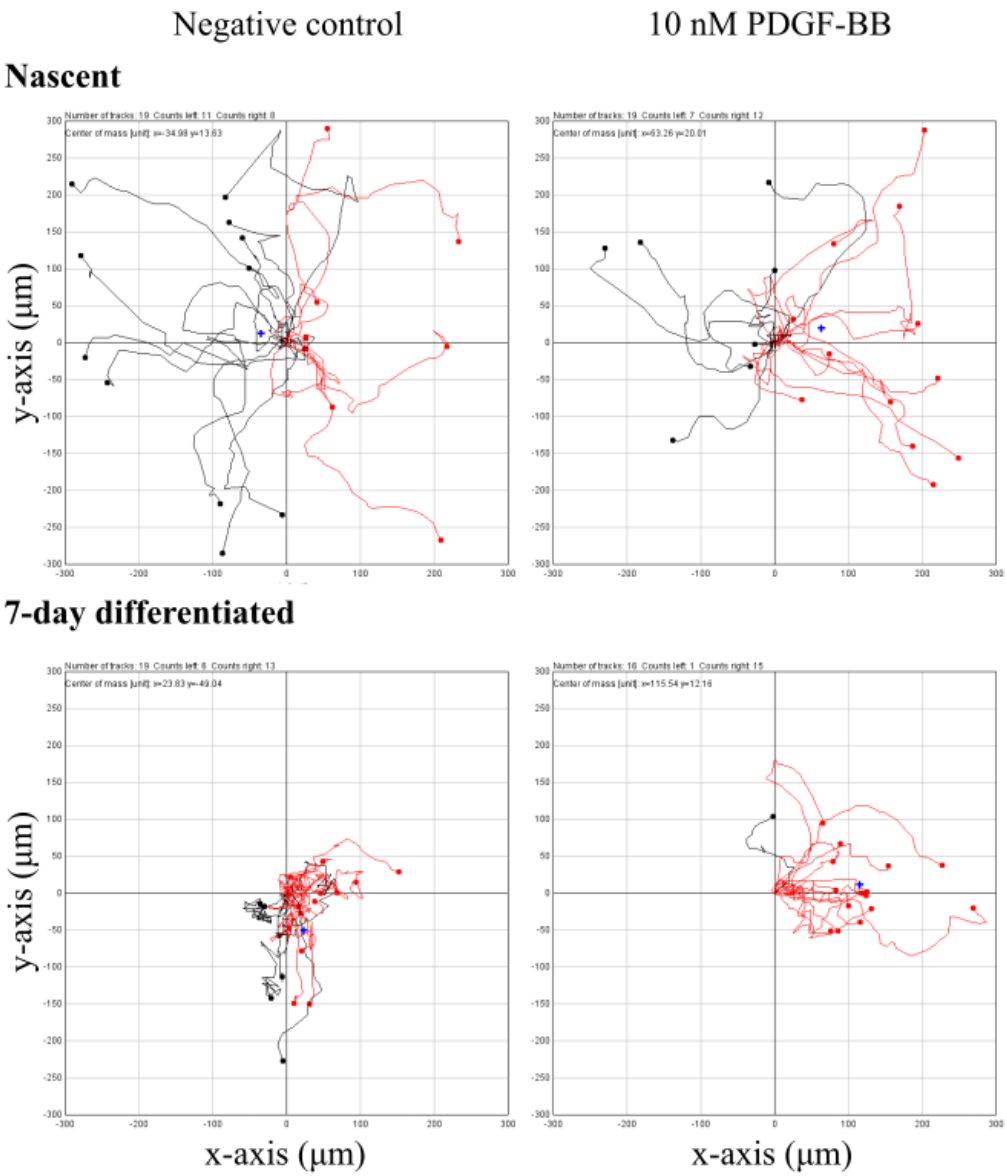

Figure 6.6 Analysis of PDGF-BB-associated chemotaxis

mPC cells were either used as undifferentiated (Nascent) cells or '7-day differentiated' and cultured into a chemotaxis chamber with PDGF-BB chemoattractant on the right hand side. Migration plots showing the net migration of the mPC cells from their point of origin in the chemotaxis chamber, represented by point 0,0. Red tracks indicate a migration towards the chemoattractant (10 nM PDGF-BB) (Right) and black tracks are towards the sink (Left). The blue cross represents the average migration point (AMP) from all of the cells analysed (n=30).

The mPC cells were cultured in the chemotaxis chamber as described in Section 6.2.3, the observation section of the chamber was imaged using time-lapse bright-field microscopy to observe and track cellular migration over an 8-hour period. As described in Section 6.2.4, an ImageJ plugin (MTrackJ) was used to track individual cellular migration over the time-period. The tracks were then compiled and analysed to create the plots in Figure 6.6 that show a representative number of cell tracks over the 8-hour period. The full dataset of 30 cell tracks was then analysed to give the AMP, as indicated by the blue cross in each plot.

The 'Negative control' plots show the cells that were not exposed to a PDGF-BB gradient; the nascent cells are highly mobile, going long distances (~250-300 μm) in random directions. This result is demonstrative of the cellular response when there is no chemoattractant signal present. When you introduce a chemoattractant, such as 10 nM PDGF-BB established as a gradient from a source, you see a directed migration towards that source. This is seen in the nascent mPC response in the nascent 10 nM PDGF-BB plot, as the tracks are predominantly red and thus moving towards the release source. The position of the AMP is 75 μm away from the origin, and towards the release source, and shows that the nascent cells were attracted towards the PDGF-BB signal. Comparing the responses of the 7-day differentiated and nascent cells, a similar degree of directed migration is evident in each case upon introduction of the PDGF-BB chemoattractant. Comparing the AMP of the two PDGF-BB plots, the 7-day differentiated cells exhibit a much greater degree of migration towards the release source. This result suggests that the 7-day differentiated cells are more responsive to the chemoattractant signal, as was hypothesised previously.

To confirm this observation, the chemotaxis experiments were repeated to give a larger dataset and compared using further ImageJ analysis.

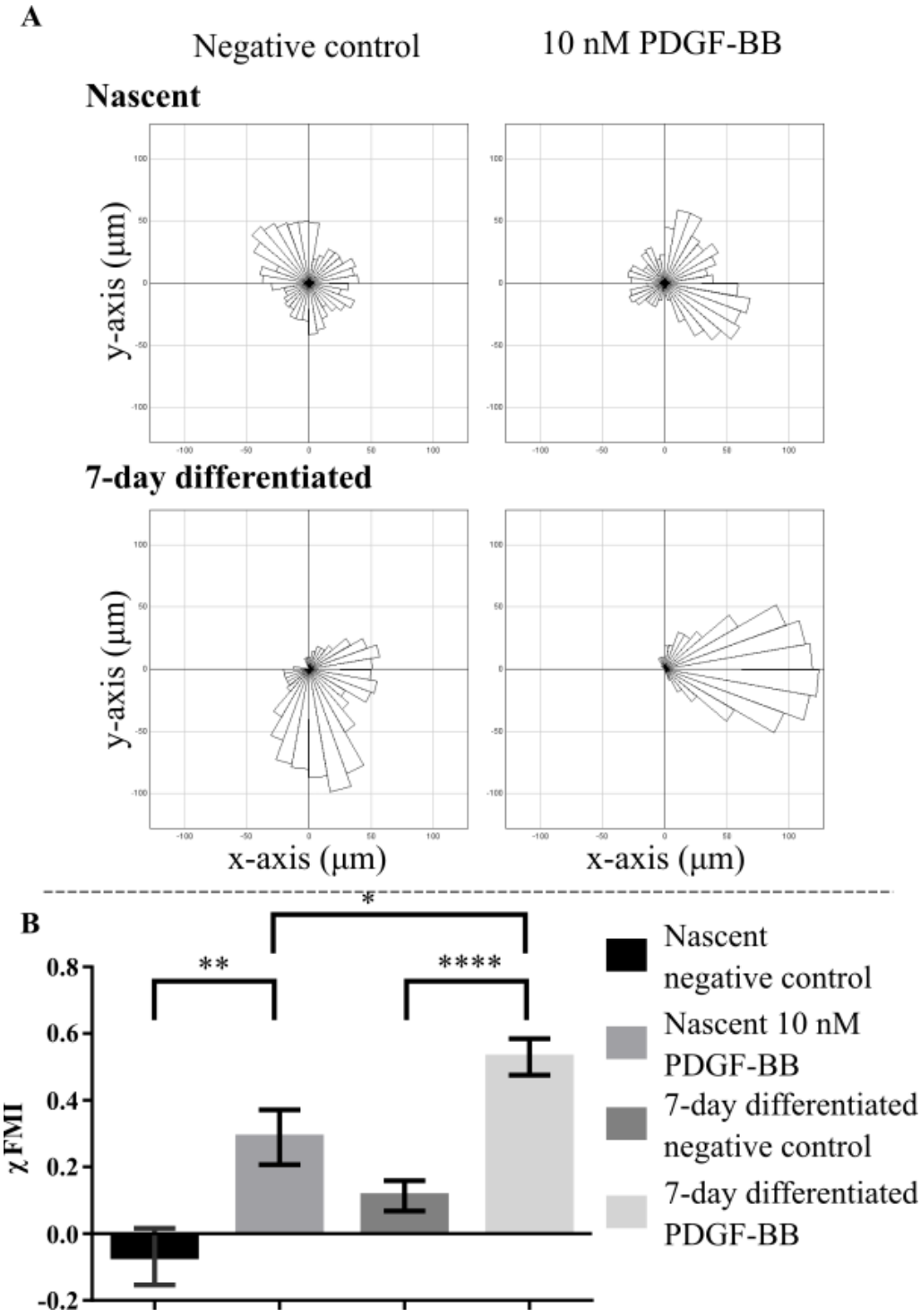

Figure 6.7 Analysis of mPC migration with and without chemoattractant

A. Representative rose plots for one of three repeats (n=30), showing the distance and direction of mPC migration paths. B. Plot showing the average x-FMI values calculated from the full dataset of mPC cells tracked for each condition (n=90). T-test analyses were performed and the significant difference was indicated accordingly, **** = <0.001, ** = 0.0045, and * = 0.0253.

Figure 6.7 shows the effect of providing a chemoattractant signal (PDGF-BB) to both nascent and 7-day differentiated mPC cells. The representative rose plots of Figure 6.7 A illustrate the migratory distance and directions of the cells analysed (n=30) per repeat. With the chemoattractant signal ('10 nM PDGF-BB'), cells were directed towards the signal origin (right of plot (0,500)) in great numbers for both the nascent and 7-day differentiated cells. In the case of the 7-day differentiated cells, almost all analysed were migrating directly towards the chemoattractant signal, with only a few cells migrating in other directions. 7-day differentiated cells were migrating over 100 µm towards the signal over the 8-hour time-period, whereas maximal migration was just over 50 µm for the chemoattractant nascent cell samples. In the absence of a chemoattractant signal ('Negative control') there was no clear directional movement of the nascent cells. The 7-day differentiated cells in the negative control showed no clear directionality in their migratory paths, however there was elevated migration along the observation channel of the chemotaxis chamber. This outlier result was most likely due to extra growth space at one end of the observation channel, providing a stimulus for cells to migrate towards it to divide. The cells were seeded in such a way that they were equally distributed across the horizontal plane. Control over the vertical plane was difficult to control due to the injection of cells through the chemotaxis chamber caps. This was an important observation as it reinforced the need for ensuring uniform cellular distribution allowing plenty of space for cells to divide without the need for migration.

Cells were equally distributed along the horizontal plane that was being analysed for directed migration, and vertical migration was not as significant a cue as the

chemotactic signal was in affecting cellular migration. This is shown by comparing the negative control samples with the 10 nM PDGF-BB samples - even when the same cellular distribution is present, cells preferentially migrate towards the chemoattractant.

Analysis of the data by rose plot permitted a certain level of assessment of the general direction each cell migrated in, however, it was not a good measure to statistically compare chemotaxis between the various samples. Figure 6.7 B shows the analysis of the full dataset of tracked mPC cells (n=90) and ranks their average migration using the FMI along the x-axis (horizontal plane). The calculation of the χ -FMI is explained in Figure 6.1 and Section 6.2.3. By compiling the χ -FMI values for each of the cells assessed in each sample, average χ-FMI values were calculated as a mean and compared by T-test. With the nascent mPC cells there was a significant difference between the average χ-FMI values (P=0.0045), the chemoattractant sample yielded a much greater average χ-FMI of 0.29 ± 0.08 compared to -0.07 ± 0.09 without chemoattractant. A similar result was seen with the 7-day differentiated cells, the chemoattractant sample yielded an even greater average χ-FMI of 0.53 ± 0.05 compared to 0.11 ± 0.05 without chemoattractant. The difference between these two samples was significantly different, with a P value of <0.0001. A further comparison to be made was the difference in chemotactic response by nascent and 7-day differentiated cells. There was no significant difference between the average χ-FMI values when no chemoattractant was used. However, the 7-day differentiated cells yielded a significantly greater average χ-FMI with a p-value of 0.0253.

The difference in response between the nascent and 7-day differentiated mPC cells was profound, and it indicated that the 7 days of osteogenic differentiation were yielding more chemotactically-responsive cells. It was hypothesised that this was due to a greater proportion of osteoblasts being present after stimulating the precursor osteoblasts in osteogenic medium.

6.3.5 Alternative release source development

Developmental biologists have previously described the use of hydrogel beads of various sorts, including agarose and gelatin, for use as simple release sources. Beads could be prepared at the required size and with appropriate-concentration hydrogels and then soaked in the molecule or protein required to be released. The beads would retain this 'cargo' and then release it through simple diffusion into the surrounding medium. Whilst this method of delivery offers fairly low control over the release kinetics, its simplicity is appealing to many investigators. If such a technology that is readily available to many researchers could be optimised to work with the HOTs patterning setup, the technology would be even more valuable.

To this end, agarose beads (Figure 6.8) were suspended in GelMA 10% and optical trapping was attempted. The beads were 50 μm in diameter, much larger than the microparticles patterned previously, and their optical properties were very different to those of the PLGA microparticles used previously. Agarose optical manipulation was attempted in GelMA 10% pre-gel solution, PBS, and cell culture medium, none of these attempts were successful and the beads could not be patterned. Whilst completing the trapping assessment, it was observed that after about 30 minutes of trying to manipulate the beads in cell culture

medium, the beads did permit optical trap formation (data not shown). The agarose beads in cell culture medium were not suitable for patterning, but the formation of an optical trap was encouraging. It was hypothesised that the issue with the beads was that their refractive index was too similar to that of the surrounding media, thus preventing optical trap formation. This theory was further supported by the fact that the beads became trappable after suspension in FCS-containing cell culture medium. The FCS was likely absorbed into the beads and bound to non-specific binding sites [257], creating a slight refractive index mismatch with the surrounding medium. This mismatch was not sufficient to facilitate optical trapping for manipulation of the bead, but it was compelling evidence for the issue's cause.

6.3.6 Agarose beads for HOTs patterning

In order to raise the refractive index of the agarose beads for optical manipulation, something with a different refractive index needed to be added to the beads. BSA was loaded into the beads at a range of different concentrations to assess its effect on optical trapping potential. The trapping assessment was completed as described in Section 3.4.4.

A

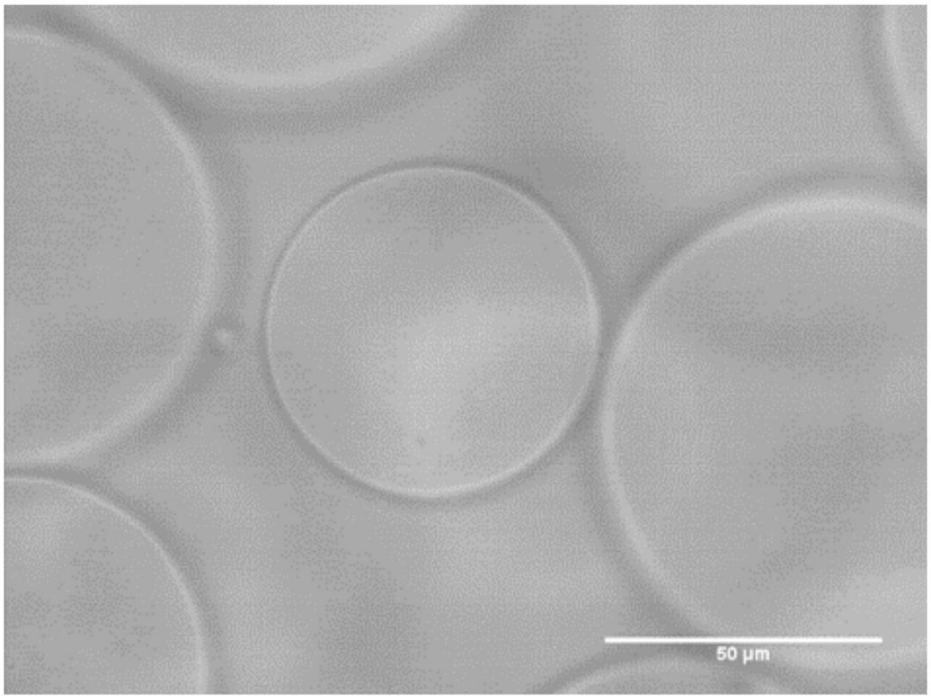

B

BSA concentration (% w/v)	Manipulation possible?	Minimum velocity achieved (32 µm/s)?
0	NO	NO
1	NO	NO
3	NO	NO
5	YES	NO
10	YES	NO

Figure 6.8 Optical trapping assessment – Agarose beads

A. Micrograph of 4.0% (w/v) agarose beads manipulated by HOTs in cell culture medium suitable for optical manipulation via the HOTs patterning platform. B. A tabulation of the results of the trapping assessment using differently soaked beads assumed to have increasing levels of BSA as the soak concentration is increased.

A trapping assessment was completed for the BSA-laden agarose beads that tested the optical trap strength formed when different concentrations of BSA were loaded into agarose beads. Figure 6.8 A shows the beads suspended in GelMA 10%, the medium that would be used for subsequent chemoattractant HOTs patterning experiments. Figure 6.8 B shows a table presenting the results of the trapping assessment; 0, 1, and 3% BSA loading was not sufficient to permit optical trap formation that would enable movement of the beads ('Manipulation possible?'). 5 and 10% BSA loading permitted the formation of optical traps that were suitable for moving the beads in a controlled manner that would be suitable for simple patterning experiments. However, none of the concentrations tested led to beads that could be manipulated at 32 μm/s (The minimum acceptable manipulation speed, Section 3.3.2). To enable better optical trapping, a greater concentration of protein could have been used, but this could potentially lead to reduced uptake of the active molecular/protein cargo if the beads were already saturated with BSA.

6.3.7 Calcein-AM-laden agarose beads

To demonstrate the basis for release from HOTs-patterned agarose beads, the beads were soaked in α-chymotrypsin and calcein green AM solution as described in Section 6.2.6. Agarose beads were soaked in solutions of α-chymotrypsin and then prepared for an *in vitro* release study to assess release kinetics. α-chymotrypsin is a good reference protein by which to assess the release kinetics of PDGF-BB due to its similar molecular weight (α-chymotrypsin = 25 kDa, PDGF-BB = 24.5 kDa) and isoelectric point (α-chymotrypsin = 9.1, PDGF-BB = 9.8) [258].

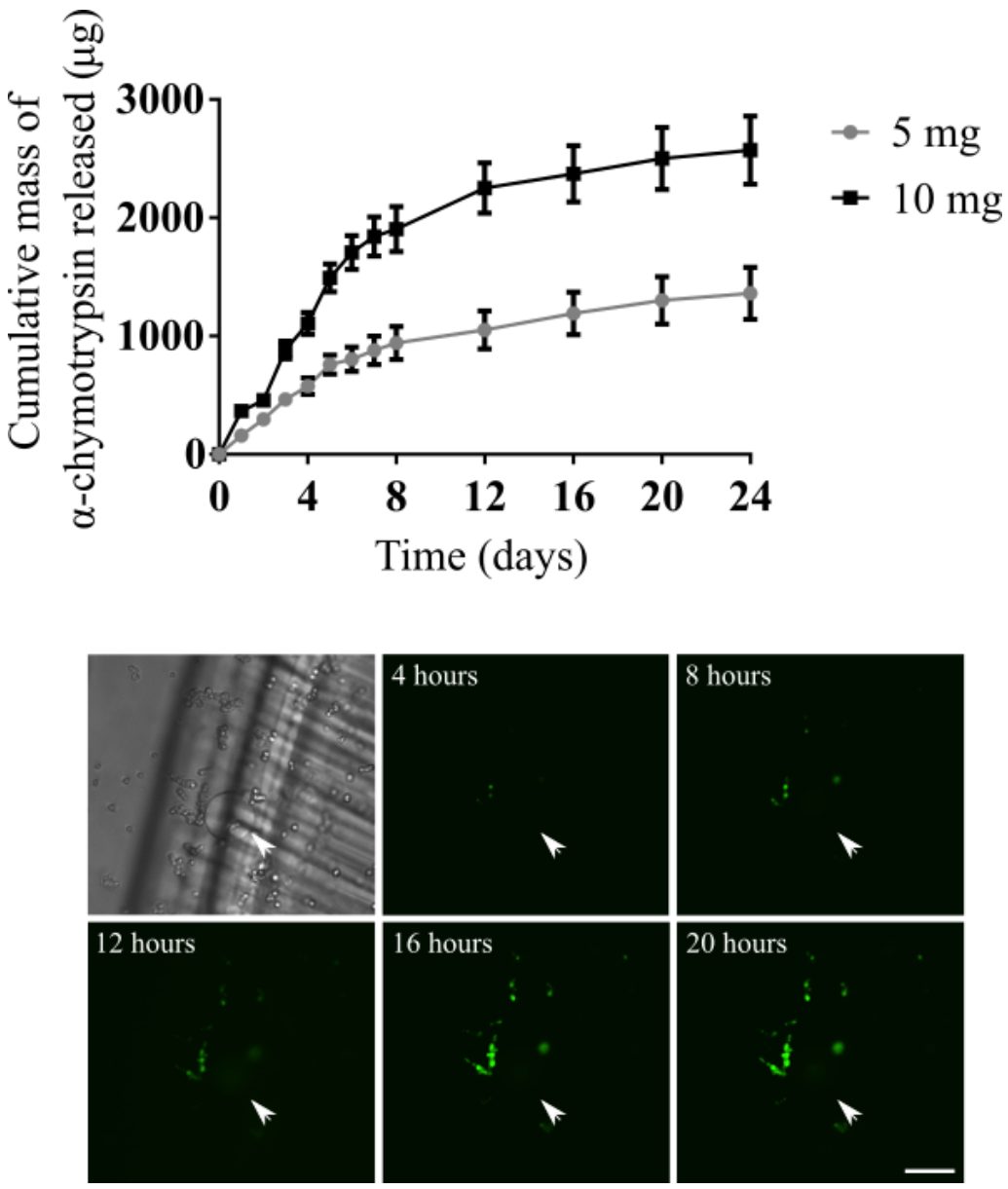

Figure 6.9 Agarose beads for delivery of calcein green AM to cells

A. An *in vitro* release study for 5 and 10% (w/v) α-chymotrypsin-soaked agarose beads into PBS, over a 24-hour time period. Errors bars display the cumulative standard error of the mean from three batches of soaked beads. B. Micrographs showing the release of calcein green AM from a single soaked agarose bead positioned in close proximity to mES cells (White arrows) with the HOTs patterning platform. Fluorescence micrographs at 4-hour intervals show the calcein-positive cells around the agarose bead fluorescing at a progressively greater distance away from the bead source with increasing time. The scale bar represents 50 µm.

Figure 6.9A shows the results of an *in vitro* release study using agarose beads soaked in α-chymotrypsin and calcein AM. To assess the release kinetics, a BCA assay was completed as previously described (Section 2.9.5). The released α-chymotrypsin was assessed at 48 hours. The total release was calculated to give the estimated total loading of α-chymotrypsin following each solution soaking. For both the 5 and 10% α-chymotrypsin-soaked beads, rapid release was observed over the first 6 hours with 55 and 58% (of the total estimated loading) of α-chymotrypsin released respectively. Following the rapid release, a slower release rate was observed until the 10-hour point. These release kinetics would be difficult to modulate with the agarose bead delivery system. It was hypothesised that by increasing the agarose concentration, release would be prolonged due to the decreased diffusion rate through the higher concentration agarose. For the delivery of PDGF-BB, to stimulate mPC chemotaxis, the release kinetics of the 4% (w/v) agarose beads tested in Figure 6.9 were suitable. Figure 6.9 B shows a single agarose bead soaked in α-chymotrypsin and calcein AM, surrounded by mES cells. After stabilisation using the GelMA hydrogel system, the cells were imaged using time-lapse microscopy, and the calcein fluorescence was observed to develop in cells in close proximity to the agarose bead. Using HOTs, two α-chymotrypsin and calcein-AM-soaked agarose beads were positioned in close proximity to one another, over a monolayer of mES cells.

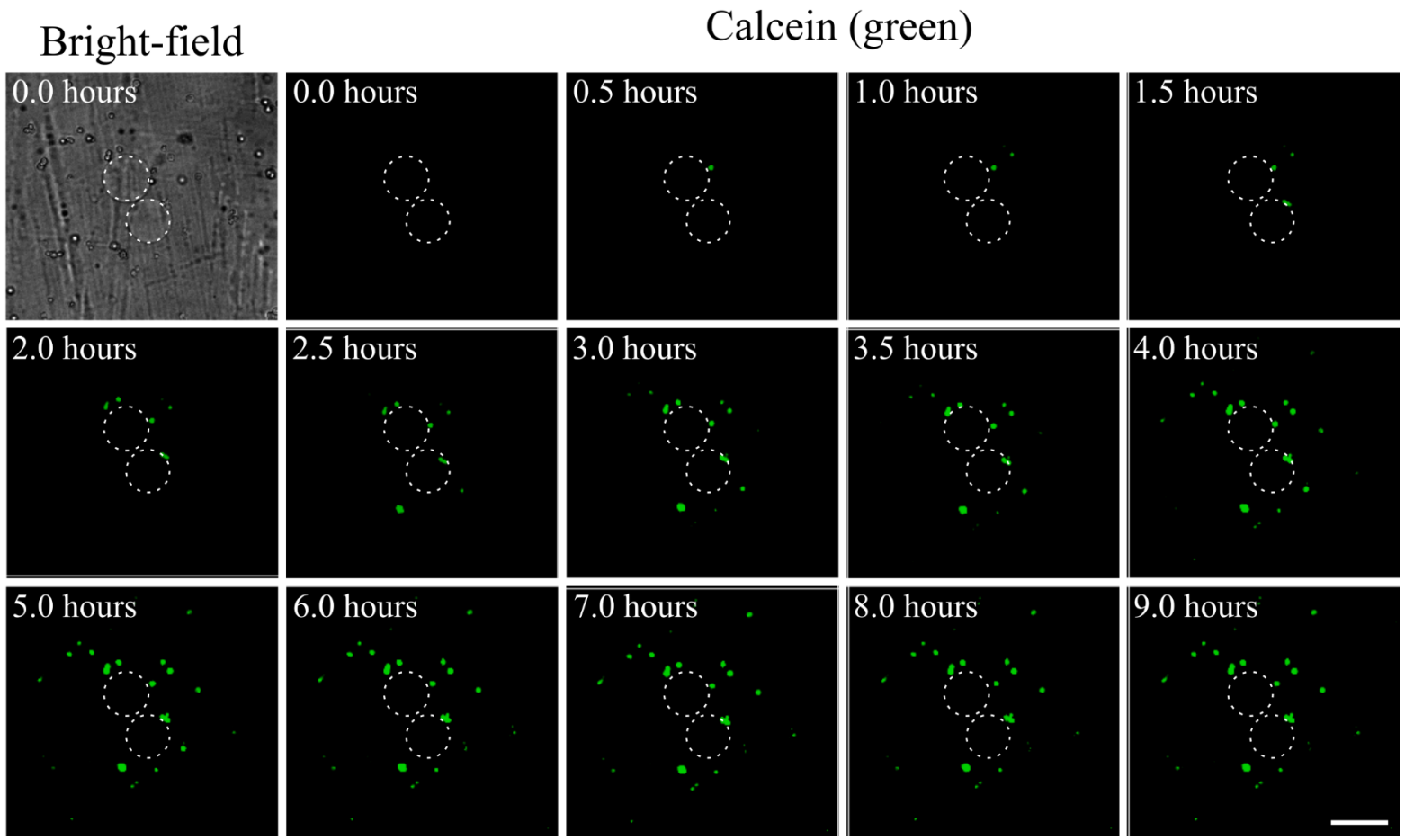

Figure 6.10 HOTs positioned agarose beads for the delivery of calcein green AM to mES cells

A. Bright-field micrograph showing the HOTs-based positioning of two calcein-AM-soaked agarose beads (Indicated by white dotted lines), surrounded by a monolayer of mES cells. Fluorescence micrographs were taken at 30-minute intervals to show the increased number of calcein-positive mES cells fluorescing at a progressively greater distance away from the bead source with increasing time over 9 hours. The scale bar represents 50 µm.

Figure 6.10 shows the micrographs from the HOTs-positioned α-chymotrypsin and calcein-AM-soaked agarose bead experiment. Fluorescence-based microscopy was used to show the release and uptake of calcein green AM by mES cells in close proximity to the agarose bead. The agarose beads were able to retain enough calcein green AM in order to successfully yield intensely stained calcein fluorescent cells. This simple method of delivery proved suitable for HOTs manipulation and positioning. Figure 6.10 shows that cells at different distances from the point of origin respond at different times. This release characteristic is of great relevance to the investigation of bone remodelling recruitment signalling. Individual osteoblast responses to recruitment signalling could be investigated using the HOTs patterning setup and agarose bead release.

6.3.8 HOTs-patterned PDGF-BB signalling

As shown in Figure 6.9 A, the release of the reference protein α-chymotrypsin occurs by a rapid release phase over the first 6 hours and then a slower release rate until the 10-hour point. This period of release is sufficient to permit mPC migration if the signal concentration propagated is great enough. The mPC cells have been shown migrate great distances in the 8-hour experiments conducted earlier (Figure 6.6 and Figure 6.7). Figure 6.10 gives a good representation of released molecules eliciting a response in cells at different time-points depending on their distance from the source. It must be acknowledged however, that the small molecule calcein green AM will diffuse at a higher rate through the GelMA matrix than will PDGF-BB. Furthermore, Figure 6.10 can be used as a crude measure of the calcein green AM ‘diffusion front’ formed over the 9-

hour time-period. At 2 hours, cells within a 50 μm zone of the agarose beads were calcein fluorescent, at 4 hours, cells within a 100 μm zone responded, and at 7 hours, cells as far as 150 μm away from the release source responded to the calcein green AM signal.

Although calcein AM does not serve as an accurate reference for large proteins, such as PDGF-BB, it does provide a means by which to estimate the diffusion front for PDGF-BB. It may be assumed that PDGF-BB is less mobile in the hydrated GelMA matrix, principally because of its size, compared to calcein AM. However, PDGF-BB elicits its recruitment effects at much lower concentrations (1-10 nM) than calcein AM (2 μM). Whilst this, and the α-chymotrypsin release study (Figure 6.9 A), serve as an estimation of the release kinetics for PDGF-BB, further analysis is required to fully understand the signals created by HOTs-positioned release sources. Later in this chapter, the development of such analysis is detailed.

An experiment was devised to show that individual mPC cells can be recruited to HOTs-patterned agarose beads. Utilising the patterning precision that the HOTs platform offers, it was possible to position PDGF-BB-loaded agarose beads at defined distances from the mPC cells such that any differential chemotactic responses might be observed.

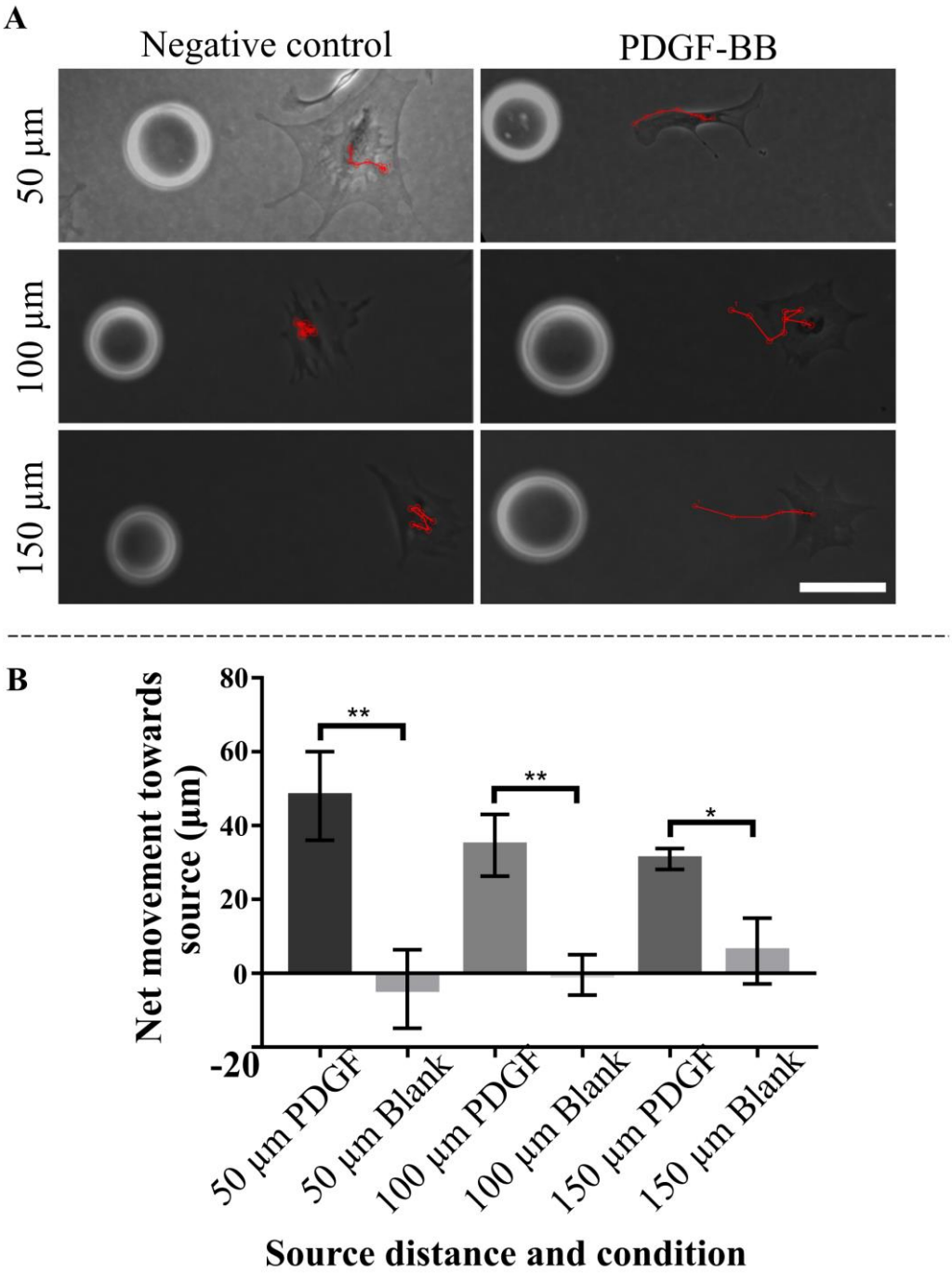

Figure 6.11 HOTs-patterned PDGF-BB-soaked agarose beads

A. Images of PDGF-BB- or un-soaked agarose beads and their effect on mPC migration. The red track shows the movement of the mPC cell from the imaged point of origin. Scale bar represents 50 µm. B. A plot displaying the average net migration with respect to the agarose bead release source. Errors bars display the standard error of the mean. T-test analyses were completed to statistically compare the results, ** = 0.0045 and * = 0.0253.

Single agarose beads soaked in PDGF-BB were positioned at specific distances from individual mPC cells. The cells were imaged and tracked over an 8-hour period to assess their migration. Figure 6.11 A shows micrographs of HOTs-positioned agarose beads and an individual mPC cell's response to it. Agarose beads were soaked in either α-chymotrypsin ('Negative control') or PDGF-BB to assess the chemotaxis of mPC cells. Negative control beads were required to ensure that the agarose beads were not stimulating chemotaxis in any way. As previously described (Section 6.2.4) ImageJ's MTrackJ plugin was used to track the movements of the mPC cell over the 8-hour experiment. The red tracks shown on the micrographs (Figure 6.11 A) indicate the migration of the cells from their initial positions (as shown). From the representative micrographs and overlaid tracks, it is clear that the PDGF-BB-soaked beads are directing chemotaxis of the mPC cells towards them.

The agarose beads were positioned at different distances from the mPC cell in an attempt to identify any different responses based on the concentration of PDGF-BB at different distances from the agarose bead release source. If a PDGF-BB concentration gradient was established across the 150 μm zone, emanating from the agarose bead, the mPC cells would theoretically migrate differently depending on their proximity to the bead, due to the distance-dependent gradation of PDGF-BB concentrations. To assess the effect of source distance upon mPC chemotaxis, the net migration with respect to the release source was assessed. Figure 6.11 B shows the plot of the assessment, showing clearly that the presence of released PDGF-BB led to significant chemotaxis towards the release source with respect to the negative control. However, when we compare the different PDGF-BB source distances, migration of the mPC cells

is fairly similar, and there is no significant difference in migration using the different source distances tested. This result suggests that either the migration of mPC cells in response to PDGF-BB does not occur in a dose-dependent manner, or that there is no significant concentration gradient being formed over the distances tested. There are, however, many publications that have shown cellular migration to be tightly linked to PDGF-BB concentration [247,254], and so it must be accepted that no significant concentration gradients were formed over the distance assessed.

To further optimise the delivery of signalling molecules by means of the agarose beads or polymer microparticles discussed previously, a method with which to assess hydrated gels such as GelMA was required.

6.3.9 Analysis of solutes in hydrated hydrogels

In order to effectively assess the solute concentrations around a release source, in this case a protein-soaked agarose bead, the dynamic hydrogel environment must be 'paused' to obtain a snapshot of the distribution of protein throughout the hydrogel. By doing this at various time-points, an understanding of how solutes are able to diffuse through the hydrogel matrix to propagate a concentration gradient may be obtained. ToF-SIMS can be utilised to assess the surface chemistry for material characterisation very effectively [259]. These methods were further developed to provide subsurface chemical analysis using Ar cluster ions with a liquid metal ion analysis source, a form of polyatomic sputtering beam. Through the sputtering of the surface of material, secondary ions are ejected and analysed as a function of etch time, permitting the formation of a depth profile throughout the material [260,261]. Difficulties, however, arise in

the preparation of hydrated samples for analysis. The SIMS technique requires a vacuum environment, and this reduced pressure causes mechanical stress and the rapid removal of volatile compounds, such as water. Therefore, the analysis of hydrated protein-containing hydrogels without sample preparation would not be appropriate for characterising solute distribution in the native hydrated state. Methods of sample preparation have been developed to closely maintain the hydrogel's native state in a high-vacuum environment, including the effective frozen-hydrated sample preparation [262].

In collaboration with Mr Michael Taylor and Prof. Morgan Alexander (University of Nottingham, UK), analysis of agarose-bead-containing hydrogels was completed using the aforementioned frozen-hydrated sample preparation. Agarose beads were prepared as described in Section 6.2.8, and hydrogel disks were prepared as described in Section 6.2.10. ToF-SIMS characterisation and analysis of all samples was completed by Mr Michael Taylor (University of Nottingham, UK). PEGDA was used as a reference hydrogel in the place of GelMA to yield better analysis outcomes due to its 'cleaner' composition and lack of organic molecules that would contribute to high levels of background signal. PEGDA was used at 10% concentration to best represent the characteristics of GelMA. Initially, a surface spectrum of the PEGDA hydrogel with absorbed α-chymotrypsin was completed to show the secondary ions to indicate PEGDA and α-chymotrypsin (Figure 6.12).

A

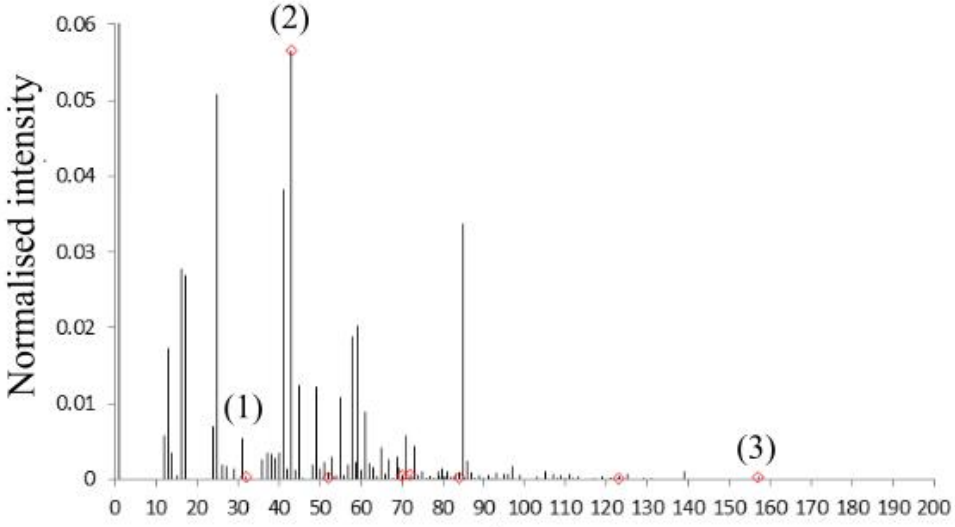

B

	Secondary Ion	m/z	Signifying Component
(1)	HS^-	**32.976**	**α-chymotrypsin**
(2)	$C_2H_3O^-$	**43.016**	**PEGDA**
	$C_3H_2N^-$	52.023	α-chymotrypsin
	$C_2NO_2^-$	69.996	α-chymotrypsin
	$C_2H_2NO_2^-$	72.011	α-chymotrypsin
	$C_3H_3NO_2^-$	85.021	α-chymotrypsin
	$C_6H_3NO_2^-$	121.011	α-chymotrypsin
(3)	$C_4H_5NO_2S^-$	**157.031**	**α-chymotrypsin**

C

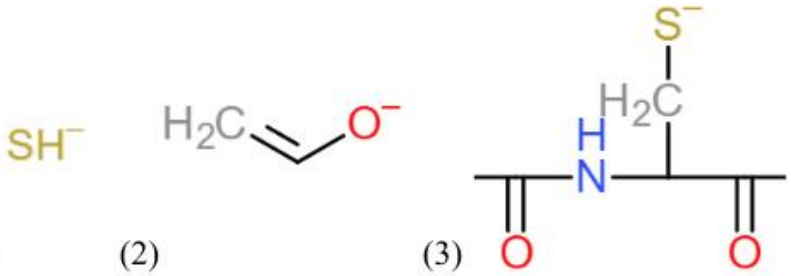

Figure 6.12 Surface analysis of PEGDA and marker secondary ions

A. Plot showing surface analysis of PEGDA hydrogel by ToF-SIMS with areas signifying components of interest circled in red. B. Secondary ion species as indicated by the red circles in A, emboldened and numbered (1-3) species are the secondary ions that are used for component identification. C. Chemical structures (1-3) of the ions used as signifying components.

Figure 6.12 shows the selection of secondary ions for markers of both PEGDA and the solute, α-chymotrypsin. Figure 6.12 B shows the two secondary ions that were chosen to signify the presence of α-chymotrypsin. Selection of markers for α-chymotrypsin was simple due to the cysteine-rich nature of the protein and the complete absence of organic chemistry within the PEGDA hydrogel. Figure 6.12 C shows the chemical structures of each of the three secondary ions selected.

Once the secondary ions were selected as suitable markers for both PEGDA and α-chymotrypsin, a standard curve was developed so as to assess the secondary ion intensity versus concentration. This enabled the calculation of α-chymotrypsin concentration throughout the gel.

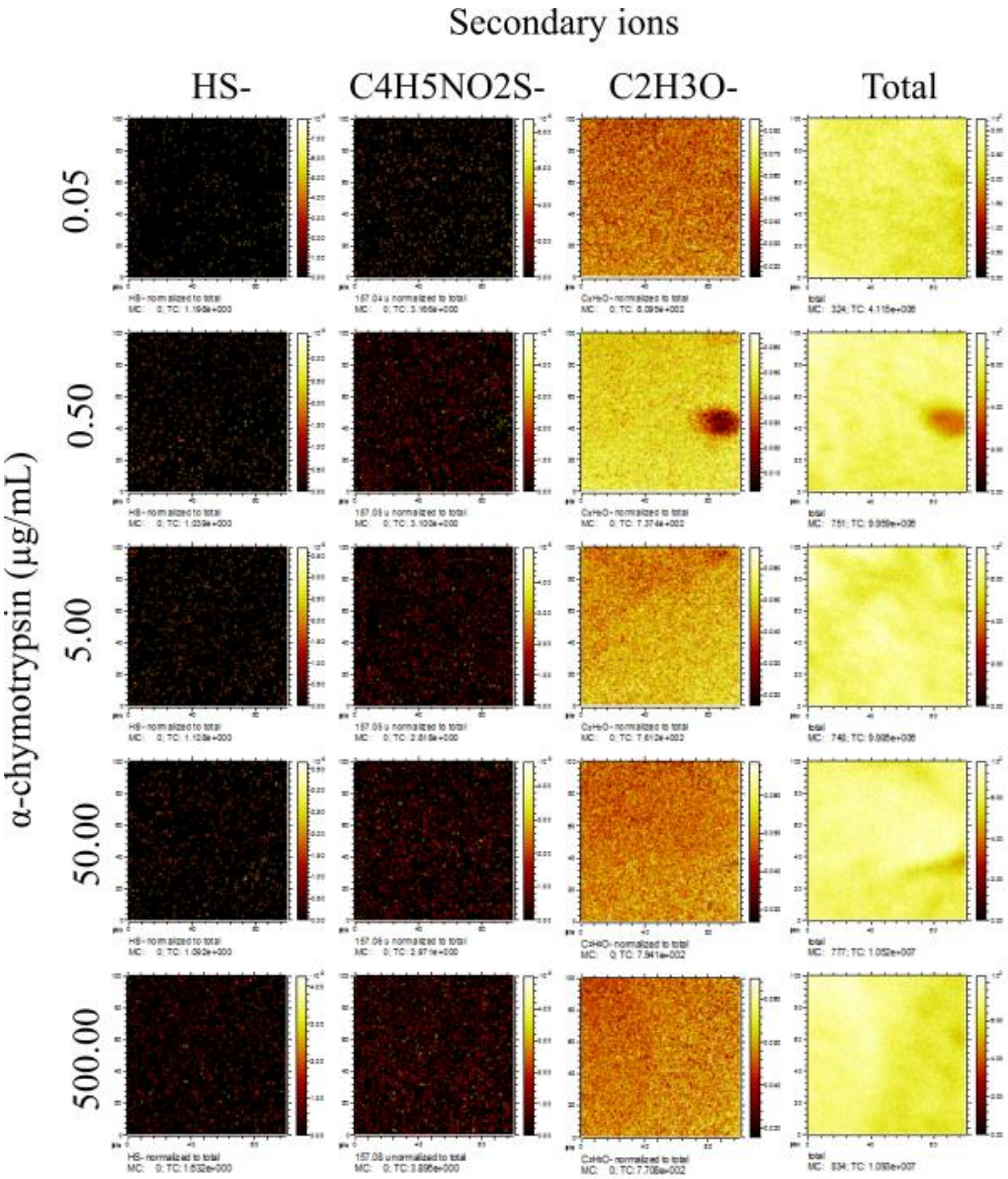

Figure 6.13 Surface analysis of α-chymotrypsin-soaked PEGDA standards

A selection of surface analysis plots of PEGDA hydrogel disks soaked in different concentrations of α-chymotrypsin. Secondary ion intensity plots are shown for HS-, C4H5NO2S-, C2H3O-, and the total.

Figure 6.13 shows intensity plots of the 100x100 µm area assessed for the intensity of the marker secondary ions. As the α-chymotrypsin concentration increases, greater intensities of HS- and C4H5NO2S- ions are recorded. The intensity of the PEGDA secondary ion (C2H3O-), however, does not seem to change with α-chymotrypsin concentration, confirming that the analysis was taken from within the PEGDA hydrogel. Peak shapes for both HS- and C4H5NO2S- were analysed to show that the peaks quantified for each sample were correct (Appendix, Section 8.3). Due to the use of 'clean' PEGDA hydrogel, the background noise was very low, and so the peak shape fitting was only required for complete assurance.

6.3.10 Chemical depth profiling release study

In order to assess the concentration of α-chymotrypsin being released from the agarose beads at different time-points, depth profiles from the top of the hydrogel disk (furthest point from source (~200 µm)) down to the agarose beads were made. Analysis took place after a 400x400 µm area of hydrogel had been etched away using the 10keV Ar_{1455} cluster ion source. The 25keV bismuth source was then rastered over an area of 100x100 µm with 128x128 pixels. Rastering through the gel was completed according to Section 6.2.11. To obtain the concentration gradient at various times from initial release, multiple samples were prepared for analysis as described in Section 6.2.11.

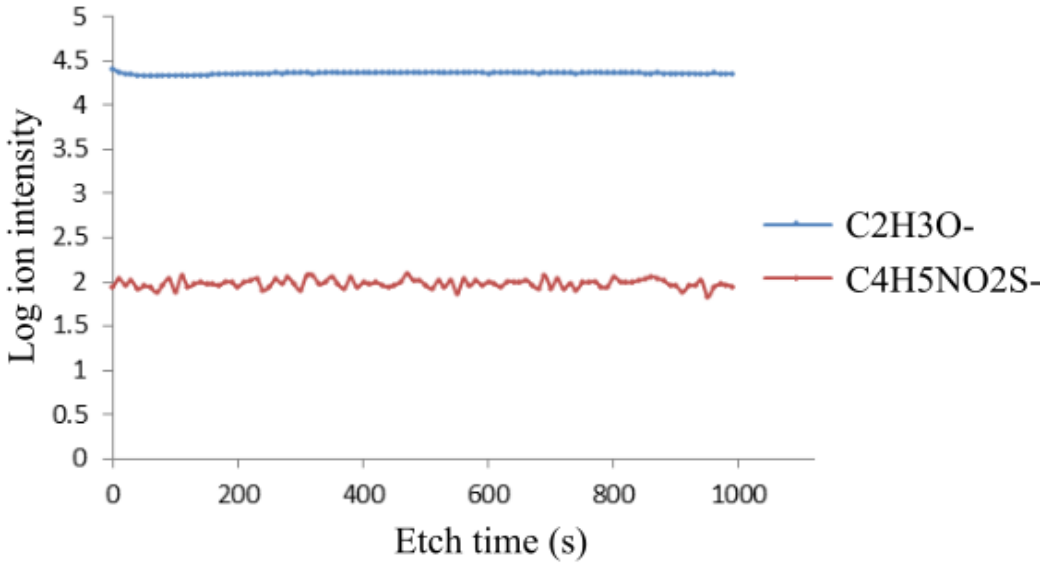

Figure 6.14 Chemical depth profiling at 1 hour

A chemical depth profile for the 1-hour release time-point of α-chymotrypsin-soaked agarose beads. The plot shows both C2H3O- (PEGDA) and C4H5NO2S- (α-chymotrypsin) log ion intensity against etch time (s). This plot is representative of all of the six time-points assessed, so these additional data are not shown.

Figure 6.14 shows the chemical depth profile of a hydrogel disk after 1 hour of incubation and α-chymotrypsin release. The C2H3O- trace shows that the etched area was completely within the PEGDA hydrogel. The largely unvarying C4H5NO2S- ion intensity, however, indicates that the PEGDA hydrogel was completely equilibrated with α-chymotrypsin. Only one plot of the chemical depth profiling is included for the 6-hour release assessment as it is representative of those made for all other time-points. The reference protein, α-chymotrypsin, is so mobile that it is able to diffuse through the whole gel and equilibrate before the first time-point. At later time-points the α-chymotrypsin concentration did increase slightly (data not shown) in line with the release study shown previously (Figure 6.9).

6.3.11 Implications for mPC chemotaxis

The assessment of α-chymotrypsin release from agarose beads gives a good representation of what was happening in the HOTs-positioned PDGF-BB-soaked bead work shown in Figure 6.11. The results from this assessment are in line with the biological data (Figure 6.11) that showed no differential mPC cell migratory response over 150 μm from the agarose beads.

The technology used to analyse these hydrogels discussed here shows great promise for characterising hydrogels and solute distribution, however the current methodology limits the depth to which analysis is possible. Furthermore, although the sample preparation does retain the molecular organisation within the hydrogel so that time-points can be assessed. It would be highly laborious to obtain the number of time-points required to observe the quick changes in solute

concentration that it is hypothesised to have occurred in the earlier microparticle-based release experiments of Chapter 5.

Recent advances in the field of mid-infrared (MIR) imaging provide a technology that might be capable of analysing such subtle concentration changes within a hydrogel environment. Chris Sammon's group (Sheffield Hallam, UK) have developed a method of analysing chemical signatures from MIR imaging [263,264], developing it to such a point that they have shown the release of encapsulated protein into surrounding water from a single microparticle [265]. Such a technology could be very useful for further analysis of the release of PDGF-BB/α-chymotrypsin from agarose beads during the first hour of release.

6.4 Conclusions

This chapter has shown that, with a degree of simplicity, agarose beads can be optimised for use with the HOTs patterning setup to create a localised delivery of bioactive signals. The principle of optical manipulation based on the formation of an optical trap requires the object to have a sufficient refractive index mismatch with the surrounding medium. The addition of proteins to the agarose beads creates this mismatch, permitting optical trapping. Although not tested in this thesis, the same principles should permit optical trapping of other similar hydrogel-based beads that are typically used for this application. The outcome of this is that the HOTs system can be easily used with many release sources currently used for localised solute delivery, thus increasing accessibility of the technology.

The use of primary osteoblasts in this study showcased the ability to conduct HOTs-based experiments with cell types of varied origin to suit the needs of the investigation. Here, it is described how primary osteoblast migration can be controlled and directed towards a PDGF-BB-releasing agarose bead precisely positioned by means of HOTs-based patterning. Having demonstrated this model of recruitment, the investigation could be developed to probe the osteoclast-osteoblast relationship further through multicellular patterning experiments as previously described. Whilst the precise positioning of agarose beads at different distances was shown to not significantly affect the migration rate of mPCs, the experiment did effectively demonstrate the basis for controlling the location of localised release sources to observe the directed chemotaxis of cells.

Over the course of this project, the need to quantify solute gradients released from either polymer microparticles or agarose beads was recognised. In this chapter we discussed the difficulties associated with this analysis. A newly improved method of characterising solutes within hydrated hydrogels was tested for its ability to characterise concentration gradients surrounding agarose bead release sources. The Tof-SIMS analysis of the agarose-bead-based α-chymotrypsin release into PEGDA indicated that a concentration gradient of PDGF-BB was unlikely to be present in the mPC recruitment experiments. As previously discussed, this result was in line with the biological data. To further investigate the signalling dynamics formed from agarose bead or microparticle-based delivery, new technologies must be pursued. As previously discussed, the use of MIR imaging could be one such suitable approach.

This chapter detailed an alternative release method for use with the HOTs patterning setup, describing how it can be used to direct mPC cells to localised points of release. The HOTs have been demonstrated to be effective at mimicking recruitment signals observed in nature, highlighting how yet another area of research could benefit from this innovation and project.

7. Final Conclusions and Future Developments

7.1 Conclusions

From the advent of stem cell engineering, thousands of studies concerning stem cells and their potential therapeutic potential have been published. This is in stark difference to the real progress that has been made in the application of cell therapies in a clinical setting. It can be concluded that there remains a large amount to be learnt about stem cell biology, their differentiation and the mechanisms that underpin their function. The regulation, survival, proliferation and development of stem cells is determined by a number of factors, both intrinsic to the cells themselves and extrinsic signals received from their microenvironment. With the need for greater understanding of these cellular microenvironments to elucidate mechanisms that may hold solutions to unlocking the true potential of cell therapies and tissue engineered therapeutics, this thesis details the use of a novel new tool and approach to investigate this basic science that is so clearly sought.

This thesis details the development of HOTs from a predominately biophysics based tool, to a micropatterning tool-set capable of controlling some of the key aspects of cell microenvironment signalling. Early attempts to manipulate cells with the HOTs within a liquid medium was shown to be non-problematic, however, attempts to manipulate polymer microparticles led to issues relating to

refractive index similarity. This resulted in the microparticles being propelled away from the field of view, not congruent to successful positioning. Following optimisation of the formulation, three differently sized microparticle batches were developed and used for demonstrating basic positioning and pattern formation. Optimisation of the release kinetics and loading of the microparticles was relatively simple by comparison to the optical trapping optimisation due to in-house expertise (Dr. Omar Qutachi, University of Nottingham, UK). However, the process of optimising microparticle formulations was noted as a potential bar to the wider scientific community taking up the eventual micropatterning tool set, Chapter 6 addresses this issue which is discussed later. Co-patterning of microparticles and cells was achieved and discussed in Chapter 3, with two methods of stabilisation proposed. Whilst the stabilisation of cell and microparticle patterns with crosslinked hydrogels was focussed on in this thesis, the developments with avidinated-microparticle stabilisation showed great promise and could be further investigated. The stabilisation of HOTs patterns did lead to new difficulties to overcome, the increased viscosity was shown to be permitting cell and surface interactions leading to the so called “sticky cell” problem. Further optimisation of the polyHEMA surface coating proved to be the solution and concluded the initial cell and microparticle patterning proof of concept work.

The early concept work gave sufficient evidence to support the case that controlled release microparticles, positioned in close proximity to cell patterns, could serve as a model of localised solute delivery. The HOTs positioning would permit great precision over the point of release and the formulation of the microparticle could be tailored to suit the require release kinetics. Chapter 4

investigated this theory further, utilising fluorophores to visualise release and with the use of acetoxymethyl dyes (Calcein AM), the cell-uptake-dependent fluorescence. Experiments with calcein AM provided a good basis for developing the patterning tool-set further, and with the design of multiple spoke patterning gaskets, the first visualisation of zonal signalling was demonstrated. The basis for the spoke design was influenced by microfluidics channels, a method applied to cell and solute patterning in its own right [266,267], using the manipulation power of the HOTs instead of fluid movement.

Chapter 5 was based around the developments of Chapters 3 and 4, the demonstration of the how the HOTs patterning platform can be used to direct cellular differentiation was a great leap forward in terms of technological development. A sufficient concentration had to be released and delivered to responsive cells that were supported in the stabilising hydrogel matrix. The experiment relied upon the supportive nature of GelMA and the high loading of retinoic acid-laden microparticles. Chapter 5 details the steps taken to reach obtain these key aspects of the biological investigation proof of concept. Through innovative methods of obtaining highly loaded microparticles, using FITC co-loading to report on retinoic acid encapsulation and FACS, this was achieved. Through these developments, previously unobtainable control over solute signalling was achieved that led to a tightly controlled zonal response in a mES cell aggregate. The ability to control diffusible signalling is particularly beneficial to a number of basic biology investigations; it is well known that diffusible factor signalling is paramount in embryonic development. Furthermore, new anti-cancer therapeutics have even looked towards the cancer cell microenvironments for way of tackling their establishment and uncontrolled

growth. Whilst this is a very different area to of study to the work detailed in this thesis, it shows that there is a widespread need to better understand cellular microenvironments, especially their growth control mechanisms [268–270].

An important consideration mentioned earlier, was the difficulty in formulating and fabricating microparticles, that were an essential aspect of the HOTs controlled signalling described previously (Chapter4 and 5). The use of hydrogel beads, however, enables a much simpler method of loading and are readily available. In order to develop a method by which hydrogel beads are used as a localised release source, a new biological investigation was attempted with the HOTs patterning setup. Bone remodelling is the process by which the skeletal system grows and repairs following damage, there exists a complex interplay between osteoblasts and osteoclasts. The former lays down new bone matrix and the latter is required to resorb bone tissues for structure changes. These cells are known to signal to one another via growth factor and chemokine signalling over short distances, facilitating chemotactic migration towards sites of bone remodelling. Using the HOTs it was shown that by soaking agarose beads in a solution of PDGF, and then positioning the beads at distances away from primary osteoblasts, cellular chemotaxis could be controlled. Further to this, a novel technology was employed to assess the growth factor distribution at different time-points from agarose beads in a hydrogel. Although, the ToF-SIMS analysis suggested that there was no clear diffusion front of chemoattractant in the gel, agreeing with the HOTs experiments, it proved itself to be a powerful tool for quantifying solutes in hydrated environments. A further development of the HOTs patterning tool-set would certainly revolve around the quantification of solute gradients following microparticle based delivery.

7.1.1 Implications of this research

This thesis describes how we have developed and demonstrated an entirely novel method of mimicking solute signalling to control the differentiation and migration of cells. The toolset allows the user to create release zones or points of release that can, and have been used in meaningful biological investigations. The ability to do this, gives the investigator the possibility to control cellular microenvironment signalling with previously unobtainable levels of precision. Using this technology, *in vitro* developmental models can be mimicked that are more faithful to the natural conditions, chemotaxis can be investigated to understand the role that spatio-temporal signalling has upon the recruitment of many different cell types. The ability to manipulate solute signalling permits a vast number of possible investigations into how cells communicate with their surroundings and *vice versa*. This offers a technology to permit new understanding into the world of cellular biology and the mechanisms that may prove essential for the successful therapeutic applications of cell therapies.

7.2 Future Developments

The proof of concept work and biological investigations described in this thesis demonstrate the significant potential of the HOTs patterning setup as a tool to generate complex *in vitro* microenvironment models of development. Control over the solute signalling dynamics has been demonstrated, and shown to be able to direct cellular differentiation and migration. To develop this further, use of multiple signalling factors, as demonstrated in the two dye calcein AM proof-of-concept work would be highly impactful. Initial studies could include the use of antagonistic or inhibitory signals like those of the embryonic dorso-ventral axis

specification. BMP4 is responsible for ventral specification and it is inhibited by chordin, noggin, and follistatin that are released on the dorsal side to create an axis [44,271].

To be able to fully control the cell microenvironment, all relevant cues must be included, one such aspect not addressed in this project is the effect of physical forces upon cellular development. An example of this, relevant to this thesis is the differentiation of osteoblasts that become trapped within bone matrix that they are forming, increased pressure and other factors are thought to lead to its differentiation into osteocytes. The impact that different forces have upon cells could be further studied using the HOTs to pattern cells on surfaces with varying elasticity, similar to the classic experiment completed by Adam Engler (2006) [272].

One area of the patterning process that requires further development is the application of automation, currently the process of patterning is labour intensive. The appropriate implementation of LabView based automation could significantly improve this, raising throughput and reducing labour for patterning experiments.

Furthermore, the incorporation of different technologies to compliment the HOTs patterning system, including the Nanokick technique, whereby mesenchymal stem cells are stimulated with high frequency vibrations, leading to differentiation into osteoblasts [273]. The combination of the HOTs patterning setup with such pioneering technological developments will ensure that it continues to be used as a cutting edge micropatterning tool.

References

1. Mason, C. & Dunnill, P. A brief definition of regenerative medicine. *Regen. Med.* **3,** 1–5 (2008).

2. Langer, R. & Vacanti, J. P. Tissue Engineering. *Science (80-.).* **260,** 920–926 (1993).

3. Bianco, P. & Robey, P. G. Stem cells in tissue engineering. *Nature* **414,** 118–121 (2001).

4. Bisceglie, V. Über die antineoplastische immunität; heterologe einpflanzung von tumoren in hühner-embryonen. *Ztschr Krebsforsch* **40,** 122–140 (1933).

5. Burke, J. F., Yannas, I. V, Quinby, W. C., Bondoc, C. C. & Jung, W. K. Successful use of a physiologically acceptable artificial skin in the treatment of extensive burn injury. *Ann. Surg.* **194,** 413–428 (1981).

6. Fuchs, J. R., Nasseri, B. A. & Vacanti, J. P. Tissue Engineering: A 21st Century Solution to Surgical Reconstruction. *Ann Thorac Surg* **72,** 577–591 (2001).

7. Stock, U. A. & Vacanti, J. P. Tissue Engineering: Current State and Prospects. *Annu. Rev. Med.* **52,** 443–451 (2001).

8. Kim, M. & Evans, D. in *Topics in Tissue Engineering* **2,** 1–22 (2005).

9. Weiner, L. Definitions and criteria for stem cells. *Neural Stem Cells* **438,** 3–4 (2008).

10. Lillegraven, J. Use of the term 'trophoblast' for tissues in therian mammals. *J. Morphol.* **183,** 293–299 (1985).

11. Ström, S. *et al.* Mechanical isolation of the inner cell mass is effective in derivation of new human embryonic stem cell lines. *Hum. Reprod.* **22,** 3051–8 (2007).

12. Wiles, M. V & Johansson, B. M. Analysis of factors controlling primary germ layer formation and early hematopoiesis using embryonic stem cell in vitro differentiation. *Leukemia* **11 Suppl 3,** 454–6 (1997).

13. Ostrer, H., Wilson, D. I. & Hanley, N. Human embryo and early fetus research. *Clin. Genet.* **70,** 98–107 (2006).

14. Evans, M. & Kaufman, M. Establishment in culture of pluripotential cells from mouse embryos. *Nature* **292,** 154–156 (1981).

15. Klimanskaya, I., Chung, Y., Becker, S., Lu, S.-J. & Lanza, R. Human embryonic stem cell lines derived from single blastomeres. *Nature* **444,** 481–485 (2006).

16. Starr, R. *et al.* Distinct roles for leukemia inhibitory factor receptor a-chain and gp130 in cell type-specific signal transduction. *J. Biol. Chem.* **272,** 19982–19986 (1997).

17. Ginis, I. *et al.* Differences between human and mouse embryonic stem cells. *Dev. Biol.* **269,** 360–380 (2004).

18. Muthusamy, T., Mukherjee, O., Menon, R., Megha, P. B. & Panicker, M. M. A method to identify and isolate pluripotent human stem cells and mouse epiblast stem cells using lipid body-associated retinyl ester fluorescence. *Stem Cell Reports* **3,** 169–184 (2014).

19. Ratajczak, M. Z., Machalinski, B., Wojakowski, W., Ratajczak, J. & Kucia, M. A hypothesis for an embryonic origin of pluripotent Oct-4(+) stem cells in adult bone marrow and other tissues. *Leuk. Off. J. Leuk. Soc. Am. Leuk. Res. Fund, U.K* **21,** 860–867 (2007).

20. Wilson, A. & Trumpp, A. Bone-marrow haematopoietic-stem-cell niches. *Nat. Rev. Immunol.* **6,** 93–106 (2006).

21. Pittenger, M. F. *et al.* Multilineage Potential of Adult Human Mesenchymal Stem Cells. *Science (80-.).* **284,** 143–147 (1999).

22. Krampera, M., Pizzolo, G., Aprili, G. & Franchini, M. Mesenchymal stem cells for bone, cartilage, tendon and skeletal muscle repair. *Bone* **39,** 678–683 (2016).

23. Summer, R. & Fine, A. Mesenchymal Progenitor Cell Research. *Proc. Am. Thorac. Soc.* **5,** 707–710 (2008).

24. Gurdon, J. Nuclear reprogramming and stem cell creation. *Proc. Natl. Acad. Sci.* **100,** 11819–11822 (2003).

25. Takahashi, K. & Yamanaka, S. Induction of Pluripotent Stem Cells from Mouse Embryonic and Adult Fibroblast Cultures by Defined Factors. *Cell* **126,** 663–676 (2006).

26. Okita, K., Ichisaka, T. & Yamanaka, S. Generation of germline-competent induced pluripotent stem cells. *Nature* **448,** 313–317 (2007).

27. Wernig, M. *et al.* In vitro reprogramming of fibroblasts into a pluripotent ES-cell-like state. *Nature* **448,** 318–324 (2007).

28. Maherali, N. *et al.* Directly reprogrammed fibroblasts show global epigenetic remodeling and widespread tissue contribution. *Cell Stem Cell* **1,** 55–70 (2007).

29. Takahashi, K. *et al.* Induction of pluripotent stem cells from adult human fibroblasts by defined factors. *Cell* **131,** 861–872 (2007).

30. Ye, F. *et al.* HDAC1 and HDAC2 regulate oligodendrocyte differentiation by disrupting

the beta-catenin-TCF interaction. *Nat. Neurosci.* **12,** 829–838 (2009).

31. Colman, A. & Dreesen, O. Pluripotent stem cells and disease modeling. *Cell Stem Cell* **5,** 244–247 (2009).

32. Kaufman, D. S., Hanson, E. T., Lewis, R. L., Auerbach, R. & Thomson, J. a. Hematopoietic colony-forming cells derived from human embryonic stem cells. *Proc. Natl. Acad. Sci. U. S. A.* **98,** 10716–10721 (2001).

33. Brizzi, M. F., Tarone, G. & Defilippi, P. Extracellular matrix, integrins, and growth factors as tailors of the stem cell niche. *Curr. Opin. Cell Biol.* **24,** 645–51 (2012).

34. Becker, P. S. *et al.* Adhesion receptor expression by hematopoietic cell lines and murine progenitors: modulation by cytokines and cell cycle status. *Exp. Hematol.* **27,** 533–41 (1999).

35. Scadden, D. T. The stem-cell niche as an entity of action. *Nature* **441,** 1075–9 (2006).

36. Le Bras, S. & Van Doren, M. Development of the male germline stem cell niche in Drosophila. *Dev. Biol.* **294,** 92–103 (2006).

37. Hardy, R. W., Tokuyasu, K. T., Lindsley, D. L. & Garavito, M. The germinal proliferation center in the testis of Drosophila melanogaster. *J. Ultrastruct. Res.* **69,** 180–190 (1979).

38. Kawase, E., Wong, M. D., Ding, B. C. & Xie, T. Gbb/Bmp signaling is essential for maintaining germline stem cells and for repressing bam transcription in the Drosophila testis. *Development* **131,** 1365–75 (2004).

39. Schulz, C. *et al.* A misexpression screen reveals effects of bag-of-marbles and TGF beta class signaling on the Drosophila male germ-line stem cell lineage. *Genetics* **167,** 707–23 (2004).

40. VanDussen, K. L. *et al.* Notch signaling modulates proliferation and differentiation of intestinal crypt base columnar stem cells. *Development* **139,** 488–497 (2012).

41. Gregorieff, A. & Clevers, H. Wnt signaling in the intestinal epithelium : from endoderm to cancer Wnt signaling in the intestinal epithelium : from endoderm to cancer. 877–890 (2005). doi:10.1101/gad.1295405

42. Spradling, a, Drummond-Barbosa, D. & Kai, T. Stem cells find their niche. *Nature* **414,** 98–104 (2001).

43. Kennedy, M. B. *et al.* Signaling Mechanisms Controlling Cell Fate and Embryonic Patterning. 1–19 (2014). doi:10.1101/cshperspect.a005975

44. Avilés, E. C., Wilson, N. H. & Stoeckli, E. T. Sonic hedgehog and Wnt: antagonists in morphogenesis but collaborators in axon guidance. *Front. Cell. Neurosci.* **7,** 86 (2013).

45. Kristensen, D. M., Kalisz, M. & Nielsen, J. H. Cytokine signalling in embryonic stem cells. *APMIS* **113,** 756–772 (2005).

46. Lane, S. W., Williams, D. A. & Watt, F. M. Modulating the stem cell niche for tissue regeneration. *Nat Biotech* **32,** 795–803 (2014).

47. Studzinski, G. P. Cell Differentiation In Vitro : Model Systems. *Encycl. Life Sci.* 1–5 (2001). doi:10.1038/npg.els.0002565

48. Edmondson, R., Broglie, J. J., Adcock, A. F. & Yang, L. Three-dimensional cell culture systems and their applications in drug discovery and cell-based biosensors. *Assay Drug Dev. Technol.* **12,** 207–18 (2014).

49. Bhadriraju, K. & Chen, C. S. Engineering cellular microenvironments to improve cell-based drug testing. *Drug Discov. Today* **7,** 612–620 (2002).

50. Birgersdotter, A., Sandberg, R. & Ernberg, I. Gene expression perturbation in vitro - A growing case for three-dimensional (3D) culture systems. *Semin. Cancer Biol.* **15,** 405–412 (2005).

51. Itzhaki, I. *et al.* Modelling the long QT syndrome with induced pluripotent stem cells. *Nature* **471,** 225–229 (2011).

52. Burridge, P. W., Keller, G., Gold, J. D. & Wu, J. C. Production of De Novo Cardiomyocytes: Human Pluripotent Stem Cell Differentiation and Direct Reprogramming. *Cell Stem Cell* **10,** 16–28 (2012).

53. Alford, P. W., Feinberg, A. W., Sheehy, S. P. & Parker, K. K. Biohybrid Thin Films for Measuring Contractility in Engineered Cardiovascular Muscle. *Biomaterials* **31,** 3613–3621 (2010).

54. Grosberg, A., Alford, P. W., McCain, M. L. & Parker, K. K. Ensembles of engineered cardiac tissues for physiological and pharmacological study: Heart on a chip(). *Lab Chip* **11,** 4165–4173 (2011).

55. Benam, K. H. *et al.* Engineered In Vitro Disease Models. *Annu. Rev. Pathol.* **10,** 195–262 (2015).

56. Shen, M. M. & Leder, P. Leukemia inhibitory factor is expressed by the preimplantation uterus and selectively blocks primitive ectoderm formation in vitro. *Proc. Natl. Acad. Sci. U. S. A.* **89,** 8240–8244 (1992).

57. Grabel, L. B. & Casanova, J. E. The outgrowth of parietal endoderm from mouse

teratocarcinoma stem-cell embryoid bodies. *Differentiation* **32,** 67–73 (1986).

58. Shukla, S. *et al.* Synthesis and Organization of Hyaluronan and Versican by Embryonic Stem Cells Undergoing Embryoid Body Differentiation. *J. Histochem. Cytochem.* **58,** 345–358 (2010).

59. Keller, G. M. In vitro differentiation of embryonic stem cells. *Curr. Opin. Cell Biol.* **7,** 862–869 (1995).

60. Itskovitz-Eldor, J. *et al.* Differentiation of human embryonic stem cells into embryoid bodies compromising the three embryonic germ layers. *Mol. Med.* **6,** 88–95 (2000).

61. Li, L. *et al.* Distinct GATA6- and laminin-dependent mechanisms regulate endodermal and ectodermal embryonic stem cell fates. *Development* **131,** 5277–5286 (2004).

62. Weitzer, G. in *Handbook of Experimental Pharmacology* **174,** 21–51 (2006).

63. Fatehullah, A., Tan, S. H. & Barker, N. Organoids as an in vitro model of human development and disease. *Nat. Cell Biol.* **18,** 246–54 (2016).

64. Miyoshi, H. & Stappenbeck, T. S. In vitro expansion and genetic modification of gastrointestinal stem cells as organoids. *Nat. Protoc.* **8,** 2471–2482 (2013).

65. Chuong, C. & Richardson, M. Pattern formation today. *Int. J. ...* **53,** 653–658 (2009).

66. Wolpert, L. Pattern formation in biological development. *Sci. Am.* **239,** 154–164 (1978).

67. Meinhardt, H. & Gierer, A. Pattern formation by local self-activation and lateral inhibition. *BioEssays* **22,** 753–60 (2000).

68. Chuong, C.-M., Wu, P., Plikus, M., Jiang, T. & Bruce Widelitz, R. Engineering Stem Cells into Organs: Topobiological Transformations Demonstrated by Beak, Feather, and Other Ectodermal Organ Morphogenesis. *Curr. Top. Dev. Biol.* **72,** 237–274 (2005).

69. Baker, R. E., Schnell, S. & Maini, P. K. Waves and patterning in developmental biology: vertebrate segmentation and feather bud formation as case studies. *Int. J. Dev. Biol.* **53,** 783–94 (2009).

70. Kondo, S., Iwashita, M. & Yamaguchi, M. How animals get their skin patterns: fish pigment pattern as a live Turing wave. *Int. J. Dev. Biol.* **53,** 851–6 (2009).

71. Shankland, M. & Goodman, C. S. Development of the dendritic branching pattern of the Medial Giant Interneuron in the grasshopper embryo. *Dev. Biol.* **92,** 489–506 (1982).

72. Davies, J. Intracellular and extracellular regulation of ureteric bud morphogenesis. *J. Anat.* **198,** 257–64 (2001).

73. Michael, L. & Davies, J. a. Pattern and regulation of cell proliferation during murine ureteric bud development. *J. Anat.* **204,** 241–55 (2004).

74. J. Sawkins, M., M. Shakesheff, K., J. Bonassar, L. & R. Kirkham, G. 3D Cell and Scaffold Patterning Strategies in Tissue Engineering. *Recent Pat. Biomed. Eng.* **6,** 3–21 (2013).

75. Hochmuth, R. M. Micropipette aspiration of living cells. *J. Biomech.* **33,** 15–22 (2000).

76. Lu, Z., Moraes, C., Ye, G., Simmons, C. a & Sun, Y. Single cell deposition and patterning with a robotic system. *PLoS One* **5,** e13542 (2010).

77. Mokaberi, B. *et al.* Automated Nanomanipulation with Atomic Force Microscopes. in *Proc. IEEE Int'l Conf. on Robotics & Automation (ICRA '07)* **781,** 1–7 (2007).

78. Kane, RS, Takayama, S, Ostuni, E, Ingber, DE, Whitesides, G. Patterning proteins and cells using soft lithography. *Biomaterials* **20,** 2363–2376 (1999).

79. Di Carlo, D., Wu, L. Y. & Lee, L. P. Dynamic single cell culture array. *Lab Chip* **6,** 1445–9 (2006).

80. Torisawa, Y., Mosadegh, B. & Luker, G. Microfluidic hydrodynamic cellular patterning for systematic formation of co-culture spheroids. *Integr. ...* **1,** 649–654 (2009).

81. Dalby, M. J., Riehle, M. O., Yarwood, S. J., Wilkinson, C. D. W. & Curtis, A. S. G. Nucleus alignment and cell signaling in fibroblasts: Response to a micro-grooved topography. *Exp. Cell Res.* **284,** 274–282 (2003).

82. Wen-Wen, L., Zhen-Ling, C. & Xing-Yu, J. Methods for cell micropatterning on two-dimensional surfaces and their applications in biology. *Fenxi Huaxue/ Chinese J. Anal. Chem.* **37,** 943–949 (2009).

83. Lee, H., Liu, Y., Ham, D. & Westervelt, R. M. Integrated cell manipulation system--CMOS/microfluidic hybrid. *Lab Chip* **7,** 331–7 (2007).

84. Ino, K. *et al.* Cell culture arrays using magnetic force-based cell patterning for dynamic single cell analysis. *Lab Chip* **8,** 134–42 (2008).

85. Nilsson, A., Petersson, F., Jönsson, H. & Laurell, T. Acoustic control of suspended particles in micro fluidic chips. *Lab Chip* **4,** 131–5 (2004).

86. Hsu, C.-H., Di Carlo, D., Chen, C., Irimia, D. & Toner, M. Microvortex for focusing, guiding and sorting of particles. *Lab Chip* **8,** 2128–34 (2008).

87. Ashkin, A, Dziedzic, JM, Bjorkholm, JE, and Chu, S. Observation of a single-beam gradient-force optical trap for dielectric particles in air. *Opt. Lett.* **11,** 288–290 (1986).

88. Gosse, C. & Croquette, V. Magnetic tweezers: micromanipulation and force measurement at the molecular level. *Biophys. J.* **82,** 3314–29 (2002).

89. Tanase, M., Biais, N. & Sheetz, M. in *Cell Mechanics* (ed. Biology, Y. W. and D. E. D. B. T.-M. in C.) **Volume 83,** 473–493 (Academic Press, 2007).

90. Bernassau, a L. *et al.* Controlling acoustic streaming in an ultrasonic heptagonal tweezers with application to cell manipulation. *Ultrasonics* (2013). doi:10.1016/j.ultras.2013.04.019

91. Frommelt, T. *et al.* Microfluidic Mixing via Acoustically Driven Chaotic Advection. *Phys. Rev. Lett.* **100,** 34502 (2008).

92. Laurell, T., Petersson, F. & Nilsson, A. Chip integrated strategies for acoustic separation and manipulation of cells and particles. *Chem. Soc. Rev.* **36,** 492–506 (2007).

93. Shi, J. *et al.* Acoustic tweezers: patterning cells and microparticles using standing surface acoustic waves (SSAW). *Lab Chip* **9,** 2890–5 (2009).

94. MacDonald, M. P. *et al.* Creation and manipulation of three-dimensional optically trapped structures. *Science* **296,** 1101–3 (2002).

95. Hoogenboom, J. P., Vossen, D. L. J., Faivre-Moskalenko, C., Dogterom, M. & van Blaaderen, a. Patterning surfaces with colloidal particles using optical tweezers. *Appl. Phys. Lett.* **80,** 4828 (2002).

96. Blaaderen, A. van & Wiltzius, P. Growing large, well oriented colloidal crystals. *Adv. Mater.* **9,** 1991–1993 (1997).

97. Guffey, M. J. & Scherer, N. F. All-optical patterning of Au nanoparticles on surfaces using optical traps. *Nano Lett.* **10,** 4302–8 (2010).

98. Abbott, J. D. *et al.* Stromal cell-derived factor-1α plays a critical role in stem cell recruitment to the heart after myocardial infarction but is not sufficient to induce homing in the absence of injury. *Circulation* **110,** 3300–3305 (2004).

99. Ara, T. *et al.* Impaired colonization of the gonads by primordial germ cells in mice lacking a chemokine, stromal cell-derived factor-1 (SDF-1). *Proc. Natl. Acad. Sci. U. S. A.* **100,** 5319–5323 (2003).

100. Jung, Y. *et al.* Regulation of SDF-1 (CXCL12) production by osteoblasts; a possible mechanism for stem cell homing. *Bone* **38,** 497–508 (2016).

101. Urbich, C. *et al.* Soluble factors released by endothelial progenitor cells promote migration of endothelial cells and cardiac resident progenitor cells. *J. Mol. Cell. Cardiol.* **39,** 733–742 (2005).

102. Chen, T. L., Shen, W.-J. & Kraemer, F. B. Human BMP-7/OP-1 induces the growth and differentiation of adipocytes and osteoblasts in bone marrow stromal cell cultures*. *J. Cell. Biochem.* **82,** 187–199 (2001).

103. Shea, C. M., Edgar, C. M., Einhorn, T. A. & Gerstenfeld, L. C. BMP Treatment of C3H10T1/2 Mesenchymal Stem Cells Induces Both Chondrogenesis and Osteogenesis. *J. Cell. Biochem.* **90,** 1112–1127 (2003).

104. Tabata, T. & Takei, Y. Morphogens, their identification and regulation. *Development* **131,** 703–712 (2004).

105. Duprez, D. *et al.* Overexpression of BMP-2 and BMP-4 alters the size and shape of developing skeletal elements in the chick limb. *Mech. Dev.* **57,** 145–157 (1996).

106. Peppas, N. A., Hilt, J. Z., Khademhosseini, A. & Langer, R. Hydrogels in biology and medicine: From molecular principles to bionanotechnology. *Adv. Mater.* **18,** 1345–1360 (2006).

107. Chen, H.-C. Boyden chamber assay. *Methods Mol. Biol.* **294,** 15–22 (2005).

108. Boyden, S. The chemotactic effect of mixtures of antibody and antigen on polymorphonuclear leucocytes. *J. Exp. Med.* **115,** 453–466 (1962).

109. Zigmond, S. H. & Hirsch, J. G. Leukocyte locomotion and chemotaxis. New methods for evaluation, and demonstration of a cell-derived chemotactic factor. *J. Exp. Med.* **137,** 387–410 (1973).

110. Zicha, D., Dunn, G. a & Brown, a F. A new direct-viewing chemotaxis chamber. *J. Cell Sci.* **99,** 769–775 (1991).

111. Kim, M. & Kim, T. Diffusion-Based and Long-Range Concentration Gradients of Multiple Chemicals for Bacterial Chemotaxis Assays. *Anal. Chem.* **82,** 9401–9409 (2010).

112. El-Ali, J., Sorger, P. K. & Jensen, K. F. Cells on chips. *Nature* **442,** 403–411 (2006).

113. Jeon, N. L. *et al.* M.Generation of Solution and Surface Gradients using Microfluidic Systems Langmuir 16, [Text Text], [CAS]. **2000 SRC,** 8311–8316 (2000).

114. Chen, Y.-C. *et al.* Single-cell Migration Chip for Chemotaxis-based Microfluidic Selection of Heterogeneous Cell Populations. *Sci. Rep.* **5,** 9980 (2015).

115. Varma, S. & Voldman, J. A Cell-Based Sensor of Fluid Shear Stress for Microfluidics. *Lab Chip* **15,** 1563–1573 (2015).

116. Zhou, Y. & Lin, Q. Microfluidic flow-free generation of chemical concentration

gradients. *Sensors Actuators B Chem.* **190,** 334–341 (2014).

117. Anderson, J. M. & Shive, M. S. Biodegradation and biocompatibility of PLA and PLGA microspheres. *Adv. Drug Deliv. Rev.* **64, Supple,** 72–82 (2012).

118. Freiberg, S. & Zhu, X. X. Polymer microspheres for controlled drug release. *Int. J. Pharm.* **282,** 1–18 (2004).

119. Kirby, G. T. S. *et al.* PLGA-Based Microparticles for the Sustained Release of BMP-2. *Polymers (Basel).* **3,** 571–586 (2011).

120. White, L. J. *et al.* Accelerating protein release from microparticles for regenerative medicine applications. *Mater. Sci. Eng. C. Mater. Biol. Appl.* **33,** 2578–83 (2013).

121. Choi, Y. *et al.* Inhibition of tumor growth by biodegradable microspheres containing all-trans-retinoic acid in a human head-and-neck cancer xenograft. *Int. J. Cancer* **107,** 145–148 (2003).

122. Chun, K. W., Yoo, H. S., Yoon, J. J. & Park, T. G. Biodegradable PLGA microcarriers for injectable delivery of chondrocytes: effect of surface modification on cell attachment and function. *Biotechnol. Prog.* **20,** 1797–1801 (2004).

123. Simmons, C. A., Alsberg, E., Hsiong, S., Kim, W. J. & Mooney, D. J. Dual growth factor delivery and controlled scaffold degradation enhance in vivo bone formation by transplanted bone marrow stromal cells. *Bone* **35,** 562–569 (2016).

124. Mahoney, M. J. & Saltzman, W. M. Transplantation of brain cells assembled around a programmable synthetic microenvironment. *Nat. Biotechnol.* **19,** 934–939 (2001).

125. Newman, K. D. & McBurney, M. W. Poly(d,l lactic-co-glycolic acid) microspheres as biodegradable microcarriers for pluripotent stem cells. *Biomaterials* **25,** 5763–5771 (2004).

126. Tatard, V. M. *et al.* Pharmacologically active microcarriers releasing glial cell line – derived neurotrophic factor: Survival and differentiation of embryonic dopaminergic neurons after grafting in hemiparkinsonian rats. *Biomaterials* **28,** 1978–1988 (2007).

127. Ashkin, A. Acceleration and trapping of particles by radiation pressure. *Phys. Rev. Lett.* **24,** 156–159 (1970).

128. Ashkin, A and Dziedzic, J. Optical Levitation by Radiation Pressure. *Appl. Phys. Lett.* **19,** 283–285 (1971).

129. Ashkin, A. History of optical trapping and manipulation of small-neutral particle, atoms, and molecules. *Sel. Top. Quantum Electron. IEEE …* **6,** 841–856 (2000).

130. Ashkin, A., Dziedzic, J. & Yamane, T. Optical trapping and manipulation of single cells using infrared laser beams. *Nature* **330,** 769–771 (1987).

131. Ashkin, A. & Dziedzic, J. M. Optical trapping and manipulation of viruses and bacteria. *Science (80-.).* **235,** 1517–1520 (1987).

132. Liesener, J., Reicherter, M., Haist, T. & Tiziani, H. Multi-functional optical tweezers using computer-generated holograms. *Opt. Commun.* **0,** 1–6 (2000).

133. Neuman, K. C. & Block, S. M. Optical trapping. *Rev. Sci. Instrum.* **75,** 2787–2809 (2004).

134. Molloy, J. E. & Padgett, M. J. Lights, action: Optical tweezers. *Contemp. Phys.* **43,** 241–258 (2002).

135. Ashkin, A. Forces of a single-beam gradient laser trap on a dielectric sphere in the ray optics regime. *Biophys. J.* **61,** 569–582 (1992).

136. Svoboda, K. & Block, S. M. Biological applications of optical forces. *Annu. Rev. Biophys. Biomol. Struct.* **23,** 247–285 (1994).

137. Ke, P. C. & Gu, M. Characterization of trapping force on metallic mie particles. *Appl. Opt.* **38,** 160–167 (1999).

138. Gouesbet, G. Validity of the localized approximation for arbitrary shaped beams in the generalized Lorenz–Mie theory for spheres. *J. Opt. Soc. Am. A* **16,** 1641–1650 (1999).

139. Novotny, L., Bian, R. & Xie, X. Theory of Nanometric Optical Tweezers. *Phys. Rev. Lett.* **79,** 645–648 (1997).

140. Grier, D. G. Optical tweezers in colloid and interface science. *Curr. Opin. Colloid Interface Sci.* **2,** 264–270 (1997).

141. Visscher, K., Brakenhoff, G. J. & Krol, J. J. Micromanipulation by 'multiple' optical traps created by a single fast scanning trap integrated with the bilateral confocal scanning laser microscope. *Cytometry* **14,** 105–114 (1993).

142. Dufresne, E. R. & Grier, D. G. Optical tweezer arrays and optical substrates created with diffractive optics. *Rev. Sci. Instrum.* **69,** 1974 (1998).

143. Reicherter, M., Haist, T., Wagemann, E. & Tiziani, H. Optical particle trapping with computer-generated holograms written on a liquid-crystal display. *Opt. Lett.* **24,** 608–610 (1999).

144. Hossack, W., Theofanidou, E., Crain, J., Heggarty, K. & Birch, M. High-speed holographic optical tweezers using a ferroelectric liquid crystal microdisplay. *Opt.*

Express **11,** 2053–2059 (2003).

145. Jared, D., Turner, R. & Johnson, K. Electrically addressed spatial light modulator that uses a dynamic memory. *Opt. Lett.* **16,** 1785–1787 (1991).

146. Curtis, J., Koss, B. & Grier, D. Dynamic holographic optical tweezers. *Opt. Commun.* **207,** 169–175 (2002).

147. Igasaki, Y., Li, F., Yoshida, N. & Toyoda, H. High efficiency electrically-addressable phase-only spatial light modulator. *Opt. Rev.* **6,** 339–344 (1999).

148. Jordan, P. *et al.* Creating permanent 3D arrangements of isolated cells using holographic optical tweezers. *Lab Chip* **5,** 1224–8 (2005).

149. Wang, C., Chowdhury, S., Gupta, S. K. & Losert, W. Optical micromanipulation of active cells with minimal perturbations: direct and indirect pushing. *J. Biomed. Opt.* **18,** 45001 (2013).

150. Kirkham, G. R. *et al.* Precision assembly of complex cellular microenvironments using holographic optical tweezers. *Sci. Rep.* **5,** 8577 (2015).

151. Kim, S., Jun, J., Shin, J. & Kang, Y. Hydrostatic pressure can control osteogenesis and osteoclastogenesis when stromal cells and osteoclast precursor cells are cocultured. *Tissue Eng. Regen. Med.* **7,** 388–394 (2010).

152. Nagatomi J, Arulanandam B, Metzger D, Meunier A, and B. R. Cyclic Pressure Affects Osteoblast Functions Pertinent to Osteogenesis. *Ann. Biomed. Eng.* **31,** 917–923 (2003).

153. Nichols, J., Evans, E. P. & Smith, a G. Establishment of germ-line-competent embryonic stem (ES) cells using differentiation inhibiting activity. *Development* **110,** 1341–8 (1990).

154. Zentner, G. M. *et al.* Biodegradable block copolymers for delivery of proteins and water-insoluble drugs. *J. Control. Release* **72,** 203–15 (2001).

155. De Bank, P. A., Kellam, B., Kendall, D. A. & Shakesheff, K. M. Surface engineering of living myoblasts via selective periodate oxidation. *Biotechnol. Bioeng.* **81,** 800–808 (2003).

156. Helfrich, M. H. *et al.* Expression of nitric oxide synthase isoforms in bone and bone cell cultures. *J. Bone Miner. Res.* **12,** 1108–1115 (1997).

157. Ecarot-charrier, B., Glorieux, F. H., Rest, M. V. A. N. D. E. R. & Pereira, G. Osteoblasts Isolated from Mouse Calvaria Initiate Matrix Mineralization in Culture Collagen Synthesis Collagens synthesized by osteoblasts during a 24-h incuba-. **4,** 639–643

158. Sherwood, S. W., Rush, D., Ellsworth, J. L. & Schimke, R. T. Defining cellular senescence in IMR-90 cells: a flow cytometric analysis. *Proc. Natl. Acad. Sci. U. S. A.* **85,** 9086–9090 (1988).

159. Nichol, J. W., Koshy, S., Bae, H., Hwang, C. M. & Khademhosseini, A. Cell-laden microengineered gelatin methacrylate hydrogels. *Biomaterials* **31,** 5536–5544 (2011).

160. Ramon-Azcon, J. *et al.* Gelatin methacrylate as a promising hydrogel for 3D microscale organization and proliferation of dielectrophoretically patterned cells. *Lab Chip* **12,** 2959–2969 (2012).

161. Gibson, G. M., Leach, J., Keen, S., Wright, A. J. & Padgett, M. J. Measuring the accuracy of particle position and force in optical tweezers using high-speed video microscopy. *Opt. Express* **16,** 405–412 (2008).

162. Leach, J. *et al.* Interactive approach to optical tweezers control. *Appl. Opt.* **45,** 897–903 (2006).

163. Bowman, R. W. *et al.* 'Red Tweezers': Fast, customisable hologram generation for optical tweezers. *Comput. Phys. Commun.* **185,** 268–273 (2014).

164. Ingram, P. N., Chen, Y. & Yoon, E. POLYHEMA SOFT LITHOGRAPY FOR SELECTIVE CELL SEEDING , MIGRATION BLOCKING , AND HIGH-THROUGHPUT SUSPENSION CELL CULTURE. in *17th International Conference on Miniaturized Systems for Chemistry and Life Sciences* 1451–1453 (2013).

165. Fukazawa, H., Nakano, S., Mizuno, S. & Uehara, Y. Inhibitors of Anchorage-Independent Growth Affect the Growth of Transformed Cells on Poly (2-Hydroxyethyl. *Int. J. cancer* **882,** 876–882 (1996).

166. Spiller, K. L. *et al.* A novel method for the direct fabrication of growth factor-loaded microspheres within porous nondegradable hydrogels: controlled release for cartilage tissue engineering. *J. Control. Release* **157,** 39–45 (2012).

167. Bible, E. *et al.* The support of neural stem cells transplanted into stroke-induced brain cavities by PLGA particles. *Biomaterials* **30,** 2985–94 (2009).

168. Sah, H. A new strategy to determine the actual protein content of poly(lactide-co-glycolide) microspheres. *J. Pharm. Sci.* **86,** 1315–8 (1997).

169. Zernicka-Goetz, M. First cell fate decisions and spatial patterning in the early mouse embryo. *Semin. Cell Dev. Biol.* **15,** 563–72 (2004).

170. Wennekamp, S., Mesecke, S., Nedelec, F. & Hiiragi, T. A self-organization framework for symmetry breaking in the mammalian embryo. *Nat Rev Mol Cell Biol* **14,** 452–459

(2013).

171. Morrison, S. J. & Scadden, D. T. The bone marrow niche for haematopoietic stem cells. *Nature* **505,** 327–34 (2014).

172. Chiou, P. Y., Ohta, A. T. & Wu, M. C. Massively parallel manipulation of single cells and microparticles using optical images. *Nature* **436,** 370–372 (2005).

173. Ma, Z. *et al.* Laser patterning for the study of MSC cardiogenic differentiation at the single-cell level. *Light. Sci. Appl.* **2,** (2013).

174. Leach, J. *et al.* Manipulation of live mouse embryonic stem cells using holographic optical tweezers. *Eur. Cells Mater.* **16,** 2262 (2009).

175. Tan, Y. *et al.* Probing the mechanobiological properties of human embryonic stem cells in cardiac differentiation by optical tweezers. *J. Biomech.* **45,** 123–128 (2016).

176. Martin, M. J., Muotri, A., Gage, F. & Varki, A. Human embryonic stem cells express an immunogenic nonhuman sialic acid. *Nat Med* **11,** 228–232 (2005).

177. Jacobs, C. L. *et al.* in *Applications of Chimeric Genes and Hybrid Proteins - Part B: Cell Biology and Physiology* (ed. Jeremy Thorner, S. D. E. and J. N. A. B. T.-M. in E.) **Volume 327,** 260–275 (Academic Press, 2000).

178. Yarema, K. J., Mahal, L. K., Bruehl, R. E., Rodriguez, E. C. & Bertozzi, C. R. Metabolic delivery of ketone groups to sialic acid residues. Application to cell surface glycoform engineering. *J. Biol. Chem.* **273,** 31168–31179 (1998).

179. Wenzel, R. N. Resistance of solid surfaces to wetting by water. *J. Ind. Eng. Chem. (Washington, D. C.)* **28,** 988–994 (1936).

180. Righini, G. C. in *Diffractive Optics and Optical Microsystems* (eds. Martellucci, S. & Chester, A. N.) 391–398 (Springer US, 1997). doi:10.1007/978-1-4899-1474-3_34

181. Hinds, K. D. *et al.* PEGylated insulin in PLGA microparticles. In vivo and in vitro analysis. *J. Control. Release* **104,** 447–60 (2005).

182. Makadia, H. K. & Siegel, S. J. Poly Lactic-co-Glycolic Acid (PLGA) as Biodegradable Controlled Drug Delivery Carrier. *Polymers (Basel).* **3,** 1377–1397 (2011).

183. Wan, C., He, Q., McCaigue, M., Marsh, D. & Li, G. Nonadherent cell population of human marrow culture is a complementary source of mesenchymal stem cells (MSCs). *J. Orthop. Res.* **24,** 21–28 (2006).

184. Liang, R. *et al.* Positive effects of an extracellular matrix hydrogel on rat anterior cruciate ligament fibroblast proliferation and collagen mRNA expression. *J. Orthop. Transl.* **3,**

114–122 (2015).

185. Minett, T., Tighe, B., Lydon, M. & Rees, D. Requirements for cell spreading on polyHEMA coated culture substrates. *Cell Biol. Int. Rep.* **8,** 151–159 (1984).

186. Bettinger, C. J., Langer, R. & Borenstein, J. T. Engineering Substrate Micro- and Nanotopography to Control Cell Function. *Angew. Chem. Int. Ed. Engl.* **48,** 5406–5415 (2009).

187. Gurdon, J. B. & Bourillot, P. Y. Morphogen gradient interpretation. *Nature* **413,** 797–803 (2001).

188. Schnorrer, F. & Dickson, B. J. Axon Guidance: Morphogens Show the Way. *Curr. Biol.* **14,** R19–R21 (2016).

189. Zou, Y. & Lyuksyutova, A. I. Morphogens as conserved axon guidance cues. *Curr. Opin. Neurobiol.* **17,** 22–28 (2007).

190. Hong, C., Hor, H. & Tang, B. L. Sonic hedgehog as a chemoattractant for adult NPCs. *Cell Adh. Migr.* **4,** 1–3 (2010).

191. Rangamani, P. & Iyengar, R. Modelling cellular signalling systems. *Essays Biochem.* **45,** 83–94 (2008).

192. Waters, J. C. Accuracy and precision in quantitative fluorescence microscopy. *J. Cell Biol.* **185,** 1135–1148 (2009).

193. Sherman, E. *et al.* Using fluorescence correlation spectroscopy to study conformational changes in denatured proteins. *Biophys. J.* **94,** 4819–27 (2008).

194. Levitt, J. a. *et al.* Simultaneous FRAP, FLIM and FAIM for measurements of protein mobility and interaction in living cells. *Biomed. Opt. Express* **6,** 3842 (2015).

195. Gendron, P.-O., Avaltroni, F. & Wilkinson, K. J. Diffusion Coefficients of Several Rhodamine Derivatives as Determined by Pulsed Field Gradient--Nuclear Magnetic Resonance and Fluorescence Correlation Spectroscopy. *J. Fluoresc.* **18,** 1093–1101 (2008).

196. Chiu, V. C. & Haynes, D. H. High and low affinity Ca2+ binding to the sarcoplasmic reticulum: use of a high-affinity fluorescent calcium indicator. *Biophys. J.* **18,** 3–22 (1977).

197. Neri, S., Mariani, E., Meneghetti, A., Cattini, L. & Facchini, A. Calcein-Acetyoxymethyl Cytotoxicity Assay: Standardization of a Method Allowing Additional Analyses on Recovered Effector Cells and Supernatants. *Clin. Diagn. Lab. Immunol.* **8,** 1131–1135 (2001).

198. Bilati, U., Allémann, E. & Doelker, E. Nanoprecipitation versus emulsion-based techniques for the encapsulation of proteins into biodegradable nanoparticles and process-related stability issues. *AAPS PharmSciTech* **6,** 594–604 (2005).

199. Bratosin, D., Mitrofan, L., Palii, C., Estaquier, J. & Montreuil, J. Novel fluorescence assay using calcein-AM for the determination of human erythrocyte viability and aging. *Cytom. Part A* **66,** 78–84 (2005).

200. Siepmann, J., Faisant, N., Akiki, J., Richard, J. & Benoit, J. Effect of the size of biodegradable microparticles on drug release: experiment and theory. *J. Control. Release* **96,** 123–134 (2004).

201. Klose, D., Siepmann, F., Elkharraz, K., Krenzlin, S. & Siepmann, J. How porosity and size affect the drug release mechanisms from PLGA-based microparticles. *Int. J. Pharm.* **314,** 198–206 (2006).

202. Laing, J. M. *et al.* Intranasal administration of the growth compromised HSV-2 vector ΔRR prevents kainate induced seizures and neuronal loss in rats and mice. *Mol. Ther.* **13,** 870–881 (2007).

203. Campisi, J. & d'Adda di Fagagna, F. Cellular senescence: when bad things happen to good cells. *Nat Rev Mol Cell Biol* **8,** 729–740 (2007).

204. Beauséjour, C. *et al.* Reversal of human cellular senescence: roles of the p53 and p16 pathways. *EMBO J.* **22,** 4212–4222 (2003).

205. Hayflick, L. The limited in vitro lifetime of human diploid cell strains. *Exp. Cell Res.* **37,** 614–636 (1965).

206. Dimri, G. P. *et al.* A biomarker that identifies senescent human cells in culture and in aging skin in vivo. *Proc. Natl. Acad. Sci.* **92,** 9363–9367 (1995).

207. Coppé, J.-P. *et al.* A Human-Like Senescence-Associated Secretory Phenotype Is Conserved in Mouse Cells Dependent on Physiological Oxygen. *PLoS One* **5,** e9188 (2010).

208. Guo, Y.-L., Chakraborty, S., Rajan, S. S., Wang, R. & Huang, F. Effects of oxidative stress on mouse embryonic stem cell proliferation, apoptosis, senescence, and self-renewal. *Stem Cells Dev.* **19,** 1321–31 (2010).

209. Aubin, H. *et al.* Directed 3D cell alignment and elongation in microengineered hydrogels. *Biomaterials* **31,** 6941–6951 (2011).

210. Hutson, C. B. *et al.* Synthesis and characterization of tunable poly(ethylene glycol): gelatin methacrylate composite hydrogels. *Tissue Eng. Part A* **17,** 1713–23 (2011).

211. Tamura, M. *et al.* Click-crosslinkable and photodegradable gelatin hydrogels for cytocompatible optical cell manipulation in natural environment. *Sci. Rep.* **5,** 15060 (2015).

212. Van Den Bulcke, A. I. *et al.* Structural and Rheological Properties of Methacrylamide Modified Gelatin Hydrogels. *Biomacromolecules* **1,** 31–38 (2000).

213. Galis, Z. S. & Khatri, J. J. Matrix metalloproteinases in vascular remodeling and atherogenesis: the good, the bad, and the ugly. *Circ. Res.* **90,** 251–262 (2002).

214. Ashe, H. L. & Briscoe, J. The interpretation of morphogen gradients. 385–394 (2004). doi:10.1242/dev.02238

215. Eltaher, H. M., Yang, J., Shakesheff, K. M. & Dixon, J. E. Highly efficient intracellular transduction in three-dimensional gradients for programming cell fate. *Acta Biomater.* 1–12 (2016). doi:10.1016/j.actbio.2016.06.004

216. Genzer, J. & Bhat, R. Surface-Bound Soft Matter Gradients. *Langmuir* **24,** 2294–2317 (2008).

217. Nguyen, E. H., Schwartz, M. P. & Murphy, W. L. Biomimetic Approaches to Control Soluble Concentration Gradients in Biomaterials. 483–492 doi:10.1002/mabi.201000448

218. Sant, S., Hancock, M. J., Donnelly, J. P., Iyer, D. & Khademhosseini, A. Biomimetic gradient hydrogels for tissue engineering. *Can. J. Chem. Eng.* **88,** 899–911 (2010).

219. Smith, A. G. *et al.* Inhibition of pluripotential embryonic stem cell differentiation by purified polypeptides. *Nature* **336,** 688–690 (1988).

220. Williams, R. L. *et al.* Myeloid leukaemia inhibitory factor maintains the developmental potential of embryonic stem cells. *Nature* **336,** 684–687 (1988).

221. Heo, J., Lee, J.-S., Chu, I.-S., Takahama, Y. & Thorgeirsson, S. S. Spontaneous differentiation of mouse embryonic stem cells in vitro: Characterization by global gene expression profiles. *Biochem. Biophys. Res. Commun.* **332,** 1061–1069 (2005).

222. Abe, K. *et al.* Endoderm-Specific Gene Expression in Embryonic Stem Cells Differentiated to Embryoid Bodies. *Exp. Cell Res.* **229,** 27–34 (1996).

223. Nishikawa, S. I., Nishikawa, S., Hirashima, M., Matsuyoshi, N. & Kodama, H. Progressive lineage analysis by cell sorting and culture identifies FLK1+VE-cadherin+ cells at a diverging point of endothelial and hemopoietic lineages. *Development* **125,** 1747–1757 (1998).

224. Giachino, C., Orlando, L. & Turinetto, V. Maintenance of genomic stability in mouse

embryonic stem cells: Relevance in aging and disease. *Int. J. Mol. Sci.* **14,** 2617–2636 (2013).

225. Gaztelumendi, N. & Nogués, C. Chromosome instability in mouse embryonic stem cells. *Sci. Rep.* **4,** 5324 (2014).

226. Andäng, M. *et al.* Histone H2AX-dependent GABA(A) receptor regulation of stem cell proliferation. *Nature* **451,** 460–4 (2008).

227. Chen, W. *et al.* Retinoic acid regulates germ cell differentiation in mouse embryonic stem cells through a Smad-dependent pathway. *Biochem. Biophys. Res. Commun.* **418,** 571–577 (2012).

228. Silva, C. *et al.* Expression profile of male germ cell-associated genes in mouse embryonic stem cell cultures treated with all-trans retinoic acid and testosterone. *Mol. Reprod. Dev.* **76,** 11–21 (2009).

229. Li, H. *et al.* Differentiation of neurons from neural precursors generated in floating spheres from embryonic stem cells. *BMC Neurosci.* **10,** 122 (2009).

230. Koubova, J. *et al.* Retinoic acid regulates sex-specific timing of meiotic initiation in mice. *Proc. Natl. Acad. Sci. U. S. A.* **103,** 2474–9 (2006).

231. Lin, Y., Gill, M. E., Koubova, J. & Page, D. C. Germ-cell-intrinsic and extrinsic factors govern meiotic initiation in mouse embryos. *Science (80-.).* **322,** 1685–1687 (2008).

232. Rhinn, M. & Dolle, P. Retinoic acid signalling during development. *Development* **139,** 843–858 (2012).

233. Mueller, R. L., Huang, C. & Ho, R. K. Spatio-temporal regulation of Wnt and retinoic acid signaling by tbx16/spadetail during zebrafish mesoderm differentiation. *BMC Genomics* **11,** 492 (2010).

234. Jeong, Y.-I. *et al.* Preparation of poly(dl-lactide-co-glycolide) microspheres encapsulating all-trans retinoic acid. *Int. J. Pharm.* **259,** 79–91 (2003).

235. Çirpanli, Y., ünlü, N., Çaliş, S. & Atİlla Hincal, A. Formulation and in-vitro characterization of retinoic acid loaded poly (lactic-co-glycolic acid) microspheres. *J. Microencapsul.* **22,** 877–889 (2005).

236. Bilati, U., Allémann, E. & Doelker, E. Development of a nanoprecipitation method intended for the entrapment of hydrophilic drugs into nanoparticles. *Eur. J. Pharm. Sci.* **24,** 67–75 (2005).

237. Ogawa, Y., Yamamoto, M., Okada, H., Yashiki, T. & Shimamoto, T. A New Technique to Efficiently Entrap Leuprolide Acetate into Microcapsules of Polylactic Acid or

Copoly(Lactic/Glycolic) Acid. *Chem. Pharm. Bul.* **36,** 1095–1103 (1988).

238. Kress, H. *et al.* Cell stimulation with optically manipulated microsources. *Nat. Methods* **6,** 905–9 (2009).

239. Yu, S. R. *et al.* Fgf8 morphogen gradient forms by a source-sink mechanism with freely diffusing molecules. *Nature* **461,** 533–6 (2009).

240. Karkkainen, M. J. *et al.* Vascular endothelial growth factor C is required for sprouting of the first lymphatic vessels from embryonic veins. *Nat. Immunol.* **5,** 74–80 (2004).

241. Hayamizu, T. F., Sessions, S. K., Wanek, N. & Bryant, S. V. Effects of localized application of transforming growth factor β1 on developing chick limbs. *Dev. Biol.* **145,** 164–173 (1991).

242. DeFalco, T., Takahashi, S. & Capel, B. Two distinct origins for Leydig cell progenitors in the fetal testis. *Dev. Biol.* **352,** 14–26 (2011).

243. Bogani, D. *et al.* Loss of mitogen-activated protein kinase kinase kinase 4 (MAP3K4) reveals a requirement for MAPK signalling in mouse sex determination. *PLoS Biol.* **7,** (2009).

244. Hadjidakis, D. J. & Androulakis, I. I. Bone remodeling. *Ann. N. Y. Acad. Sci.* **1092,** 385–396 (2006).

245. Frost, H. M. & STRAATSMA, C. R. Bone remodelling dynamics. *Plast. Reconstr. Surg.* **33,** 315–333 (1964).

246. Suda, T. *et al.* Modulation of Osteoclast Differentiation and Function by the New Members of the Tumor Necrosis Factor Receptor and Ligand Families. *Endocr. Rev.* **20,** 345–357 (1999).

247. Sanchez-Fernandez, M. A., Gallois, A., Riedl, T., Jurdic, P. & Hoflack, B. Osteoclasts control osteoblast chemotaxis via PDGF-BB/PDGF receptor beta signaling. *PLoS One* **3,** e3537 (2008).

248. Wang, D. *et al.* Isolation and Characterization of MC3T3-E1 Preosteoblast Subclones with Distinct In Vitro and In Vivo Differentiation/Mineralization Potential. *J. Bone Miner. Res.* **14,** 893–903 (1999).

249. Czekanska, E. M., Stoddart, M. J., Ralphs, J. R., Richards, R. G. & Hayes, J. S. A phenotypic comparison of osteoblast cell lines versus human primary osteoblasts for biomaterials testing. *J. Biomed. Mater. Res. Part A* **102,** 2636–2643 (2014).

250. Taylor, M. *et al.* 3D chemical characterization of frozen hydrated hydrogels using ToF-SIMS with argon cluster sputter depth profiling. *Biointerphases* **11,** 02A301 (2015).

251. Koch, L., Gruene, M., Unger, C. & Chichkov, B. Laser assisted cell printing. *Curr. Pharm. Biotechnol.* **14,** 91–7 (2013).

252. Steffen, A. *et al.* Rac function is crucial for cell migration but is not required for spreading and focal adhesion formation. *J. Cell Sci.* **126,** 4572–4588 (2013).

253. Lhoest, J., Wagner, M. S., Tidwell, C. D. & Castner, D. G. Characterization of adsorbed protein films by time of flight secondary ion mass spectrometry. *Biomed. Mater.* (2001).

254. Kundra, V., Anand-Apte, B., Feig, L. A. & Zetter, B. R. The chemotactic response to PDGF-BB: Evidence of a role for Ras. *J. Cell Biol.* **130,** 725–731 (1995).

255. Ahlen, K. *et al.* Platelet-derived growth factor-BB modulates membrane mobility of beta1 integrins. *Biochem. Biophys. Res. Commun.* **314,** 89–96 (2004).

256. Clunn, G., Refson, J., Lymn, J. & Hughes, A. Platelet-Derived Growth Factor β-Receptors Can Both Promote and Inhibit Chemotaxis in Human Vascular Smooth Muscle Cells. *Arterioscler. Thromb. Vasc. Biol.* **17,** 2622–2629 (1997).

257. Trinkle-Mulcahy, L. *et al.* Identifying specific protein interaction partners using quantitative mass spectrometry and bead proteomes. *J. Cell Biol.* **183,** 223–239 (2008).

258. Wells, L. a. & Sheardown, H. Extended release of high pI proteins from alginate microspheres via a novel encapsulation technique. *Eur. J. Pharm. Biopharm.* **65,** 329–335 (2007).

259. Brown, B. N. *et al.* Surface Characterisation of Extracellular Matrix Scaffolds. *Biomaterials* **31,** 428–437 (2010).

260. Shard, A. G. *et al.* Argon Cluster Ion Beams for Organic Depth Profiling: Results from a VAMAS Interlaboratory Study. *Anal. Chem.* **84,** 7865–7873 (2012).

261. Winograd, N. Molecular Depth Profiling. *Surf Interface Anal.* **45,** 3–8 (2015).

262. Piwowar, A. M. *et al.* C60-ToF SIMS imaging of frozen hydrated HeLa cells. *Surf. Interface Anal.* **45,** 302–304 (2013).

263. Keles, H., Naylor, A., Clegg, F. & Sammon, C. Investigation of factors influencing the hydrolytic degradation of single PLGA microparticles. *Polym. Degrad. Stab.* **119,** 228–241 (2015).

264. Keles, H., Naylor, A., Clegg, F. & Sammon, C. The application of non-linear curve fitting routines to the analysis of mid-infrared images obtained from single polymeric microparticles. *Analyst* **139,** 2355–2369 (2014).

265. Keles, H., Naylor, A., Clegg, F. & Sammon, C. Studying the release of hGH from

gamma-irradiated PLGA microparticles using ATR-FTIR imaging. *Vib. Spectrosc.* **71,** 76–84 (2014).

266. Cosson, S. & Lutolf, M. P. Microfluidic patterning of protein gradients on biomimetic hydrogel substrates. *Methods Cell Biol.* **121,** 91–102 (2014).

267. Khademhosseini, A. *et al.* Microfluidic patterning for fabrication of contractile cardiac organoids. *Biomed. Microdevices* **9,** 149–157 (2007).

268. Kim, Y., Lin, Q., Glazer, P. M. & Yun, Z. Hypoxic tumor microenvironment and cancer cell differentiation. *Curr. Mol. Med.* **9,** 425–34 (2009).

269. Quail, D. & Joyce, J. Microenvironmental regulation of tumor progression and metastasis. *Nat. Med.* **19,** 1423–1437 (2013).

270. Balkwill, F. R., Capasso, M. & Hagemann, T. The tumor microenvironment at a glance. *J. Cell Sci.* **125,** 5591–5596 (2012).

271. Takaoka, K. & Hamada, H. Cell fate decisions and axis determination in the early mouse embryo. *Development* **139,** 3 LP-14 (2011).

272. Engler, A. J., Sen, S., Sweeney, H. L. & Discher, D. E. Matrix elasticity directs stem cell lineage specification. *Cell* **126,** 677–89 (2006).

273. Pemberton, G. D. *et al.* Nanoscale stimulation of osteoblastogenesis from mesenchymal stem cells: nanotopography and nanokicking. *Nanomedicine (Lond).* **10,** 547–60 (2015).

8. Appendix

8.1 Rheology of ULGT agarose

8.1.1 Methods

The visco-elastic gelation properties of agarose were determined by rheological measurements across a given temperature range. All measurements were performed using an Anton Parr Modular Compact Rheometer (MCR302) using PP50 (parallel plate of 50 mm diameter) (SN16858) set at 0.5 mm gap. 1.0% (w/v) Agarose type IX-A ULGT was prepared in PBS and autoclaved at 126°C for 22 minutes prior to use using a prestige medical classic portable autoclave.

8.1.2 Results

Figure 8.1 shows the rheology data for agarose ULGT hydrogel (1.0%), it was determined that the agarose remained a liquid at 37^{o}C and then gelled rapidly at temperatures below 25^{o}C, and once the hydrogel structure was formed, melting would not occur below 55^{o}C.

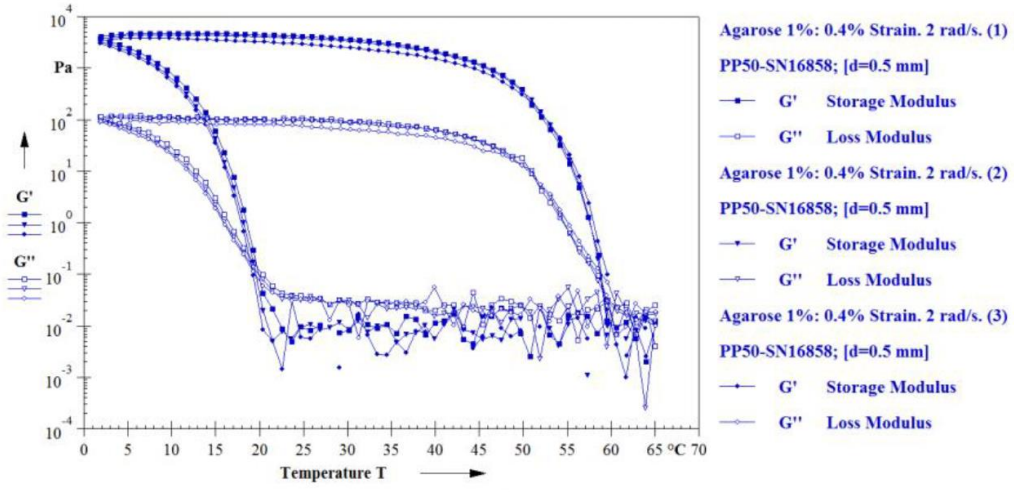

Figure 8.1 Rheology temperature sweep

A temperature sweep from 65-2°C and then back up to 65°C at 4% γ and 2 rad/s ω for a 1% agarose solution (n=3). Heating and cooling rate was 1°C/min and to prevent solvent evaporation, samples were surrounded by silicone oil DC 200/200cs fluid prior to measurements.

8.2 FCS batch testing

8.2.1 Methods

Five batches of serum were tested as detailed in. mES cells were induced to form embryoid bodies (EBs) by a mass suspension method containing each serum. Cells were detached and passaged under standard trypsinisation procedures. After centrifugation, the pellet was resuspended in standard cell culture medium and seeded to a non-adherent 60 mm petri dish at 200,000 cells/mL density. After 3 days, the EBs were imaged (Figure 8.2) and then dissociated, using trypsin/EDTA treatment, to yield a cell suspension.

Cells were then seeded in tissue-culture-treated plastic 6-well plates coated with 0.1% gelatin as described previously (Section 2.5.1), and were then cultured for 7 days in standard culture medium for germ layer analysis (Section 2.7). Cells were also differentiated in osteogenic medium as per Section 6.2.1, with added dexamethasone (10 μM) for 21 days.

8.2.2 Results

Table 8.1 shows the five new sera batches tested and then Figure 8.2, the quality testing of the cells cultured in each serum containing medium.

Table 8.1 Sera for batch testing

Serum	Supplier	Lot number
Old	Sigma-Aldrich	091M3397
A	Sigma-Aldrich	034M3398
B	Life technologies	07F1686K
C	Labtech	500-31003H
D	Labtech	500-30502
E	HyClone	SYL20005

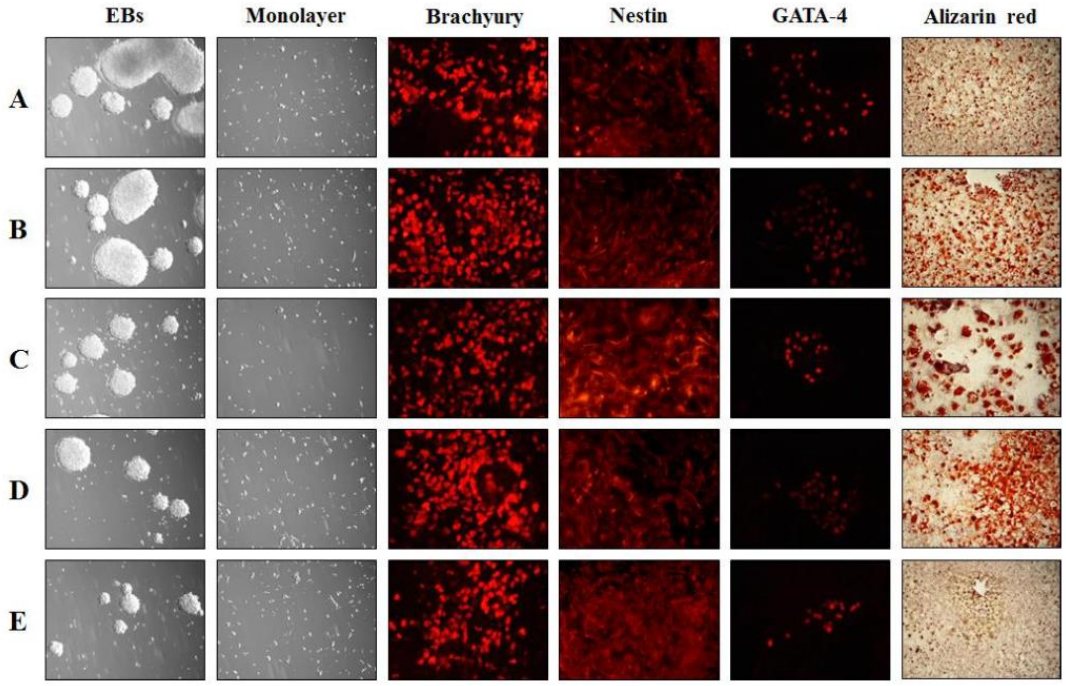

Figure 8.2 Serum batch testing results

Sera (A-E) used for the culture of CGR8 mES cells, ability to form embryoid bodies (EBs), differentiate into the three germ layers, and form bone nodules following osteogenic differentiation (bone nodule formation shown by alizarin red staining. Figure created with help from Dr. Emily Britchford (University of Nottingham, UK).

8.3 ToF-SIMS peak shape

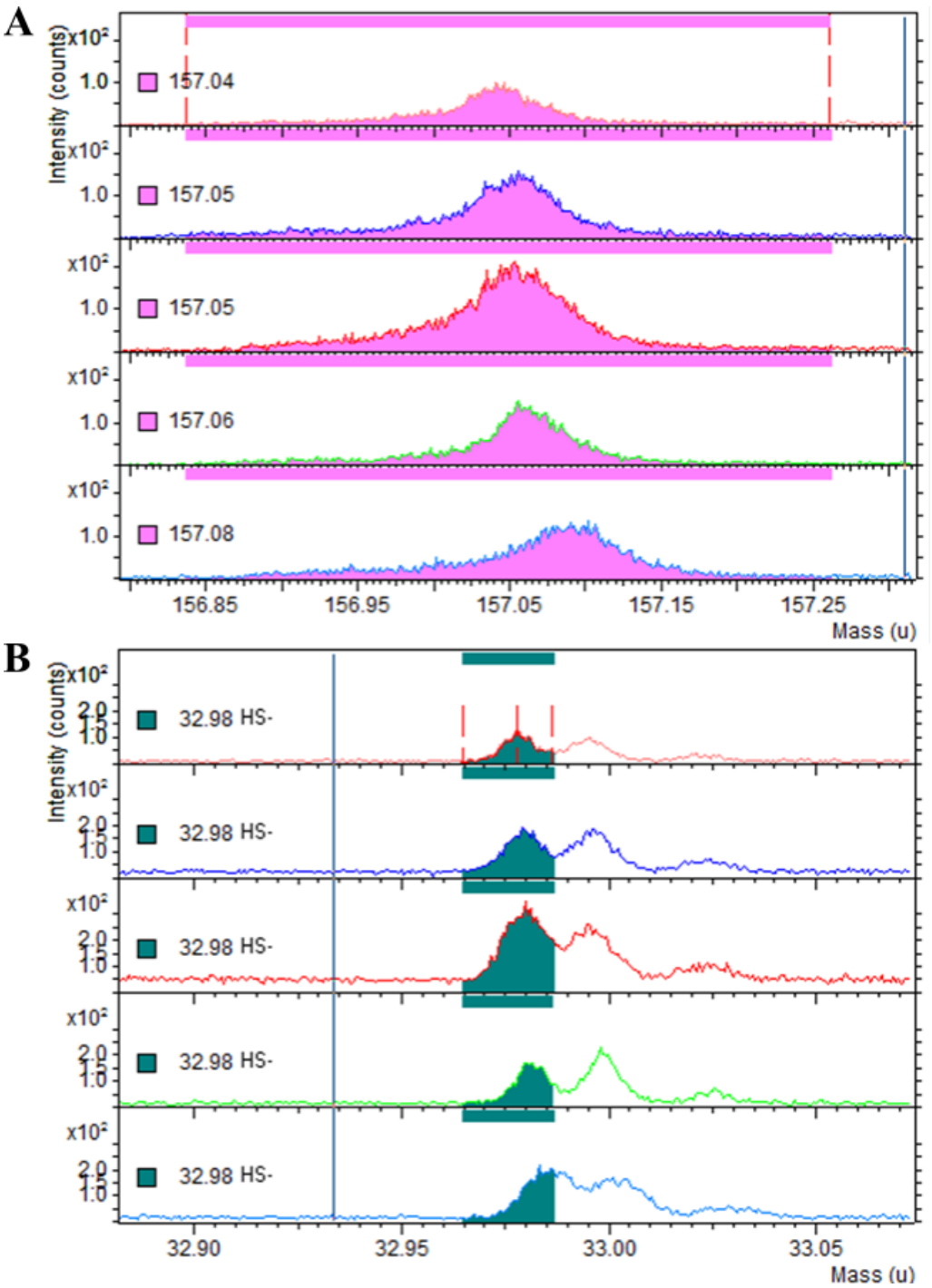

Figure 8.3 Peak shapes used for ToF-SIMS sample analysis

A. shows the peak shape for the HS peak and B. the $C_4H_5NO_2S$, with each of the samples displayed from top to bottom.